Universidad Complutense de Madrid
Facultad de Ciencias Físicas
Dpto. de Física Atómica, Molecular y Nuclear

Grupo de Física Nuclear
(Unidad asociada al Instituto de Estructura de la Materia, CSIC)

CARACTERIZACIÓN, MEJORA Y DISEÑO DE ESCÁNERES PET PRECLÍNICOS

ESTHER VICENTE TORRICO

Tesis dirigida por:

Dr. José Manuel Udías Moinelo
Dr. Joaquín López Herraiz
Dr. Juan José Vaquero López

Madrid 2012

Übung macht den Meister

Anonymous

Contents

AGRADECIMIENTOS

Si he de poner fecha de inicio a cómo he llegado hasta aquí, ésa debería ser en mis últimos años de carrera, cuando asistí a la defensa de una tesis y, tras terminar casi hundida en la silla en la fase de preguntas, tuve claro lo que quería hacer tras terminar la carrera: todo menos un doctorado. Y es así, queridos lectores, como empecé mi trayectoria de seguir fielmente mis primeras impresiones. A esto hay que añadir que en mi último año de carrera quería buscar un trabajo académicamente dirigido (o pseudo proyecto de fin de carrera, para que los ingenieros me entiendan) que uniera las dos especialidades que había estudiado: Astrofísica y Física Fundamental. Así fue como me fui a hablar con José Luis Contreras, quien trabajaba en proyectos relacionados con Física de altas energías y astropartículas (que bien unificaban mis dos especialidades). Fue en esa conversación cuando oí por primera vez hablar de PET y me encandiló (por ser cursi, que en los agradecimientos no te lo toman tan a mal) y, continuando con mi trayectoria de seguir fielmente mis primeros pensamientos, ya no pude escuchar nada más. Adiós Astrofísica, hola Física Médica. Gracias, José Luis, por aquella conversación y por toda tu ayuda e interés durante estos años.

Una vez abierta la veda de agradecimientos, abróchense los cinturones porque va para largo:

Gracias, José Manuel, por escribirme ese mail en el que me invitabas a continuar trabajando en PET tras el trabajo dirigido; por esos primeros meses y por los siguientes años que sucedieron a mi paso por el hospital hasta ahora, en los que he aprendido mucho. Gracias, Samuel y Joaquín, porque fuisteis mis primeros compañeros en este largo viaje; he aprendido muchísimo con vosotros y de vosotros; pero sobre todo, gracias por vuestra amistad. Gracias a ti, Rosa, 'la hija del conserje', la sevillana más salá que siempre tiene una palabra de ánimo y un 'qué bien lo pasamos'. Gracias a mis compañeros de doctorado, con los que pasé tan buenos momentos por Sevilla, Madrid y Salamanca.

Gracias a toda la gente del LIM, donde tuve el honor de aprender durante dos años de un grupo tan heterogéneo y multidisciplinar: a Manolo por darme la oportunidad de trabajar en su laboratorio y por sus sabios consejos; a Juanjo por guiarme en mi paso por el LIM y por esos momentos inolvidables en SUINSA (por aquél entonces no era aún SEDECAL) en los que medíamos el tiempo de decaimiento del mismo Derenzo, tras observar la poca resistencia de las bolsas de basura al ser usadas como centrifugadoras. Gracias a mis compañeros del LIM: a Mónica, mi compi de mesa 'desalineada'; a David, que aunque estuvo muy poco tiempo, dejó un poso muy grande y siempre será recordado como 'blandito'; a Lorena Ricón por su dulzura y su incansable risa contagiosa: Spidercerdo! (ella me entiende); a Trajana por su tremenda eficiencia y mucho más por su gran apoyo y su amistad; a Jesús por toda su ayuda y cariño en el tiempo que estuvo por el LIM; a Edu y Cleo (te ha tocado en el lote del LIM, guapa), mis ex-vecinillos de barrio, de esas parejas entrañables con las que da gusto pasar el rato (¡qué bien lo pasamos por Costa Rica!); a Santi Redondo (o Santi pequeño), Gus, Gonzalo y Rebe, por mil situaciones divertidas y entrañables, en especial que vinieran a Valencia a mi DEA, lo recuerdo con gran cariño; a Angelico, por ser siempre el alma de la fiesta y contagiar a todo el mundo su buen humor; a Vero, la del plan de dominar el mundo, por preocuparse siempre por mí y estar siempre dispuesta ayudar; a Chemaco, por su ingenio y astucia, porque siempre que se estropea algo en el LIM es culpa suya (¡jeje!) y por su destreza con la guitarra (Chema, ¿cuándo ensayamos?); a Irina, mi gran compañera de voz; a Cris, por su alegría que contagia (y hablando de voz… ¿alguien ha dicho karaoke?); a Paula por su dulzura, a Juanolas, por su sentido del humor y lo fácil que es 'colarle' una rima (¡coorrecto!), a Judit por preocuparse por mí y tener siempre una palabra de ánimo y de cariño; a los antiguos buffer: Alvarico, Josete (¡vaya dúo!) y Javi Mora, por la alegría que siempre transmitían; a Joost, el holandés entrañable con el que me encanta hablar de la vida en general acompañados de una cerveza fresquita y a Ana (¡eres parte del LIM!), que siempre es una alegría cuando se pasa a vernos; a Javi Navas, mi cuentachistes preferido, por hacerme reír y tratarme siempre con tanto cariño; a Quique y María (otra para el lote del LIM), que aún siguen siendo mis vecinillos, porque siempre es genial quedar con ellos y tomarse unas 'tapas'; a Yasser, nuestro querido cubano, que allá por el año 2006 era joven y que hace unos 'puecos' alucinantes; a Fidel,

persona divertida donde las haya (¡eres un grande!); a Sandrica, por todas las adquisiciones que me ha ayudado a hacer y por la dulzura y cariño con que siempre me trata; a María La Calle, una gran guía turística de Montreal y genial maestra de biología (tú también, Javi, ¡no te pongas celosón!); a Eu, por su disponibilidad ('dime sitio y hora y allí estaré') y sonrisa de oreja a oreja; a Eva, esa marchosilla con tantísimo encanto; a Marina, porque siempre supo apagar la vela; a Alexia, Juan Abascal, Marco, Lorena, Carmen, Elena, Ángela, Gonzalo Higuera y a los más nuevos, que aún no conozco mucho, pero nos quedan muchas ocasiones: Natalia, Aurora, Claudia, Carlos Crespillo, Juanjo Sánchez y otros, que aún no conozco sus nombres. Gracias también a las 'psicolocas': Aran, María Mayoral, Olaya y Maite y a Javier Pascau, Javi Sánchez, Marisa, Cristina Santa Marta (¡esa física que resuena un montón!) y Carlos Antoranz. Y muy especialmente a Santi Reig, una bellísima persona que se nos fue demasiado pronto.

Un punto y aparte, porque cambio de grupo, pero no cambien de 'canash' que aún hay mucho 'mash':

Tras mi paso por el LIM, volví al GFN, donde pude conocer a Elenita, pequeñita de estatura pero una grandísima compañera y amiga; gracias por estar siempre ahí, en lo bueno y en lo malo. Gracias también a Cristina, la lepera más simpaticona; a César, siempre dispuesto a echar una mano o… una casa en Boston (¡mil gracias por aquello!); a Laura, por su risa contagiosa; a Oscar, porque desde los cursos de doctorado puse cara a la genial persona que se escondía tras el 'otro Oscar'; a Paloma, por su gran eficiencia y, sobre todo, por su buen humor y la gracia con la que cuenta sus anécdotas de sonámbulos (o de lo que sea), divirtiendo a todo el mundo en las cenas de grupo; a Pablo ('qué callao estoy hoy, Pablo') por sus canciones y comentarios y por cambiarme los tóners (te dije que lo pondría, ¿no?); a Jacobo ('¿qué?'), el galleguiño despistadillo; a Esteban, por acercarnos la calidez que caracteriza a los ticos; a Bruno, ese chiquillo callado que estuvo al principio en mi despacho con los mismos espectros todos los días (y no te preocupes, hombre, que ya no me acuerdo que me llamaste 'rajada' el día que me dio la apendicitis, jeje) y a Luis Mario, por su apoyo e interés y su buen humor (a ratos… jeje, ¡es broma!). Gracias también a Joaquín Retamosa, José María y Elvira. Para los que prefieren la lengua de Shakespeare en vez de la de Cervantes (o más bien, la entienden mejor): thank you, Martin (the 'football porra' winner) for being always so nice; Khaled: thank you for being my taxi-driver!, and for the nice conversations during each trip and thank you, Henryk, the locksmith of the group. Gracias a los 'nuevos' (y será así para siempre, jeje) porque le habéis devuelto la vidilla al grupo: a mis gallinitas, mis geniales compañeras de despacho (tú también estás en este lote, Elena, no te pongas nerviosa…): a Vicky (Victoooria!), por su dulzura e inocencia (pero cuidadito como te coja el cepillo de dientes…) y a Paulyn, perdón, digo, a Paula y a Mailyn: a Paula (she loves cats!) por su alegría y porque pierde el autobús si es necesario para que no decaiga el momento y a Mailyn por su risa tan sincera (como todo en ella) y su acento… encantador. Ah! Y gracias al 'acoplado', Edu, un químico que siempre quiso ser físico, aunque aún no se ha dado cuenta. Siguiendo con los 'nuevos': gracias a Vadym, porque es una fuente de ingresos seguros cuando apuestas con él (y esto es muy valioso en época de crisis, oiga); a Richi, que las mata callando, porque es emo… cionante acudir a sus fiestas y gracias a Raúl, 'pa que veas que has calao, mi arma' (aunque no te quedes a mi tesis). Gracias a los que estuvieron en el grupo y ya se fueron (¡se os echa de menos!): Rosita: la bondad personificada, Borja: el viajante del tiempo (pero sólo 5 minutos… ¿hacia adelante o hacia atrás?), Paloma, Dani, Marta, Miguelito, Joaquín III, Javi, Raquel: la reina de los plátanos y Armando, nuestro gran escritor, por las agradables conversaciones de regreso a casa y por enseñarnos a salvar el mundo con un hipercubo. Y no podría dejar de dar las gracias a Mary, Bea, Yotuella y Sofi, porque han contribuido a mantener mi ánimo durante estos últimos meses de escritura.

Gracias a toda la gente del Instituto de la Materia del CSIC con las que he tratado gracias a mi beca, porque me han tratado siempre fenomenal y con mucho cariño: a Eduardo Garrido, mi tutor, por interesarse siempre por cómo me van las cosas y por los cafés tan agradables que nos tomábamos en mis visitas al CSIC y a María Teresa, Eva, Concha y Carmen, por su siempre cálida ayuda.

A toda la gente que conocí en mis estancias, que también prefieren a Shakespeare (pobres, no tienen ni idea…): From Davis: Thank you, Dr. Qi, for giving me the opportunity of working in your

Lab; thanks to everyone in the group, specially: thank you, Michel: my favorite English teacher and a very good friend, Andrea: my favorite Italian friend, Anita and Jessica (I miss you guys!). From Maryland: Thank you Jurgen and Mike for letting me work with you and being so kind with me. Y al resto, en español, que lo entienden perfectamente: gracias a Esther, mi tocaya del labo, por su gran ayuda y cercanía y tratarme con tanto cariño; gracias a Laura y Antonio por hacer que nuestra estancia fuera tan especial (¡sois estupendos!), al igual que Irene y Pepe (genial la casualidad de cómo nos conocimos), por lo bien que lo pasamos.

Gracias a mis hermanitas postizas: Afri (preguntadle cómo se cerró un cliclo cuando estuvimos viviendo juntas, jeje), por ser desde hace tantos años mi mejor amiga que, aunque no vea mucho, siempre está presente (¡la vaaaaaaaaaca!). Y gracias a Rocío, mi hermanita pequeña, por estar siempre pendiente de cómo me va todo y por su espíritu emprendedor, digno de imitar.

Gracias también a mis compis del cole, de la facultad (compañeros de carrera y compañeros de ahora, de otros departamentos), amiguetes varios del CSIC, a toda la pandilla Goofy y a todas las personas que se han cruzado en mi camino en este tiempo.

Y por último, pero no por ello menos importante, gracias a mi familia, en especial a mis padres, Alfonso y Mariví, dos grandísimas personas (y no es porque sean mis padres), por su cariño, apoyo y confianza. Y gracias a ti, Alex, por estar siempre ahí, en lo bueno y en lo malo, por apoyarme, por aguantarme (¡que no es poco!), por hacerme reír, por toda tu ayuda y por hacerme sentir segura y confiar más en mí misma.

No puedo, aunque me gustaría (porque ya sabéis lo que me gusta enrollarme cual persiana, como acabo de demostrar), personalizar todos los momentos y situaciones particulares por las que os debo tanto a cada uno de vosotros, porque quedaría raro si la sección de agradecimientos fuera más larga que la tesis en sí, pero sabed que sin todos y cada uno de vosotros hoy no estaría aquí y esta tesis no habría sido posible. Por todo ello:

¡UN MILLÓN DE GRACIAS!

Motivation and Objectives

In 1953, the young daughter of a Rhode Island farmer traveled to Boston to find a doctor to diagnose a neurological problem that left her unable to read. When her neurosurgeon at Massachusetts General Hospital could not help her, he enlisted the help of a colleague, Dr. Gordon L. Brownell. As Time magazine reported the following year, Dr. Brownell along with William H. Sweet developed a scanning machine [Sweet, 1951, Brownell *et al.*, 1969, Burnham and Brownell, 1972] that isolated, within a third of an inch (8.5 mm), the location of a tumor that the neurosurgeon successfully removed from the girl's brain. The technology Dr. Brownell invented was the basis of positron emission tomography (PET). A few years later, in 1973, Michael E. Phelps and collaborators built the first PET tomograph, known as PETT I [Ter-Pogossian *et al.*, 1975, Phelps *et al.*, 1975]. Phelps was one of the first to show how different parts of the brain are activated when performing mental tasks.

Since this first PET scanner, positron emission tomography has been established in oncology, cardiology and neurology. The extension of this technique to preclinical research has represented a great challenge ever since the development of the first dedicated small-animal PET system in the mid 1990s ([Watanabe *et al.*, 1992, Pavlopoulos and Tzanakos, 1993, 1996, Tzanakos and Pavlopoulos, 1993, Bloomfield *et al.*, 1995]), with the required improvement in performance in terms of spatial resolution and sensitivity. The interest of this improvement lies in the fact that images with higher resolution can improve our capability of studying human diseases using animal models.

Besides the higher resolution requirements, many small-animal PET system designs deal with new geometries which may also hinder direct application of algorithms initially developed for clinical scanners. This poses the necessity of developing protocols adapted to the specific small animal systems in use and, at the same time, leads to questions about how the typical sources of error in clinical scanners scale to small animal systems.

In order to improve the quantification properties of PET images in clinical and preclinical practice, data- and image-processing methods are subject of intense research and development. The evaluation of such methods often relies on the use of simulated data and images since these offer control of the ground truth. Monte Carlo simulations are widely used for PET since they can take into account all the processes involved in PET imaging, from the emission of the positron to the detection of the photons by the detectors. Simulation techniques have become an indispensable complement to a wide range of problems that could not be addressed by experimental or analytical approaches [Rogers, 2006].

Simulations of PET scanners with Monte Carlo methods also allow the optimization of the design of new scanners, the study of singled-out factors affecting image quality and the validation of correction methodologies for effects such as pile-up and dead-time, scatter, attenuation, detector misalignments, partial volume, etc; everything with the aim of improving image quantification, as well as developing and testing new image reconstruction algorithms. Another major advantage of simulations is that they make possible to study parameters that are not measurable in practice.

This thesis is embedded in one of the research lines carried out at the Nuclear Physics Group (Grupo de Física Nuclear, GFN) of the Universidad Complutense de Madrid in close collaboration with the Medical Imaging Laboratory (Laboratorio de Imagen Médica, LIM) of Hospital General Universitario Gregorio Marañón, whose objectives are to design, develop and evaluate new systems of data acquisition, processing and reconstruction of images for applications in biomedical research. In this context, the present thesis deals with the study and performance evaluation of the specific small-animal PET systems available at the Medical Imaging Laboratory, the study of the sources of error that limit the quality of the images with the investigation of algorithms to compensate them, and the study of new scanner designs in collaboration with two more research centers: Department of Biomedical

Engineering, University of California, (Davis, CA) and the National Institutes of Health (NIH), Bethesda, MD [Molecular Imaging Program, National Cancer Institute], where the author of this thesis was working as a part of an internship of the JAEPredoctoral (2008) program[1].

The main goal of this thesis is to contribute to the improvement of the quality of PET images for preclinical research with small animals by means of intensive use of Monte Carlo simulations, either for studying limiting problems in existing scanners, providing methods to compensate them, either for guiding in the design of new prototypes, analyzing advantages and drawbacks before taking the final decision. Specific objectives are as follows:

1. To evaluate the performance of two of the small-animal PET systems available at the Medical Imaging Laboratory, following, as far as possible, a standard methodology in order to compare systems between them and with other commercial preclinical systems under similar conditions [Vicente *et al.*, 2006 , Goertzen *et al.*, 2012, Vicente *et al.*, 2010a].

2. To study the sources of error that limit the quality of reconstructed PET images using Monte Carlo simulations and to investigate new methods and algorithms to compensate for these errors [Vicente *et al.*, 2011, Vicente *et al.*, 2012a, Abella *et al.*, 2012, Vicente *et al.*, 2010b].

3. To use Monte Carlo simulations for the design of new prototypes, performing the necessary modifications in the Monte Carlo package employed (peneloPET, [España *et al.*, 2009]) and in the reconstruction methods (as GFIRST [Herraiz *et al.*, 2011]) in order to make them suitable for the non-conventional geometries of the new designs [Vicente *et al.*, 2012b].

The algorithms developed in this thesis are not exclusive of any scanner in particular; they have been designed to be flexible and suitable for different architectures with only a few constrains. However, since this work takes advantage of the access to real data collected by the specific systems available at the Medical Imaging Laboratory, the development and testing of the different methods were adapted to the particular geometry of these systems ([Wang *et al.*, 2006b, Vaquero *et al.*, 2005a]).

As a final consideration, it is worth mentioning that significant part of the results presented in this thesis, besides giving rise to scientific publications, are being incorporated into the preclinical high-resolution systems manufactured by SEDECAL and distributed worldwide under technology transfer agreements with the Medical Imaging Laboratory of the Hospital General Universitario Gregorio Marañón and the Nuclear Physics Group of the Universidad Complutense de Madrid.

[1] Ph.D. fellowship from Instituto de Estructura de la Materia, Consejo Superior de Investigaciones Científicas (CSIC), Madrid, Spain

Thesis Outline

After a brief general theoretical introduction in Chapter 1, Chapter 2 presents the description of the materials used in this work. Specifically, we describe the two scanners employed for the characterization (Chapter 3) and the study of several data corrections (Chapter 4). Moreover, we present the main features of the Monte Carlo simulation tool, PeneloPET [España *et al.*, 2009] and the 3D-OSEM reconstruction method, FIRST [Herraiz *et al.*, 2006a], used in this thesis.

Chapter 3 presents the characterization of rPET [Vaquero *et al.*, 2005a] and Argus scanners [Wang *et al.*, 2006b] and a detailed study of the accuracy of the NEMA NU 4-2008 standard [NEMA-NU4, 2008] to estimate the scatter fraction with ^{18}F and with a radionuclide with a lager positron range such as ^{68}Ga.

In Chapter 4 we study some of the most important corrections that should be applied to PET data. The correction algorithms have been developed for the two scanners whose performance evaluation is presented in Chapter 3, but they can be applied to other systems. The main contributions resulting from this part of the thesis are a new method to correct pile-up and dead-time effects, a study of the effect of mechanical misalignments of PET scanners and a protocol to detect and measure them, and an attenuation correction method based on CT images.

Chapter 5 presents the study and the performance characterization of new preclinical PET scanner prototypes using Monte Carlo simulations (PeneloPET). This chapter shows examples of the modifications on simulation codes and reconstruction methods needed to adapt the existing codes to the non-conventional geometry of some designs.

At the end of this manuscript we present the general conclusions of the thesis, the publications derived from the work presented here and the lists of figures and tables shown in the document.

References

Abella, M., Vicente, E., Rodríguez-Ruano, A., España, S., Lage, E., Desco, M., Udias, J. M. & Vaquero, J. J. 2012. Misalignments calibration in small-animal PET scanners based on rotating planar detectors and parallel-beam geometry. *Phys Med Biol (Submitted)*.

Bloomfield, P. M., Rajeswaran, S., Spinks, T. J., Hume, S. P., Myers, R., Ashworth, S., Clifford, K. M., Jones, W. F., Byars, L. G., Young, J. & et al. 1995. The design and physical characteristics of a small animal positron emission tomograph. *Phys Med Biol,* 40**,** 1105-26.

Brownell, G. L., Burnham, C. A., Wilensky, S., Aronow, S., Kazemi, H. & Streider , D. 1969. New developments in positron scintigraphy and the application of cyclotron produced positron emitters. *In:* Medical Radioisotope Scintigraphy, 1969 Vienna, Austria. International Atomic Energy Agency, 163–176.

Burnham, C. A. & Brownell, G. L. 1972. A Multi-Crystal Positron Camera. *Nuclear Science, IEEE Transactions on,* 19**,** 201-205.

España, S., Herraiz, J. L., Vicente, E., Vaquero, J. J., Desco, M. & Udias, J. M. 2009. PeneloPET, a Monte Carlo PET simulation tool based on PENELOPE: features and validation. *Phys Med Biol,* 54**,** 1723-42.

Goertzen, A. L., Bao, Q., Bergeron, M., Blankemeyer, E., Blinder, S., Cañadas, M., Chatziioannou, A. F., Dinelle, K., Elhami, E., Jans, H.-S., Lage, E., Lecomte, R., Sossi, V., Surti, S., Tai, Y.-C., Vaquero, J. J., Vicente, E., Williams, D. A. & Laforest, R. 2012. NEMA NU 4-2008 Comparison of Preclinical PET Imaging Systems. *The Journal of Nuclear Medicine (Accepted)*.

Herraiz, J. L., Espana, S., Vaquero, J. J., Desco, M. & Udias, J. M. 2006a. FIRST: Fast Iterative Reconstruction Software for (PET) tomography. *Phys Med Biol,* 51**,** 4547-65.

Herraiz, J. L., España, S., Cabido, R., Montemayor, A. S., Desco, M., Vaquero, J. J. & Udias, J. M. 2011. GPU-Based Fast Iterative Reconstruction of Fully 3-D PET Sinograms. *Nuclear Science, IEEE Transactions on,* 58**,** 2257-2263.

National Electrical Manufacturers Association (NEMA). 2008. Performance Measurements of Small Animal Positron Emission Tomographs. NEMA Standards Publication NU4-2008. Rosslyn, VA. National Electrical Manufacturers Association

Pavlopoulos, S. & Tzanakos, G. 1993. Design and performance evaluation of a high resolution small animal positron tomograph. *In:* Nuclear Science Symposium and Medical Imaging Conference, 1993., 1993 IEEE Conference Record., 31 Oct-6 Nov 1993 1993. 1697-1701 vol.3.

Pavlopoulos, S. & Tzanakos, G. 1996. Design and performance evaluation of a high-resolution small animal positron tomograph. *Nuclear Science, IEEE Transactions on,* 43**,** 3249-3255.

Phelps, M. E., Hoffman, E. J., Mullani, N. A. & Ter-Pogossian, M. M. 1975. Application of annihilation coincidence detection to transaxial reconstruction tomography. *J Nucl Med,* 16**,** 210-24.

Rogers, D. W. 2006. Fifty years of Monte Carlo simulations for medical physics. *Phys Med Biol,* 51**,** R287-301.

Sweet, W. H. 1951. The uses of nuclear disintegration in the diagnosis and treatment of brain tumor. *N Engl J Med,* 245**,** 875-8.

Ter-Pogossian, M. M., Phelps, M. E., Hoffman, E. J. & Mullani, N. A. 1975. A positron-emission transaxial tomograph for nuclear imaging (PETT). *Radiology,* 114**,** 89-98.

Tzanakos, G. & Pavlopoulos, S. 1993. Design and performance evaluation of a new high resolution detector array module for PET. *In:* Nuclear Science Symposium and Medical Imaging Conference, 1993., 1993 IEEE Conference Record., 31 Oct-6 Nov 1993 1993. 1842-1846 vol.3.

Vaquero, J. J., Lage, E., Ricon, L., Abella, M., Vicente, E. & Desco, M. 2005a. rPET detectors design and data processing. *In:* Nuclear Science Symposium Conference Record, 2005 IEEE, 23-29 Oct. 2005 2005a. 2885-2889.

Vicente, E., Herraiz, J. L., Canadas, M., Cal-Gonzalez, J., Espana, S., Desco, M., Vaquero, J. J. & Udias, J. M. 2010a. Validation of NEMA NU4-2008 Scatter Fraction estimation with 18F and 68Ga for the ARGUS small-animal PET scanner. *In:* Nuclear Science Symposium Conference Record (NSS/MIC), 2010 IEEE, Oct. 30 2010-Nov. 6 2010 2010a. 3553-3557.

Vicente, E., Herraiz, J. L., Espana, S., Herranz, E., Desco, M., Vaquero, J. J. & Udias, J. M. 2011. Deadtime and pile-up correction method based on the singles to coincidences ratio for PET. *In:* Nuclear Science Symposium and Medical Imaging Conference (NSS/MIC), 2011 IEEE, 23-29 Oct. 2011 2011. 2933-2935.

Vicente, E., Herraiz, J. L., España, S., Herranz, E., Desco, M., Vaquero, J. J. & Udías, J. M. 2012a. Improved effective dead-time correction for PET scanners: Application to small-animal PET. *Phys Med Biol (Submitted)*.

Vicente, E., Herraiz, J. L., Seidel, J., Green, M. V., Desco, M., Vaquero, J. J. & Udias, J. M. 2012b. Regularization of 3D Iterative Reconstruction for a Limited-Angle PET Tomograph. *In:* Nuclear Science Symposium Conference Record (NSS/MIC), 2012 IEEE (*Accepted*), 2012b.

Vicente, E., Udías, A. L., Herraiz, J. L., Desco, M., Vaquero, J. J. & Udías, J. M. 2010b. Corrección de atenuación de imágenes PET usando datos de TAC en el escáner para animales pequeños Argus PET/CT. *Libro de Actas, CASEIB 2010.*

Vicente, E., Vaquero, J. J., Lage, E., Tapias, G., Abella, M., Herraiz, J. L., España, S., Udías, J. M. & Desco, M. 2006 Caracterización del Tomógrafo de Animales rPET. *Libro de Actas, CASEIB 2006*.

Wang, Y., Seidel, J., Tsui, B. M., Vaquero, J. J. & Pomper, M. G. 2006b. Performance evaluation of the GE healthcare eXplore VISTA dual-ring small-animal PET scanner. *J Nucl Med,* 47**,** 1891-900.

Watanabe, M., Uchida, H., Okada, H., Shimizu, K., Satoh, N., Yoshikawa, E., Ohmura, T., Yamashita, T. & Tanaka, E. 1992. A high resolution PET for animal studies. *Medical Imaging, IEEE Transactions on,* 11**,** 577-580.

1. Introduction

Positron Emission Tomography (PET) [Cherry *et al.*, 2003] is a nuclear medicine technique that uses radioactive substances for the diagnosis and staging of diseases. These radioactive substances consist of a radionuclide (tracer), chemically bound to a biologically active molecule. Once administered to the patient, the molecule concentrates at specific organs or cellular receptors with a certain biological function. This allows nuclear medicine to image the location and extent of a disease in the body, based on the cellular and physiologic functions. PET is considered essential in the management of many human cancers [Papathanassiou *et al.*, 2009]. This ability to visualize physiological function separates nuclear medicine imaging techniques from traditional anatomic imaging techniques, such as Computed Tomography (CT). When combined with anatomic imaging, such as CT or Magnetic Resonance Imaging (MRI), PET provides the best available information on tumor staging and assessment of many common cancers [Macmanus *et al.*, 2009].

PET is based on the decay mechanism of positron-emitting nuclides. The emitted positron interacts with an electron of the surrounding matter, resulting in an annihilation of the positron and the electron. In this annihilation process energy and momentum are conserved. Therefore, two gamma rays are emitted, each having an energy equal to the rest mass of the electron or the positron (mc^2 = 511keV), which propagate in the opposite direction of each other. These two gamma rays are registered in coincidence by the ring detectors of the tomograph (Figure 1) defining a line of response (LOR) where the positron annihilation took place. The information recorded in every LOR is assembled and it is employed to produce an image of the activity and thereby of the functionality of the organism.

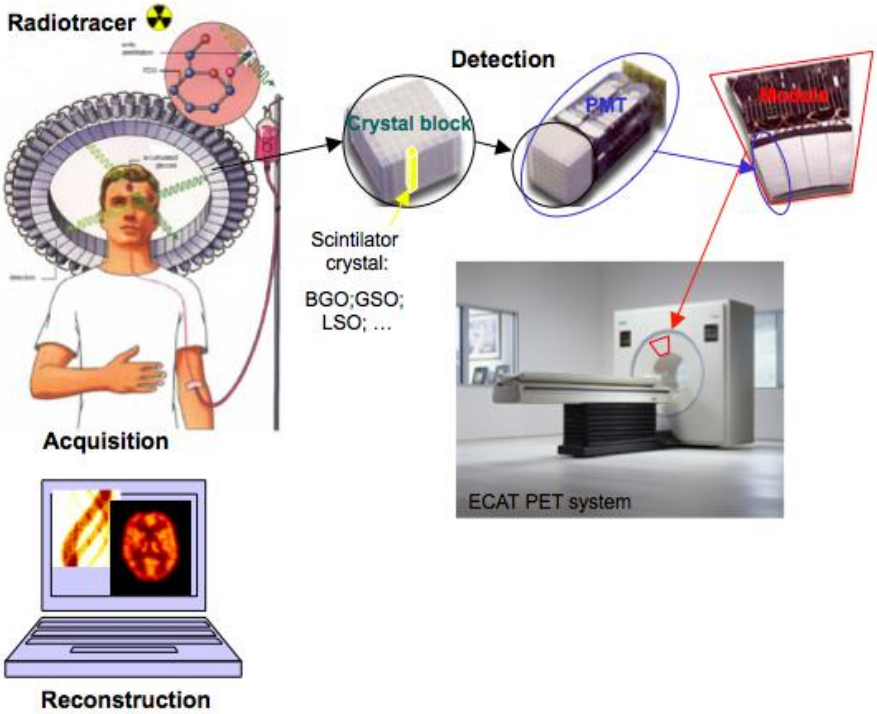

Figure 1. *Schematic representation of a PET scanner and data processing principles [Ter-Pogossian, 1982].*

This chapter describes a brief theoretical introduction required to follow the contents of this thesis. The explanation includes some notions of the physics background, detection system, main corrections as well as the tools used to simulate and reconstruct PET data.

1.1. Principles of PET I - Physics Background

Two main physical effects are involved in PET. One is the beta decay of the radioisotope and the annihilation of the positron with electrons in the tissue generating two gamma rays. The other one is the interaction of these gamma rays with matter. Both effects are discussed in more detail in this section, along with a short description of the radioisotopes used in PET and its production.

1.1.1. Beta decay

Beta particles are 'fast' electrons or positrons produced in the (weak interaction mediated) decay of neutrons or protons in neutron or proton rich nuclei [Krane, 1987]. In a neutron rich nucleus a neutron can transform into a proton via the process:

$$n \rightarrow p^{+} + e^{-} + \bar{\upsilon}_e \qquad 1)$$

where an electron and an antineutrino are emitted. Free neutrons also decay according to this disintegration scheme with a half-life of 10.25 minutes [Krane, 1987]. The daughter nucleus now contains one extra proton so that its atomic number Z increases in one unit. This can be written as:

$$X_N^Z \rightarrow X_{N-1}^{Z+1} + e^{-} + \bar{\upsilon}_e \qquad 2)$$

In proton-rich nuclei, a positron and a neutrino are emitted in the complementary process [Krane, 1987] to the one previously described:

$$p^{+} \rightarrow n + e^{+} + \upsilon_e \qquad \textbf{(3)}$$

This β^{+} process cannot happen to free, isolated protons, due to energy constrains, but the corresponding decay in nuclei can arise when it is energetically possible [Krane, 1987, Powsner and Powsner, 2006] and it is written as:

$$X_N^Z \rightarrow X_{N+1}^{Z-1} + e^{+} + \upsilon_e \qquad \textbf{(4)}$$

The daughter nucleus now contains one proton less after the decay; therefore the atomic number has decreased by one unit. There is also a third process in nuclei mediated by the weak interaction. It is called electron capture [Krane, 1987]. In this process an atomic electron is captured by the nucleus

$$p^{+} + e^{-} \rightarrow n + \bar{\upsilon}_e \qquad \textbf{(5)}$$

A basic characteristic of the β-decay process is the continuous energy spectrum of the β-particles. This is because the available energy in the decay is shared between the β particle and the neutrino or antineutrino. Typical energy spectra are shown in Figure 2.

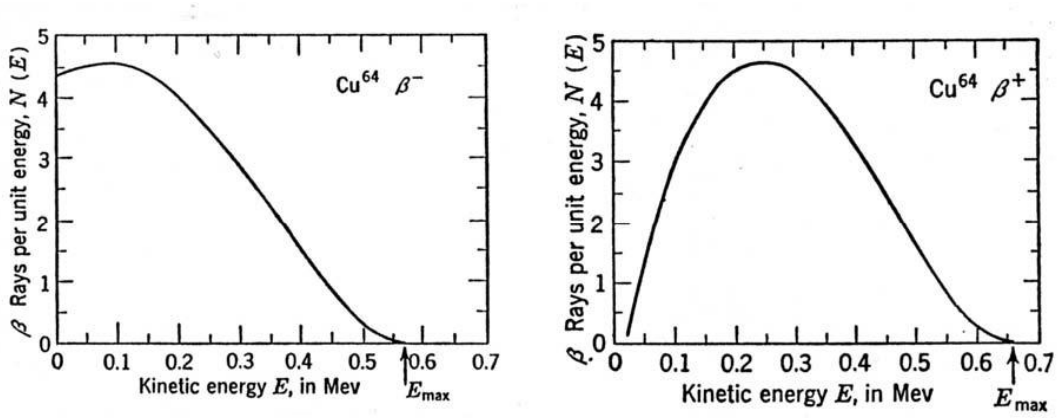

Figure 2. *Experimental β-spectra obtained from decaying ^{64}Cu. β^- particles (left) are affected by the electric field of the positively charged nuclei and thus the energy spectrum is shifted towards lower energies. β^+ particles, on the other hand, are repelled by the nuclei so the energy spectrum it is shifted towards higher energies [Krane, 1987].*

The distance from the emission point to the annihilation point is known as positron range. Positron range is one of the main limiting factors to the spatial resolution of PET [Levin and Hoffman, 1999] and depends both on the energy of the emitted positrons and the surrounding materials. The distance in the normal direction to the location of the decaying atom to the LOR is the positron range blurring, relevant for PET projection data (see Figure 3). Because positrons are emitted with a range of energy and follow a tortuous path in tissue, the positron range is a non-Gaussian distribution as described by Derenzo [1979] and Levin and Hoffman [1999].

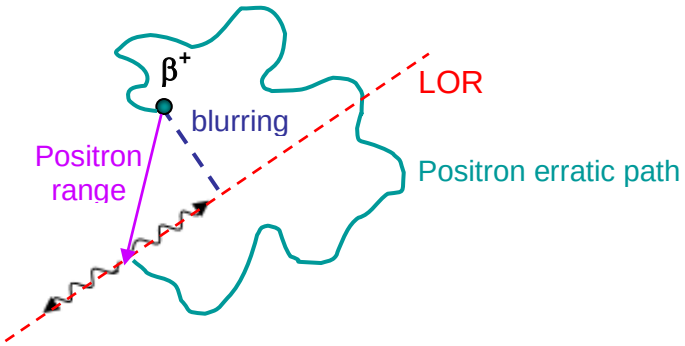

Figure 3. *Scheme representing the definition of the positron range. From its emission, the positron follows an erratic path until the annihilation process.*

As the majority of annihilations occur with both positron and electron at thermal energies (a few eV, much less than their rest masses), by energy and momentum conservation, two photons with a characteristic energy of 511 keV, with a relative angle of approximately 180º are emitted [Debenedetti *et al.*, 1950]. These almost collinear gamma rays can be used for PET because their direction includes information about the annihilation position. Nevertheless, there is a non negligible probability in which the annihilation occurs with a non-zero momentum in the laboratory system. This creates a slight deviation from collinearity, $\Delta\varphi$. DeBenedetti et *al.* [1950] measured $\Delta\varphi \approx 0.4º–0.5º$ which will cause some errors in the identification of the annihilation position.

1.1.2. PET Radionuclides

The most common PET radioisotope tracers are produced in a cyclotron. Proton or deuteron beams irradiate targets filled with the raw material for radionuclide production: N_2 (containing a small amount of oxygen) for the production of ^{11}C and ^{15}O, Ne (containing a low percentage of molecular

fluorine) and ^{18}O enriched water for the production of ^{18}F [Stöcklin and Pike, 1993].

There are other isotopes like ^{82}Rb, ^{68}Ga which are obtained from generators. These generators contain relatively long-life mother isotopes, producing the desired isotopes as a result of their decay process. The separation of the daughter nuclei is made through a chemical processes.

The choice of the radionuclide is imposed by its physical and chemical characteristics and its availability [Raichle, 1983]. Table 1 lists the most frequently used positron emitting radionuclides with some of their physical characteristics. The positron energy and its resulting range in water are inversely correlated with the PET image resolution obtained, especially when using high resolution PET for small animal imaging. Before application to the patient, the tracer must be tested for radionuclidic, radiochemical, chemical, and pharmaceutical quality, as well as for sterility. Details on the quality control of radiopharmaceuticals can be found for example in [Stöcklin and Pike, 1993].

Table 1. *Physical properties of positron emitters. (Adapted from [Bailey, 2005] and [Cherry et al., 2003]).*

Radionuclide	Half-life (min)	Production	Range in water (mm)		Max. Emission energy (MeV)
			Max	Mean	
^{11}C	20.4	cyclotron	4.1	1.1	0.959
^{13}N	9.97	cyclotron	5.1	1.5	1.197
^{15}O	2.03	cyclotron	7.3	2.5	1.738
^{18}F	109.8	cyclotron	2.4	0.6	0.633
^{82}Rb	1.25	generator	14.1	5.9	3.400
^{68}Ga	68	generator	8.9	2.9	1.899

1.1.3. Interaction of gamma radiation with matter

When a monoenergetic gamma beam with intensity I_0 passes through matter, the most relevant interaction occurs with the electrons of the material. As a result of these interactions, some gamma rays will be removed out of the incident beam by either photoelectric absorption (absorption coefficient τ), Compton or Rayleigh effects (absorption coefficient σ), or pair production (absorption coefficient κ) [Knoll, 2000]. An overall absorption coefficient μ results from these three individual absorption coefficients:

$$\mu = \tau + \sigma + \kappa \quad \textbf{(6)}$$

Thus, the overall absorption can be described by:

$$I = I_0 e^{-\mu x} \quad \textbf{(7)}$$

where I_0 is the incident and I the resulting intensity after crossing a distance x of material.

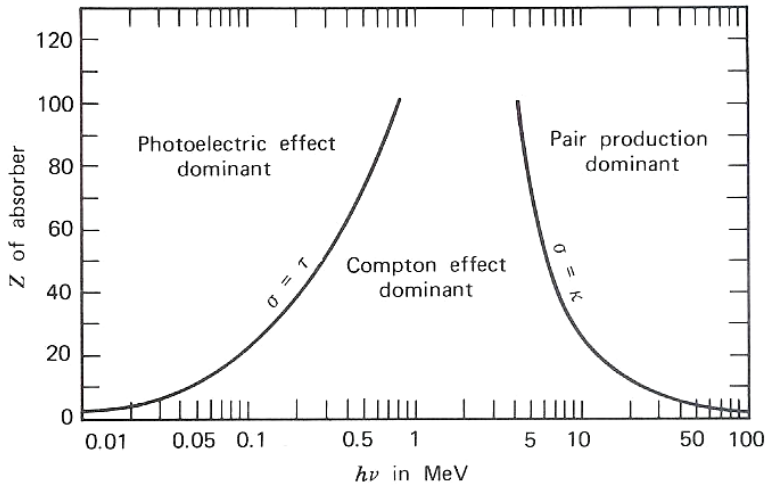

Figure 4. *Relative importance of the three major types of gamma-ray interaction. The lines show the values of Z and hν for which the two neighboring effects are just equal. [Knoll, 2000]*

Figure 4 shows the relative importance of the three major types of gamma-ray interactions for different combinations of Z and hν (for more details on the Z-dependency see [Knoll, 2000, Evans, 1955]). For 511 keV gamma rays, only photoelectric absorption and Compton interaction are relevant, whereas pair production can be neglected. These types of interaction are briefly described below.

1.1.3.1. Photoelectric absorption

During photoelectric absorption, the incident gamma ray with energy E_γ is absorbed by an atom of the traversed material. An electron from the electron shell of this atom is then ejected with energy:

$$E_{e^-} = E_\gamma - E_{bound} \quad \textbf{(8)}$$

where E_{bound} is the binding energy of the knocked out electron. The resulting hole in the electron shell is filled by the remaining electrons within the shell or by the capture of a free electron from the surrounding medium.

1.1.3.2. Compton and Rayleigh scattering

A gamma ray of energy E_γ, that interacts with a shell electron of the traversed material by the Compton effect (Compton scattering), is deflected from its incident direction by an angle θ and loses energy given by conservation of momentum as:

$$E_{e^-} = E_\gamma - E_{bound} - E'_\gamma \quad \textbf{(9)}$$

where E'_γ is the energy of the gamma ray after the interaction. This amount of energy is transferred to the electron. E'_γ depends on the scatter angle θ according to [Knoll, 2000]:

$$E'_\gamma = \frac{E_\gamma}{1 + \frac{E_\gamma}{m_e c^2}(1 - \cos\theta)} \quad \textbf{(10)}$$

$m_e c^2$ being the rest-mass energy of the electron (511 keV). The maximum energy transferred to the electron occurs when the scattering angle $\theta = \pi$:

$$E_{e^-,\max} = E_\gamma \left(\frac{2E_\gamma / m_e c^2}{1 + 2E_\gamma / m_e c^2} \right) \quad \textbf{(11)}$$

This gives rise to the Compton edge in the energy spectrum of monoenergetic gamma rays as seen in detectors of finite size [Knoll, 2000].

When elastic scattering occurs, the incident photon is scattered without ionizations or other energy losses in excitations of the internal states of the constituents of the material. This process is known as Rayleigh scatter.

1.1.3.3. Pair production

The energy threshold for pair production

$$\gamma \rightarrow e^+ + e^- \quad \textbf{(12)}$$

is 2×511 keV = 1.022 MeV. This interaction can only take place in the presence of a nucleus to pick up recoiling energy and momentum so that energy-momentum conservation can be verified. Additional energy of the gamma ray will be converted into kinetic energy of the electron, positron and recoiling partner. As this latter is usually a relatively heavy nucleus, its recoiling energy can be neglected. Both electrons and positrons produced will undergo interactions with matter, and additionally these positrons will finally produce annihilation radiation at the end of their paths.

1.2. Principles of PET II - Detectors

Detection systems are key components of any imaging system, and an understanding of their properties is important for establishing appropriate operating criteria or designing schemes. Scintillation detectors are widely used as radiation detectors in PET imaging. They are very fast, can have high stopping power and exhibit low electronic noise. A scintillation detector primarily consists of a crystal that produces scintillation light after interaction with radiation, and a photodetector that converts the scintillation light into an electrical signal [Wernick and Aarsvold, 2004, Melcher, 2000]. This section primarily discusses the scintillation detector components and design considerations.

1.2.1. Scintillators

Gamma rays can be detected with scintillators, which produce scintillation photons in the visible and ultraviolet range of wavelengths (100 - 800 nm). As discussed in the previous section, only photoelectric absorption and Compton scattering are relevant interaction mechanisms for detecting 511 keV gamma photons [Knoll, 2000]. During a photoelectric absorption, the entire energy of the gamma photon is converted to the release of a photoelectron, a knock-on electron. This electron then excites higher energy states of the crystal lattice, which decay by emitting lower energy scintillation photons. During Compton scatter, only part of the energy of the gamma photon is converted to the knock-on electron. The rest of the energy is taken by the scattered, 'degraded' photon. This scattered photon in turn can produce additional scintillation centers by the Compton and photoelectric effect. Compton scattering inside the scintillation crystal can thus produce various scintillation centers. This *position blurring* affects the position determination. Unlike Compton scatter, the photoelectric effect produces a single scintillation center and is the preferred interaction process. The photoelectric cross section σ_p is a function of the density ρ and of the effective atomic number Z_{eff} of the crystal. The photoelectric cross section is proportional to $\rho(Z_{eff})^x$, with the power x varying with gamma-ray energy between 3 and 4, typically. In contrast, the Compton cross section is linearly related to the electron density, and thus proportional to ρ [Eijk, 2002].

A scintillator should thus have a high density for a high absorption probability and a high atomic number for a large fraction of photons undergoing photoelectric absorption. These two requirements are commonly parametrized as the attenuation length $1/\mu$ (the distance where the probability that a particle has not been absorbed drops to 1/e) and photoelectric absorption probability *PE* or photofraction, defined as the probability that a gamma photon interacts by the photoelectric effect $PE = 100\ [\sigma_p/(\sigma_p + \sigma_c)]$

High light yield (number of emitted scintillation photons per MeV absorbed energy) is another important requirement for PET. A large number of detected scintillation photons N_{ph} imply a better energy, timing and position resolution. This is because photon counting is dominated by Poisson statistics, such that the relative statistical spread is proportional to $1/\sqrt{N_{ph}}$.

Associated with the light yield requirement is a high light collection efficiency of the crystal, such that a large fraction of the emitted scintillation photons are detected. Optical self-absorption of the scintillation photons should therefore be minimal. Furthermore, the scintillator can be surrounded by a reflector at all surfaces except that at which the photosensor is located, to recapture the light that would otherwise escape from the crystal. Also, the emission spectrum should overlap with the spectral sensitivity of the photodetector. It is further desirable that the light output is proportional to the deposited energy. If this would not be the case, the light output would be different for a full 511 keV energy absorption by a single photoelectric effect, compared to a full energy absorption by multiple, lower energy, Compton interactions. This would broaden the full energy peak.

The time structure of the light emitted by scintillators can often be approximated by [Ljungberg *et al.*, 1998]:

$$N(t) = N_0 \frac{e^{-t/\tau_{FALL}} - e^{-t/\tau_{RISE}}}{\tau_{FALL} - \tau_{RISE}} \quad \textbf{(13)}$$

where $N(t)$ is here the number of photons emitted by the scintillators at time t, N_0 is the total number of photons emitted, and τ_{FALL} and τ_{RISE} are fall and rise constants of the scintillator.

A fast decay time allows a high count rate performance of the detector. This is especially important for 3D-mode PET, where high counting rates exist and the system sensitivity will be limited by pulse pile-up (see section 1.3.7) if slow scintillators are used. Additionally, a fast decay time (as well as a high light yield) implies a large initial scintillation photon emission rate N_0. The rise time, τ_{RISE}, is associated with the luminescence process in scintillators. It should be fast enough to allow a short coincidence time window to limit the amount of random coincidences (see section 1.3.4). Like a fast decay time, a fast rise time is associated with a large initial scintillation photon emission rate N_0, and thus a high timing resolution can be obtained for TOF-PET (PET with time-of-flight).

Scintillator materials can be organic-based (liquid or plastic) or inorganic. Organic scintillators are generally fast, but have a low light yield. Inorganic scintillators have a higher light yield, but are relatively slow. For all current commercial PET scanners, inorganic scintillators are employed. Table 2 lists some of the properties of scintillators found in many PET detector designs. Note that some of these specifications are subject to change as developers change dopants and trace elements in the scintillator growth. For example, the light output, peak wavelength, decay time and density for LYSO and LFS will vary somewhat for different makers.

Table 2. *Properties of some scintillators used in PET detectors. (Adapted from [Lewellen, 2008]).*

	NaI(Tl)	BaF_2	LSO	GSO	LYSO	$LaBr_3$	LFS	LuAP	LuI_3
Effective atomic no. (Z)	51	54	66	59	60	47	63	65	60
μ (cm^{-1})	0.34	0.44	0.87	0.62	0.86	0.47	0.82	0.9	~0.56
Density (gm cm^{-3})	3.67	4.89	7.4	6.7	7.1	5.3	7.3	8.34	5.6
Index of refraction	1.85	-	1.82	1.85	1.81	1.88	1.78	1.95	-
Light yield (% NaI(Tl))	100	5	75	30	80	160	77	16	190
Peak wavelength (nm)	410	220	420	430	420	370	430	365	470
Decay constant (ns)	230	0.8	40	65	41	25	35	18	30
Hygroscopic	yes	slight	no	no	no	no	no	no	yes

In order to achieve the best possible spatial resolution, most PET systems use segmented scintillators that try to minimize the uncertainty in the location of the interaction. Current high resolution PET scanners employ arrays of pixelated scintillator crystals [Casey and Nutt, 1986]. Scanners with blocks made of continuous crystal are less frequently used for high resolution scanners [Lerche *et al.*, 2005, Joung *et al.*, 2001].

1.2.2. Photosensors

A typical scintillation detector consists of a scintillating crystal coupled to a photomultiplier tube (PMT) housed in a metallic shield. Photomultipliers are constructed from glass vacuum tubes which house a photocathode, several dynodes, and an anode. Incident photons strike the photocathode material which is present as a thin deposit on the entry window of the device, with electrons being produced as a consequence of the photoelectric effect. These electrons are directed by the focusing electrode towards the electron multiplier, where electrons are multiplied by means of secondary emission [Knoll, 2000].

The electron multiplier consists of several electrodes, called dynodes. Each dynode is held at a more positive voltage than the previous one. The electrons leave the photocathode, with the energy of the incoming photon, minus the work function of the photocathode. As they move towards the first dynode they are accelerated by the electric field and arrive with larger energy. After striking the first dynode, more low energy electrons are emitted and these, in turn, are accelerated toward the second dynode. The geometry of the dynode chain is such that a cascade occurs with an ever-increasing number of electrons being produced at each stage. Finally, the electrons reach the anode where the accumulation of charge results in a sharp current pulse indicating the arrival of a photon at the photocathode. The PMT will give an electric pulse proportional to the number of scintillation light quanta that reach the photocathode which is proportional to the energy deposited. Thus, energy spectroscopy is possible with scintillation detectors and PMTs. The gain is defined as the total number of electrons that arrive to the anode for each single electron produced in the photocathode. Gains from 10^5 to 10^8 can be reached with these devices.

Photomultiplier tubes typically require a power voltage of 1000 to 2000 V for proper operation. The most negative pole is connected to the cathode, and the most positive pole is connected to the anode. Voltages are distributed to the dynodes by a resistive voltage divider. The divider design influences aspects such as frequency response and rise time, and therefore may be critical to certain applications. While powered, photomultipliers must be shielded from ambient light to prevent their destruction through over excitation.

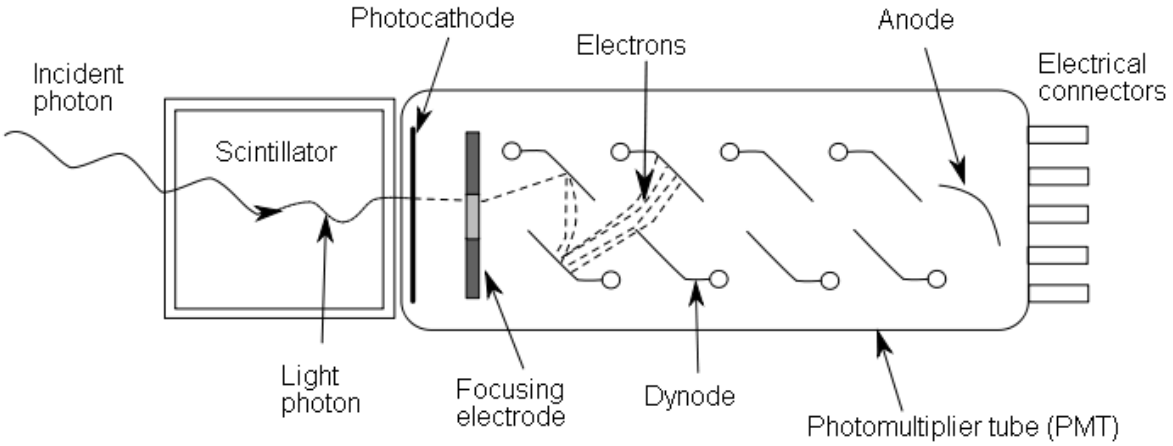

Figure 5. *Principle of operation of a photomultiplier tube (PMT)[Knoll, 2000].*

As mentioned before, spatial resolution is an important parameter in PET. Scintillation arrays are usually coupled to a single photomultiplier that must be able of localize the point where the light has entered the device. For this purpose, position sensitive photomultipliers (PS-PMT) were developed. These devices have an array of anodes where the collected charge is distributed. The distribution of charges among different anodes can be used to calculate the position of the incident light [Anger, 1969].

Other devices such as APDs [Pichler *et al.*, 1997], PIN-DIODES or more recently SiPMs are also being used [Otte *et al.*, 2005, España *et al.*, 2008, España *et al.*, 2010].

1.2.3. Electronics

1.2.3.1. Pulse processing

In order to measure time intervals precisely, the arrival times of different events must be recorded to achieve optimal time resolution. To obtain good timing signals, Constant Fraction Discriminators (CFD) may be employed. The output pulse coming from the anode of the PMT, is fed to the input of the CFD. The principle of operation of a CFD is illustrated in Figure 6.

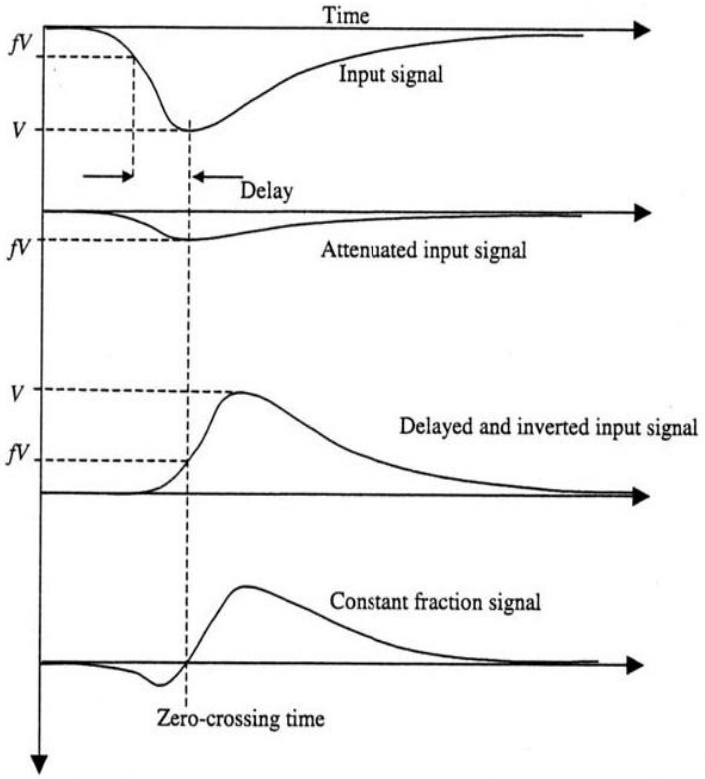

Figure 6. *The formation of the constant-fraction signal [Knoll, 2000].*

The CFD is designed to trigger on a certain optimum fraction of the pulse height, thus making the performance (labeling of the onset of the pulse) of the CFD independent of pulse amplitude[2]. Furthermore, leading-edge discriminators (LED) are employed to provide energy selection. Events with energy below the threshold will not give rise to a signal from the CFD and thus will be excluded.

The events triggered in a detector are fed into coincidence units that test whether each event is close enough in time to other events from other detectors, so that they can be considered as coincidence events. The time-of-flight taken by the gamma photons from the positron annihilation time to the detector is of the order of hundreds of picoseconds, less than the time resolution of most of PET scanners. However, scanners with time-of-flight (TOF) capabilities have been developed [Allemand *et al.*, 1980, Mullani *et al.*, 1981, Moszynski *et al.*, 2006]. The time resolution achievable by the scanner is the result of a convolution of the time resolution of each scintillator, PMT and

[2] Assuming all pulses have the same shape. Noise and baseline shifts can prevent this.

electronics. It is usually of the order of a few nanoseconds [Knoll, 2000]. However, modern PET scanners can reach below 500 ps time resolution [Lois *et al.*, 2010, Jakoby *et al.*, 2011].

1.2.3.2. Data acquisition system

Once pulses have passed all discriminators, the amplitude of the signal, that contains the energy information for the event, must be obtained. All output lines of the PS-PMT that have been triggered are integrated to obtain the total charge for the energy calculation and the location of the interaction. This is usually performed by electronic modules that, first, integrate the charge of each output line and convert the resulting integrated charge into a digital number (ADC conversion) that is transmitted and stored in a PC. The transmission of this information to the PC may be performed via Ethernet, fireware, USB, PCI-X or other connections [Lewellen *et al.*, 2001, Lage *et al.*, 2010].

1.2.3.3. Event classification

There are different kinds of events that can be recorded in a PET acquisition:

- **Single Event (s_i):** A single gamma ray is detected in one of the detectors independently of its associated second gamma ray.

- **True Event (T):** Two gamma rays that originate from the same e^+e^- annihilation and leave the body without interaction are measured within the same coincidence timing window (τ) (Figure 7a).

  However, due to limitations of the detectors used in PET and the possible interaction of the 511 keV photons in the body before they reach the detector, the coincidences measured are contaminated with undesirable events which includes scattered, random and multiple coincidences. All these events degrade the quality of the measurement and need to be corrected in order to produce an image that represents as closely as possible the true radioactivity concentration under measurement.

  Another point to consider is that the vast majority of photons detected by PET scanners are single events, for which only one of the two annihilation photons is registered. The partner photon may be on a trajectory such that it does not intersect a detector (most PET scanners provide relatively modest solid angle coverage around the object), it can be attenuated in the patient or object placed in the FOV, or the photon may not deposit sufficient energy in a detector to be registered or may not interact at all. These single events are not accepted by the PET scanner, but they are responsible for random, multiple coincidence and pile-up events. Because they must still be processed by the electronics to see if they form part of a coincidence pair, they are an important contribution to detector dead-time (see sections 1.3.6 and 4.1).

- **Scatter Event (S):** Like a true event, the scatter event originates from a single e^+e^- annihilation, but one (or both) gamma ray undergoes a scatter process while passing through the body. As a result, the gamma is deflected by an angle θ and its energy decreases according to equation (10). In a case where this energy is still within the energy window of the PET scanner, the assigned LOR does not contain any information about the origin of the positron decay (Figure 7e), resulting in reduction of spatial resolution and image contrast. If not corrected, scattered events produce a low spatial frequency background that reduces contrast. The distribution of scattered events depends on the distribution of the radioactivity and the properties of the scattering medium but it does not depend on the amount of activity administered. In clinical studies, the scatter-to-true coinicidence ratio ranges from 0.2 to 0.5 for brain and form 0.4 to 2 for abdominal imaging; in preclinical studies it ranges from 0.1 to 0.6, depending on the size of the object and the geometry and energy resolution of the PET scanner [Cherry *et al.*, 2003].

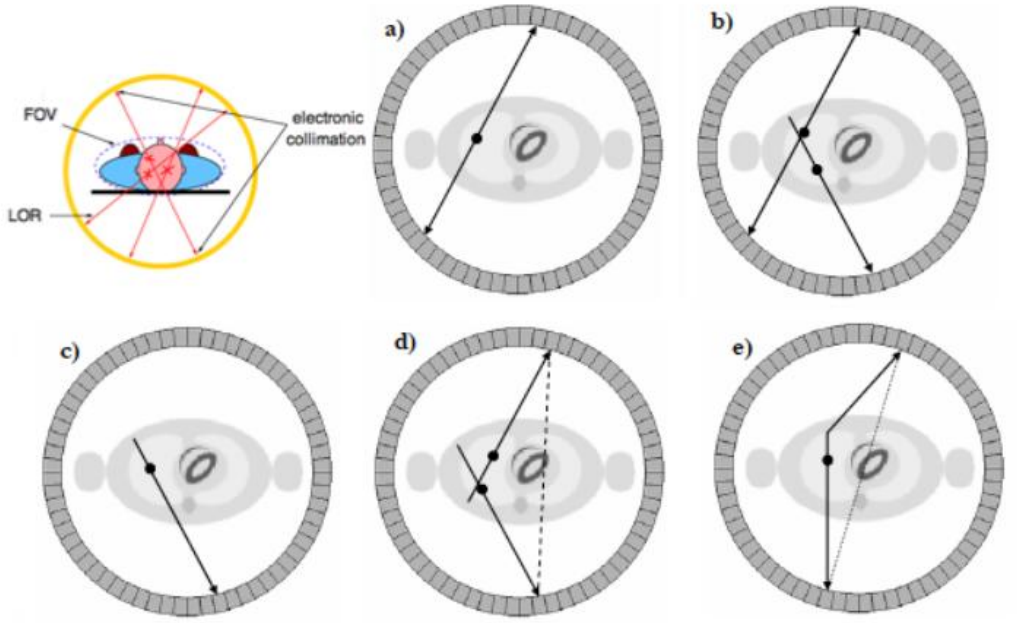

Figure 7. *Illustration of the main coincidence event types:* ***a)*** *true;* ***b)*** *multiple;* ***c)*** *single;* ***d)*** *random and* ***e)*** *scattered. (Adapted from [Cherry* et al.*, 2003]).*

- **Random Event (*R*):** A random, or accidental, coincidence occurs when two positrons annihilate and one gamma ray from each annihilation is detected. If the two events occur close enough in time, then the coincidence electronics will register the event as a coincidence (or a prompt event). However, such randoms are distributed uniformly in time and only the portion of random events included in the prompt window contaminates the primary dataset. The assigned LOR again does not include useful information about the tracer distribution (Figure 7d).

- **Multiple Event (*M*):** Multiple events result from more than one annihilation and correspond to the detection, within the same coincidence window, of three or more gamma rays (Figure 7b). Since there is an ambiguity in deciding which photons make a valid pair, resulting from the same annihilation, these events are usually discarded by the system.

- **Pile-up Event (*Pu*):** This kind of event occurs in the detection process if one (or both) gamma ray is being integrated and an extra gamma ray deposits its energy in the same detector. If the final energy of the pile-up event is still inside the energy window, it will cause mispositioning of the true event so the assigned LOR will not contain accurate information about the tracer distribution.

- **Prompt Event (*P*):** All coincident events, measured by the coincidence controller, are called prompt events:

$$P = T + S + R + Pu \tag{14}$$

These events consist of true, scattered, and accidental coincidences where the true coincidences are the only ones that carry information regarding the spatial distribution of the radiotracer. It is, therefore, necessary to estimate what fraction of the measured prompt coincidences arises from scattered and accidental coincidences for each of the LORs [Sorenson and Phelps, 1987, Tarantola *et al.*, 2003, Bailey, 2005, Valk *et al.*, 2006]

1.3. Principles of PET III - Corrections

Quantitative and artifact-free images require applying several corrections to the acquired data. This section introduces some of the corrections that are commonly applied to PET acquisitions.

1.3.1. Decay

Correcting for decay is often required in procedures involving radioactivity. During a study, the tracer activity decreases due to radioactive decay of the radionuclide. Therefore, it is necessary to scale the acquired data by a decay correction factor, D_i, which can be calculated as follows [Bailey, 2005]:

The number (N) of counts measured during the acquisition time Δt_i is:

$$N = \int_{t_i}^{t_i+\Delta t_i} A(t) = \int_{t_i}^{t_i+\Delta t_i} A_0 e^{-\lambda t} = \frac{A_0}{\lambda} e^{-\lambda t_i}\left(1 - e^{-\lambda \Delta t_i}\right) \quad \textbf{(15)}$$

with Δt_i the duration of the frame that was started at time t_i, A_0 the initial activity and λ the decay constant. If A_i is the mean tracer activity during frame i, we can also write:

$$N = A_i \Delta t_i \quad \textbf{(16)}$$

Using (15) and (16) we can obtain:

$$A_0 = A_i D_i \quad \textbf{(17)}$$

where D_i is the decay correction factor:

$$D_i = \frac{\Delta t_i \lambda e^{\lambda t_i}}{1 - e^{-\lambda \Delta t_i}} \quad \textbf{(18)}$$

This correction factor depends on the duration of the frame, Δt_i, and the decay constant of the isotope. This information is usually stored in acquisition files.

1.3.2. Attenuation

Annihilation photons in PET are subject to attenuation as they travel through the imaged object reducing the number of photons detected in each line of response (LOR). If the anatomical properties of the object/subject are known, the measurement along each line of response can be corrected for this attenuation effect [Huang *et al.*, 1979]. A coincidence event requires the simultaneous detection of both photons coming from the annihilation of a positron. If either photon is absorbed within the body or scattered out of the field of view, the coincidence will be lost. For this reason, the probability of detection depends on the combined path of both photons. Since the total path length is the same for all sources lying on the line that joins two detectors, the probability of attenuation is the same for all such sources, independently on the source position.

Therefore, the problem of correcting for photon attenuation within the body is equivalent to the determination of the probability of attenuation for all sources lying along every line of response

[Bailey, 2005]. The probability of attenuation for each LOR can be determined by using an external (transmission) source. With the advent of dual modality scanners capable of acquiring PET and CT data during the same imaging session, there has been considerable effort put into the development of methods to employ CT data for PET attenuation correction.

A more detailed description of this correction is depicted in chapter 4 (section 4.3).

1.3.3. Scatter

When a positron annihilates in the body, there is a finite probability that one or both of the annihilation photons scatter in the body or in the detector itself. At the energy of annihilation photons (511 keV), the most likely type of interaction is Compton scattering. As it was mentioned in section 1.2.3.3, since the scattered LOR is no longer collinear with the annihilation point, such events degrade the quality of PET image. Indeed, except for high energy resolution detectors (CZT, HPGe, Si(Li), BrLa(Ce)) [Vaska *et al.*, 2005, Cooper *et al.*, 2007], scattered coincidences are not easily discriminated from unscattered ones, solely based on their energy, and thus may significantly degrade both image quality (due to loss of contrast) and quantitative accuracy [Wirth, 1989]. The fraction of accepted coincidences which have undergone Compton scattering prior to detection, is named as the scatter fraction and its magnitude depends on several factors, including size and density of the scattering medium, geometry of the PET scanner and width of the energy acceptance window. There are several characteristics of scattered coincidences which can be exploited to estimate their distribution (and potentially correct for them) in the measured data [Bailey, 2005]:

- LORs recorded outside object boundaries can only be explained by scatter in the object, assuming that random coincidences (see next subsection) have been subtracted.
- The distribution of scatter counts is very smooth, i.e., it contains mainly low spatial frequencies.
- The region of the coincidence energy spectrum below the photopeak has a large contribution from scattered events.
- Scattered coincidences that fall within the photopeak window are mainly due to photons that have scattered only once.

These various characteristics have given rise to a wide variety of approaches for estimating and correcting scattered coincidences in PET data [Bailey and Meikle, 1994, Levin *et al.*, 1995, Cherry *et al.*, 1993].

1.3.4. Random coincidences

As explained in section 1.2.3.3, random coincidences arise when two unrelated photons are detected in opposing detectors, close enough in time to be accepted by the time-window criteria that the system employs to identify coincidences. Random coincidences add uncorrelated background counts to PET images and hence decrease image contrast, if no correcting measures are taken [Bailey, 2005].

The number of random coincidences detected can be reduced by choosing the scanner geometry so that the field of view (FOV) for single events is reduced [Badawi *et al.*, 2000] or by reducing as much as possible the time coincidence window of the system. The noise introduced by random coincidences can also be reduced by estimating the number of random counts on each LOR and taking this estimation into account during reconstruction. The number of random coincidences on a particular LOR can be estimated in different ways [Cooke *et al.*, 1984]. For instance, the rate of random

coincidences R_{ij} on a LOR joining two detectors i and j is:

$$R_{ij} = 2\tau s_i s_j \quad \textbf{(19)}$$

where s_i and s_j are the uncorrelated singles rates on detectors i and j respectively [Oliver and Rafecas, 2008], and τ is the width of the logic pulses produced when a photon is absorbed in the detector. The term 2τ is often referred to as the coincidence timing window [Knoll, 2000]. When the single rate is measured, all correlated and uncorrelated events are detected. Thus, correlated single events, those that produce true coincidence events, must be substracted from the total singles rate in order to achieve a more accurate estimation of random coincidences.

Another way of estimating random coincidences employs delayed coincidence measurements. In this scheme, timing signals from one detector are delayed by a time significantly greater than the time coincidence window. In this way, all detected coincidences will be uncorrelated and the number of coincidences found will be a good estimate of the number of random coincidences in the prompt signal. This resulting estimate is then subtracted from the number of prompt coincidences to yield the combined number of true and scattered coincidences [Knoll, 2000]. The advantage of this method is that the delayed channel has identical dead-time (see section 1.3.6) properties to the prompt channel. The disadvantage is that the statistical quality of the random coincidences estimate is poorer, as R_{ij}, s_i and s_j are subject to Poisson statistics and R_{ij} may be a significantly smaller quantity than either s_i or s_j [Casey and Hoffman, 1986].

More information about methods to estimate and correct the effects of random coincidences in PET studies can be found for example in [Williams *et al.*, 1979, Badawi *et al.*, 1999, Stearns *et al.*, 2003, Brasse *et al.*, 2005].

1.3.5. Normalization

LORs in PET datasets have different sensitivity due to variations in detector efficiency, solid angle subtended, etc [Bailey, 2005]. Information on these variations is required for the reconstruction of quantitative, artifact-free images. Indeed, most algorithms require that these variations are removed prior to reconstruction. The process of correcting for these effects is usually known as normalization [Hoffman *et al.*, 1989, Badawi and Marsden, 1999a] .

In a block detector system, detector elements vary in efficiency because of position of the element in the block, physical variations in the crystal and light guides and variations in the gains of the photomultiplier tubes or corresponding detector elements. Other causes of differenced sensitivity are the energy window selected for each crystal element and the time window alignment [Bailey, 2005].

Accurate normalization is essential for good quantitation in PET. Traditional solutions to the normalization problem include direct [Defrise *et al.*, 1991b, Vicente *et al.*, 2006], component-based [Hoffman *et al.*, 1989, Casey *et al.*, 1996, Badawi and Marsden, 1999a] or iterative methods [Hermansen *et al.*, 1997, Bai *et al.*, 2002]. With direct methods, a known source of activity is scanned, then the normalization factors are estimated as the ratio between the known ideal number of coincidences and those actually measured [Defrise *et al.*, 1991a]. The main problem with this method is that it requires the accumulation of a very large number of counts in order to achieve acceptable statistical accuracy for each LOR. Component-based methods divide the normalization factors into detector efficiency and spatial distortion correction, intrinsic detector efficiency, geometric factors, crystal interference, dead-time factors, etc [Badawi and Marsden, 1999a] .

1.3.6. Dead-time

PET scanners may be regarded as a series of subsystems, each of which requires a minimum amount of time to elapse between successive events, for them to be registered as separated. Since radioactive decay is a random process, there is always a finite probability that successive events will occur within any minimum time interval, and at high count-rates, the fraction of events falling in this category can become very significant. The main effect of this phenomenon is a loss of the linear relationship between the number of coincidence events registered by the PET scanner and the total activity inside the FOV. The parameter that characterizes the counting behavior of the system at high event rates is known as dead-time [Knoll, 2000]. The fractional dead-time of a system at a given count-rate is defined as the ratio of the measured count-rate and the count-rate that would have been obtained if the system behaved in a linear manner [Casey *et al.*, 1996].

Dead-time correction schemes are usually constructed measuring the live-time (1–fractional dead-time) for each subsystem. If this is not possible, an analytic model incorporating knowledge of the system architecture is constructed, and fitted to data from decaying source experiments. The decay correction scheme then consists of applying a set of measured and modeled correction factors to the data acquired.

Dead-time models usually treat system dead-time as being separable into two components, described as paralyzable and non-paralyzable [Knoll, 2000]. The paralyzable component describes the situation where the system is unable to process events for a fixed amount of time τ[3] after each event. If one event arrives while the system is busy due to a preceding event, the system remains dead for a further τ seconds from the time of arrival of the second event. The relationship between the measured event rate *m*, the actual event rate *n*, and the dead-time resulting from a single event is given by:

$$m = ne^{-n\tau} \tag{20}$$

In the non-paralyzable case, the system is again rendered dead for a time τ after each event, but while the system is dead, further events have no effect. For such systems, the measured count rate tends asymptotically to a limiting value of τ-1 as the actual count-rate increases, and the relationship between m, n and τ is given by [Knoll, 2000]:

$$m = \frac{n}{1-n\tau} \tag{21}$$

1.3.7. Pile-up

As it was mentioned before, pulse pile-up occurs when a photon deposits energy in the detector crystal while the signal from the previous event is still being integrated. Pile-up events cause two types of errors in PET data. The first one occurs when the pile-up event provides a large enough signal to fall outside the energy window and the event is lost. Under this situation, deadtime corrections will be required for quantitative measurement. The second error is interaction mispositioning. In detection systems, which employ a 2-D matrix of crystals and analog logic to identify the crystal of interaction, the scintillation photons from all crystals are processed as a single event, and for pile-up events the apparent location of the interaction results from an average of the crystals that absorbed radiation. If these events are not rejected, they will cause mispositioning of valid coincidence events. This will cause loss of resolution and contrast in the image, and a transfer of counts between image planes, leading to loss of counts in the originating plane and additional background events in the destination plane [Germano and Hoffman, 1990, Badawi and Marsden, 1999b].

For more information about pile-up and dead-time corrections see chapter 4, section 4.1.

[3] Although we use the same notation 'τ' to refer to dead-time and coincidence time window, these two parameters have totally different meaning, as the reader can figure out from the explanation above.

1.4. Monte Carlo Simulations

Monte Carlo simulation methods can be described as statistical methods that use random numbers as a base to model problems involving stochastic processes [Kalos and Whitlock, 1986]. The name of the technique was chosen during the World War II Manhattan Project due to the close connection to games of chance and the location of the famous casino in Monte Carlo. The general concept of Monte Carlo simulation is to create a model, as similar as possible to the real system and to simulate interactions with that system based on *a priori* known probabilities of occurrence through random sampling of Probability Density Functions (PDFs).

Due to the stochastic nature of radiation emission and detection processes, the Monte Carlo method is particularly interesting for medical physics in areas such as radiotherapy, radiation protection and nuclear medicine [Andreo, 1991]. In fact, this simulation technique is nowadays an essential research tool in nuclear medicine to study the response of imaging systems, like PET and SPECT (Single Photon Emission Computer Tomography) scanners, predicting the performance of new detectors and optimizing their design [Zaidi, 1999]. In addition, Monte Carlo data is currently essential for the development, validation and comparative evaluation of image reconstruction techniques and for the assessment of correction methods such as photon attenuation and scattering. One of the advantages of Monte Carlo simulations is the possibility to change different parameters and to investigate the effects of such modifications on the performance of scanners, allowing testing several detection configurations that may be impracticable using an experimental approach. Following the development of more powerful computing systems, Monte Carlo has recently been used to produce simulation data that allows to anticipate the lesion detectability performance of imaging systems under development as well as to calculate the system matrix for image reconstruction algorithms, as an alternative to analytical models.

The success of this approach is due to the ability of Monte Carlo techniques to accurately describe the physics of the interaction of particles with matter by using pseudo–random number generators, and rules to sample probability distributions and cross–sections to determine the interaction probability of particles traveling through a given material. When simulating photon interactions, the partial and total cross section data (based on the material constitution) represent such information and are used to calculate the path length and type of interaction for this particle. Afterwards, the PDFs are sampled by predefined sampling rules using randomly generated numbers. The energy of such a photon can be dissipated along its path or the photon can cross all scattering and attenuating media to reach the detector where a new PDF sampling decides whether it should be accounted for in the scoring region or be discarded [Zaidi, 1999, Buvat and Castiglioni, 2002].

A detailed description of the general principles and applications of the Monte Carlo method can be found in [Andreo, 1991, Ljungberg *et al.*, 1998, Zaidi, 1999, Zaidi and Sgouros, 2003, Zaidi, 2006].

1.4.1. Random numbers and probability distribution function

Monte Carlo simulations employ random numbers. A sequence of random numbers is such that it is impossible to predict which will be the next number in the sequence. Sequences of perfectly random numbers are almost impossible to generate in a computer, by definition. Instead, pseudo-random numbers are employed. These pseudo-random numbers are generated by an algorithm that produces sequences of reasonably unpredictable appearance and with very long repetition cycles. These algorithms use a seed or initial number as a starting point for the generation of the sequence. Two sequences will be identical if they are generated from the same seed and algorithm and therefore, different seeds must be used in each simulation. In addition, these sequences of random numbers are often built so that they produce random variables that follow an uniform distribution in a specific range of values, that is, the probability of appearance of any number in the interval would be the same [Kalos and Whitlock, 1986].

Most programming languages include algorithms to generate sequences of random numbers uniformly distributed in the interval (0, 1). These are used as the basis for the generation of more complex distributions suitable for Monte Carlo methods. In what follows we introduce a few statistical definitions that will be useful for Monte Carlo methods.

The mentioned probability distribution function (PDF) of a continuous variable x ($p(x)$) is the function that contains the probability for x taking a specific value. This function must be positive and normalized to unity in a range of values (x_{min}, x_{max}) [Ljungberg *et al.*, 1998].

$$p(x) \geq 0 \qquad \int_{x_{\min}}^{x_{\max}} p(x)\,dx = 1 \tag{22}$$

The cumulative distribution function (CDF) of a variable x is the function that contains the probability that the value of the random variable falls within a particular interval [x_{min}, x]. It is therefore a non-decreasing function from $P(x_{min})=0$ to $P(x_{max})=1$[Ljungberg *et al.*, 1998].

$$\mathrm{P}(x) \equiv \int_{x_{\min}}^{x} p(x')\,dx' \tag{23}$$

The first ingredient of a Monte Carlo calculation is the numerical sampling of random variables with specified PDFs. Different techniques to generate random values of a variable x, distributed in the interval (x_{min}, x_{max}) according to a given PDF, $p(x)$, are explained in more detail for instance in [Sempau *et al.*, 2003a].

1.4.2. Monte Carlo Packages for Nuclear Medicine

Several Monte Carlo computer codes for the simulation of radiation transport are available in the public domain. The majority of Monte Carlo codes were initially designed for high energy physics experiments or nuclear physics that later found applications also outside their original domain. For that reason, there is a large community of researchers continuously maintaining and improving these codes as well as contributing to their validation.

Currently there are many Monte Carlo simulation packages with different characteristics, suitable for either PET or SPECT processes, at different levels of reliability. Accurate and versatile general-purpose simulation packages such as EGS4 [Rogers, 1984], MCNP [Briesmeister, 1993], and most recently PENELOPE [Baró *et al.*, 1995] and Geant4 [Agostinelli, 2003] have been made available. These latter packages require a lot of expertise in order to model emission tomography configurations. Further, SimSET [Harrison *et al.*, 1993], GATE [Jan *et al.*, 2004b], Eidolon [Zaidi and Scheurer, 1999], PETSIM [Thompson *et al.*, 1992b], PeneloPET [España *et al.*, 2009], and GAMOS [Arce *et al.*,

2008] are powerful simulation codes for specific applications in PET and SPECT. Nowadays, SimSET and GATE are probably the most extensively used [Barret *et al.*, 2005, Du *et al.*, 2002, Lazaro *et al.*, 2004, Chen *et al.*, 2006]. Table 3 shows the principal features of these Monte Carlo codes.

Table 3. *Main features of PET Monte Carlo codes. Voxelized attenuation body and activity distributions are employed to define very complex geometries. Simulation of positron range and non-collinearity is mandatory to achieve realistic results. If pixelated detector capability is included, the reflector material placed among crystals can be considered. Random coincidences are very important when simulating high count rates. Some of the codes have been validated against experimental data.*

	Reference	Voxelized att / act distrib.	Positron Range / Non-collinearity	Pixelated Detectors	Randoms	Validated
PETSIM	[Thompson *et al.*, 1992b]	No	Yes	Yes	Yes	No
GATE	[Jan *et al.*, 2004b]	Yes	Yes	Yes	Yes	Yes
Eidolon	[Zaidi and Scheurer, 1999]	Yes	Yes	Yes	No	No
SimSET	[Harrison *et al.*, 1993]	Yes	Yes	No	No	Yes
PeneloPET	[España *et al.*, 2009],	No / Yes	Yes	Yes	Yes	Yes

1.5. Basics of Image Reconstruction

Tomographic images are 2D representations of structures lying within a selected plane in a 3D object. Tomography projective systems use detectors placed (or rotated) around the object to acquire many angular views (also known as projections) of a certain property of the object under study. Mathematical algorithms are then used to reconstruct the object.

Tomography image reconstruction is a problem that has attracted a lot of attention in the last forty years producing numerous reconstruction schemes. There are two basic approaches to image reconstruction. One approach is analytic in nature and utilizes the mathematics of computed tomography that relates line integral measurements to the activity distribution in the object. These algorithms have a variety of names, including Fourier reconstruction and filtered backprojection (FBP). The second approach is to use iterative methods that model the data collection process in a PET scanner and attempt, in a series of successive iterations, to find the image that is most consistent with the measured data. Figure 8 shows a possible classification of the reconstruction algorithms based on their mathematical foundation. In this section, the main features of these methods are briefly described along with different methods to sort PET data.

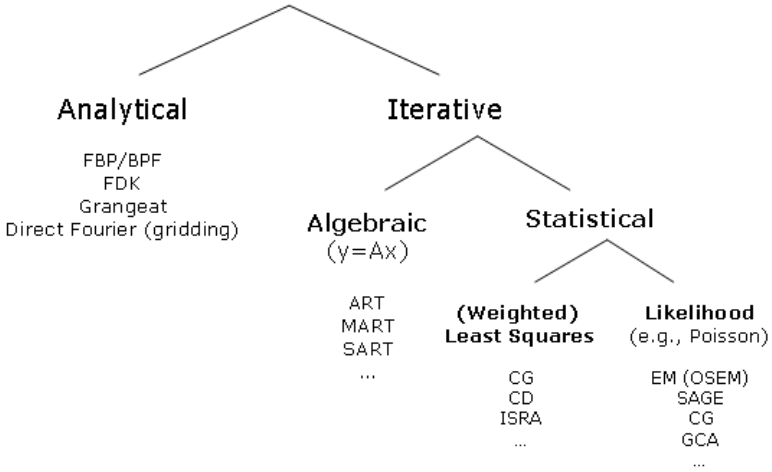

Figure 8. *Classification of image reconstruction algorithms [Fessler, 2008].*

Currently, the most commonly used image reconstruction methods are FBP and OSEM. They have been the ones employed in this thesis and will be explained in more detail in the following sections.

1.5.1. Data organization

1.5.1.1. List-mode data

The quantity of interest in PET is the 3D spatial distribution of a tracer inside the body, f (x,y,z). The raw data collected by a PET scanner are a list of 'coincidence events', representing near-simultaneous detection of annihilation photons by a pair of detectors. Each coincidence event defines a line in space along which the positron emission occurred, referred to as line of response (LOR), as it was introduced before.

One way to store the measured coincidence events for further processing is to write the information from prompt events in order of occurrence in the acquisition system. An event packet would include crystal number, energy, positioning, etc. In addition, gantry information (e.g. count rate

and time information) as well as external data (e.g. gating and patient motion information) can be included into the list-mode stream in the form of tag words [Byme, 2001, Parra and Barrett, 1998].

The event packets stored are processed afterwards and eventually transformed into sinogram datasets (see section 1.5.1.2) or LOR histograms [Kadrmas, 2004], while the timing information is analyzed so that the dataset can be split into different time frames.

1.5.1.2. Projections and sinograms

Considering the two dimensional case, a projection is defined as the number of counts in a set of parallel LORs at a specific angle ϕ *[Bailey, 2005]*

$$p(s,\phi) = \int_{-\infty}^{\infty} f(x,y)\,dy_r \qquad \textbf{(24)}$$

where f (x,y) is a two-dimensional representation of the activity distribution, s is the radial coordinate, and y_r is the transversal direction coordinate. Projections from all angles can be arranged in a matrix. Because a point source will describe a sinusoidal trajectory in this matrix representation (see Figure 9), the matrix is called a sinogram [Bailey, 2005, Bendriem and Townsend, 1998]. Sinograms are the basis of most of the image reconstruction schemes [Bendriem and Townsend, 1998].

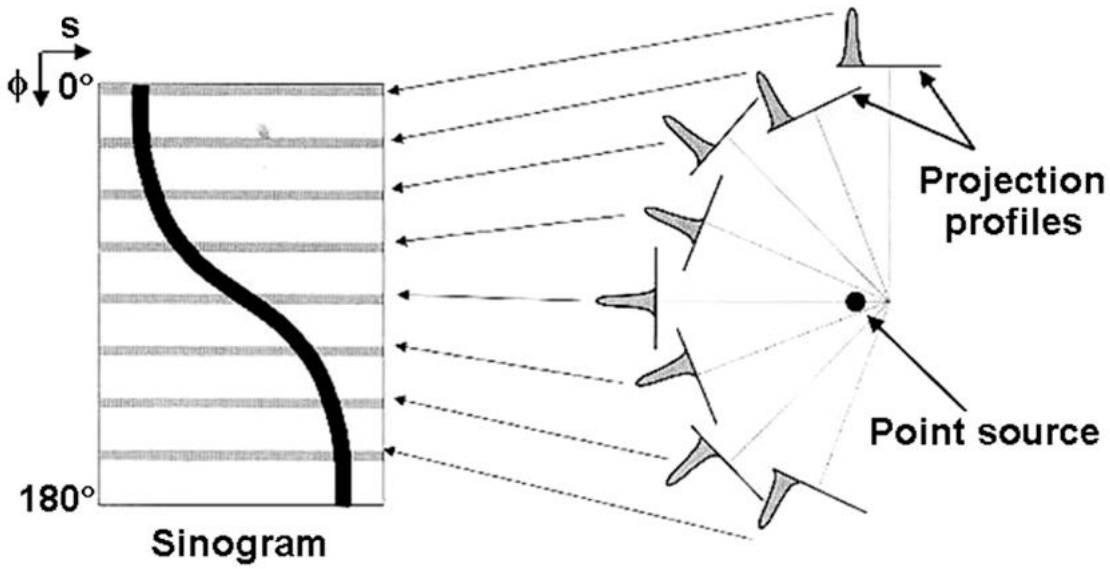

Figure 9. *The projections of a point source at different angles (right) are represented with a sine curve in a sinogram representation the data acquired [Bailey, 2005].*

1.5.1.3. Data rebinning

Rebinning algorithms allow for the sorting of data from oblique sinograms of a 3D dataset into the corresponding planes of a 2D dataset. This way, it is possible to reconstruct a 3D dataset with conventional 2D reconstruction schemes, while maintaining the sensitivity of 3D acquisitions. Mainly two approaches are used in clinical routine: single slice rebinning (SSRB) [Daube-Witherspoon and Muehllehner, 1987] and Fourier rebinning (FORE) [Defrise *et al.*, 1997].

Single-Slice *Rebinning (SSRB)*

This approximate algorithm [Daube-Witherspoon and Muehllehner, 1987] is based on the assumption that each oblique LOR measured crosses only a single transaxial section within the support of tracer distribution. SSRB defines the rebinned sinograms by [Bailey, 2005]:

$$p_{ssrb}(s,\phi,z) = \frac{1}{2\theta_{\max}(s,z)} \int_{-\theta_{\max}}^{\theta_{\max}} p_s(s,\phi,\zeta = z,\theta)\, d\theta \qquad \textbf{(25)}$$

$$\theta_{\max}(s,z) = \arctan\left(\frac{\min[z, L-z]}{\sqrt{R_d^2 - s^2}} \right) \qquad \textbf{(26)}$$

where θ_{max} is the maximum axial aperture for a LOR at a distance s from the axis in slice z, R_d is the scanner radius, and L the number of transaxial sections sampled. The algorithm is exact for tracer distributions which are linear in z. For realistic distributions, the accuracy of the approximation will decrease with increased transaxial FOV radius and with increased θ_{max}. Axial blurring and transaxial distortions, which increase with the distance to the axis of the scanner and θ, are the main drawbacks of the SSRB approximation.

Fourier rebinning (FORE)

The approximate Fourier rebinning algorithm [Defrise *et al.*, 1997] is more accurate than the SSRB algorithm and extends the range of 3D PET studies that can be processed using rebinning algorithms. The main characteristic of FORE is that it proceeds via a 2D Fourier transform of each oblique sinogram. Rebinning is based on the following relation between Fourier transforms of oblique and direct sinograms [Bailey, 2005]

$$P_s(\nu, k, z, 0) \cong P_s(\nu, k, \zeta = z + k\tan\theta/(2\pi\nu), \theta) \qquad \textbf{(27)}$$

where k is the azimuthal Fourier index. The FORE method slightly amplifies the statistical noise, as compared to SSRB, but results in significantly less azimuthal distortion.

1.5.2. Analytical methods

The central-section theorem states that, in a 2D slice, the Fourier transform of a one-dimensional projection is equivalent to a section, or profile, at the same angle through the center of the two-dimensional Fourier transform of the object [Kak and Slaney, 1988]. Figure 10 shows a pictorial description of the central-section theorem, where $\mathcal{F}1\{p(s,\phi)\}$ is the one–dimensional Fourier transform of a projection, $\mathcal{F}2\{f(x,y)\}$ is the two-dimensional Fourier transform of the image, and υ_x is the Fourier space conjugate of x. The central-section theorem indicates that if we know $P(\upsilon_S, \phi)$ at all angles, then we can fill in values for $F(\upsilon_x, \upsilon_y)$. The inverse two dimensional Fourier transform of $F(\upsilon_x, \upsilon_y)$ will give $f(x,y)$.

$$P(\upsilon_s,\phi) = \Im_1(p(s,\phi)) = \Im_2(f(x,y))\big|_\phi = F(\upsilon_x,\upsilon_y)\big|_\phi \qquad \textbf{(28)}$$

Backprojection is the adjoint operation to the forward projection process that yields the

projections of the object. Figure 11 shows the backprojection along a fixed angle ϕ. Conceptually, backprojection can be described as placing a value of $p(s,\phi)$ back into an image array along the appropriate LOR but, since the knowledge of where the values came from was lost in the projection step, a constant value is placed into all elements along the LOR [Henkin *et al.*, 2006].

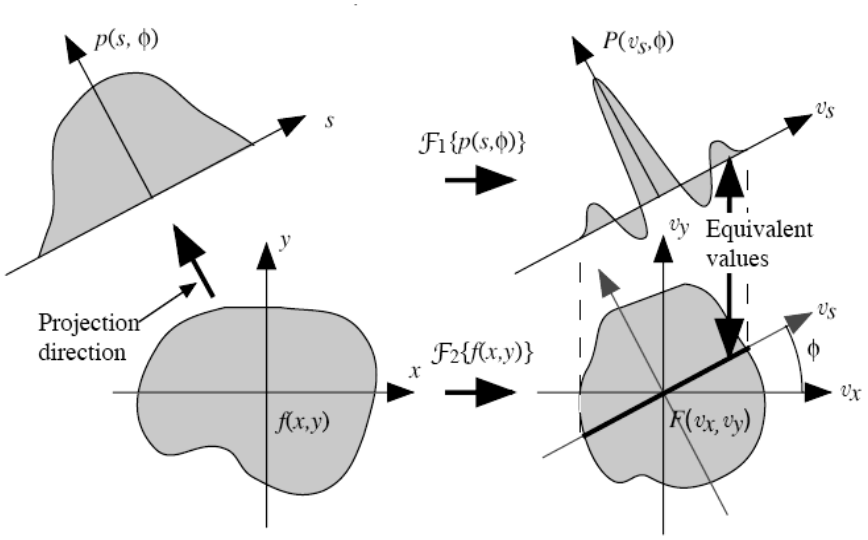

Figure 10. *Pictorial illustration of the two-dimensional central-section theorem, showing the equivalency between the one-dimensional Fourier transform (top right) of a projection at angle ϕ (top left) and the central-section at the same angle (bottom left) through the two-dimensional Fourier transform of the object (bottom right) [Bailey, 2005].*

A simple backprojection of all the collected projections is not enough to obtain a good image due to the oversampling in the center of the Fourier space. This oversampling in the center of Fourier space needs to be filtered in order to have equal sampling throughout the Fourier space. Basically, the Fourier transform of the backprojected image must be filtered with a ramp filter $\left(\upsilon = \sqrt{\upsilon_x^2 + \upsilon_y^2}\right)$. This cone filter accentuates the values at the edge of the Fourier space and reduces the ones at the center.

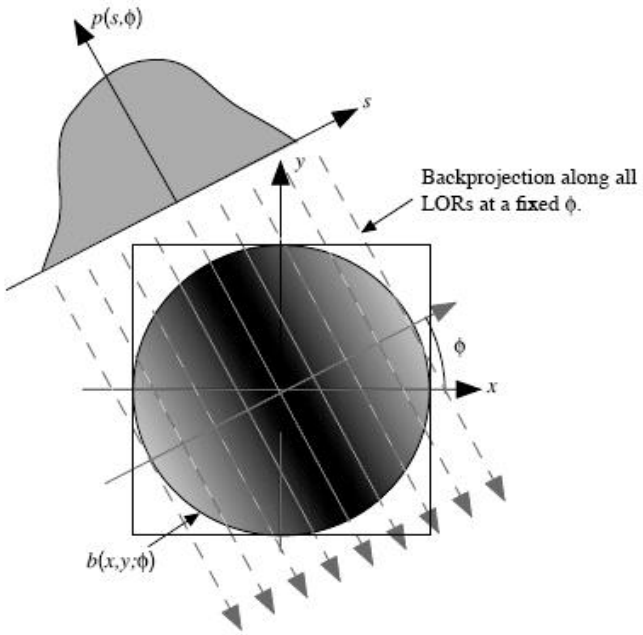

Figure 11. *Backprojection, $b(x,y;\phi)$, into an image reconstruction array of all values of $p(s,\phi)$ for a fixed value of ϕ [Henkin et al., 2006].*

The filtered-backprojection (FBP) reconstruction algorithm is the most well-known method for image reconstruction which applies the concept of backprojection and filtering explained before. Within FBP, the general expression employed to calculate the source distribution from projection data is [Herman, 1980]:

$$f(x,y)=\int_0^{\pi}\Im_1^{-1}\left\{|\upsilon_s|\,\Im_1\left\{p(s,\phi)\right\}\right\}d\phi \qquad \textbf{(29)}$$

In order to reduce the noise in the images, additional filters like Hanning or Butterworth are commonly used [Cherry *et al.*, 2003].

The advantages of FBP consist on its linearity, reproducibility, relatively easy implementation, and low computational cost. As it is considered the standard reconstruction method, it employed in to compair scanners [Goertzen *et al.*, 2012]. However, it has some important disadvantages in PET: it assumes Gaussian, instead of Poisson noise, therefore may create streak artifacts [Cherry *et al.*, 2003], it does not allow resolution recovery as iterative methods do. Additionally it may produce images with spurious negative values. In this thesis FBP has been used at times to evaluate the performance of different scanners.

1.5.3. Iterative methods

The imaging process of estimating the *y(i)* counts on each of the *i* pair of detectors, from an object discretized in *x(j)* voxels, can be described by the operation:

$$y(i)=\sum_j A(i,j)\,x(j) \qquad \textbf{(30)}$$

where *A(i,j)* is the system response matrix (SRM). The vector *x(j)* corresponds to the voxelized image and *y(i)* to the measured data, equivalent to *f(x,y)* and *p(s,ϕ)* respectively in the analytical reconstruction framework. Notation has been modified to keep the text congruent with most of the iterative reconstruction methods in literature.

Each element *A(i,j)* is defined as the probability of detecting an annihilation event coming from image voxel *j* by a detector pair *i*. This probability depends on factors such as the solid angle subtended by the voxel to the detector element, the attenuation and scatter in the source volume and the detector response characteristics.

The forward projection operation just introduced above, estimates the projection data from a given activity distribution of the source. Backward projection estimates a source volume distribution of activity from the projection data. The operation corresponds to:

$$b(j)=\sum_i A(i,j)\,y(i) \qquad \textbf{(31)}$$

where *b(j)* denotes an element of the backward projection image. Both the forward and backward projection operations require the knowledge of the SRM [Frese *et al.*, 2001, Rafecas *et al.*, 2004]. Iterative reconstruction algorithms repeatedly use the forward and backward projection operations, which are the most time-consuming parts of iterative reconstruction programs. Some implementations trade accuracy for speed by making approximations that neglect some physical processes, such as positron range, scatter and fractional energy collection at the scintillators or visible light loses in the detectors [Vaquero *et al.*, 2004, Lee *et al.*, 2000, Yamaya *et al.*, 2003]. This approach simplifies these operations to gain speed, but this tradeoff often leads to non-optimal images.

1.5.3.1. EM-ML

The most widely applied algorithm for finding the maximum-likelihood (ML) estimation of activity *f* given the projections *p*, is the expectation maximization (EM). This was first applied to the emission tomography problem by Shepp and Vardi [Shepp and Vardi, 1982]. ML, though, is a general statistical method, formulated to solve many different optimization problems in physics, biology, economy and others. The EM-ML algorithm can be written as [Herraiz *et al.*, 2006b]:

$$x^{it+1}(j) = x^{it}(j) \frac{\sum_i A(i,j) \dfrac{y(i)}{\sum_{j'} A(i,j') x^{it}(j')}}{\sum_i A(i,j)} \qquad \textbf{(32)}$$

where $x^{it}(j)$ is the expected value of voxel *j* at iteration *it*. The accuracy of the SRM will be extremely important for the quality of the images resulting from the reconstruction method [Mumcuoglu *et al.*, 1996].

Usually, iterative algorithms based on ML statistical models assume that the data being reconstructed retain Poisson statistics [Shepp and Vardi, 1982]. However, to preserve the Poisson statistical nature of data, it is usually necessary to avoid pre-corrections [Qi *et al.*, 1998] to the data. Corrections for randoms, scatter and other effects should be incorporated into the reconstruction procedure itself, rather than being applied as pre-corrections to the data. At times, sophisticated rebinning strategies are employed to build sinograms into radial and angular sets. This also changes the statistical distribution of the data, which may no longer be Poisson like [Kadrmas, 2004].

A serious disadvantage of the EM procedure is its slow convergence [Lewittt *et al.*, 1994]. Typically, hundreds of image updates are required. This is due to the fact that the image is updated only after a full iteration is finished, that is, when all the LORs have been projected and back projected at least once. In the ordered subset EM (OSEM) algorithm, proposed by [Hudson and Larkin, 1994], the image is updated more often, which has been shown to reduce the number of necessary iterations to achieve a convergence equivalent to that of EM:

$$convergence: \; Subiterations = Iterations \times Subsets$$

According to the literature, EM methods have another important drawback: noisy images are obtained from over-iterated reconstructions, and this is usually attributed to either the fact that there is no stopping rule in this kind of iterative reconstruction [Johnson, 1987] or to the statistical (noisy) nature of the detection process and reconstruction method [Bettinardi *et al.*, 2002, Biemond *et al.*, 1990]. In practice, an image of reasonable quality is obtained after a few iterations [Hudson and Larkin, 1994].

Several techniques have been proposed to address the noisy nature of the data: filtering the image either after completion of the reconstruction, during iterations or between them [Slijpen and Beekman, 1999], removal of noise from the data using wavelet based methods [Mair *et al.*, 1996] or smoothing the image with Gaussian kernels (Sieves method) [Snyder *et al.*, 1987, Liow and Strother, 1991].

Maximum *a priori* (MAP) algorithms are also widely used [Green, 1990]. MAP adds *a priori* information during the reconstruction process, the typical assumption being that due to the inherent finite resolution of the system the reconstructed image should not have abrupt edges. Thus, MAP methods apply a penalty function to those voxels which differ too much from their neighbours. Whether the maximum effective resolution achievable is limited, or even reduced, by the use of these methods is still an open issue [Alessio *et al.*, 2003]. On the other hand, a proper choice of the

reconstruction parameters, such as the number of iterations, the use of an adequate system response and a smart choice of subsetting, allows high quality images to be obtained by the EM procedure [Herraiz *et al.*, 2006b].

In this thesis the iterative method has been extensively used because it produces images with higher quality. Futhermore, a new regularization procedure has been implemented in order to get a more uniform resolution in the image for certain scanner configurations.

1.6. References

Agostinelli, S. 2003. GEANT4 - a simulation toolkit. *Nucl. Inst. Meth. In Phy. Res. A,* 506**,** 250-303.

Alessio, A., Sauer, K. & Bouman, C. A. 2003. MAP reconstruction from spatially correlated PET data. *Nuclear Science, IEEE Transactions on,* 50**,** 1445-1451.

Allemand, R., Gresset, C. & Vacher, J. 1980. Potential advantages of a Cesium Floride scintillator for time-of-flight positron camera. *J. Nucl. Med.,* 21**,** 153-5.

Andreo, P. 1991. Monte Carlo techniques in medical radiation physics. *Physics in Medicine and Biology,* 36**,** 861.

Anger, H. O. 1969. Scintillation Camera and Multiplane Tomographic Scanner. *Kaku Igaku,* 62**,** 125-48.

Arce, P., Rato, P., Canadas, M. & Lagares, J. I. 2008. GAMOS: A Geant4-based easy and flexible framework for nuclear medicine applications. *In:* Nuclear Science Symposium Conference Record, 2008. NSS '08. IEEE, 19-25 Oct. 2008 2008. 3162-3168.

Badawi, R. D., Kohlmyer, S. G., Harrison, R. L., Vannoy, S. D. & Lewellen, T. K. 2000. The effect of camera geometry on singles flux, scatter fraction and trues and randoms sensitivity for cylindrical 3D PET-a simulation study. *Nuclear Science, IEEE Transactions on,* 47**,** 1228-1232.

Badawi, R. D. & Marsden, P. K. 1999a. Developments in component-based normalization for 3D PET. *Physics in Medicine and Biology,* 44**,** 571.

Badawi, R. D. & Marsden, P. K. 1999b. Self-normalization of emission data in 3D PET. *IEEE Transactions on Nuclear Science,* 46**,** 709-712.

Badawi, R. D., Miller, M. P., Bailey, D. L. & Marsden, P. K. 1999. Randoms variance reduction in 3D PET. *Phys Med Biol,* 44**,** 941-54.

Bai, B., Li, Q., Holdsworth, C. H., Asma, E., Tai, Y. C., Chatziioannou, A. & Leahy, R. M. 2002. Model-based normalization for iterative 3D PET image reconstruction. *Physics in Medicine and Biology,* 47**,** 2773.

Bailey, D. L. 2005. *Positron emission tomography: basic sciences*, Springer.

Baró, J., Sempau, J., Fernández-Varea, J. M. & Salvat, F. 1995. PENELOPE: An algorithm for Monte Carlo simulation of the penetration and energy loss of electrons and positrons in matter. *Nucl. Inst. Meth. In Phy. Res. B,* 100**,** 31-46.

Barret, O., Carpenter, T. A., Clark, J. C., Ansorge, R. E. & Fryer, T. D. 2005. Monte Carlo simulation and scatter correction of the GE Advance PET scanner with SimSET and Geant4. *Phys. Med. Biol.,* 50**,** 4823-40.

Bendriem, B. & Townsend, D. W. 1998. The theory and practice of 3D PET. Kluwer Academic.

Bettinardi, V., Pagani, E., Gilardi, M. C., Alenius, S., Thielemans, K., Teras, M. & Fazio, F. 2002. Implementation and evaluation of a 3D one-step late reconstruction algorithm for 3D positron emission tomography brain studies using median root prior. *Eur. J. Nucl. Med. Mol. Imaging,* 29**,** 7-18.

Biemond, J., Lagendijk, R. & Mersereau, R. 1990. Iterative methods for image deblurring *In:* IEEE NSS-MIC, 1990. 856-883.

Brasse, D., Kinahan, P. E., Lartizien, C., Comtat, C., Casey, M. & Michel, C. 2005. Correction methods for random coincidences in fully 3D whole-body PET: impact on data and image quality. *J Nucl Med,* 46**,** 859-67.

Briesmeister, J. F. 1993. MNCP 4 A, Monte Carlo N-Particle Transport System. Los Alamos, New Mexico: Los Alamos National Laboratory.

Buvat, I. & Castiglioni, I. 2002. Monte carlo simulations in spet and pet. *The quarterly journal of nuclear medicine,* 46**,** 48–61.

Byme, C. L. 2001. Likelihood maximization for list-mode emission tomographyc image reconstruction. *IEEE Trans. Med. Imaging,* 20**,** 1084-92.

Casey, M. E., Gadagkar, H. & Newport, D. 1996. A component based method for normalization in volume PET. *In:* GRANGEAT, P. & AMANS, J. L., eds. Three-Dimensional Image Reconstruction in Radiology and Nuclear Medicine, 1996 Aix-Les-Bains, France. Kluwer Academic, 66-71.

Casey, M. E. & Hoffman, E. J. 1986. Quantitation in positron emission computed tomography: 7. A technique to reduce noise in accidental coincidence measurements and coincidence efficiency calibration. *J Comput Assist Tomogr,* 10**,** 845-50.

Casey, M. E. & Nutt, R. 1986. A Multicrystal Two Dimensional BGO Detector System for Positron Emission Tomography. *IEEE Trans. Nuc. Sci.,* 33**,** 460-463.

Cooke, B. E., Evans, A. C., Fanthome, E. O., Alarie, R. & Sendyk, A. M. 1984. Performance Figures and Images from the Therascan 3128 Positron Emission Tomograph. *Nuclear Science, IEEE Transactions on,* 31**,** 640-644.

Cooper, R., Turk, G., Boston, A., Boston, H., Cresswell, J., Mather, A., Nolan, P., Hall, C., Lazarus, I. & Simpson, J. 2007. Position sensitivity of the first SmartPET HPGe detector. *Nuclear Instruments and Methods in Physics Research Section A: Accelerators, Spectrometers, Detectors and Associated Equipment,* 573**,** 72-75.

Chen, Y., Liu, B., O'Connor, M., Didier, C. S. & Glick, S. J. 2006. Comparison of Scatter/Primary Measurements with GATE Simulations for X-Ray Spectra in Cone Beam CT Mammography. *In:* IEEE NSS-MIC, 2006 San Diego.

USA, 3909-14.

Cherry, S. R., Sorenson, J. A. & Phelps, M. E. 2003. *Physics in nuclear medicine*, Saunders.

Daube-Witherspoon, M. E. & Muehllehner, G. 1987. Treatment of axial data in three-dimensional PET. *J Nucl Med,* 28**,** 1717-24.

DeBenedetti, S., Cowan, C. E., Konneker, W. R. & Primakoff, H. 1950. On the angular distribution of two-photon annihilation radiation. *Physical Review,* 77**,** 205-212.

Defrise, M., Kinahan, P. E., Townsend, D. W., Michel, C., Sibomana, M. & Newport, D. F. 1997. Exact and approximate rebinning algorithms for 3-D PET data. *Medical Imaging, IEEE Transactions on,* 16**,** 145-158.

Defrise, M., Townsend, D. & Clack, R. 1991a. Favor: a fast reconstruction algorithm for volume imaging in PET. *In:* Nuclear Science Symposium and Medical Imaging Conference, 1991., Conference Record of the 1991 IEEE, 2-9 Nov 1991 1991a. 1919-1923 vol.3.

Defrise, M., Townsend, D. W., Bailey, D., Geissbuhler, A. M. C. & Jones, T. 1991b. A normalization technique for 3D PET data. *Physics in Medicine and Biology,* 36**,** 939.

Derenzo, S. E. 1979. Precision measurement of annihilation point spread distributions for medically important positron emitters. *In:* 5th Int. Conf. of Positron Annihilation, 1979 Lake Yamanaka, Japan. 819–23.

Du, Y., Frey, E. C., Wang, W. T., Tocharoenchai, C., Baird, W. H. & Tsui, B. M. W. 2002. Combination of MCNP and SimSET for Monte Carlo simulation of SPECT with medium- and high-energy photons. *IEEE Trans. Nuc. Sci.,* 49**,** 668-74.

Eijk, C. W. E. v. 2002. Inorganic scintillators in medical imaging. *Physics in Medicine and Biology,* 47**,** R85.

España, S., Fraile, L. M., Herraiz, J. L., Udías, J. M., Desco, M. & Vaquero, J. J. 2010. Performance evaluation of SiPM photodetectors for PET imaging in the presence of magnetic fields. *Nuclear Instruments and Methods in Physics Research Section A: Accelerators, Spectrometers, Detectors and Associated Equipment,* 613**,** 308-316.

España, S., Herraiz, J. L., Vicente, E., Vaquero, J. J., Desco, M. & Udias, J. M. 2009. PeneloPET, a Monte Carlo PET simulation tool based on PENELOPE: features and validation. *Phys Med Biol,* 54**,** 1723-42.

España, S., Tapias, G., Fraile, L. M., Herraiz, J. L., Vicente, E., Udias, J., Desco, M. & Vaquero, J. J. 2008. Performance evaluation of SiPM detectors for PET imaging in the presence of magnetic fields. *In:* Nuclear Science Symposium Conference Record, 2008. NSS '08. IEEE, 19-25 Oct. 2008 2008. 3591-3595.

Fessler, J. A. 2008. Iterative Methods for Image Reconstruction (ISBI Tutorial).

Frese, T., Rouze, N. C., Bouman, C. A., Sauer, K. & Hutchins, G. D. 2001. Quantitative comparison of FBP, EM, and Bayesian reconstruction algorithms, including the impact of accurate system modeling, for the IndyPET scanner. *In:* Nuclear Science Symposium Conference Record, 2001 IEEE, 2001 2001. 1806-1810.

Germano, G. & Hoffman, E. J. 1990. *A study of data loss and mispositioning due to pileup in 2-D detectors in PET*.

Goertzen, A. L., Bao, Q., Bergeron, M., Blankemeyer, E., Blinder, S., Cañadas, M., Chatziioannou, A. F., Dinelle, K., Elhami, E., Jans, H.-S., Lage, E., Lecomte, R., Sossi, V., Surti, S., Tai, Y.-C., Vaquero, J. J., Vicente, E., Williams, D. A. & Laforest, R. 2012. NEMA NU 4-2008 Comparison of Preclinical PET Imaging Systems. *The Journal of Nuclear Medicine (Accepted)*.

Green, P. J. 1990. Bayesian reconstructions from emission tomography data using a modified EM algorithm. *Medical Imaging, IEEE Transactions on,* 9**,** 84-93.

Harrison, R. L., Vannoy, S. D., Haynor, D. R., Gillispie, S. B., Kaplan, M. S. & Lewellen, T. K. 1993. Preliminary Experience With The Photon History Generator Module Of A Public-domain Simulation System For Emission Tomography. *In:* Nuclear Science Symposium and Medical Imaging Conference, 1993., 1993 IEEE Conference Record., 31 Oct-6 Nov 1993 1993. 1154-1158.

Henkin, R. E., Bova, D., Dillehay, G. L. & Karesh, S. M. 2006. *Nuclear medicine*, Philadelphia, Elsevier Health Sciences.

Herman, G. T. 1980. *Image reconstruction from projections: the fundamentals of computerized tomography*, Academic Press.

Hermansen, F., Spinks, T. J., Camici, P. G. & Lammertsma, A. A. 1997. Calculation of single detector efficiencies and extension of the normalization sinogram in PET. *Phys Med Biol,* 42**,** 1143-54.

Herraiz, J. L., España, S., Vaquero, J. J., Desco, M. & Udias, J. M. 2006b. FIRST: Fast Iterative Reconstruction Software for (PET) tomography. *Phys. Med. Biol.,* 51**,** 4547-4565.

Hoffman, E. J., Guerrero, T. M., Germano, G., Digby, W. M. & Dahlbom, M. 1989. PET system calibrations and corrections for quantitative and spatially accurate images. *Nuclear Science, IEEE Transactions on,* 36**,** 1108-1112.

Huang, S. C., Hoffman, E. J., Phelps, M. E. & Kuhl, D. E. 1979. Quantitation in positron emission computed tomography: 2. Effects of inaccurate attenuation correction. *J Comput Assist Tomogr,* 3**,** 804-14.

Hudson, H. M. & Larkin, R. S. 1994. Accelerated image reconstruction using ordered subsets of projection data. *Medical Imaging, IEEE Transactions on,* 13**,** 601-609.

Jakoby, B. W., Bercier, Y., Conti, M., Casey, M. E., Bendriem, B. & Townsend, D. W. 2011. Physical and clinical performance of the mCT time-of-flight PET/CT scanner. *Phys Med Biol,* 56**,** 2375-89.

Jan, S., Santin, G., Strul, D., Staelens, S., Assie, K., Autret, D., Avner, S., Barbier, R., Bardies, M., Bloomfield, P. M.,

Brasse, D., Breton, V., Bruyndonckx, P., Buvat, I., Chatziioannou, A. F., Choi, Y., Chung, Y. H., Comtat, C., Donnarieix, D., Ferrer, L., Glick, S. J., Groiselle, C. J., Guez, D., Honore, P. F., Kerhoas-Cavata, S., Kirov, A. S., Kohli, V., Koole, M., Krieguer, M., van der Laan, D. J., Lamare, F., Largeron, G., Lartizien, C., Lazaro, D., Maas, M. C., Maigne, L., Mayet, F., Melot, F., Merheb, C., Pennacchio, E., Perez, J., Pietrzyk, U., Rannou, F. R., Rey, M., Schaart, D. R., Schmidtlein, C. R., Simon, L., Song, T. Y., Vieira, J. M., Visvikis, D., Van de Walle, R., Wieers, E. & Morel, C. 2004b. GATE: a simulation toolkit for PET and SPECT. *Phys Med Biol,* 49**,** 4543-61.

Johnson, V. E. 1987. A note on stopping rules in EM-ML reconstructions of ECT images. *IEEE Trans. Med. Imaging,* 13**,** 569-71.

Joung, J., Miyaoka, R. S. & Lewellen, T. K. 2001. cMiCE:a high resolution animal PET using continuous LSO with a statistics based positioning scheme. *In:* IEEE NSS-MIC, 2001. 1137-1141 vol.2.

Kadrmas, D. J. 2004. LOR-OSEM: statistical PET reconstruction from raw line-of-response histograms. *Phys. Med. Biol.,* 49**,** 4731-4744.

Kak, A. C. & Slaney, M. 1988. *Principles of Computerized Tomographic Imaging,* New York, Society for Industrial Mathematics.

Kalos, M. H. & Whitlock, P. A. 1986. *Monte Carlo Methods, vol. 1,* New York, Wiley.

Knoll, G. F. 2000. *Radiation detection and measurement / Glenn F. Knoll,* New York :, Wiley.

Krane, K. S. 1987. *Introductory Nuclear Physics,* New York, Wiley.

Lage, E., Tapias, G., Villena, J., Desco, M. & Vaquero, J. J. 2010. Data acquisition electronics for gamma ray emission tomography using width-modulated leading-edge discriminators. *Physics in Medicine and Biology,* 55**,** 4291.

Lazaro, D., Buvat, I., Loudos, G., Strul, D., Santin, G., Giokaris, N. & Donnarieix, D. 2004. Validation of the GATE Monte Carlo simulation platform for modelling a CsI(Tl) scintillation camera dedicated to small-animal imaging. *Phys. Med. Biol.,* 49**,** 271-285.

Lee, J., Vaquero, J. J., Barbosa, F. J., Seidel, J. & Green, M. V. 2000. High performance phoswich detector module for small animal PET. *J. Nucl. Med.,* 41.

Lerche, C. W., Benlloch, J. M., Sanchez, F., Pavon, N., Escat, B., Gimenez, E. N., Fernandez, M., Torres, I., Gimenez, M., Sebastia, A. & Martinez, J. 2005. Depth of γ-ray interaction within continuous crystals from the width of its scintillation light-distribution. *Nuclear Science, IEEE Transactions on,* 52**,** 560-572.

Levin, C. S. & Hoffman, E. J. 1999. Calculation of positron range and its effect on the fundamental limit of positron emission tomography system spatial resolution. *Phys. Med. Biol.,* 44**,** 781-799.

Lewellen, T. K. 2008. Recent developments in PET detector technology. *Phys Med Biol,* 53**,** R287-317.

Lewellen, T. K., Laymon, C. M., Miyaoka, R. S., Ki Sung, L. & Kinahan, P. E. 2001. Design of a Firewire based data acquisition system for use in animal PET scanners. *In:* Nuclear Science Symposium Conference Record, 2001 IEEE, 2001 2001. 1974-1978.

Lewittt, R. M., Muehllehner, G. & Karpt, J. S. 1994. Three-dimensional image reconstruction for PET by multi-slice rebinning and axial image filtering. *Phys Med Biol,* 39**,** 321-39.

Liow, J. S. & Strother, S. C. 1991. Practical tradeoffs between noise, resolution and quantitation, and number of iterationsfor maximum likelihood reconstructions. *IEEE Trans. Med. Imag.,* 10**,** 563-571.

Ljungberg, M., Strand, S. E. & King, M. A. 1998. *Monte Carlo calculations in nuclear medicine: applications in diagnostic imaging,* Institute of Physics Pub.

Lois, C., Jakoby, B. W., Long, M. J., Hubner, K. F., Barker, D. W., Casey, M. E., Conti, M., Panin, V. Y., Kadrmas, D. J. & Townsend, D. W. 2010. An assessment of the impact of incorporating time-of-flight information into clinical PET/CT imaging. *J Nucl Med,* 51**,** 237-45.

MacManus, M., Nestle, U., Rosenzweig, K. E., Carrio, I., Messa, C., Belohlavek, O., Danna, M., Inoue, T., Deniaud-Alexandre, E., Schipani, S., Watanabe, N., Dondi, M. & Jeremic, B. 2009. Use of PET and PET/CT for radiation therapy planning: IAEA expert report 2006-2007. *Radiother Oncol,* 91**,** 85-94.

Mair, B. A., Carroll, R. B. & Anderson, J. M. M. 1996. Filter banks and the EM algorithm. *In:* Nuclear Science Symposium, 1996. Conference Record., 1996 IEEE, 2-9 Nov 1996 1996. 1747-1751 vol.3.

Melcher, C. L. 2000. Scintillation crystals for PET. *J Nucl Med,* 41**,** 1051-5.

Moszynski, M., Kapusta, M., Nassalski, A., Szczesniak, T., Wolski, D., Eriksson, L. & Melcher, C. L. 2006. New Prospects for Time-of-Flight PET with LSO Scintillators. *IEEE Trans. Nuc. Sci.,* 53**,** 2484-8.

Mullani, N. A., Ficke, D. C., Hartz, R., Markham, J. & Wong, G. 1981. System design of a fast PET scanner utilizing time-of-flight. *IEEE Trans. Nuc. Sci.,* NS-28**,** 104-7.

Mumcuoglu, E. U., Leahy, R. M. & Cherry, S. R. 1996. Bayesian reconstruction of PET images: methodology and performance analysis. *Phys Med Biol,* 41**,** 1777-807.

Oliver, J. F. & Rafecas, M. 2008. Revisiting the singles rate method for modeling accidental coincidences in PET. *In:* Nuclear Science Symposium Conference Record, 2008. NSS '08. IEEE, 19-25 Oct. 2008 2008. 4288-4291.

Otte, A. N., Barral, J., Dogolshein, B., Hose, J., Klemin, S., Lorenz, E., Mirzoyan, R., Popova, E. & Teshima, M. 2005. A Test of Silicon Photomultipliers as Readout for PET. *Nucl.Instrum.Meth.A***,** 705-715.

Papathanassiou, D., Bruna-Muraille, C., Liehn, J. C., Nguyen, T. D. & Cure, H. 2009. Positron Emission Tomography in oncology: present and future of PET and PET/CT. *Crit Rev Oncol Hematol,* 72**,** 239-54.

Parra, L. & Barrett, H. H. 1998. List-mode likelihood: EM algorithm and image quality estimation demonstrated on 2D PET. *IEEE Trans. Med. Imag.,* 17**,** 228-35.

Pichler, B., Lorenz, E., Mirzoyan, R., Pimpl, W., Roder, F., Schwaiger, M. & Ziegler, S. I. 1997. Performance test of a LSO-APD PET module in a 9.4 Tesla magnet. *In:* Nuclear Science Symposium, 1997. IEEE, 9-15 Nov 1997 1997. 1237-1239 vol.2.

Powsner, R. & Powsner, E. 2006. *Essential Nuclear Medicine Physics*, Haryana, Blackwell Publishing.

Qi, J., Leahy, R. M., Cherry, S. R., Chatziioannou, A. & Farquhar, T. H. 1998. High-resolution 3D Bayesian image reconstruction using the microPET small-animal scanner. *Phys Med Biol,* 43**,** 1001-13.

Rafecas, M., Mosler, B., Dietz, M., Pogl, M., Stamatakis, A., McElroy, D. P. & Ziegler, S. I. 2004. Use of a Monte Carlo-based probability matrix for 3-D iterative reconstruction of MADPET-II data. *Nuclear Science, IEEE Transactions on,* 51**,** 2597-2605.

Raichle, M. E. 1983. Positron Emission Tomography. *Ann. Rev. Neurosci.,* 6**,** 249-267.

Rogers, D. W. O. 1984. Low energy electron transport with EGS. *Nucl. Inst. Meth. In Phy. Res. A,* 227**,** 535-48.

Sempau, J., Fernández-Varea, J. M., Acosta, E. & Salvat, F. 2003a. Experimental benchmarks of the Monte Carlo code penelope. *Nuclear Instruments and Methods in Physics Research Section B: Beam Interactions with Materials and Atoms,* 207**,** 107-123.

Shepp, L. A. & Vardi, Y. 1982. Maximum Likelihood Reconstruction for Emission Tomography. *Medical Imaging, IEEE Transactions on,* 1**,** 113-122.

Slijpen, E. T. P. & Beekman, F. J. 1999. Comparison of post-filtering and filtering between iterations for SPECT reconstruction. *Nuclear Science, IEEE Transactions on,* 46**,** 2233-2238.

Snyder, D. L., Miller, M. I., L. J. Thomas, J. & Politte, D. G. 1987. Noise and edge artifacts in maximum-likelihood reconstruction for emission tomography. *IEEE Trans. Nuc. Sci.,* MI-6**,** 228-238.

Sorenson, J. A. & Phelps, M. E. 1987. *Physics in nuclear medicine*, Grune & Stratton.

Stearns, C. W., McDaniel, D. L., Kohlmyer, S. G., Arul, P. R., Geiser, B. P. & Shanmugam, V. 2003. Random coincidence estimation from single event rates on the Discovery ST PET/CT scanner. *In:* Nuclear Science Symposium Conference Record, 2003 IEEE, 19-25 Oct. 2003 2003. 3067-3069 Vol.5.

Stöcklin, G. & Pike, V. W. 1993. *Radiopharmaceuticals for positron emission tomography: methodological aspects*, Kluwer Academic Publishers.

Tarantola, G., Zito, F. & Gerundini, P. 2003. PET instrumentation and reconstruction algorithms in whole-body applications. *J Nucl Med,* 44**,** 756-69.

Ter-Pogossian, M. M. 1982. Positron emission tomography (PET). *J Med Syst,* 6**,** 569-77.

Thompson, C. J., Moreno-Cantu, J. & Picard, Y. 1992b. PETSIM: Monte Carlo simulation of all sensitivity and resolution parameters of cylindrical positron imaging systems. *Phys Med Biol,* 37**,** 731-49.

Valk, P. E., Delbeke, D. & Bailey, D. L. 2006. *Positron emission tomography: clinical practice*, Springer.

Vaquero, J. J., Molins, A., Ortuño, J., Pascau, J. & Desco, M. 2004. Preliminary results of the small animal rotational positron emission tomography scanner. *In:* Mol. Imag. Biol., 2004. 102.

Vaska, P., Bolotnikov, A., Carini, G., Camarda, G., Pratte, J. F., Dilmanian, F. A., Park, S. J. & James, R. B. 2005. Studies of CZT for PET applications. *In:* Nuclear Science Symposium Conference Record, 2005 IEEE, 23-29 Oct. 2005 2005. 2799-2802.

Vicente, E., Vaquero, J. J., Espana, S., Herraiz, J. L., Udias, J. M. & Desco, M. 2006. Normalization in 3D PET: Dependence on the Activity Distribution of the Source. *In:* Nuclear Science Symposium Conference Record, 2006. IEEE, Oct. 29 2006-Nov. 1 2006 2006. 2206-2209.

Wernick, M. N. & Aarsvold, J. N. 2004. *Emission tomography: the fundamentals of PET and SPECT*, Elsevier Academic Press.

Williams, C. W., Crabtree, M. C. & Burgiss, S. G. 1979. Design and Performance Characteristics of a Positron Emission Computed Axial Tomograph--ECATÂ®-II. *Nuclear Science, IEEE Transactions on,* 26**,** 619-627.

Wirth, V. 1989. Effective energy resolution and scatter rejection in nuclear medicine. *Phys Med Biol,* 34**,** 85-90.

Yamaya, T., Hagiwara, N., Obi, T., Yamaguchi, M., Kita, K., Ohyama, N., Kitamura, K., Hasegawa, T., Haneishi, H. & Murayama, H. 2003. DOI-PET image reconstruction with accurate system modeling that reduces redundancy of the imaging system. *Nuclear Science, IEEE Transactions on,* 50**,** 1404-1409.

Zaidi, H. 1999. Relevance of accurate Monte Carlo modeling in nuclear medical imaging. *Med Phys,* 26**,** 574-608.

Zaidi, H. 2006. *Quantitative analysis in nuclear medicine imaging*, Springer.

Zaidi, H. & Scheurer, C. 1999. An object-oriented Monte Carlo simulator for 3D cylindrical positron tomographs. *Comput. Methods Programs Biomed.,* 58**,** 133-45.

Zaidi, H. & Sgouros, G. 2003. *Therapeutic applications of Monte Carlo calculations in nuclear medicine*, IOP, Institute of Physics Pub.

2. Materials

In this chapter we describe the materials used in this thesis. The specific materials for each particular task are described in their corresponding sections for major clarity. Specifically, in sections 2.1 and 2.2, we describe the two scanners employed for the characterization (chapter 3) and the study of several data corrections (chapter 4). Moreover, sections 2.3 and 2.4 present the main features of the Monte Carlo simulation tool and the 3D-OSEM reconstruction method used in this thesis, respectively.

2.1. The rPET scanner

The system presented in this section was envisioned for high resolution small animal PET imaging (mice and rats mainly) looking for the maximum performance achievable at a reasonable cost [Vaquero *et al.*, 2005a]. The rPET scanner has four large detectors arranged in two orthogonal pairs which rotate 180º. Here we report the design and some characteristics of the detector modules.These modules are based on position sensitive photomultipliers (PS-PMT) directly coupled to a lutetium based scintillator crystal array.

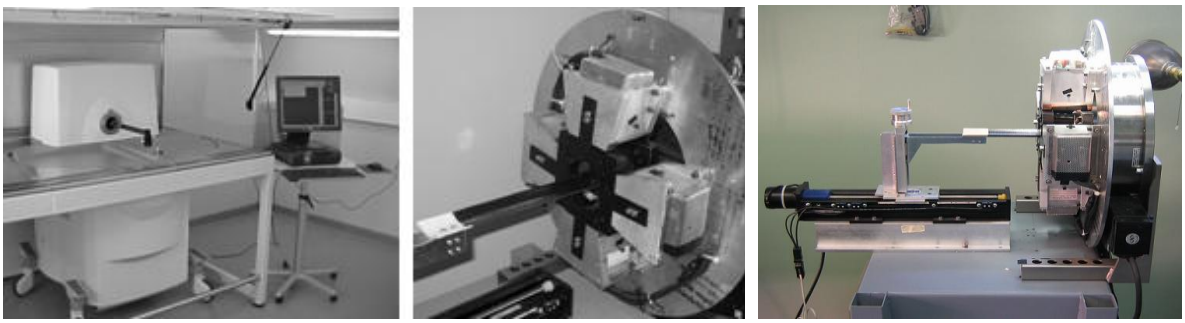

Figure 12. *rPET scanner commercialized by SEDECAL Medical Systems. The left panel shows a real experimental setup. The two right panels show two points of view of the first prototype with the covers removed (Pictures courtesy of Laboratorio de Imagen Médica (LIM) of Hospital General Universitario Gregorio Marañón).*

2.1.1. System description

Table 4. *General specifications of the rPET scanner (Adapted from [Vaquero et al., 2005a]).*

Characteristic	Specification
Scintillators	1.5x1.5x12 mm^3 LSO
Photomultipliers	Position sensitive
FOV	48x48 mm^2 (real)
Separation between detectors	160 mm
Slice thickness	0.81 mm
Number of slices	55
Energy windows	100 - 700 kev 250 - 700 kev 400 - 700 kev

rPET detectors are based on 1.5×1.5×12 mm^3 MLS crystals (Glendfield Partners, Canada) with all the facets mechanically polished (Figure 13A). MLS is a not-hygroscopic and rugged material based on lutetium, what makes it radioactive, producing a background of around 260 cps per cubic centimeter [Miyaoka *et al.*, 2001, Melcher and Schweitzer, 1992]. The individual crystals are assembled on a 30×30 matrix with 100 microns thick Lumirror reflector (Toray Corp., Japan) between crystals, achieving a packing fraction of 88%. The array is optically coupled to an H8500 flat-panel PS-PMT (Hamamatsu, Japan) [Engels *et al.*, 2003, Inadama *et al.*, 2004] using silicon grease BC-630 (Bicron/SaintGobain, The Netherlands) which index of refraction is 1.465. Weighted position readout circuits preprocess the 64 signals from the 8×8 anodes matrix which, in turn, are amplified without shaping and digitized using a charge integrating converter (A&D Precision, MA). This readout scheme, although in its current implementation suffers from the same detector dead-time limitation described in [Riboldi *et al.*, 2003], implements a modified center of gravity (COG) calculation for the event positioning [Pani *et al.*, 2003, Olcott *et al.*, 2003, Majewski *et al.*, 2001, Popov *et al.*, 2003, Siegel *et al.*, 1996, Lage *et al.*, 2010], and integrates gain compensation for each individual anode.

The amplification electronics, including the trigger signal for coincidence detection and the high voltage supply are contained in three stacked PCBs (Printed Circuit Boards), forming a base attached to the back of the PS-PMT (Figure 13B). The whole assembly is enclosed in a light tight, lead-shielded aluminum box that doubles as an EM screen. Previous works referenced in the literature [Miyaoka *et al.*, 2001, Vaquero *et al.*, 1998, Majewski *et al.*, 2001] have demonstrated that this combination of PS-PMTs, high light output scintillators arrays and charge sensitive readouts schemes is well suited for high resolution, high sensitivity PET imaging systems.

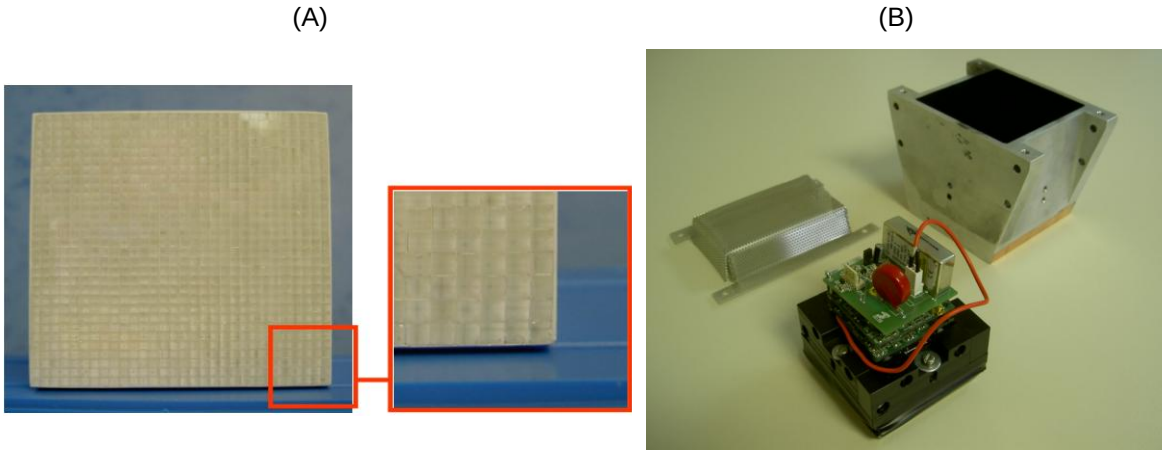

Figure 13. *(A): MLS crystals matrix. (B): rPET detector module. The crystal array and the PS-PMT are packed together in a black Delrim enclosure, with the detector electronics directly coupled to the PS-PMT sockets (front). This assembly fits on the aluminum Pb-shielded box (back-right) in which the detector is locked. The RF shield (back-left) closes the detector box. (Pictures courtesy of LIM of Hospital General Universitario Gregorio Marañón).*

2.1.2. Data acquisition and processing

Figure 14 shows a flowchart of the data processing in rPET scanner. The analog base output is directly connected to the charge integrating ADCs (Analog-to-digital converters) with a multi-coaxial cable, and the digitized events are screened and histogramed. A modified COG algorithm eliminates from the position calculation those anode signals with poor signal-to-noise ratio. The method used to filter these signals is based on a dynamic threshold value, calculated for each event. If the integrated charge for any given signal is greater than the calculated threshold, it is included in the COG calculation; otherwise the anode signal is excluded. The resulting position value is mapped to an individual crystal by means of a look-up table (LUT) previously computed, and the energy value for that event is histogramed on the corresponding crystal spectrum.

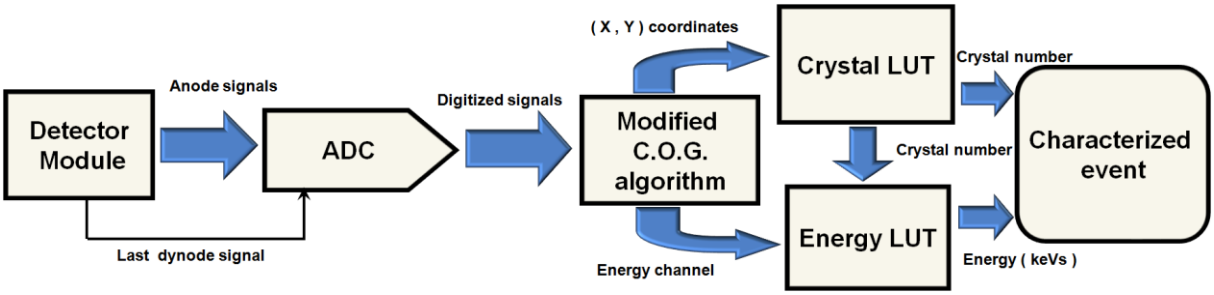

Figure 14. *Flowchart of the data processing in rPET scanner (Adapted from [Vaquero* et al.*, 2005a]).*

The data acquisition trigger is done using the signal from the last dynode of the PS-PMT, amplified at the base and filtered by a high/low discriminator that selects those events whose energy is within the hardware energy window (50-800 keV). This single, wide energy window is set for the whole PS-PMT, preventing the truncation of individual crystal spectra with different gains. This scheme allows compensating for gain variation across the detector FOV by means of a variable software energy window whose variation follows the gain variation pattern.

The rPET system acquires data in 3D-mode only, and images are reconstructed by either single slice rebinning (SSRB) followed by 2D filtered backprojection or 2D-OSEM, or by 3D-OSEM.

2.2. The Argus PET/CT scanner

The Sedecal Argus, formerly marketed by GE Healthercare as the GE eXplore Vista [Wang *et al.*, 2006b], is based on the design of the National Institutes of Health ATLAS preclinical PET system [Seidel *et al.*, 2003].

Figure 15. *Argus scanner commercialized by SEDECAL Medical Systems. (Picture courtesy of SEDECAL[4]).*

2.2.1. System description

The system, described in Table 5, consists of 36 detector modules arranged in two rings around a circle such that the face-to-face diameter of each ring is 11.8 cm. Each detector module is placed in time coincidence with the 14 opposite modules to give an effective transverse field of view of 6.7 cm and an axial FOV of 4.8 cm. Each detector module consists of a 13×13 array of 1.45×1.45 mm^2 by 15 mm long elements optically isolated from each other by reflective material. A notable feature is its depth of interaction (DOI) or parallax-correcting capability, implemented by dual-scintillator phosphor sandwich (phoswich) detector modules [Carrier *et al.*, 1988, Dahlbom *et al.*, 1997, Seidel *et al.*, 1999, Dahlbom *et al.*, 1998]. These modules comprise densely packed, square arrays of small-crosssection phoswich elements, each element created by optically joining together end to end two different scintillators. In Argus, this crystal pair is cerium-doped lutetium–yttrium orthosilicate (LYSO) in the front crystal layer and cerium-doped gadolinium orthosilicate (GSO) in the rear layer. The GSO layer is optically coupled to a Hamamatsu R8520-C12 PSPMT to create the Argus detector module.

These phoswich elements play the role of the usual single scintillation crystal in other types of small-animal PET scanners. Scintillation light from a phoswich element, each optically isolated from its neighbors, decays with the characteristic light decay time (LYSO, 40 ns; GSO, 60 ns) of the scintillator in which the annihilation γ-ray from the target interacted. Thus, if the light decay time of the event can be determined for every event, then the interaction site can be assigned to one or the other phoswich scintillator, front or back. This knowledge, in turn, locates the interaction site to the center of either scintillator and provides a two-valued estimate of the (radial) DOI of the event. Knowledge of this depth, in turn, allows for partial compensation of the DOI effect (or parallax error) that progressively degrades radial spatial resolution with increasing radial position in all PET scanners with cylindrical geometry. Thus, a DOI correcting system can use crystal elements of greater (combined) depth to improve sensitivity while at the same time suppressing resolution and resolution uniformity degradation with increasing radial position—effects that otherwise occur in machines with

[4] http://www.sedecal.com

identical geometry but without this capability.

Table 5. *Sedecal Argus PET System description [Wang et al., 2006b]*

Item	Parameter	Description or value
Detector modules	Type of module	Dual-layer phoswich (front layer: LYSO; back layer: GSO)
	Phoswich element dimensions	1.45 mm × 1.45 mm × 7 mm for LYSO and 1.45 mm × 1.45 mm × 8 mm for GSO (total length: 15 mm)
	Light decay time	LYSO: 40 ns; GSO: 60 ns
	Phoswich element arrays	13 × 13 (outside dimensions: 20 mm × 20 mm)
	Phoswich pitch	1.55 mm
	Phototubes	Hamamatsu R8520-C12
System	No. of detector modules	36 (2 rings of 18)
	No. of phoswich elements	6,084
	Total no. of crystals	12,168
	Ring diameter	11.8 cm
	Gantry aperture	8 cm
	Axial field of view	4.8 cm
	Effective transaxial field of view	6.7 cm
	Normalization or transmission source	^{68}Ge annulus
	Overall dimensions	121 cm wide × 151 cm high × 82 cm deep
	Estimated gantry weight	~200 kg
	Power	120 V alternating current, <20 A
Datasets	Acquisition mode	3D only
	Total no. of lines of response	28.8 million
	No. of 2D sinograms	61
	2D sinogram size	175 spatial samples × 128 angles
	2D dataset size	5.2 megabytes

The Argus PET/CT model integrates, besides the PET modality, a fully functional CT system. The CT is composed of a micro-focus X-ray tube and a digital flat panel detector (flat panel CMOS technology with a micro-columnar CsI:Tl scintillator plate) on a rotary gantry. Table 6 reports the main characteristics of the Argus CT system.

Table 6. *Sedecal Argus CT System description. (Adapted from [Vaquero et al., 2008])*

Item	Characteristic	Specification
Detector	FOV	75 × 75 mm
	Detector Active Area	120 × 120 mm
	Pixel Size	50, 100, 200 μm
	Scintillation Material	CsI:Tl
X-Ray Source	Focal Spot	35 μm
	X-Ray Peak energy	0-50 kV (Variable)
	Max Current	1 mA
	Max Power	50 Watts continuous

2.2.2. Data acquisition

ARGUS PET system acquires coincidence events in 3D using a data acquisition system based on charge integrating ADC modules (A&D Precision, MA) and a custom coincidence logic controller, all of them connected to the main signal processor using high-speed Ethernet links. The user may select the CT only, PET only or dual scan in any order. Dataset are intrinsically registered and fusion display tools are available in a single workstation.

Argus PET images are reconstructed either by Fourier rebinning (FORE) followed by 2D filtered backprojection or 2D-OSEM, or by 3D-OSEM.

2.3. Monte Carlo simulations: PeneloPET

As it was discussed in chapter 1 (section 1.4), there are several Monte Carlo codes that simulate the transport of radiation through matter, e.g. GEANT4 [Agostinelli, 2003], MCNP [Briesmeister, 1993], EGS4 [Kawrakow and Bielajew, 1998], and PENELOPE [Baró *et al.*, 1995, Salvat *et al.*, 2006]. Either based upon these codes, or in tables of photon cross-sections, a number of tools for PET simulation have been developed, such as SIMSET [Harrison *et al.*, 1993], PETSIM [Thomson *et al.*, 1992] or Eidolon [Zaidi and Scheurer, 1999], based on MCNP, and GATE, based in GEANT4 [Jan *et al.*, 2004a]. Probably one of the most widely known is GATE which, being based in GEANT4, can include a large variety of photon detectors and targets the large community of high energy and nuclear physics users that have acquaintance with GEANT4 [Buvat and Lazaro, 2006]. GEANT4 is powerful and flexible enough to simulate PET scanners; however, its learning curve is both steep and long. A superficial knowledge of C++ is insufficient to optimally use GEANT4, and the installation process requires more than basic computer skills. This is why GATE was developed. GATE consists of hundreds of classes that provide useful functionalities for PET simulations. No C++ programming is involved and thus it is easier to learn and use, unless there is a need to create new classes to address specific problems.

However, we chose PeneloPET [España *et al.*, 2009] as our PET simulation tool. PeneloPET is based on PENELOPE [Baró *et al.*, 1995], a Monte Carlo code which is written using FORTRAN. PENELOPE is a Monte Carlo code for the simulation of the transport in matter of electrons, positrons and photons with energies from a few hundred eV to 1 GeV. It is then less generally aimed as GEANT4, but it suits well PET needs, it is fast and robust, and it is extensively used for other medical physics applications, particularly for dosimetry and radiotherapy [Sempau and Andreo, 2006, Panettieri *et al.*, 2007, Vilches *et al.*, 2007].

We chose PeneloPET, instead of another simulation tool, because it was developed by our group (GFN, Universidad Complutense Madrid), which means a benefit whether modifications are required in order to fit our needs of this work. Besides, PeneloPET is an easy to use simulation package. It allows for realistic simulations, including high detail in physics and electronics processing of detector pulses. The ample variety of detector configurations allowed by the combination GEANT/GATE is appealing, but it comes at the cost of increased need for computing resources [Buvat and Lazaro, 2006]. However, thanks to the reduction of simulation time in PeneloPET, faster simulations are achieved without loss of simulation detail. For its versatility, speed, and easy-to-analyze outputs, PeneloPET is a tool useful for scanner design, system response calculations, development of corrections methods, and many other applications. In this section we describe briefly some of the main characteristics of PeneloPET. For further details see [España *et al.*, 2009]

2.3.1. Main features of PeneloPET

The basic components of a PeneloPET simulation are detector geometry and materials definition (including non-detecting materials, like shiedls), source definitions, non-active materials in the field of view of the scanner, and electronic chain of detection. All these components are defined using parameters in the input files. Different levels of output data are available for analysis, from sinogram and LORs histogramming to fully detailed list-mode. These data can be further exploited with the preferred programming language, including ROOT. The detailed list-mode generates a file with all the hits, single or coincidence events, and the corresponding information about interaction coordinates, deposited energy in the detectors, and time and type of coincidence: random, scatter, true, with pile-up, etc [España *et al.*, 2009].

2.3.1.1. PeneloPET structure

The source code consists of two main modules. The first one deals with the PENELOPE simulations and the level of detail chosen for these, and takes care of the information about scanner detectors and materials, source and decay. This module includes the routines involved in the distribution of isotopes and emission of particles generated in the decay processes, as well as their interactions.

The second module post-processes the decay and interaction data generated by the first module. It takes into account, for instance, Anger logic for positioning the interaction inside the crystal array, detector pile-up, energy resolution in the scintillator, and aspects of the electronics, such as coincidence time window, dead-time, time resolution, and integration time. No PENELOPE routines are generally involved in this second module. Energy windows can be applied in this second module. Continuous or pixelated detectors can be managed by this second stage of the simulation package.

In order to run the simulations on clusters of computers, a simple and portable Python[5] script is provided with the code. The use of Python enables to run the script under Windows, Linux/Unix, and Mac OS X. After configuring PeneloPET for the execution of the desired setup in a single-CPU, the Python script launches the simulation on the number of CPUs desired, with different random seeds, and takes care of the initial activity and acquisition time for each sub-process, in order to simulate the same number of decay events as the equivalent single-CPU run. In this way, the simulation time is reduced proportionally to the number of CPUs employed.

2.3.1.2. Description of PeneloPET input files

Four input files have to be prepared by the user in order to set up a simulation. As an example, Table 7 shows these input files for the simulation of a point source in the previously described rPET scanner (section 2.1, [Vaquero *et al.*, 2005a]).

The first input file in Table 7 (main.inp) contains the general parameters of the simulation, such as the acquisition protocol and acquisition time. It also enables simulation of secondary particles, if desired, and controls whether positron range and non-collinearity are taken into account. This file contains options also for scanner rotation, energy and coincidence windows, contributions to dead time, output format, and type of study.

In the second file (scanner.inp), which contains the scanner definition, multiple rings and layers of crystals can be specified. Although our main goal was to simulate pixelated detectors for high-resolution small animal PET imaging, PeneloPET is also suitable for continuous scintillator blocks or even detectors not based on scintillators (such as CZT or silicon strips) with small or no changes.

Non-radioactive materials other than the scintillator (already defined in the file scanner.inp), such as surrounding materials and shielding, are defined in a third file (object.inp). The radioactive source is defined separately in a fourth input file (source.inp), which contains source geometry and information about activity and isotope. Keeping separated definitions for sources and materials simplifies the comparison of simulations of ideal sources, without scatter or attenuation, to more realistic sources. Details about PeneloPET input files and options can be found in the PeneloPET manual[6].

Typical materials for crystals, shielding and phantoms are predefined in PeneloPET and, if necessary, new materials can be created in a straightforward way. The visualization tools built in PENELOPE (gview2d, gview3d [Salvat *et al.*, 2006]) are also available in PeneloPET to display and test geometries. This is especially useful during scanner design stages.

[5] http://www.python.org/
[6] http://nuclear.fis.ucm.es/penelopet/

Although the work presented in this thesis deal with preclinical scanners, PeneloPET is also capable of simulating clinical PET scanners. [Abushab *et al.*, 2011]

Table 7. *PeneloPET input files needed to simulate a point source in the rPET scanner [Vaquero et al., 2005a]. Full detail about these input files and options can be found in the PeneloPET manual[7]. In this input file, 'F' stands for false or disabled option, while 'T' stands for true or enabled option.*

--- GENERAL PARAMETERS --- (main.inp)	
12345 54321	!Random number generator seeds
9000 1 F	!Acquisition time (sec); Number of Frames; Read Frame List File
1000	!Limit number of interactions for each particle
F T T	!Secondary Particles Simulation; Positron Range; Non-Collinearity
0 180 3000 40	!Initial & Final and pos (deg); Numb of Steps per cycle; time per cycle (sec)
0.	!Lower Level Energy Threshold (eV)
1000000.	!Upper Level Energy Threshold (eV)
5	!Coincidence Time Window (ns)
0.1	!Trigger's Dead-Time (ns)
150	!Integration Time (ns)
1200	!Coincidence's Dead-Time (ns)
F F T	!Hits LIST; Singles LIST; Coincidences LIST
F	!Write LOR Histogram
T 117 190 4.49684	!Write Sinogram; radial bins; angular bins; maximum radio
F 99 99 55 4.48 4.2	!Write Emission Image; X Y Z voxels, Transaxial & Axial FOV (cm)
F	!Hits checking
T	!Verbose
F	!Neglecting events if more than 2 singles in the coincidence time window
--- SCANNER PARAMETERS --- (scanner.inp)	
4	!Number of Detectors per Ring
1	!Number of Detectors in Coincidence in the same Ring
1	!Number of Rings
0.	!Gap Between Rings (cm)
30	!Number of transaxial crystals per detector (columns)
30	!Number of axial crystals per detector (rows)
1	!Number of crystal layers per detector
1.2 13 0.26 1 40 0.01	!LAYER: Length (cm); Mat; E Resol.; Rise & Fall Tim (ns); Tim Error (ns)
0.16 0.16	!Pitch: Distance between centres of adjacent crystals (cm)
8.	!Radius: Centre FOV - Centre Front of Detector (cm)
--- BODY PARAMETERS --- (object.inp)	
C 1 0. 0. 0. 0. 1.62 5.0 0. 0.	!Shape Mat X Y Z R1 R2 HEIGHT (cm) PH TH (deg)
--- SOURCE PARAMETERS --- (source.inp)	
P 1E6 F 1 0.5 1. 2. 0. 0. 0. 0. 0. 0. 0. 0. 180 ! Shap Act Units Isot X Y Z R1 R2 H PH TH TH1 TH2	

2.3.1.3. Description of PeneloPET output files

Output files generated by PeneloPET can offer three different levels of detail. At the highest level, all the information about each interaction is recorded for further analysis. At the intermediate level, just the single events and the information needed for their analysis are recorded. The possibility of pile-up and cross talk is taken here into account. At the third, and lowest, level of detail, only coincidence events are recorded in a compact List-mode. Information about pile-up, scatter, random and self-coincidence events, obtained from the simulation, is also summarily available.

A coincidence event is labeled as pile-up when at least one of the single events has suffered pulse pile-up. A coincidence is considered to be a scatter coincidence when at least one of the photons that trigger the detectors has interacted before reaching the scintillator. A coincidence is considered a

[7] http://nuclear.fis.ucm.es/penelopet/

random when the two photons in the coincidence pair come from two different, uncorrelated, annihilation processes. Self-coincidence events may arise when the same photon, after scattering in a first detector, reaches a second detector. If the energy deposited in each detector is above the detection threshold, it may trigger two single events and yield a self-coincidence count. The remaining coincidences are considered as true events.

PeneloPET generates several output histograms that help to understand the results of the simulations, as for instance sinogram projections, LOR histogram, single and coincidence maps, and energy spectrum. In order to simplify the reconstruction of simulated data, the format of the sinograms conforms to that expected by the STIR library[8].

ROOT [Brun and Rademakers, 1997] is an object-oriented data analysis framework that provides tools for the analysis of experimental data. PeneloPET LIST files can be converted into ROOT format.

2.3.2. PENELOPE

As it was mentioned, PENELOPE is the core of PeneloPET. PENELOPE [Salvat *et al.*, 2006] consists of a package of subroutines, invoked by a main program that controls the evolution of the stories of particle counters and accumulates the magnitudes of interest for each specific application. These subroutines are written in the FORTRAN77 programming language, and are distributed by Nuclear Energy Agency - Organization for Economic Co-operation and Development (NEA-OECD). The authors are Francesc Salvat and Jose M. Fernández-Varea of the Physics Department of the Universidad de Barcelona and Josep Sempau of the Institute of Energy of the Universidad Politécnica de Cataluña.

The simulation of electrons and positrons includes the following types of interactions:

- Hard elastic collision ($\theta > \theta c$).
- Hard inelastic collision ($\theta > \theta c$).
- Hard Bremsstrahlung emission.
- Delta interaction.
- Artificially soft event ($\theta<\theta c$).
- Inner-Shell impact ionization.
- Annihilation (only for positrons).
- Auxiliary interaction (an additional mechanism that may be defined by the user, e.g., to simulate photonuclear interactions).

The simulation of photons includes the following interactions:

- Coherent scattering (Rayleigh).
- Incoherent scattering (Compton).
- Photoelectric absorption.
- Electron-Positron pair production.
- Delta interaction.
- Auxiliary interaction.

For further explanation of the physics included in these interactions the reader is referred to [Sempau *et al.*, 2003b].

Each interaction can lead to secondary particles which can be later tracked and simulated. For example, the positron annihilation leads to γ photons and the photoelectric effect will lead to free

[8] http://stir.sourceforge.net

electrons.

The use of PENELOPE requires preparing a main program which will be responsible for calling PENELOPE subroutines and for storing the information about the trajectories of the particles simulated. The main program should provide PENELOPE with the information about the geometry and materials, and also other parameters such as type of particle, energy, position and direction of movement of the particle to be simulated. Through appropriate use of these tools, the user can create a simulation environment to carry out the desired studies. PENELOPE is of relatively common use in experimental nuclear physics and medical physics [Panettieri *et al.*, 2007].

PENELOPE includes a subroutine for generating sets of random numbers, that is based in an algorithm due to [L'ecuyer, 1988]. This algorithm yields 32-bit real numbers distributed uniformly over an open interval between zero and one. Its period is approximately 10^{18}, which can be considered as infinite for most practical purposes.

2.4. Image reconstruction: FIRST

Small animal PET scanners require high spatial resolution and good sensitivity. To reconstruct high-resolution images in 3D-PET, iterative methods, such as OSEM, are superior to analytical reconstruction algorithms, although their high computational cost is still a serious drawback [Johnson *et al.*, 1997, Herraiz *et al.*, 2006b]. The performance of modern computers could make iterative image reconstruction fast enough and able of dealing with the large number of probability coefficients of the system response matrix, in high-resolution PET scanners, which is a difficult task that prevents the algorithms from reaching peak computing performance. As it was discussed in chapter 1 (section 1.5.3), one of the key advantages of iterative reconstructions is the ability to incorporate accurate models of the PET acquisition process through the use of the system response matrix (SRM). However, SRM for 3D systems are of the order of several billions of elements, which imposes serious demands for statistical iterative methods in terms of the time required to complete the reconstruction procedure and the computer memory needed for the storage of the SRM.

In this section we describe the FIRST algorithm, the 3D-OSEM reconstruction method used in this thesis. Section 2.4.1 presents the main features of the standard FIRST algorithm and section 2.4.2 depicts an adaptation of FIRST algorithm, GFIRST, which uses the computing capabilities of Graphic Processing Units (GPUs).

2.4.1. Main features of the FIRST algorithm

FIRST (Fast Iterative Reconstruction Software for (PET) tomography) is a fully 3D-OSEM non-sinogram-based reconstruction algorithm implemented by our group (GFN, Universidad Complutense Madrid) [Herraiz *et al.*, 2006b], which uses a compressed SRM that contains the resolution recovery properties of EM. This reconstruction method includes the possibility of MAP by means of a generalized one-step late MAP-OSEM algorithm, similar to the one described in Lewitt and Matej [2003] and Kadrmas [2004]:

$$x^{n,s+1}(j) = x^{n,s}(j)\left[\frac{\sum_{i\in SubsetS} A(i,j)\dfrac{y(i)}{\left(R_i^n + S_i\right)}}{\sum_{i\in SubsetS} A(i,j)\left(1+Penalty(j,n)\right)}\right] \qquad \textbf{(33)}$$

where the $x(j)$ is the activity of voxel j (j = 1, maximum voxel number V), $x^{n,s}(j)$ is the expected value of voxel j at iteration n and subiteration s, $A(i, j)$ is the SRM, $y(i)$ is the projection from the object measured at LOR i (experimental data), S_i is the object scatter + random coincidences at LOR i, $Penalty(j,n)$ is the penalty value at voxel j and iteration n, R_i^n is the projection estimated for the image reconstructed at iteration n:

$$R_i^n = \sum_{j=1}^{Voxels} A(i,j)\,x^n(j) \qquad \textbf{(34)}$$

This MAP-OSEM algorithm can be considered as a generalization of the ML–EM. It incorporates a penalty MAP function which can be chosen in different ways [Stayman and Fessler, 2001, Yu and Fessler, 2002, Nuyts and Fessler, 2003], and scatter and random counts estimates, that may require additional modeling of these processes. OSEM reconstruction without MAP regularization is obtained by setting the penalty function to zero.

As it was introduced before, an important problem of iterative methods is the size of the SRM. If the SRM does not fit in RAM, the performance of the reconstruction is affected significantly, due to the large time required to access the hard disk. For example, for the Argus scanner described in section 2.2 [Wang *et al.*, 2006b], for a nominal image resolution of 175 × 175 × 62 voxels (near 1.9 millions of voxels), the number of elements in the SRM (number of LORs × number of voxels) is of the order of 5×10^{13}. Storing all the elements of the SRM would require more than 10 TB. This exceeds the resources of any ordinary workstation, making it necessary to disregard all redundant elements and to perform approximations in order to be able to store the SRM in the limited amount of RAM of ordinary workstations. To achieve this goal, three techniques were used in the FIRST algorithm:

- null or almost-null element removal (matrix sparseness),
- intensive use of system symmetries,
- compression of the resulting SRM employing quasi-symmetries.

Using these techniques, it was possible to reduce the memory needed to store the SRM well below 150 MB, being the reconstructed images indistinguishable from the ones obtained without compression. This fact allows keeping the whole response matrix of the system inside the RAM present in ordinary industry-standard computers, so that the reconstruction algorithm can achieve near peak performance. Besides, the elements of the SRM are stored as cubic spline profiles and matched to voxel size during reconstruction. In this way, the advantages of on-the-fly calculation and of fully stored SRM are combined. The on-the-fly part of the calculation (matching the profile functions to voxel size) of the SRM accounts for 10–30% of the reconstruction time, depending on the number of voxels chosen.

In addition, the FIRST algorithm can include the usage of the message passing interface (MPI) protocol [Gropp *et al.*, 1999] to launch parallel tasks on the available CPUs (or CPU cores) in a cluster of computers.

The flexibility, reduced reconstruction time, accuracy and resolution of the resulting images prove that the methodologies used to implement the FIRST reconstruction can be applied to real studies of high-resolution small animal PET scanners.

2.4.2. GFIRST: GPU-Based Fast Iterative Reconstruction of Fully 3-D PET Sinograms

Graphics Processing Units (GPU) has been proposed for many years as potential accelerators in complex scientific problems [*General-Purpose Computing on Graphics Processing Units repository*] like image reconstruction, with large amount of data and high arithmetic intensity. Indeed, tomographic reconstruction codes are suitable for massive parallelization, as the two main time-consuming parts of the code (forward and backward projection) can be organized as single instruction multiple data (SIMD) tasks and distributed among the available processing units by assigning part of the data to each unit [Jones and Yao, 2004, Hong *et al.*, 2007].

GFIRST is an adaptation of FIRST to use the efficient computing capabilities of GPUs developed by our group [Herraiz *et al.*, 2011]. The main goal was to obtain a significant acceleration of the algorithm without compromising the quality of the reconstructed images, and with speed-ups large enough to compete with the reconstruction times obtained in a cluster of CPUs. The code does not have GPU-specific optimizations, allowing possible future modifications with no significant additional effort. Besides, the GPU code is as similar as possible to the CPU code, what makes it easier to handle and debug. Indeed, approximations in the forward and backward projection kernels were avoided and the same SRM as in the original CPU code was used in order to avoid a loss of accuracy or artifacts in the final images.

At variance with previously proposed reconstruction codes for the GPU [Pratx *et al.*, 2009, Reader *et al.*, 2002] which dealt with list-mode data, GFIRST was designed to work with sinograms [Fahey, 2002]. Although list-mode data, for which all the relevant information from each detected coincidence is stored, might provide optimal images, sinogram data organization also has some interesting features. First, sinograms are commonly used in most of the current commercial scanners [Fahey, 2002], and they are often easily available to the user. Usually, their size is smaller than list-mode files, so they are easier to handle and store. Furthermore, in a sinogram, data are spatially ordered and can thus be accessed in a simple and ordered way. This allows for very fast backward projection implementations. Finally, under certain approximations imposed by the sinogram, the simulated system exhibits many symmetries, thus reducing the size of the SRM.

The code is implemented in CUDA [*NVIDIA CUDA Programming Guide v.2.5.0*], an application programming interface (API), which allows writing programs in C language with extensions to execute part of them (CUDA kernels) on the GPU. Since forward and backward projections take up most of the reconstruction time, only these two steps are implemented as CUDA kernels called from the main reconstruction C code, running in the CPU. Figure 16 shows the data flow between CPU and GPU.

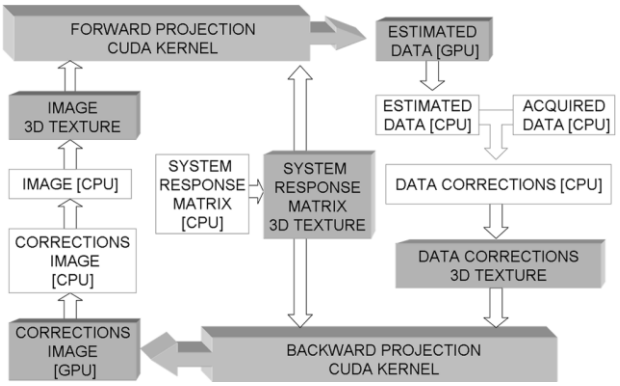

Figure 16. *Flowchart of the implementation of the code in the GPU [Herraiz et al., 2011].*

Due to the large number of threads that can be executed in parallel on GPUs, the usual bottlenecks of these implementations are memory access. GFIRST uses texture memory, a kind of global memory available in the GPU that is allocated and indexed for fast access [Sanders and Kandrot, 2010].

As shown in Figure 16, three 3-D textures are defined in GFIRST: one for the image being reconstructed, another for the SRM, and a third corresponding to the corrections obtained after comparing measured and estimated data. The SRM is uploaded into GPU global memory as a 3-D array and then attached to a 3-D texture at the start of the program.

With GFIRST we achieved a very significant improvement in reconstruction time (with a speed-up factor of up to 72, see Table 8) for the fastest GPU compared to a single core of a high-end CPU. This is remarkable, as FIRST had already been shown to be a highly optimized reconstruction code.

Table 8. *Reconstruction time for one image (one bed, one-frame acquisition, one full iteration) for different architectures [Herraiz et al., 2011].*

Architecture	Time (s)	Speed-up factor
CPU–Intel® Core™ i7 (2.93GHz) (6GB) DDR3 - 800 MHZ RAM	3456	1×
GPU - 8600 GT - 256 MB – 4 SM	509	7×
GPU - 8800 GTS - 640MB – 12 SM	175	20×
GPU - 8800 GT - 512 MB – 14 SM	128	27×
GPU - TESLA C1060 - 4GB – 27 SM	49	72×

For further information about the GFIRST implementation the reader is referred to [Herraiz *et al.*, 2011].

In this thesis (see chapter 5, section 5.2) we use an adaptation of GFIRST, which instead of using the SRM, uses the PSF information with a new regularization method [Vicente *et al.*, 2012b].

2.5. References

Agostinelli, S. 2003. GEANT4 - a simulation toolkit. *Nucl. Inst. Meth. In Phy. Res. A,* 506**,** 250-303.

Baró, J., Sempau, J., Fernández-Varea, J. M. & Salvat, F. 1995. PENELOPE: An algorithm for Monte Carlo simulation of the penetration and energy loss of electrons and positrons in matter. *Nucl. Inst. Meth. In Phy. Res. B,* 100**,** 31-46.

Briesmeister, J. F. 1993. MNCP 4 A, Monte Carlo N-Particle Transport System. Los Alamos, New Mexico: Los Alamos National Laboratory.

Brun, R. & Rademakers, F. 1997. ROOT - An object oriented data analysis framework. *Nucl. Inst. & Meth. in Phys. Res. A,* 389**,** 81-86.

Buvat, I. & Lazaro, D. 2006. Monte Carlo simulations in emission tomography and GATE: An overview. *Nucl. Inst. Meth. In Phy. Res. A,* 569**,** 323-29.

Carrier, C., Martel, C., Schmitt, D. & Lecomte, R. 1988. Design of a high resolution positron emission tomograph using solid state scintillation detectors. *Nuclear Science, IEEE Transactions on,* 35**,** 685-690.

Dahlbom, M., MacDonald, L. R., Eriksson, L., Paulus, M., Andreaco, M., Casey, M. E. & Moyers, C. 1997. Performance of a YSO/LSO phoswich detector for use in a PET/SPECT system. *Nuclear Science, IEEE Transactions on,* 44**,** 1114-1119.

Dahlbom, M., MacDonald, L. R., Schmand, M., Eriksson, L., Andreaco, M. & Williams, C. 1998. A YSO/LSO phoswich array detector for single and coincidence photon imaging. *Nuclear Science, IEEE Transactions on,* 45**,** 1128-1132.

Desco, M. Cursos 97-98, 98-99, 00-01. Asignatura "Bioestadística" (Especialidad de Laboratorio). Escuela Técnico Profesional de la Salud de la Comunidad de Madrid. Hospital General Universitario Gregorio Marañón.

Engels, R., Clemens, U., Kemmerling, G. & Schelten, J. 2003. High spatial resolution scintillation detector based on the H8500 photomultiplier. *In:* Nuclear Science Symposium Conference Record, 2003 IEEE, 19-25 Oct. 2003 2003. 692-695 Vol.1.

España, S., Herraiz, J. L., Vicente, E., Vaquero, J. J., Desco, M. & Udias, J. M. 2009. PeneloPET, a Monte Carlo PET simulation tool based on PENELOPE: features and validation. *Phys Med Biol,* 54**,** 1723-42.

Fahey, F. H. 2002. Data acquisition in PET imaging. *J Nucl Med Technol,* 30**,** 39-49.

General-Purpose Computing on Graphics Processing Units repository [Online]. Available: www.gpgpu.org. [September 2010].

Gropp, W., Lusk, E. & Skjellum, A. 1999. *Using MPI: portable parallel programming with the message-passing interface,* MIT Press.

Harrison, R. L., Vannoy, S. D., Haynor, D. R., Gillispie, S. B., Kaplan, M. S. & Lewellen, T. K. 1993. Preliminary Experience With The Photon History Generator Module Of A Public-domain Simulation System For Emission Tomography. *In:* Nuclear Science Symposium and Medical Imaging Conference, 1993., 1993 IEEE Conference Record., 31 Oct-6 Nov 1993 1993. 1154-1158.

Herraiz, J. L., España, S., Cabido, R., Montemayor, A. S., Desco, M., Vaquero, J. J. & Udias, J. M. 2011. GPU-Based Fast Iterative Reconstruction of Fully 3-D PET Sinograms. *Nuclear Science, IEEE Transactions on,* 58**,** 2257-2263.

Herraiz, J. L., España, S., Vaquero, J. J., Desco, M. & Udias, J. M. 2006b. FIRST: Fast Iterative Reconstruction Software for (PET) tomography. *Phys. Med. Biol.,* 51**,** 4547-4565.

Hong, I. K., Chung, S. T., Kim, H. K., Kim, Y. B., Son, Y. D. & Cho, Z. H. 2007. Ultra Fast Symmetry and SIMD-Based Projection-Backprojection (SSP) Algorithm for 3-D PET Image Reconstruction. *Medical Imaging, IEEE Transactions on,* 26**,** 789-803.

Inadama, N., Murayama, H., Watanabe, M., Omura, T., Yamashita, T., Kawai, H., Umehara, T., Kasahara, T., Orita, N. & Tsuda, T. 2004. Performance of a PET detector with a 256ch flat panel PS-PMT. *Nuclear Science, IEEE Transactions on,* 51**,** 58-62.

Jan, S., Santin, G., Strul, D., Staelens, S., Assié, K., Autret, D. & Avner, S. 2004a. GATE: a simulation toolkit for PET and SPECT. *Phys. Med. Biol.,* 49**,** 4543-4561.

Johnson, C. A., Seidel, J., Carson, R. E., Gandler, W. R., Sofer, A., Green, M. V. & Daube-Witherspoon, M. E. 1997. Evaluation of 3D reconstruction algorithms for a small animal PET camera. *IEEE Trans. Nuc. Sci.,* 44**,** 1303-1308.

Jones, M. D. & Yao, R. 2004. Parallel programming for OSEM reconstruction with MPI, OpenMP, and hybrid MPI-OpenMP. *In:* Nuclear Science Symposium Conference Record, 2004 IEEE, 16-22 Oct. 2004 2004. 3036-3042.

Kadrmas, D. J. 2004. LOR-OSEM: statistical PET reconstruction from raw line-of-response histograms. *Phys. Med. Biol.,* 49**,** 4731-4744.

Kawrakow, I. & Bielajew, A. F. 1998. On the condensed history technique for electron transport. *Nucl. Inst. Meth. In Phy. Res. B,* 142**,** 253-280.

L'Ecuyer, P. 1988. Efficient and portable combined random number generators. *In:* ACM, 1988 New York. ACM, 742-51.

Lage, E., Tapias, G., Villena, J., Desco, M. & Vaquero, J. J. 2010. Data acquisition electronics for gamma ray emission tomography using width-modulated leading-edge discriminators. *Physics in Medicine and Biology,* 55**,** 4291.

Lewitt, R. M. & Matej, S. 2003. Overview of methods for image reconstruction from projections in emission computed tomography. *In:* IEEE NSS-MIC, 2003. 1588-1611.

Majewski, S., Kieper, D., Curran, E., Keppel, C., Kross, B., Palumbo, A., Popov, V., Wisenberger, A. G., Welch, B., Wojcik, R., Williams, M. B., Goode, A. R., More, M. & Zhang, G. 2001. Optimization of dedicated scintimammography procedure using detector prototypes and compressible phantoms. *Nuclear Science, IEEE Transactions on,* 48**,** 822-829.

Melcher, C. L. & Schweitzer, J. S. 1992. Cerium-doped lutetium oxyorthosilicate: a fast, efficient new scintillator. *Nuclear Science, IEEE Transactions on,* 39**,** 502-505.

Miyaoka, R. S., Kohlmyer, S. G., Jinhun, J. & Lewellen, T. K. 2001. Performance characteristics of a second generation micro crystal element (MiCE2) detector. *In:* Nuclear Science Symposium Conference Record, 2001 IEEE, 4-10 Nov. 2001 2001. 1124-1127 vol.2.

Nuyts, J. & Fessler, J. A. 2003. A penalized-likelihood image reconstruction method for emission tomography compared to postsmoothed maximum-likelihood with matched spatial resolution. *IEEE Trans Med Imaging*, 1042-1052.

NVIDIA CUDA Programming Guide v.2.5.0 [Online]. Available: http://developer.nvidia.com/object/gpu_programming_guide.html. [September 2010].

Olcott, P. D., Talcott, J. A., Levin, C. S., Habte, F. & Foudray, A. M. K. 2003. Compact readout electronics for position sensitive photomultiplier tubes. *In:* Nuclear Science Symposium Conference Record, 2003 IEEE, 19-25 Oct. 2003 2003. 1962-1966 Vol.3.

Panettieri, V., Wennberg, B., Gagliardi, G., Duch, M. A., Ginjaume, M. & Lax, I. 2007. SBRT of lung tumours: Monte Carlo simulation with PENELOPE of dose distributions including respiratory motion and comparison with different treatment planning systems. *Phys Med Biol,* 52**,** 4265-81.

Pani, R., Pellegrini, R., Cinti, M. N., Trotta, C., Trotta, G., Garibaldi, F., Scafè, R. & Del Guerra, A. 2003. Flat Panel PMT for photon emission imaging. *Nuclear Instruments and Methods in Physics Research Section A: Accelerators, Spectrometers, Detectors and Associated Equipment,* 505**,** 590-594.

Popov, V., Majewski, S. & Weisenberger, A. G. 2003. Readout electronics for multianode photomultiplier tubes with pad matrix anode layout. *In:* Nuclear Science Symposium Conference Record, 2003 IEEE, 19-25 Oct. 2003 2003. 2156-2159 Vol.3.

Pratx, G., Chinn, G., Olcott, P. D. & Levin, C. S. 2009. Fast, Accurate and Shift-Varying Line Projections for Iterative Reconstruction Using the GPU. *Medical Imaging, IEEE Transactions on,* 28**,** 435-445.

Reader, A. J., Ally, S., Bakatselos, F., Manavaki, R., Walledge, R. J., Jeavons, A. P., Julyan, P. J., Sha, Z., Hastings, D. L. & Zweit, J. 2002. One-pass list-mode EM algorithm for high-resolution 3-D PET image reconstruction into large arrays. *Nuclear Science, IEEE Transactions on,* 49**,** 693-699.

Riboldi, S., Seidel, J., Green, M., Monaldo, J., Kakareka, J. & Pohida, T. 2003. Investigation of signal readout methods for the Hamamatsu R8500 flat panel PSPMT. *In:* Nuclear Science Symposium Conference Record, 2003 IEEE, 19-25 Oct. 2003 2003. 2452-2456 Vol.4.

Salvat, F., Fernández-Varea, J. M. & Sempau, J. 2006. *PENELOPE-2006: A Code System for Monte Carlo Simulation of Electron and Photon Transport,* France, NEA.

Sanders, J. & Kandrot, E. 2010 *CUDA by Example: An Introduction to General-Purpose GPU Programming*, Addison-Wesley.

Seidel, J., Vaquero, J. J. & Green, M. V. 2003. Resolution uniformity and sensitivity of the NIH ATLAS small animal PET scanner: Comparison to simulated LSO scanners without depth-of-interaction capability. *Nuclear Science, IEEE Transactions on,* 50**,** 1347-1350.

Seidel, J., Vaquero, J. J., Siegel, S., Gandler, W. R. & Green, M. V. 1999. Depth identification accuracy of a three layer phoswich PET detector module. *Nuclear Science, IEEE Transactions on,* 46**,** 485-490.

Sempau, J. & Andreo, P. 2006. Configuration of the electron transport algorithm of PENELOPE to simulate ion chambers. *Phys Med Biol,* 51**,** 3533-48.

Sempau, J., Fernández-Varea, J. M., Acosta, E. & Salvat, F. 2003b. Experimental benchmarks of the Monte Carlo code PENELOPE. *Nucl. Inst. Meth. In Phy. Res. B,* 207**,** 107-123.

Siegel, S., Silverman, R. W., Yiping, S. & Cherry, S. R. 1996. Simple charge division readouts for imaging scintillator arrays using a multi-channel PMT. *Nuclear Science, IEEE Transactions on,* 43**,** 1634-1641.

Stayman, W. & Fessler, J. A. 2001. Nonnegative Definite Quadratic Penalty Design for Penalized-Likelihood Reconstruction. *In:* IEEE Nuc. Sci. Symp., 2001.

Thomson, C. J., Moreno-Cantu, J. & Picard, Y. 1992. PETSIM: Monte Carlo simulation of all sensitivity and resolution parameters of cylindrical positron imaging systems. *Phys. Med. Biol.,* 37**,** 731-749.

Vaquero, J. J., Lage, E., Ricon, L., Abella, M., Vicente, E. & Desco, M. 2005a. rPET detectors design and data processing. *In:* Nuclear Science Symposium Conference Record, 2005 IEEE, 23-29 Oct. 2005 2005a. 2885-2889.

Vaquero, J. J., Redondo, S., Lage, E., Abella, M., Sisniega, A., Tapias, G., Montenegro, M. L. S. & Desco, M. 2008. Assessment of a New High-Performance Small-Animal X-Ray Tomograph. *Nuclear Science, IEEE Transactions on,* 55**,** 898-905.

Vaquero, J. J., Seidel, J., Siegel, S., Gandler, W. R. & Green, M. V. 1998. Performance characteristics of a compact position-sensitive LSO detector module. *Medical Imaging, IEEE Transactions on,* 17**,** 967-978.

Vicente, E., Herraiz, J. L., Seidel, J., Green, M. V., Desco, M., Vaquero, J. J. & Udias, J. M. 2012b. Regularization of 3D Iterative Reconstruction for a Limited-Angle PET Tomograph. *In:* Nuclear Science Symposium Conference Record (NSS/MIC), 2012 IEEE (*Accepted*), 2012b.

Vilches, M., García-Pareja, S., Guerrero, R., Anguiano, M. & Lallena, A. M. 2007. Monte Carlo simulation of the electron transport through thin slabs: A comparative study of PENELOPE, GEANT3, GEANT4, EGSnrc and MCNPX. *Nucl. Inst. Meth. In Phy. Res. B,* 254**,** 219-30.

Wang, Y., Seidel, J., Tsui, B. M., Vaquero, J. J. & Pomper, M. G. 2006b. Performance evaluation of the GE healthcare eXplore VISTA dual-ring small-animal PET scanner. *J Nucl Med,* 47**,** 1891-900.

Yu, D. F. & Fessler, J. A. 2002. Edge-preserving tomographic reconstruction with nonlocal regularization image processing. *IEEE Trans Med Imaging,* 21**,** 159-173.

Zaidi, H. & Scheurer, C. 1999. An object-oriented Monte Carlo simulator for 3D cylindrical positron tomographs. *Comput. Methods Programs Biomed.,* 58**,** 133-45.

3. Performance Evaluation of Preclinical PET Scanners

Due to the nature of the underlying physical phenomena, design and engineering of PET systems involve a compromise of sensitivity and spatial resolution specifications which are difficult to optimize simultaneously. For this reason, it can be found in the literature multiple architectures and designs aiming to different performance balance depending on the final application of the system [Weber and Bauer, 2004, Vaquero and Desco, 2005]. In order to compare systems it is necessary to characterize the performance of the scanners in terms of objective parameters.

The evaluation of a PET tomograph consists of quantitative measurements with a standardized methodology, which sets a baseline of system performance under typical imaging conditions. The measurement procedure should be as independent as possible of the PET scanner under test and applicable to a wide range of models and geometries. Standardization facilitates acceptance testing, routine performance monitoring and comparison among systems from different vendors or different designs from a given vendor [Goertzen *et al.*, 2012]. To address this need for a standard set of measurements the NEMA NU 4 standard was published in 2008 [NEMA-NU4, 2008]. Prior to this, there was no agreed upon method to evaluate the performance of preclinical PET systems and as a result manufacturers could not provide specifications for these PET systems in the same way in which specifications for clinical systems could be provided under the NEMA NU 2-1994 [NEMA-NU2, 1994] and NU 2-2001 [NEMA-NU2, 2001] standards. An additional consequence of the previous lack of a NEMA standard for preclinical PET systems is that performance evaluation papers of earlier preclinical PET systems used ad-hoc modifications from the NEMA standard specified for clinical PET systems making it difficult to compare these early systems both to each other and to newer scanners.

The standard protocols to measure performance include two types of tests, some designed to study the intrinsic parameters of the scanner such as spatial resolution or sensitivity, and others aiming to estimate the accuracy of the corrections involved in the reconstruction of images. These tests estimate the following standardized performance parameters:

- Sensitibity
- Spatial resolution
- Energy resolution
- Scatter Fraction
- Noise equivalent count (NEC) rate
- Image quality from a standard phantom

Comparison of scanners based upon standardized procedures, and analysis of the ability of these procedures to measure the performance of the scanner is of paramount importance in PET design research. In this chapter we survey the contributions in this area made by this thesis. In section 3.1 of this chapter we present an application of the standard evaluation protocols to the characterization of the rPET [Vaquero *et al.*, 2005b] and the Argus [Wang *et al.*, 2006b] scanners. Further, section 3.2 shows a study of the evaluation protocol itself, by assessing the accuracy of the NEMA NU 4-2008 procedure to estimate the scatter fraction from ^{18}F acquisitions and also the problems it faces when a radionuclide with a lager positron range as ^{68}Ga is used.

3.1. Characterization of rPET & Argus scanners

As it was mentioned above, in this section we present the performance evaluation of rPET and Argus preclinical PET scanners [Vicente *et al.*, 2006 , Goertzen *et al.*, 2012]. Since part of this work was done prior to the publication of the final version of the NEMA NU 4-2008 standard, some of the tests were performed in slightly different ways for each scanner. This was taken into account during the interpretation of the results of both scanners.

3.1.1. Materials & Methods

3.1.1.1. Sensitivity

The sensitivity of a PET scanner represents its ability of detecting coincident photons emitted from inside the FOV of the scanner. It is mainly determined by two parameters of the scanner: geometry and detection efficiency for 511 keV photons. The scanner geometry defines the fraction of the total solid angle covered. Small-diameter and large axial FOV geometries typically lead to high-sensitivity scanners. Given the geometry, the efficiency of a PET detector depends on the type of detector being used. Usually, high density and atomic number scintillation detectors provide high stopping power for PET imaging with acceptable energy resolution. A high stopping power, which allows for shorter crystals, is also desirable for the reduction of parallax error due to depth of interaction [Bailey, 2005].

Acquisition method

The NU 4-2008 protocol for measuring sensitivity (section 5 of [NEMA-NU4, 2008]) uses a ^{22}Na point source. However, in previous versions of the draft, a line source was proposed and this was the method used for both scanners. Table 9 shows the acquisitions done with each scanner.

Table 9. *Acquisitions employed to measure the sensitivity of rPET and Argus scanners*

	rPET scanner	**Argus scanner**		
Phantom	Line source (capillary) Inner diameter ~ 1.0 mm Length = 7.3 cm	Line source (capillary) Inner diameter ~ 1.0 mm Length = 6 cm		
Isotope	^{18}F	^{18}F		
Activity (μCi)	7	27	25	23
Energy Windows (keV)	100 - 700	100 - 700	250 - 700	400 - 700
Comments	The line source is placed at the center of the FOV aligned along the geometric axis of the scanner.	The line source is wrapped in 10 layers of Al foil and placed at the center of the FOV aligned along the geometric axis of the scanner.		

Data processing and analysis

The absolute central point sensitivity (ACS) was computed from the following expression:

$$ACS\ (\%) = 2 \cdot \frac{C}{\left(\frac{FOV_{axial}}{L}\right) \cdot A \cdot BR} \cdot 100 \qquad \textbf{(35)}$$

where: C: Measured count rate (cps)
L: Capillary length filled with ^{18}F solution
A: Activity of the source (Bq)
BR: Branching ratio of the source (BR(^{18}F) = 0.97)
FOV_{axial}: FOV length in axial direction.

The factor 2 is needed to estimate the ACS from a line source measurement as it is explained in [Cherry *et al.*, 2003]. This assumes simple scanner geometries but it has been tested with simulations that the factor of 2 is accurate enough for both scanners presented here.

3.1.1.2. Spatial resolution

Spatial resolution can be defined as the minimum distance at which two point sources can be acquired and disentangled by the scanner [Bailey, 2005]. Spatial resolution is usually measured from the width of the profile obtained when an object much smaller than the expected resolution of the system is imaged. A common method consists of imaging a point source and measuring the point spread function (PSF). This measurement corresponds to the best resolution of the system under ideal conditions. Usually, the resolution is expressed as the full width at half maximum (FWHM) of the profile. Very often this profile is approximated by a Gaussian function [Bailey, 2005].

There are many factors that influence resolution:

- Non-zero positron range after radionuclide decay.
- Non-collinearity of the annihilation photons due to the residual momentum of the positron.
- Distance between detectors.
- Width of detectors.
- Stopping power of the scintillator.
- Incident angle of the photon at the detector.
- Depth of the interaction of the photon.
- Number of angular samples.
- Reconstruction parameters (matrix size, reconstruction filter, ...).

Usually, the resolution is measured along several directions across the FOV of the PET scanner such as transaxial and axial, as sampling is not necessarily equal in all directions. Generally, ring-PET systems are over-sampled transaxially (in the x-y plane), while axial (z-direction) sampling is just enough to realize the intrinsic resolution of the detectors. Transaxial resolution is often measured for both radial and tangential directions at different distances off the central axis of the scanner, as it changes in ring geometries at different locations in the x-y plane [Bailey, 2005].

Acquisition method

The section 3 of NU 4-2008 protocol [NEMA-NU4, 2008] proposes to use a ^{22}Na point source to measure the spatial resolution. This was the procedure employed in rPET scanner; however, since the Argus spatial resolution was measured before the publication of the final version of this protocol, for this scanner the measurement was performed using a line source. For this reason, axial resolution could not be measured in this case. Table 10 describes the acquisitions performed to measure the spatial resolution with each scanner.

Table 10. *Acquisitions employed to measure the spatial resolution of rPET and Argus scanners*.

	rPET scanner	**Argus scanner**
Phantom	Point source Diameter = 0.3 mm (encapsulated in a 1 cm^3 epoxy box)	Line source (capillary) Inner diameter = 0.35 mm Outer diameter = 1.22 mm Length = 6 cm
Isotope	^{22}Na	^{18}F
Activity (μCi)	~20	~20
Energy Window (keV)	100 - 700	100 – 700
Comments	Acquisitions of 10 minutes were performed with the source placed at the center of the FOV and at different radial positions towards the edge of the FOV (at the central slice).	

Data processing and analysis

Data were reconstructed using FBP and RAM-LAK filter without additional corrections. Activity profiles were drawn in the images in three directions, two in the transverse plane (to obtain radial and tangential resolution) and one in the axial direction (only in rPETsystem). These profiles were fitted to Gaussians and the FWHM was obtained from the Gaussian fits.

3.1.1.3. Energy resolution

Energy resolution indicates the precision of the system in determining the energy deposited by incident photons. It is defined as the width at half maximum or FWHM of the photopeak (E_γ = 511 keV for PET gamma-rays) and is expressed as:

$$FWHM(\%) = \frac{\Delta E}{E_\gamma} \times 100 \quad \textbf{(36)}$$

Energy resolution is usually measured by histograming the energy of the events acquired and plotting the number of events versus its energy. In scintillation detectors energy resolution depends on the light output of the scintillator, as well as its intrinsic energy resolution. This intrinsic energy resolution accounts for non-statistical effects that arise in the gamma detection process. Good energy resolution is necessary for a PET detector in order to achieve good image contrast and to reduce background counts [Levin *et al.*, 2006].

Data processing and analysis

Energy resolution measurements were performed on single crystal spectra as well as on the average spectrum obtained by scaling and aligning the spectra of all crystals of the same detector to a known reference once the energy calibration was performed.

3.1.1.4. Scatter fraction (SF) and Noise equivalent count (NEC)

The scatter fraction (SF) is defined as the ratio between the number of events scattered over all the measured events (scattered or not), provided the rate of random events is vanishingly small [Bailey, 2005, NEMA-NU4, 2008]. Scattered events decrease image contrast in PET by misplacing events, and cause errors in the distribution of reconstructed radioactivity. As discussed in the introduction (section 1.2.3.3), scatter can arise from three major sources: scatter inside the object, scatter at detector elements, and scatter from the gantry and surrounding materials and shiedls. The SF measures the system ability to reject these scattered events which deteriorate image quality.

The SF is a critical component of the noise equivalent count (NEC) rate computation, widely used as a golden measure to optimize acquisition parameters such as timing and energy windows, and for making comparisons among different clinical [NEMA-NU2, 2001] or preclinical [NEMA-NU4, 2008] scanners.

The noise equivalent count (NEC) rate [Strother *et al.*, 1990] represents the effective performance of a counting system, taking into account the random and scattered events, and reflecting dead-time effects of the system. It is related to the time that the system needs to process a photon. After a photon is detected in the crystal, a series of optical and electronic steps take place, each of which requires a finite amount of time. As these combine in series, a slow component in the chain can introduce a significant dead time. NEC curve is a measurement defined by the NEMA standard (section 4 of [NEMA-NU4, 2008]) according to the following expression:

$$NEC = \frac{T^2}{T + S + kR} \qquad \textbf{(37)}$$

where, as we defined in chapter 1 (section 1.2.3.3), *T, S* and *R* are the true, scattered and random count rates respectively and *k* is a factor which depends on the way of estimating random counts, being $k = 1$ when direct subtraction is made, or $k = 2$ when variance reduction techniques are used to estimate the ramdom counts distribution. Some caution is required when comparing NEC results from various systems, namely which value of scatter fraction was used and how it was determined, how the random fraction (*R*) was determined and how random subtraction was applied. However, NEC curves allow count rate comparisons, and therefore are often employed to compare count rate performance among systems [Bailey *et al.*, 1991, Goertzen *et al.*, 2012].

Acquisition method

The method employed in PET for count rate and dead-time determination uses a source of a relatively short-lived tracer in a multi-frame dynamic acquisition protocol. A number of short duration data frames are recorded spanning several half-lives of the source. Often, a cylinder containing a solution of ^{18}F in water is used. From these data, count rates are determined for true, random, and scatter components [Strother *et al.*, 1990, Watson *et al.*, 2004].

In the results we present here, two NEMA phantoms were used to measure the NEC; the mouse and rat sized phantoms (see Appendix A) for the Argus scanner. However, since the transaxial FOV of rPET scanner was not large enough, only the mouse phantom was used. The phantom was placed in the FOV with its long axis parallel to the axis of the scanner and several acquisitions were made.

Data processing and analysis

According to section 4 of [NEMA-NU4, 2008], the analysis to get the SF and the NEC was performed on data arranged in sinograms without any correction. For further information about how the SF is obtained see section 3.2.1.2.

For each acquisition *j*, the system total event rate $R_{TOT,j}$ is computed as the sum of $R_{TOT,i,j}$ over all slices *i*:

$$R_{TOT,j} = \frac{\sum_i C_{TOT,i,j}}{T_{acq,j}} \quad \textbf{(38)}$$

where $T_{acq,j}$ is the acquisition time (notation has been modified to be consistent with the NU 4-2008 standard) .

Similarly, true (R_t), random (R_r) and scatter (R_s) count rates are respectively computed as:

$$R_{t,j} = \frac{\sum_i \left(C_{TOT,i,j} - C_{r+s,i,j}\right)}{T_{acq,j}} \quad \textbf{(39)}$$

$$R_{r,j} = \sum_i \left(R_{TOT,i,j} - \left(\frac{R_{t,i,j}}{1 - SF_i} \right) \right) \quad \textbf{(40)}$$

$$R_{s,j} = \sum_i \left(\frac{SF_i}{1 - SF_i} \right) R_{t,i,j} \quad \textbf{(41)}$$

where SF_i is the Scatter Fraction in the slice *i*.

Finally, the NEC is computed as:

$$R_{NEC,j} = \sum_i \frac{R_{t,i,j}^2}{R_{TOT,i,j}} \quad \textbf{(42)}$$

3.1.1.5. Image Quality

Because of the complex interplay of different aspects of system performance, it is desirable to be able to compare the image quality of different imaging systems for a standardized imaging situation. In order to achieve this aim, a set of measurements are carried out on a given phantom with different regions simulating a whole-body study. Contrast recovery coefficients measured in hot regions are indicative of the resolution and sensitivity of the system. Noise in the uniform region (background) is used to calculate the signal to noise ratio (SNR), while uniformity measurements in this uniform region gives information about accuracy of attenuation and scatter correction, also obtained from contrast measurements in cold regions.

Acquisition method

The image quality measurements were made using the NEMA Image quality phantom (see Appendix A). The total activity inside the phantom was about 200 μCi, distributed between the hot cylinder of the upper part of the phantom (see Figure 17), the uniform region and the five rods placed at the inferior part of the phantom (see Figure 18). The uniform region is connected with the five rods, so the activity concentration in the uniform region and in the five cylinders was the same. Regarding the two cylinders of the upper part of the phantom, one was filled with non-radioactive water (cold cylinder) to simulate attenuation only and the other one was filled with 4 times the activity concentration of the uniform area (hot cylinder).

Static studies of 20 minutes acquisitions were performed with the phantom placed at the center of the FOV aligned along the geometric axis of the scanner.

Data processing and analysis

Values of hot/cold contrasts, image uniformity and recovery coefficients were extracted. We used a different method than the one proposed in the section 6 of NEMA NU4-2008 because the measurements were performed before the publication of the final version of this protocol. This alternate method is described below.

A) Contrast and uniformity measurements

The analysis was performed in the upper part of the phantom image (see Figure 17)

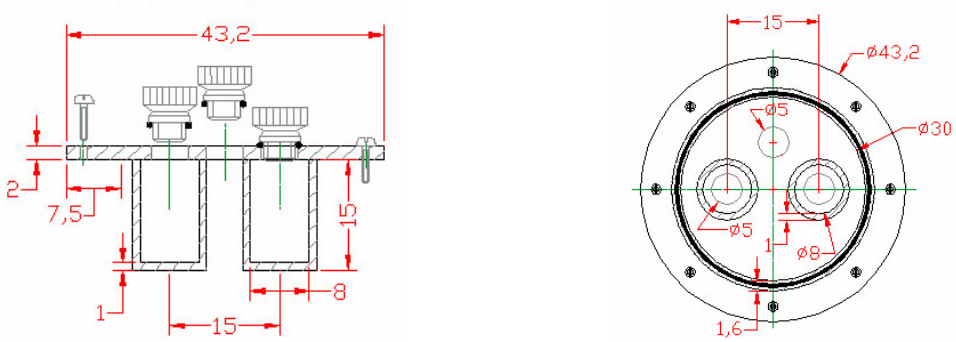

Figure 17. *Coronal and transverse cross sections of upper part of image quality phantom.*

A circular region of interest (ROI) of 8 mm (the diameter of the cylinders) was drawn in the central slice of each cylinder. ROIs of the same size were also drawn on the surrounding uniform activity area. The same procedure was made on two more slices at ± 4 mm. The average of counts in each region was used to determine the value of the contrast Q and the standard deviation to measure uniformity in the uniform region:

$$Q_H(\%) = \frac{C_H / C_B - 1}{A_H / A_B - 1} * 100 \qquad \textbf{(43)}$$

where: Q_H: hot cylinder contrast,
C_H: average of counts in hot cylinder ROIs,
C_B: average of counts in background ROIs,
A_H: activity concentration in hot cylinder,

A_B: activity concentration in the background area.

$$Q_C(\%) = \left(1 - \frac{C_C}{C_B}\right) * 100 \quad \textbf{(44)}$$

where: Q_C: cold cylinder contrast,
C_C: average of counts in cold cylinder ROIs,
C_B: average of counts in background ROIs.

$$N(\%) = \frac{SD}{C_B} * 100 \quad \textbf{(45)}$$

where: *N:* Uniformity (percent background variability)
SD: standard deviation of the background ROI counts calculated as:

$$SD = \sqrt{\sum_{j=1}^{K} \left(C_{B,j} - C_B\right)^2 \Big/ (K-1)} \quad \textbf{(46)}$$

where K is the number of background ROIs (6 in our case).

B) Recovery Coefficients (RC)

The recovery coefficients (RC) measure the variability of the activity concentration seen in the image as a function of the volume (partial volume effect). The analysis was performed in the image corresponding to the lower part of phantom (see Figure 18)

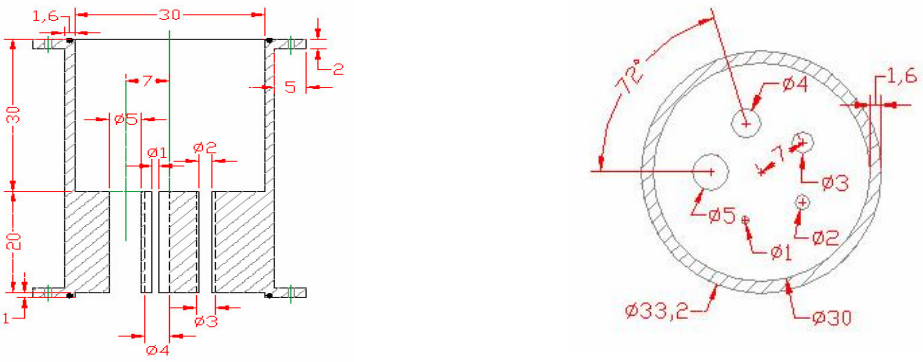

Figure 18. *Coronal and transverse cross sections of lower part of image quality phantom.*

ROIs with same diameter than the cylinders were drawn on each one of them (2, 3, 4 and 5 mm respectively) in their central slice. The ROI on the cylinder of 1 mm was not drawn because it was not well solved for the rPET scanner. The same procedure was made on two more slices (at ± 4 mm). The average of counts was calculated in each ROI to study the activity concentration variability in function of the volume. Background activity concentration was measured on the intermediate region of the phantom drawing circular ROIs of 20 mm diameter in several slices and the average was calculated. Recovery coefficients were calculated using the expression [Kisung *et al.*, 2004]:

$$RC_i = \frac{C_i}{C_B} \quad \textbf{(47)}$$

where: C_i: counts concentration in the cylinder with diameter i (with i = 2, 3, 4 y 5)
C_B: background concentration.

C) Recovery Coefficients (NEMA NU4-2008)

We should be aware of the fact that different methods to estimate performance parameters or scanner specifications can lead to very different results. To show a typical example of this, we computed, for the Argus scanner, the values of RC both with the method described in the previous subsection and using the NU4-2008 methodology. In the NU4-2008 protocol, cylindrical volumes of interest (VOIs) are drawn over the 5 rods with a diameter twice the diameter of the rod. The maximum values in each plane of the VOIs are measured and the ratios of these values with respect to the average activity concentration in the uniform region (22.5 mm diameter ROI) are calculated.

3.1.2. Results

3.1.2.1. Sensitivity

The computed absolute central point sensitivity (ACS) is reported in Table 11 for both scanners along with the sensitivity for other commercial scanners. The uncertainties in the ACS values were computed from the uncertainties of the measurements, namely [see eq. (35)] the measured count rate (±5%), the capillary length and FOV length in axial direction (±0.05 cm each one) and the activity of the source (±5%).

As expected, the sensitivity for rPET is lower than the Argus one. However, 2.2% is a reasonable value for a partial-ring system and improves the sensitivity of other systems based on rotating planar detectors as, for example, YAP-(S)PET (see Table 11). On the other hand, the Argus system has a very competitive ACS value showing similar or improved sensitivity compared to other full-ring scanners, some of them with greater axial FOV. Some examples are shown in Table 11.

Table 11. *Absolute central point sensitivity (ACS) results for rPET and Argus systems and comparison with other small animal PET scanners.*

System	Reference	Energy Window (keV)	ACS (%)
rPET	[Vicente *et al.*, 2006]	100-700	2.2 ± 0.3
Argus	[Goertzen *et al.*, 2012]	100-700	6.8 ± 0.8
		250-700	4.3 ± 0.5
		400-700	2.3 ± 0.3
YAP-(S)PET	[Del Guerra *et al.*, 2006]	50-850	1.87
microPET P4	[Tai *et al.*, 2001]	250-750	2.3
microPET R4	[Knoess *et al.*, 2003]	250-750	4.4
Mosaic HP	[Surti *et al.*, 2005]	250-665	3.6

3.1.2.2. Spatial resolution

Figure 19 and Table 12 show the spatial resolution (FWHM) in the three directions (two for Argus, as commented in section 3.1.1.2) measured at several radial positions. The values at 25 mm off-center are only reported for Argus scanner since rPET has a smaller transaxial FOV. The uncertainties in the resolution measurements reported in Table 12 were estimated from several measurements in each position. We can see that all the FWHM values are better than 2.3 mm in all

directions for both scanners. This means a good resolution for preclinical scanners.

In the rPET scanner the best resolution is achieved along the radial direction, with values between 1.5 and 1.8 mm, because the planar detectors and parallel-beam geometry degrade the resolution more slowly with increasing radial position than in full-ring scanners (with parallax error), where the depth of interaction (DOI) progressively degrades radial spatial resolution.

In the Argus system, on the other hand, the best resolution is achieved along the tangential direction with values below 1.7 mm, even at the edge of the transaxial FOV. The radial resolution is a little worse but is degraded more slowly than in other full-ring scanners due to the DOI compensation capability of the phoswich detector modules (see Table 12).

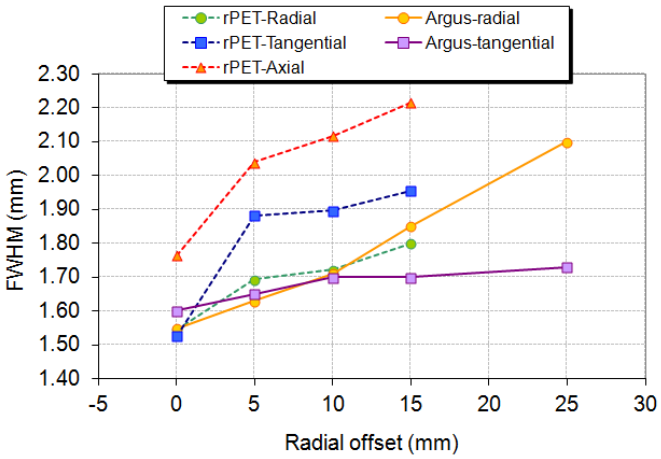

Figure 19. *Spatial resolution for rPET and Argus systems.*

Table 12. *Spatial resolution for rPET and Argus systems at different radial offsets.*

System	Reference	FWHM (mm)	Radial offset (mm)				
			0	5	10	15	25
rPET (SSRB+2DFBP)	[Vicente *et al.*, 2006]	Radial	1.5 ± 0.1	1.7 ± 0.1	1.7 ± 0.1	1.8 ± 0.1	--
		Tangencial	1.5 ± 0.1	1.9 ± 0.1	1.9 ± 0.1	2.0 ± 0.3	--
		Axial	1.8 ± 0.3	2.0 ± 0.3	2.1 ± 0.3	2.2 ± 0.3	--
Argus (FORE+2DFBP)	[Goertzen *et al.*, 2012]	Radial	1.5 ± 0.1	1.6 ± 0.1	1.7 ± 0.1	1.9 ± 0.1	2.1± 0.2
		Tangencial	1.6 ± 0.1	1.7 ± 0.1	1.7 ± 0.1	1.7 ± 0.1	1.7± 0.2
Inveon (FORE+2DFBP)	[Bao *et al.*, 2009a]	Radial	1.5	1.6	1.8	2.0	2.5
Mosaic HP (3D-FRP)	[Surti *et al.*, 2005]	Radial	2.3	2.3	2.5	2.4	2.6
microPET P4 (FORE+2DFBP)	[Tai *et al.*, 2001]	Radial	1.8	2.3	2.4	2.4	2.6
microPET R4 (FORE+2DFBP)	[Knoess *et al.*, 2003]	Radial	1.7	2.1	2.3	2.9	3.3

3.1.2.3. Energy resolution

Average energy resolution across the tube surface in rPET system, once excluded outlier crystals at the edges, was 16.5 % with a standard deviation of 2%. The worst crystal energy resolution in this detector was 23.4 %, while the best one was 12.7 %. Figure 20 shows on the left, the energy spectrum for one of the central crystals for which the energy resolution is 13.5 %, and on the right the averaged

spectrum for the whole tube after all the photopeaks were scaled and aligned; the energy resolution measured on this averaged spectrum is 19.6%.

We did not measure the energy resolution in the Argus scanner, however to compare with rPET results we quote here the performance evaluation of Wang *et al.* [2006b]. Argus energy resolution averaged over all crystals in the LYSO layer was 26%, and in the GSO layer it was 33% (29.6% average system energy resolution). Many factors can explain these differences in energy resolution such as differences between PMT designs, packing fraction and quantum efficiency of the crystals. Besides, visible photons generated at the LYSO layer in Argus scanner have to cross the GSO layer prior to reach the photomultiplier and they can therefore be attenuated during their path. This attenuation process contributes to decrease the number of photoelectrons generated in the photocathode, decreasing the energy resolution.

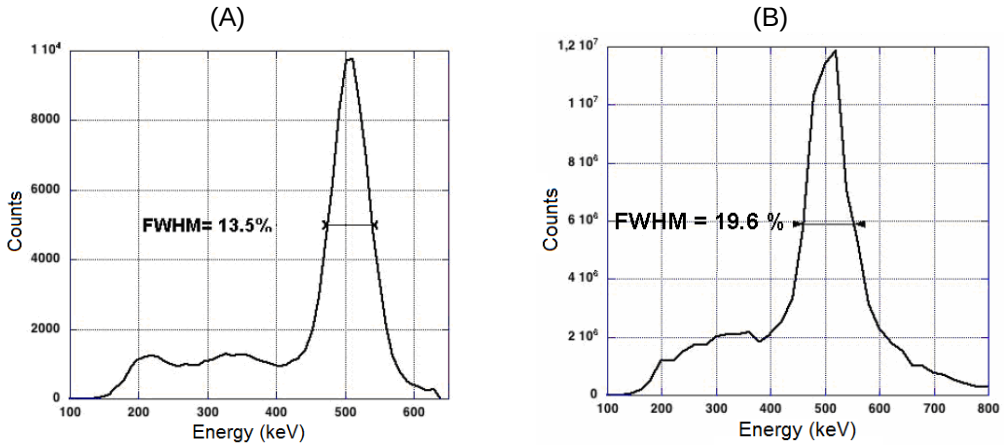

Figure 20. (A)*: energy spectrum for one of the central crystals in rPET.* ***(B)****: averaged energy spectrum for the block detector in rPET, after all the individual crystals were scaled and aligned to a common reference channel.*

3.1.2.4. Scatter fraction (SF) and Noise equivalent count (NEC)

Table 13 summarizes the results of the count rate test for the mouse and rat sized phantoms. For rPET scanner the NEC curve was only measured in the 100-700 keV energy window. For each system and phantom tested we report $R_{NEC,peak}$, the peak NEC value, A_{peak}, the activity at which $R_{NEC,peak}$ occurs, and SF, the scatter fraction. In addition, as it was done in [Goertzen *et al.*, 2012], we report the value of R_{NEC} at 3.7 MBq for the mouse phantom and 10 MBq for the rat phantom. These activity levels correspond to typical values encountered in routine imaging of mice and rats.

As expected, the peak NEC values are higher for the Argus scanner in all the energy windows, even for the 400-700 keV, whose ACS is similar to the rPET one in the 100-700 keV window, as shown in section 3.1.2.1. Differences between these two latter curves are mainly due to coincidence time window, dead-time and integration time differences between both scanners and because the line source is placed in the mouse sized phantom 1 cm-off-center, where the sensitivity is slightly lower in rPET (100-700 keV) than in Argus (400-700 keV).

However, the SF value (mouse sized phantom) for rPET (100-700 keV) is smaller than for Argus for the same energy window and equal to the Argus value in the 250-700 keV energy window. This is most likely due to the fact that rPET is a partial ring system so that there is significantly less scatter from the materials of the gantry. This is consistent with the work of Yang and Cherry [2006], who showed that for mouse sized phantoms imaged in the microPET II system, the dominant source of scattered events was scatter on the gantry. Another example of this fact can be found in the next

section (see Table 17 in section 3.2.2.2) where the importance of the contribution to the total SF due to shiedls is shown using simulations of the mouse sized phantom in the Argus system.

Table 13. *Summary of count rate tests results for the mouse and rat phantoms.*

System	Energy Window (keV)	Mouse Phantom $R_{NEC,peak}$ (kcps)	Mouse Phantom A_{peak} (MBq)	Mouse Phantom R_{NEC} @ 3.7 MBq (kcps)	Mouse Phantom SF (%)	Rat Phantom $R_{NEC,peak}$ (kcps)	Rat Phantom A_{peak} (MBq)	Rat Phantom R_{NEC} @ 10 MBq (kcps)	Rat Phantom SF (%)
rPET	100-700	70	25	<20	21	--	--	--	--
Argus	100-700	126	33	32	28	38	32	24	48
	250-700	117	35	26	21	40	34	23	34
	400-700	86	46	18	9	33	37	19	17

Figure 21 shows the NEC curves for the systems for the mouse (left) and rat (right) phantoms respectively. The general shape of the curves is similar for both systems, exhibiting a near-linear range of the NEC vs. activity below the peak NEC value. This region covers at least up to an activity of 20 MBq for both systems, which is sufficient for routine rodent imaging studies.

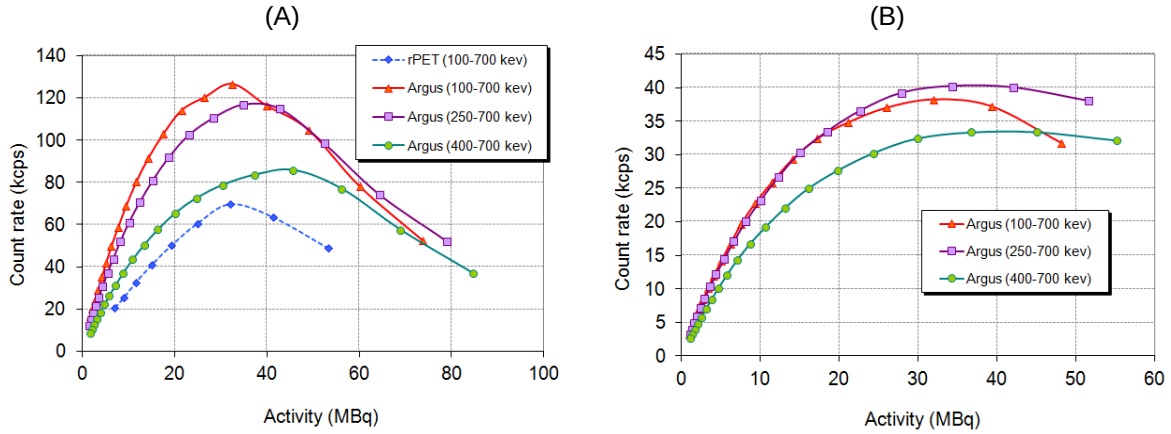

Figure 21. *Plot of the NEC vs. activity in different energy windows.* ***(A)****: Mouse sized phantom.* ***(B)****: Rat sized phantom (only for Argus scanner).*

It is worth commented on the very similar NEC curves in 100-700 and 250-700 keV energy windows for the rat sized phantom of the Argus system (Figure 21B). Many scanners show higher NEC values for the wider energy windows, usually due to the higher sensitivity. But one must be aware that NEC is the result of cancellation of several effects and it is not obvious at first sight what the behavior one should expect is. In order to study in more detail these curves, we plot in Figure 22 the count rates for both energy windows (prompts (triangled symbols), scatter+randoms (squared symbols) and true (circled symbols) rates). We can see that, as expected because of the higher sensitivity, all the count rates are higher in 100-700 keV. Scatter+randoms rate is much higher because the scatter detected is higher in the wider energy window. The true rate is only slightly greater in the 100-700 keV window. It is straight forward to see that, if there are more scatter (and maybe randoms) and true events, the prompts rate will be higher. Thus, we can state that the scanner is working correctly, but the relationship $(True)^2/Total$ happens to be almost the same for both energy windows for this scanner and this phantom.

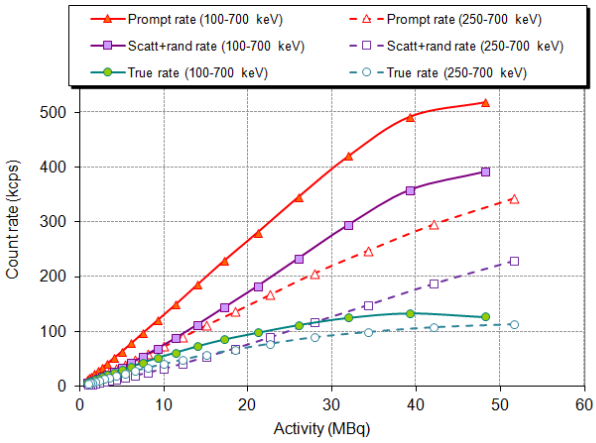

Figure 22. *Comparison of the count rates in 100-700 and 250-700 keV energy windows for the Argus scanner (rat sized phantom).*

3.1.2.5. Image Quality

It is important to remark in this section that the results of image quality tests depend on the reconstruction algorithm and the corrections applied to the data. The variability observed in the results from each system shows that caution must be used when comparing results of image quality phantom across systems. Table 14 describes the main features of the different reconstruction methods employed in this section for each system.

Table 14. *Main features of the reconstruction methods employed in each system.*

System	Reconstruction method	Description	Image resolution
rPET	SSRB + 2D-FBP	Axial difference (SSRB): 10 Filter: Butterworth { order: 12, cut-off: 0.35} Applied corrections: {dead-time, decay}	55×55×55 bins (0.81×0.81×0.81 mm^3)
	3D-FBP	Axial difference: 14 Filter: RAM-LAK Applied corrections: {dead-time, decay}	55×55×55 bins (0.81×0.81×0.81 mm^3)
	3D-OSEM	Iterations: 1 Subsets: 75 Applied corrections: {dead-time, decay}	99×99×55 bins (0.45×0.45×0.81 mm^3)
Argus	FORE + 2D-FBP	FORE: {span: 3, max. difference: 13} Filter: Hanning { alpha: 1.00, cut-off: 1.00} Applied corrections: {dead-time, decay}	175×175×61 bins (0.3875×0.3875×0.7750 mm^3)
	FORE + 2D-OSEM	FORE: {span: 3, max. difference: 13 } Filter: none Iterations: 2 Subsets: 32 subsets Applied corrections: {dead-time, decay}	175×175×61 bins (0.3875×0.3875×0.7750 mm^3)
	FORE + 2D-OSEM-SC (2D-OSEM with scatter correction)	FORE: {span: 3, max. difference: 13 } Filter: none Iterations: 2 Subsets: 32 subsets Applied corrections: {dead-time, decay, scatter } Method of scatter correction: linear background subtraction	175×175×61 bins (0.3875×0.3875×0.7750 mm^3)
	3D-OSEM	Iterations: 1 Subsets: 50 Filter: Gaussian (sigma: 0.58 mm [1.5 pix]) Applied corrections: {dead-time, decay, attenuation}	175×175×61 bins (0.3875×0.3875×0.7750 mm^3)

A) Contrast and uniformity measurements

Table 15 reports the values of the hot contrast measured in the hot rod (Q_H), the cold contrast measured in the cold cylinder (Q_C) and the uniformity (N) for both scanners and different reconstruction methods (see Table 14) . These results indicate that in principle cold lesions can be detected more easily than hot ones for both scanners, but this depends on the size of the lesion. Indeed, small hot lesions generally have better detectability than cold ones [Cherry *et al.*, 2003].

Table 15. *Contrast for the hot (Q_H) and cold (Q_C) cylinders and background variability (N).*

System	Energy Window (keV)	Reconstruction method	Q_H (%)	Q_C (%)	N (%)
rPET	100-700	SSRB + 2D-FBP	57	73	7
		3D-FBP	58	77	5
		3D-OSEM	65	81	8
Argus	100-700	FORE + 2D-FBP	62	79	3
		FORE + 2D-OSEM	64	79	3
		FORE + 2D-OSEM-SC	66	81	4
	250-700	FORE + 2D-FBP	66	85	6
		FORE + 2D-OSEM	67	84	7
		FORE + 2D-OSEM-SC	68	85	6
	400-700	FORE + 2D-FBP	67	88	1
		FORE + 2D-OSEM	69	86	2
		FORE + 2D-OSEM-SC	69	86	2

Even though there is a strong dependence on the reconstruction method, as already mentioned, we see that contrast and uniformity are slightly better for the Argus scanner.

B) Recovery Coefficients (RC)

Figure 23 plots the recovery coefficients obtained from different reconstruction methods for each scanner. Again we can see a strong dependence on the reconstruction method used. However, as the recovery coefficients are a measurement of the partial volume effect and this effect is tightly related with the spatial resolution, there is no wonder that RCs are higher for the Argus system.

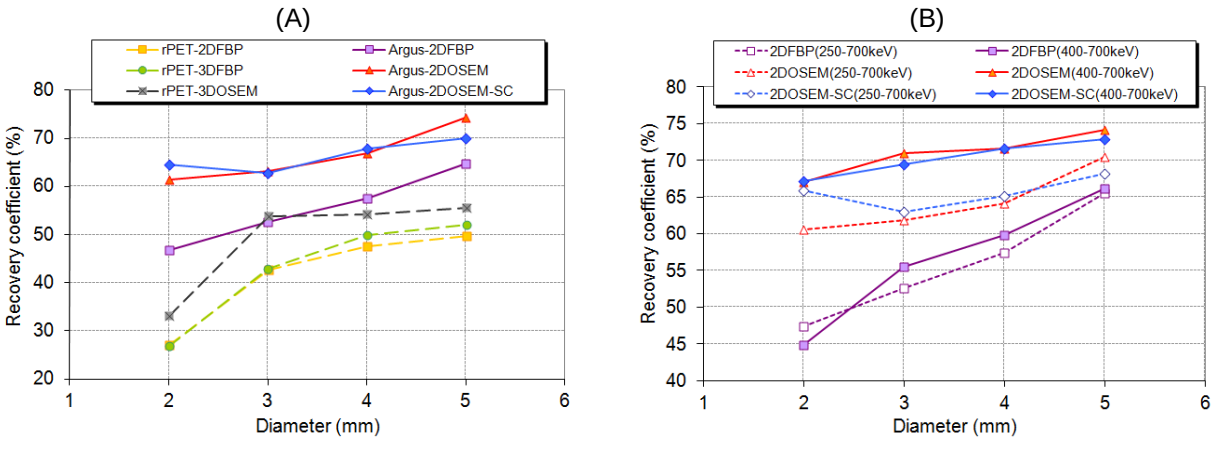

Figure 23. *Recovery coefficients as a function of the rod diameter.* ***(A)****: Comparison between rPET and Argus*

systems in the 100-700 keV energy window. ***(B)****: RCs for two more energy windows for the Argus system.*

C) Recovery Coefficients (NEMA NU4-2008)

Figure 24 shows the recovery coefficients computed using the NEMA N4-2008 (section 6 of [NEMA-NU4, 2008]) for the Argus in the 250-700 keV energy window. This is an illustration of the variation of the results depending on the protocol employed to estimate RCs. As we can see in the figure, values are significantly higher with this latter protocol for all the reconstruction methods. This is due to the fact that the recovery coefficient value in NEMA N4-2008 protocol is based on a single pixel measurement taken from the average image created by summing the slices in a 10 mm axial region. In our view this is not a robust method to measure partial volume effects and has a very high uncertainty. Besides, recovery coefficients greater than 1 can be measured with iterative reconstruction methods for larger rod sizes due to a combination of two factors: Gibb's artifacts (higher peaks at the edges of the hot rod) in the image and statistical fluctuations due to the fact that the recovery coefficient in this procedure is based on a single pixel measurement. In the example plotted in Figure 24, the use of a moderate Gaussian filter was necessary in the 3D-OSEM reconstruction to help to yield more realistic values for the RCs.

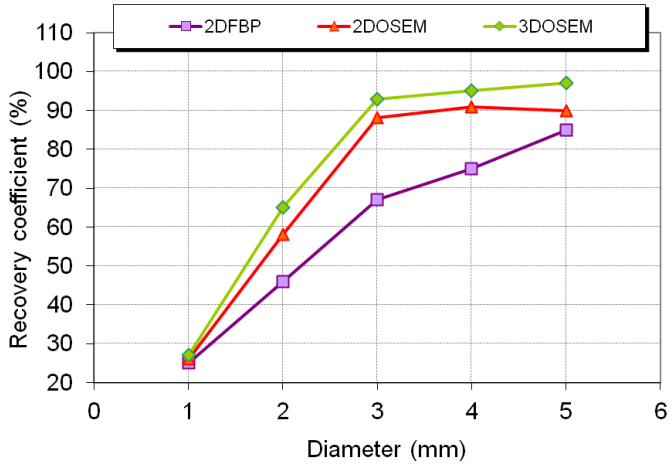

Figure 24. *Recovery coefficients as a function of rod diameter for the Argus scanner using the NU4-2008 method (250-700 keV).*

3.1.3. Conclusions

We have evaluated the performance of two scanners with very different geometries and features: rPET, a partial ring system based on four rotating planar detectors and parallel-beam geometry and Argus, a more standard system consisting in two full-rings of smaller detector modules. The work has been performed following, as far as possible, a standard methodology in order to compare the systems in the same conditions. A critical sight on the methodologies employed to measure standard performance parameters has been also taken. However, this is a very difficult task because the tests sometimes do not show the suitability of the PET system for the specific imaging and one must also consider the cost of the scanner. Knowing these limitations, the results of the presented characterization show that both scanners have very competitive features improving in some parameters the performance of other commercial systems.

3.2. Scatter Fraction estimation using ^{18}F and ^{68}Ga sources

As it was mentioned in section 3.1.1.4, the scatter fraction (SF) in PET data represents the fraction of coincidence events in which at least one of the two emitted photons have been scattered before being detected. Scattered events decrease image contrast in PET by misplacing events during reconstruction, and cause errors in the reconstructed radioactivity concentration. Scatter can arise from three major sources: scatter inside the object, detector backscatter, and scatter from the gantry and surrounding environment. A good understanding of the contributions from the three sources is essential to accurately correct for scatter in PET imaging.

In this section we present an evaluation of the procedure proposed by NEMA (section 4 of [NEMA-NU4, 2008]) to estimate SF with ^{18}F. Further, we study the case of employing ^{68}Ga for this estimation. The main advantage of ^{68}Ga over ^{18}F is that it can be obtained on-site, since it is extracted from a gallium-68 generator, and a cyclotron is not necessary and it is becoming increasingly employed. However ^{68}Ga is a radionuclide with lager positron range and this fact may have an impact in the determination of scatter fraction and other performance parameters. We will try to see whether using the same protocols as with ^{18}F, the values obtained can be compared to the ones determined from ^{18}F acquisitions [Vicente *et al.*, 2010a].

For this study, experimental data acquired with the Argus small-animal PET scanner ([Wang *et al.*, 2006b], section 2.2) as well as peneloPET simulations ([España *et al.*, 2009], section 2.3) are used.

3.2.1. Materials & Methods

3.2.1.1. Real and simulated data

In order to estimate SF with the protocol proposed by NEMA (section 4 of [NEMA-NU4, 2008]), real data acquired with the Argus small-animal PET scanner (see section 2.2) as well as simulations of the same scanner using peneloPET (see section 2.3), were used. The results were obtained using the mouse sized phantom (see Appendix A) and a wide energy window (100-700 keV). The activity in the line source inserted in the phantom was low to ensure that the number of random counts was negligible (less than 1% of true rates). Simulated data were obtained with and without scanner shielding and animal bed materials.

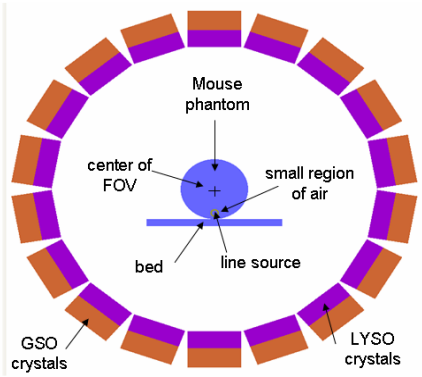

Figure 25. *Diagram of Argus PET/CT and phantom.*

An accurate simulation of the positron range, taking into account the small region of air between the line source tube and the polyethylene phantom, was necessary to reproduce the width of the line source profiles measured for both radionuclides, especially in the case of the ^{68}Ga.

3.2.1.2. SF estimation (NEMA NU4-2008)

According to NEMA (section 4 of [NEMA-NU4, 2008]), data was sorted into sinograms using single slice rebinning (SSRB) with 175 radial bins, 128 angular bins and 61 slices. Background from intrinsic radioactivity of lutetium was subtracted from experimental data while simulations did not include crystal intrinsic radioactivity.

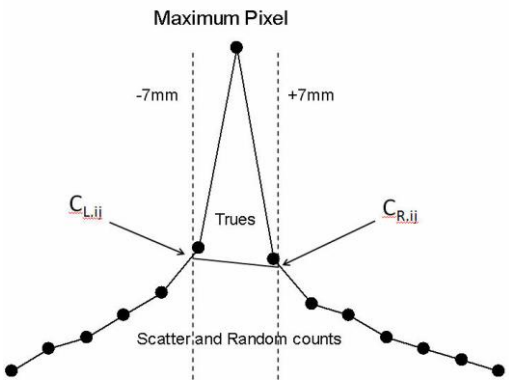

Figure 26. *Boundaries for integration of background counts inside and outside the 14 mm strip, as recommended in NEMA.*

After sinogram alignment, a sum projection was performed such that a pixel in the sum projection represents the sum of the pixels in each angular projection having the same radial offset. The resulting profiles had 175 bins with 0.3885 mm/bin. According to NEMA a 14 mm wide strip at the center of the sinogram was drawn to separate scatter from true coincidences (see Figure 26).

Using the same notation than in the previous section (see 3.1.1.4), the total scatter fraction of the acquisition is defined as:

$$SF = \frac{\sum_{i}\sum_{j'} C_{r+s,i,j'}}{\sum_{i}\sum_{j'} C_{TOT,i,j'}} \quad \textbf{(48)}$$

3.2.1.3. Suggestion to improve the NEMA protocol

Due to the way that the SF is computed in the NEMA procedure, isotopes with large positron ranges may lead to spurious estimations of the scattered counts because present widen activity profiles in the sinograms. In order to make the NEMA protocol isotope range-independent, in this work we propose the deconvolution of these profiles to remove the effect of positron range.

In the results presented here, the deconvolution was performed in the sinogram profiles using what some authors call '$aPSF_{sin}$' [Blanco, 2006, Cal-Gonzalez *et al.*, 2010], which is the projection of the positron range 3D distribution (3D aPSF) onto one direction (see Figure 27) and its distribution contributes directly to the sinogram. We used a very simple EM-ML (in one dimension) to apply the deconvolution to the sinogram profiles, where the known data is the 1D-sinogram-profile and the solution is the deconvoluted profile. The convolution was performed both in the forward- and backward-projection using the $aPSF_{sin}$ obtained from simulations for each isotope.

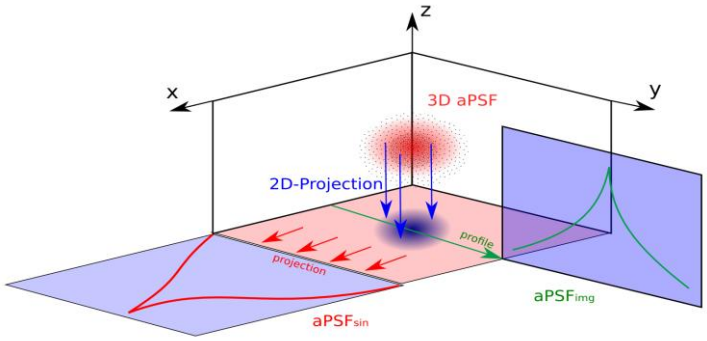

Figure 27. *Schematic procedure to obtain $aPSF_{sin}$ and $aPSF_{img}$ from the original 3D aPSF [Cal-Gonzalez* et al.*, 2010].*

3.2.2. Results

3.2.2.1. Experimental results

In Figure 28, ^{18}F and ^{68}Ga sinogram profiles for low activity concentrations are compared for experimental acquisitions. It can be observed a wider line source profile for ^{68}Ga due to the positron range effect.

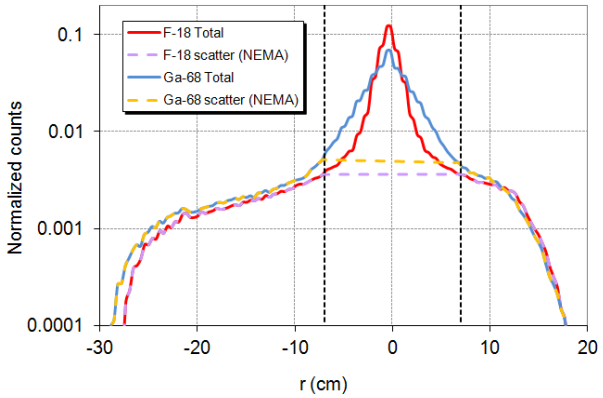

Figure 28. *^{18}F and ^{68}Ga radial profiles for experimental acquisitions in the ARGUS system. Y-axis is in logarithmic scale. Profiles are normalized dividing by the total counts of the profile*

Profiles were normalized dividing by the total counts of the profile. The two vertical lines show the edges of the 14 mm wide strip which was used to estimate, using the NEMA NU4-2008 protocol, the scatter coincidences distribution or 'scatter (NEMA)' as we call it in this work. This 'scatter (NEMA)' is shown in the plot using dashed lines, and reported in Table 16 for both isotopes. We can see that the SF value obtained using ^{68}Ga is higher than using ^{18}F. However, the SF is the same for both isotopes, as we can see from the results of the simulations (Table 17, third column), where the scatter fraction is computed from the actual scatter counts, known in a simulation, instead from estimations as in the real case. The increased width of the ^{68}Ga profile due to positron range leads to a spurious estimation of the fraction of scattered counts because contributions coming from the tail of the profile of true counts contaminate the 'scatter region' defined by NEMA.

Table 16. *Scatter Fraction values for real data using NEMA NU4-2008 protocol*

Isotope	SF (%) (NEMA)
^{18}F	28
^{68}Ga	35

3.2.2.2. Analysis using simulations

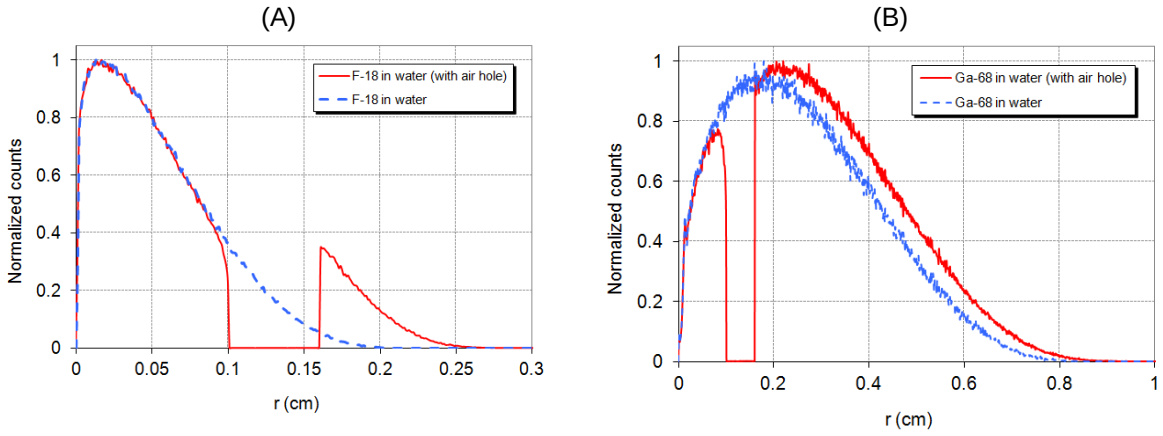

Figure 29. *Radial profiles of positron annihilation events in water and in water plus the observed air gap.* ***(A)****:* ^{18}*F isotope.* ***(B)****:* ^{68}*Ga isotope.*

Figure 29 shows the radial profiles of positron range in water and in water plus the observed air gap in the experimental setup in between the capillary tube and the phantom. These profiles were used in the simulations.

Figure 30 and Figure 31 show a comparison between real and simulated data (with and without scanner shields and two different positron range profiles (Figure 29)) for ^{18}F (Figure 30) and ^{68}Ga (Figure 31) respectively. For each plot, it is shown, besides the sinogram profiles of the total number of coincidences (red and blue solid lines for real and experimental data respectively), the scatter estimation using the NEMA method (scatter (NEMA), purple and orange dashed lines for real and experimental data respectively), and the scatter estimated from the simulation (scatter (in sim.), green dashed line).

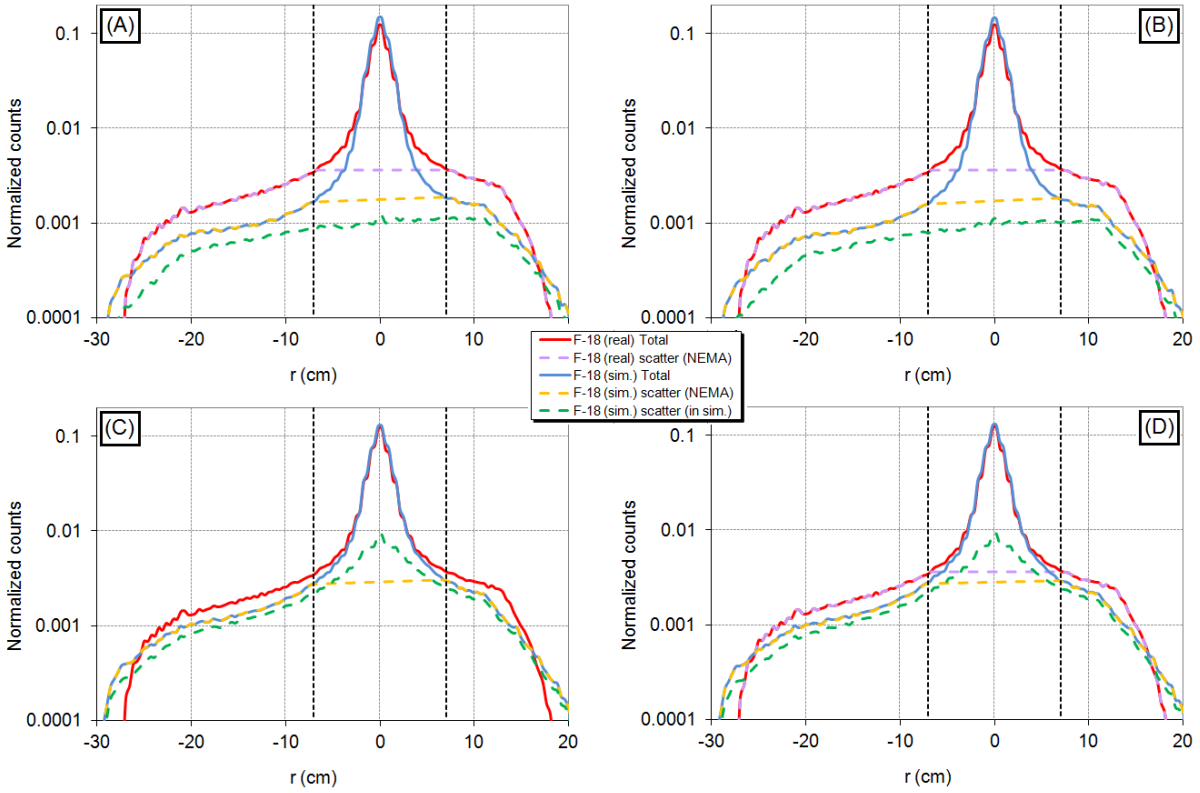

Figure 30. *^{18}F radial profiles for real acquisitions compared to different simulations:* ***(A)****: Scanner without shields. Positron range in water.* ***(B)****: Scanner without shields. Positron range in water plus a thin air layer.* ***(C)****: Scanner with shields. Positron range in water.* ***(D)****: Scanner with shields. Positron range in water plus a thin air layer.*

Differences between simulations (with shields and realistic positron range) and real data are probably due to additional shields not considered in the simulation. We did not find these differences in the rPET scanner as it is shown in [España *et al.*, 2009]. Despite these differences, simulated data reveal interesting results:

- Simulated sinogram profiles in left plots (A and C) were performed using simulations of positron range in water. On the other side, right plots (B and D) were performed using a more realistic simulation of the positron range which took into account the air gap in between the capillary tube and the phantom (water plus a thin air layer). No significant differences are observed in ^{18}F profiles (Figure 30), however, the ^{68}Ga profile using 'water plus a thin air layer positron range simulation' resembles more closely the experimental profile (Figure 31D).

- Taking into account the contribution from the shields, plots in the upper side (A and B) were simulated without shields, while in the bottom plots (C and D) an approximation of the gantry and the environment surrounding the scanner (what we call 'shields') were introduced in the simulation. Flat scatter profiles are the result of having no shield as we can see in the green dashed line profiles in both Figure 30 and Figure 31, A and B. Nevertheless, peaked profiles are obtained for both isotopes when shields are a simulated. This peak (close to the line source location) is due to low angle scatter at the shields.

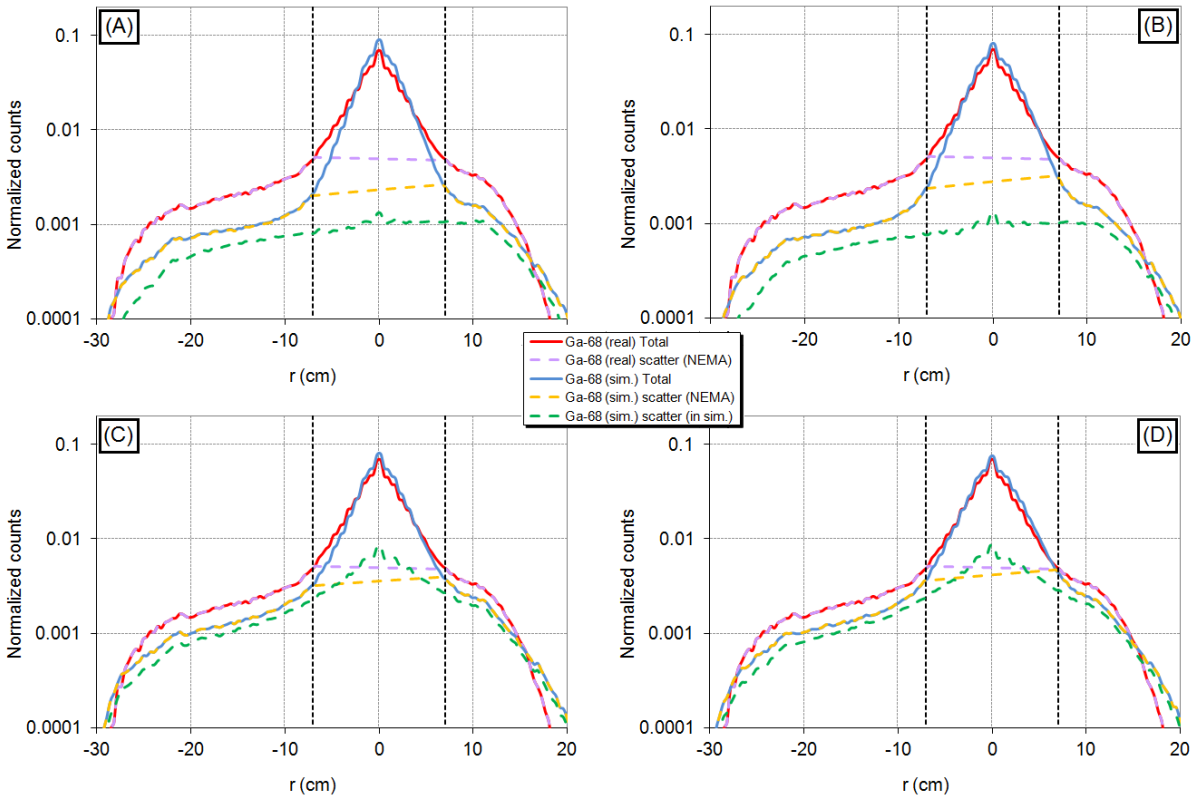

Figure 31. *^{68}Ga radial profiles for real acquisitions compared to different simulations:* ***(A)****: Scanner without shields. Positron range in water.* ***(B)****: Scanner without shields. Positron range in water plus a thin air layer.* ***(C)****: Scanner with shields. Positron range in water.* ***(D)****: Scanner with shields. Positron range in water plus a thin air layer.*

Table 17 reports the SF values for all the cases simulated for both isotopes. For each case, two SF values are reported, the NEMA estimation and the value obtained from the simulation which is called 'actual value'. These values show that there is an important contribution coming from the shields as it was discussed in [Yang and Cherry, 2006]. Taking into account the NEMA scatter estimation, we observe the same overestimation that it was seen in real data (Table 16) when ^{68}Ga is employed due to positron range effects. Besides, we can see that NEMA estimation gives a SF value in between the SF due to the object in the FOV (the mouse sized phantom) and the total SF due to both object and scanner shields.

Table 17. *Scatter Fraction values for simulated data with realistic positron range*

Isotope	Shields	SF (%) in simulations	
		Actual value	NEMA
^{18}F	No	11	13
^{68}Ga	No	11	18
^{18}F	Yes	29	21
^{68}Ga	Yes	29	26

3.2.2.3. Suggestion to improve the NEMA protocol

Table 16 and Table 17 show that the NEMA protocol overestimates the SF for ^{68}Ga due to its large positron range. In order to make the NEMA protocol isotope range-independent, in this work we propose the deconvolution of the radial profiles to remove the effect of positron range from the profile (Figure 32).

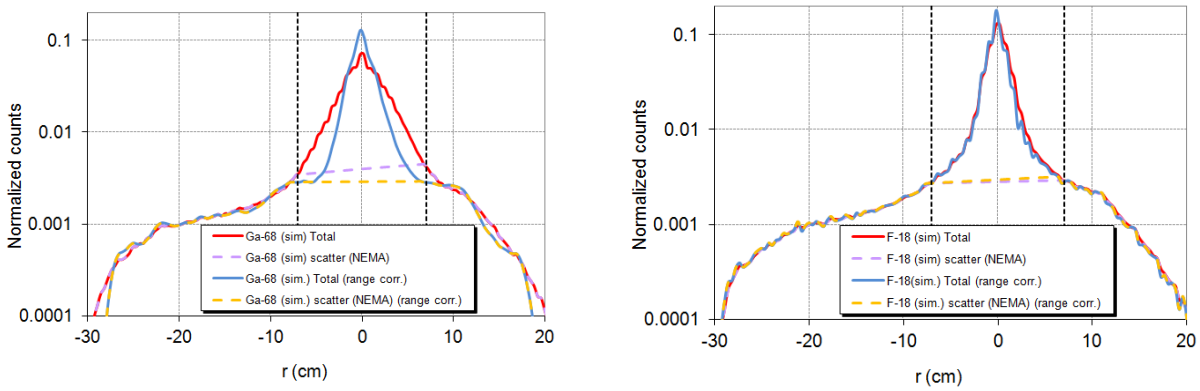

Figure 32. *^{68}Ga (left) and ^{18}F (right) radial profiles and SF values with and without positron range correction*

The results of the NEMA SF values with and without positron correction for both isotopes are shown in Table 18. We can see that for ^{18}F there are not differences in SF values with and without the correction but SF for ^{68}Ga provides the same value than ^{18}F after positron range correction. Correcting the profiles for range effect (a relatively simple procedure), would allow using isotopes with relatively large range together with the NEMA protocol.

Table 18. *Scatter Fraction values for simulated data with and without positron range correction*

Isotope	Range correction	SF (%) (NEMA)
^{68}Ga	No	26
	Yes	21
^{18}F	No	21
	Yes	21

3.2.3. Conclusions

Positron range corrections are necessary if isotopes with significantly large positron range (as ^{68}Ga) are used to estimate the SF using the NEMA protocol.

Simulations show that scatter profiles are quite flat when no shields are taken into account, which means that the scatter coming from the object produces a relatively flat count distribution background. On the other hand, peaked scatter profiles (with the peak close to the line source location) are observed when shields are simulated, having the scatter in the shields a very important contribution to the total scatter fraction. In order to reproduce adequately the experimental data, simulations should model shields accurately. Counts scattered on the shields would be taken for true counts when analyzed in

terms of the NEMA SF protocol, which was designed assuming a flat scatter background. This seems to be the main reason for the underestimation of the total SF in the NEMA NU4-2008 protocol. Results obtained with this method yield a value in between the SF due to the object solely and the total SF due to the object and the scanner shields.

As a summary of this chapter, we have argued for the importance of standardized protocols to assess the performance of scanner systems and used them to compare two PET scanners between them and to other scanners available on the market. We have also shown that we should be aware that these protocols are not flawless. We have analyzed in detail some examples and, with the help of very detailed and realistic simulations, we have been able to propose improvements to these protocols.

3.3. References

Bailey, D. L. 2005. *Positron emission tomography: basic sciences*, Springer.

Bailey, D. L., Jones, T., Spinks, T. J., Gilardi, M.-C. & Townsend, D. W. 1991. Noise equivalent count measurements in a neuro-PET scanner with retractable septa. *IEEE Trans. Med. Imaging,* 10**,** 256-60.

Bao, Q., Newport, D., Chen, M., Stout, D. B. & Chatziioannou, A. F. 2009a. Performance evaluation of the inveon dedicated PET preclinical tomograph based on the NEMA NU-4 standards. *J Nucl Med,* 50**,** 401-8.

Cherry, S. R., Sorenson, J. A. & Phelps, M. E. 2003. *Physics in nuclear medicine*, Saunders.

Del Guerra, A., Bartoli, A., Belcari, N., Herbert, D., Motta, A., Vaiano, A., Di Domenico, G., Sabba, N., Moretti, E., Zavattini, G., Lazzarotti, M., Sensi, L., Larobina, M. & Uccelli, L. 2006. Performance evaluation of the fully engineered YAP-(S)PET scanner for small animal imaging. *Nuclear Science, IEEE Transactions on,* 53**,** 1078-1083.

España, S., Herraiz, J. L., Vicente, E., Vaquero, J. J., Desco, M. & Udias, J. M. 2009. PeneloPET, a Monte Carlo PET simulation tool based on PENELOPE: features and validation. *Phys Med Biol,* 54**,** 1723-42.

Goertzen, A. L., Bao, Q., Bergeron, M., Blankemeyer, E., Blinder, S., Cañadas, M., Chatziioannou, A. F., Dinelle, K., Elhami, E., Jans, H.-S., Lage, E., Lecomte, R., Sossi, V., Surti, S., Tai, Y.-C., Vaquero, J. J., Vicente, E., Williams, D. A. & Laforest, R. 2012. NEMA NU 4-2008 Comparison of Preclinical PET Imaging Systems. *The Journal of Nuclear Medicine (Accepted)*.

Kisung, L., Kinahan, P. E., Miyaoka, R. S., Jae-Seung, K. & Lewellen, T. K. 2004. Impact of system design parameters on image figures of merit for a mouse PET scanner. *Nuclear Science, IEEE Transactions on,* 51**,** 27-33.

Knoess, C., Siegel, S., Smith, A., Newport, D., Richerzhagen, N., Winkeler, A., Jacobs, A., Goble, R. N., Graf, R., Wienhard, K. & Heiss, W. D. 2003. Performance evaluation of the microPET R4 PET scanner for rodents. *Eur J Nucl Med Mol Imaging,* 30**,** 737-47.

Levin, C. S., Foudray, A. M. K. & Habte, F. 2006. Impact of high energy resolution detectors on the performance of a PET system dedicated to breast cancer imaging. *Physica Medica,* 21**,** 28-34.

National Electrical Manufacturers Association (NEMA). 1994. Performance Measurements of Positron Emission Tomographs. NEMA Standards Publication NU2-1994. Rosslyn, VA. National Electrical Manufacturers Association

National Electrical Manufacturers Association (NEMA). 2001. Performance Measurements of Positron Emission Tomographs. NEMA Standards Publication NU2-2001. Rosslyn, VA. National Electrical Manufacturers Association

National Electrical Manufacturers Association (NEMA). 2008. Performance Measurements of Small Animal Positron Emission Tomographs. NEMA Standards Publication NU4-2008. Rosslyn, VA. National Electrical Manufacturers Association

Strother, S. C., Casey, M. E. & Hoffman, E. J. 1990. Measuring PET scanner sensitivity: relating countrates to image signal-to-noise ratios using noise equivalents counts. *Nuclear Science, IEEE Transactions on,* 37**,** 783-788.

Surti, S., Karp, J. S., Perkins, A. E., Cardi, C. A., Daube-Witherspoon, M. E., Kuhn, A. & Muehllehner, G. 2005. Imaging performance of a-PET: a small animal PET camera. *Medical Imaging, IEEE Transactions on,* 24**,** 844-852.

Tai, C., Chatziioannou, A., Siegel, S., Young, J., Newport, D., Goble, R. N., Nutt, R. E. & Cherry, S. R. 2001. Performance evaluation of the microPET P4: a PET system dedicated to animal imaging. *Phys Med Biol,* 46**,** 1845-62.

Vaquero, J. J. & Desco, M. 2005. Limitaciones tecnológicas de la tomografía por emisión de positrones (PET) para pequeños animales de laboratorio. [Technical limitations of the positron emission tomography (PET) for small laboratory animals]. *Rev Esp Med Nucl,* 24**,** 334-47.

Vaquero, J. J., Lage, E., Ricón, L., Abella, M., Vicente, E. & Desco, M. 2005b. rPET Detectors Design and Data Processing. *IEEE Nuclear Science Symposium Conference Record*.

Vicente, E., Herraiz, J. L., Canadas, M., Cal-Gonzalez, J., Espana, S., Desco, M., Vaquero, J. J. & Udias, J. M. 2010a. Validation of NEMA NU4-2008 Scatter Fraction estimation with 18F and 68Ga for the ARGUS small-animal PET scanner. *In:* Nuclear Science Symposium Conference Record (NSS/MIC), 2010 IEEE, Oct. 30 2010-Nov. 6 2010 2010a. 3553-3557.

Vicente, E., Vaquero, J. J., Lage, E., Tapias, G., Abella, M., Herraiz, J. L., España, S., Udías, J. M. & Desco, M. 2006 Caracterización del Tomógrafo de Animales rPET. *Libro de Actas, CASEIB 2006*.

Wang, Y., Seidel, J., Tsui, B. M., Vaquero, J. J. & Pomper, M. G. 2006b. Performance evaluation of the GE healthcare eXplore VISTA dual-ring small-animal PET scanner. *J Nucl Med,* 47**,** 1891-900.

Weber, S. & Bauer, A. 2004. Small animal PET: aspects of performance assessment. *Eur J Nucl Med Mol Imaging,* 31**,** 1545-55.

Yang, Y. & Cherry, S. R. 2006. Observations regarding scatter fraction and NEC measurements for small animal PET. *Nuclear Science, IEEE Transactions on,* 53**,** 127-132.

4. Data-Corrections in Preclinical PET

As it was introduced in chapter 1, (section 1.3), in order to provide quantitative images from PET scanners, the data must be processed taking into account physical effects such as attenuation, scatter, or decay time of the radioactive source. Furthermore, the scanner electronics produces random counts, pile-up and dead-time effects, and the efficiency of individual detector elements as well as the exact geometry of the scanner may differ slightly from the ideal expectation, due to statistical variations in the properties of the detectors and unavoidable variations during construction of scanner and detector elements. All of these effects cause the scanner to depart from the ideal behavior and they must be taken into account to reproduce a linear relation between tracer activity in the scanner and activity measured.

In this chapter we study in detail some of these corrections, with examples taken from the two scanners whose performance evaluations were presented in the previous chapter, but they can be also applied to other systems. In section 4.1we introduce a novel method to take into account pile-up and dead-time effects. Section 4.2 presents a quantitative study of the effect on the image quality of small mechanical misalignments in rotating PET systems made of planar detectors and a calibration protocol to correct for them. This later correction was not described in chapter 1 since it is not such a usual correction in PET systems as it is for CT and SPECT scanners. Finally, in section 4.3 we describe an attenuation correction method based on CT images. This is a rather standard implementation based on previous works, but we wanted to include it in this thesis as an example of the software developed by our group and that is being commercialized as part of the reconstruction software for the Argus System.

4.1. Modeling of pile-up and dead-time for small animal PET scanners

In a photon detector system, pile-up occurs when a photon deposits energy in the detector while the signal from a previous event is still being integrated [Knoll, 2000]. Pile-up effects are more significant at high count rates. They become increasingly important when large-area detectors are used [Mankoff *et al.*, 1989, Smith *et al.*, 1994, Vicente *et al.*, 2007, Vicente *et al.*, 2008], where every channel of the electronic acquisition system is employed to read a substantial detector area, making the possibility of achieving high count rates per electronic channel more likely.

Pile-up events induce two kinds of errors in PET data [Furrer *et al.*, 1984]. On one hand, they worsen resolution and contrast in detection systems which employ position sensitive block detectors (either pixelated or monolithic) when they are read with multiplexed electronics using analog logic to identify the position of interaction. If additional photons reach the detector after the trigger event and during the integration time, they will be processed along with the photon which originated the trigger as part of the same single event. For these pile-up events, the apparent location of the interaction will be inaccurate and, if they are not rejected, will cause miss-positioning of coincidence events [Germano and Hoffman, 1990, Badawi and Marsden, 1999b].

Figure 33C shows the distribution of pile-up events at high activity (2400 μCi in the Field of View (FOV)) in a simulated flood histogram for a Hamamatsu H8500 flat-panel PS-PMT coupled to an array of 28×28 LYSO crystals irradiated with a uniform source. Pile-up events would yield energy to two different crystals of the same detectors. One can easily show that if we pick two crystals at random and draw the mid-point of the segment joining both crystals, this mid-point tends to be located on average at the central region of the surface of the detector. Thus, when there is noticeable pile-up in the acquisition, the distribution of counts recorded in the detector tends to concentrate in the central crystals of the array. At low activities (Figure 33, A and B), where pile-up is not significant, the count distribution is uniform.

On the other hand, if the pile-up event provides a signal large enough to fall beyond the Upper Level Discriminator (ULD) of the energy window employed in the acquisition, the event will be rejected. When this happens, the number of coincidences acquired is reduced and consequently the count statistics of the image. Moreover, as pile-up is a non-linear effect, if it is not taken into account, quantification may be compromised.

In Figure 33D energy spectra for the same three acquisitions above-mentioned are shown. Profiles are normalized to the same number of coincidences. The spectra for low activities (dotted and light-color curves) are quite similar, but we can see in the 240 μCi spectrum a lower photopeak height and a slight excess of counts around the 1022 keV peak, corresponding to the pile-up of two photons of 511 keV each one. At 2400 μCi (dark line), count losses at the photopeak and below ~200 keV are very important and there is an evident excess of counts above the photopeak, due to all the photon pile-up combinations, having the 1022 keV peak higher probability.

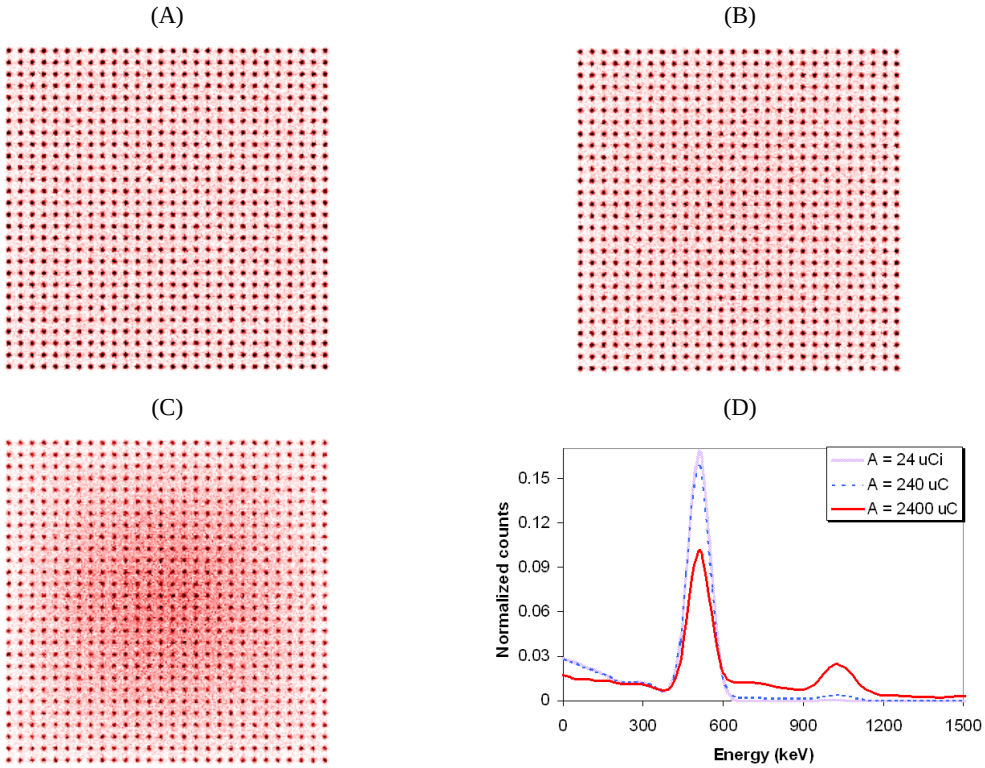

Figure 33. ***(A)****, **(B)** and **(C)**: Simulated flood histogram for a Hamamatsu H8500 flat-panel PS-PMT coupled to an array of 28×28 LYSO crystals with 24, 240 and 2400 μCi inside the FOV, respectively.* ***(D)****: Energy spectra for the same three activities. Profiles are normalized to the same number of coincidences.*

We classify in more detail, as a function of the effect within the energy window used, the different situations that may arise when one of the two singles of a coincidence is affected by pile-up. Let E_1 and E_2 be the energy of each photon of the pile-up event (assuming pile-up of 2 photons) and LLD and ULD the Lower and Upper Level Discriminators of the energy window respectively. Let us assume that the photon with energy E_1 is the one which is in true coincidence (before filtering by the energy window) with another photon (E3∈ [LLD, ULD], for simplicity). We can distinguish three cases, as shown in Table 19, with regard to the effect of pile-up in the count rate:

Table 19. *Classification of pile-up events.*

	CASE 1 $E_1 + E_2 < LLD$	**CASE 2** $LLD \leq E_1 + E_2 \leq ULD$	**CASE 3** $ULD \leq E_1 + E_2$
A) E_1 < LLD	No effect	Coincidence gain. Distorted position and energy information	No effect
B) E_1 ∈ [LLD,ULD]	---	No Coincidence gain. Distorted position and energy information	Coincidence loss
C) E_1 > ULD	---	---	No effect

There are different ways to reduce pile-up effects at the hardware level [Smith *et al.*, 1994]. One way is to use the shortest possible integration time to reduce the probability of pile-up. But integration time cannot be arbitrarily short since enough light has to be integrated to keep acceptable spatial and

energy resolutions. This measure relies on finding scintillators with shorter light decay times. Another way to reduce the effect of pile-up on the count rate capability of the system is to use a restricted energy window. Another method is increasing the number of electronic channels which read the detectors, so that the count rate associated to every electronic channel is reduced, for the same count rate in the dectector. Further methods to reject pile-up events can be found, for example, in [Germano and Hoffman, 1991, Sjöland and Kristiansson, 1994, Imperiale and Imperiale, 2001]. Pile-up rejection mechanisms can significantly reduce the spectral distortions associated to pile-up, but count losses must be still corrected in the quantitative analysis.

The count rate in a PET scanner as a function of the activity in the Field of View (FOV) has non-linear contributions coming not only from pile-up, but also from dead-time and random coincidences [Knoll, 2000, Cherry *et al.*, 2003]. An accurate estimation of these non-linear effects is essential for quantitative PET studies [Bendriem and Townsend, 1998]. Methods to estimate and correct the effects of random coincidences in PET studies can be found in [Knoll, 2000, Williams *et al.*, 1979, Casey and Hoffman, 1986, Badawi *et al.*, 1999, Stearns *et al.*, 2003, Brasse *et al.*, 2005]. In this work we focus on pile-up and dead-time effects, what we call 'effective dead-time', as they are closely related. By dead-time we refer to the loss of counts due to the inability of detectors, electronics, computer disk and software, or any other part of the signal chain, of processing all physical valid events because the system is busy processing a previous event. In a sense, pile-up, when causing loss of counts, can be considered as an ingredient of a general dead-time concept. Such is the case that it is often found in the literature that both dead-time and pile-up effects are referred to simply as dead-time.

Several methods for characterizing the count rates of a PET scanner and data losses due to pile-up and dead-time effects have been proposed. For instance, in Hoffman *et al*. [1983], corrections for dead-time loss are calculated from the 'on-line' measurement of triple coincidence events. Stearns et al. [1985] measured dead-time losses for both single events and total coincidence events independently to obtain the total dead-time. Mazoyer et al. [1985] proposed a scheme which was based on the paralyzing dead-time model using the total coincidence rate correcting both, the emission and transmission data (used for attenuation correction). Yamamoto *et al.* [1986] proposed a method to correct dead-time using a nonlinear function of the 'off-line' measured random coincidences. They showed that the dead-time is a function of the object size as is the random count rate. Daube-Witherspoon *et al.* model [1991], for emission and transmission 2D PET scanners, takes into account coincidence losses due to singles losses and multiple events, as well as misspositioning errors at higher count rates caused by pulse pile-up within a detector block. Eriksson *et al.* [1994] model assumes that data losses can be factorized into two components, one part coming from the detector processing system and one part coming from the data processing system.

As it can be seen from these examples, corrections of count losses due to dead-time and pile-up is usually derived from a combination of analytical models that describe the individual electronics components and empirical data derived from scanning phantoms at various input count rates. Dead-time models usually treat system dead-time as being separable into two components, paralyzable and non-paralyzable [Knoll, 2000].

Nevertheless, to the best of our knowledge, there are no simple protocols to estimate and to take into account pile-up effects valid for a general acquisition since it depends on the material and object size placed in the FOV and the source distribution (inside/outside the FOV) because it changes the ratio between the number of coincidences and the number of singles. This means that the quantification properties of images obtained from high-activity acquisitions (with large pile-up effects) are usually compromised by pile-up effects. In the method outlined by Yamamoto *et al.* [1986] this is taken into account, but in their procedure it is necessary to measure the 'off-line' random coincidences, which is not always possible or practical.

In this work [Vicente *et al.*, 2012a, Vicente *et al.*, 2011] we propose to use an effective dead-time, τ, which can be easily computed for any acquisition and scanner, and linearizes the dependence of the count rates with the activity. This effective dead-time takes into account pile-up losses and gains and

dead-time losses. The method requires only two calibration acquisitions and is based on the linear relationship between τ and the Singles-to-Coincidences ratio (SCR). We have verified that the method is valid even when the effects of pile-up are important, as it is the case of one of the scanners used in this study, rPET [Vaquero *et al.*, 2005b], with large area detectors and without electronic pile-up rejection. We present results for this specific scanner, but the method was also applied to other systems, such as SEDECAL Argus scanner (formerly GE eXplore Vista) [Wang *et al.*, 2006b], demonstrating its applicability.

4.1.1. Materials & Methods

4.1.1.1. Count rate linearization

The decaying source method to estimate the effective dead-time

Dead-time behaviour in a PET scanner as a function of the count rate is often estimated by means of a decaying source experiment [Knoll, 2000]. Repeated measurements of total coincidence rates are obtained for different activities of a decaying source. In the limit of very low activities, when dead-time (and other nonlinear effects) vanishes, the measured count rate, *m(t)*, would coincide with the true incident count rate *n(t)*. Since the true incident count rate for larger activities can be easily calculated according to the decay time correction, the ratio of incident to measured counts ($[m(t)]_d/[n(t)]_d$, where the subscript *d* stands for decay corrected) can be estimated for any activity. This allows to obtain empirically a dead-time correction for a given acquisition and scanner. It is a common procedure to fit this dead-time correction factor $[m(t)]_d/[n(t)]_d$ to an analytic expression containing an effective dead-time τ, using either paralyzable, non paralyzable or mixed models [Knoll, 2000].

Sometimes dead-time corrections for a given scanner are obtained by means of a reference acquisition of an intermediate size phantom [Knoll, 2000, Germano and Hoffman, 1988]. Once the effective dead-time τ is obtained from this phantom, corrections evaluated with the same value of τ are applied to all acquisitions performed by the same scanner. In what follows, we refer to this method as 'single-parameter method'.

New method to estimate effective dead-times: the SCR-based method

Yamamoto et al [1986] and Thompson and Meyer [1987] studied the dependence of τ on the size of the object in the FOV. We deepened on this study, performing simulations of decaying sources with different materials and sizes of the phantoms, and different energy windows for the acquisition. Table 20 summarized the simulated phantoms used, ranging from point sources to capillary sources in cylinders of different materials and sizes. The effective dead-time for each phantom acquisition was obtained with the decaying source method explained in the previous section. We expected these effective dead-time values τ to depend on the Singles-to-Coincidences ratio (SCR) for each acquisition. Thus, we plotted effective dead-times against the true SCR[9] values for each acquisition. By 'true' we mean SCR free from dead-time, pile-up and random count effects. These can be easily obtained from a decaying source experiment in the limit of vanishing activity.

It can be shown that a linear relationship between the effective dead-time, τ, and the SCR exists (see Appendix 4.1A). This relationship can be explained as the result of two contributions: a dead-time involving only events from detected coincidences, τ_C, and an additional dead-time which affects every single event, irrespectively of whether it results or not in an actually detected coincidence, represented by the singles effective dead-time, τ_S, which accounts for pile-up effects. Namely the expression is:

[9] No energy window was applied to measure the singles rates.

$$\tau = 2 \cdot \tau_s \cdot SCR + \tau_C \quad \textbf{(49)}$$

Thus, the method proposed is based on two parameters (τ_C and τ_S) unlike the single-parameter presented in the previous section. We propose to correct for pile-up and dead-time using two calibration acquisitions, one with high SCR and one with low SCR, in order to estimate the τ_C and τ_S, parameters which can be used to compute the effective dead-time, τ, of any other acquisition following equation (49)(See Figure 34). We call this procedure the 'SCR-based method'.

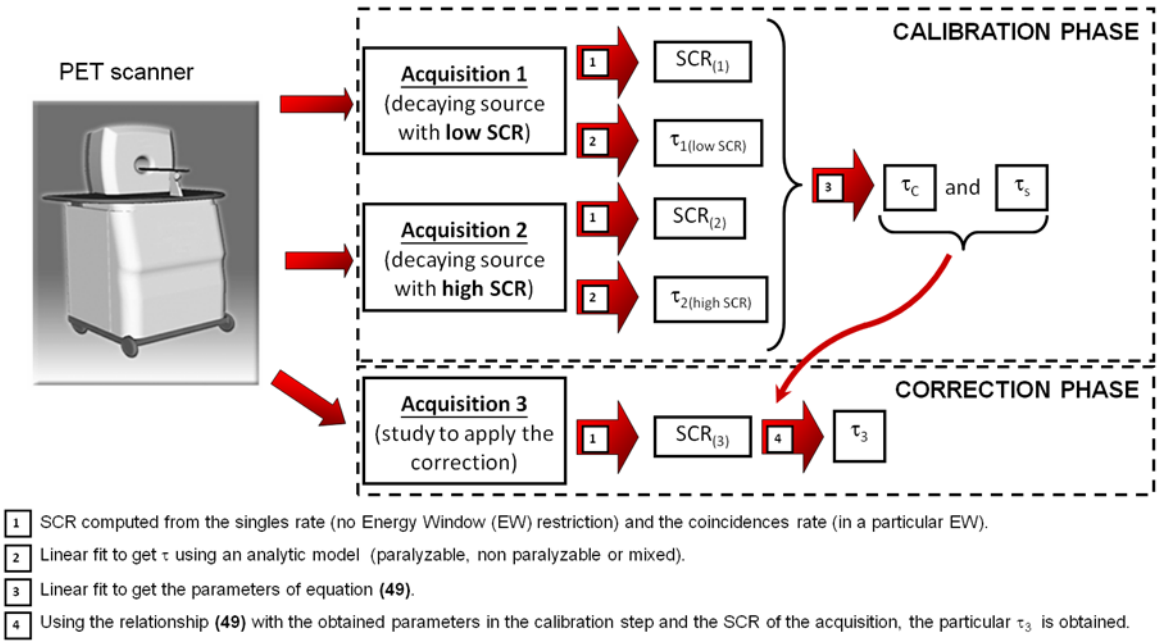

Figure 34. *Flowchart of the SCR-based method to obtain the effective dead-time correction.*

Table 20. *Description of the phantoms simulated. Notation: PS: point source; SC: small cylinder; LC: large cylinder; LS: line source; C: cylinder; d: cylinder diameter in cm (d=[0.4, 1, 2, 3, 4, 5]); ϕ: cylinder diameter; h: cylinder height.*

Phantom Name	Description[a]		Dimensions	
	Source (Isotope: ^{18}F)	Object	Source ϕ / h (cm)	Object ϕ / h (cm)
PS	Point source	Water cubic box	0.05 / --	x = 1 y = 1 z = 1
Water (SC)	Small cylinder (*SC*)	Small water cylinder	0.9 / 6.5	0.9 / 6.5
Al (SC)		Small aluminium cylinder		0.9 / 6.5
GSO (SC)		Small GSO cylinder		0.9 / 6.5
Pb (SC)		Small lead cylinder		0.9 / 6.5
Water (LC)	Large cylinder (*LC*)	Large water cylinder	5.5 / 5.0	5.5 / 5.0
Water (SL&Cd) d=[0.4,1,2,3,4,5]	Line Source (*LS*)	Water cylinder (*C*)	0.2 / 0.4	d / 4.0
Al (SL&Cd) d=[0.4,1,2,3,4,5]		Aluminium cylinder (*C*)		d / 4.0

[a]All phantoms (sources and objects) are placed at the centre of the FOV

Validation of the SCR-based method

In order to evaluate the method proposed to correct by dead-time and pile-up effects we first analyzed the decaying source method using both real data and simulations for the *Water (SC)* phantom acquired with the rPET scanner [Vaquero *et al.*, 2005b]. In this work we assumed a non-paralyzable behaviour, although similar results are achieved with paralyzable expressions when the values of the dead-time correction factor are not extreme, as it is the case of the scanners analyzed in this work under their usual operational ranges. We performed a decaying source experiment with the rPET system using a small cylinder (SC) phantom (0.9 cm diameter, 6.5 cm length) filled with ^{18}F in water ('*Water (SC)*') placed at the centre of the FOV of the scanner. For reference, although it is not needed in the procedure, the initial activity was measured in a well-counter with an accuracy of ±5%. Several consecutive acquisitions of 5 minutes with an energy window of 400-700 keV were taken, starting from an initial activity of 900 μCi, with an activity concentration of 254.6 μCi/cc and a total count rate of 130 kcps. Also, acquisitions of this source were simulated with PeneloPET [España *et al.*, 2009] mimicking the experimental setup. In the simulations, we used a coincidence dead-time of 1.6 μs, which includes the conversion time of the ADC and an integration time of 0.22 μs, values which suit rPET hardware. From the simulations it is possible to estimate the individual contributions to the total effective dead-time that can be split into three components: strict dead-time (τ_{DT}), pile-up losses ($\tau_{p(loss)}$) and pile-up gains ($\tau_{p(gain)}$), according to:

$$\tau = \tau_{DT} + \tau_{p(loss)} - \tau_{p(gain)} \quad \textbf{(50)}$$

The simulated phantoms described in Table 20 were used to study and validate the SCR-based method. The effective dead-time for each phantom acquisition was estimated with the decaying source method. The SCR-based method was applied using the PS and the *Water (LC)* phantoms as the two calibration experiments, for both scanners described in chapter 2: rPET [Vaquero *et al.*, 2005b] and Argus [Wang *et al.*, 2006b] systems. Random counts in the Argus scanner were removed from the acquisition prior to the analysis of data to compute τ. For the rPET scanner this was not necessary as the fraction of random counts for this scanner was negligible.

We also estimated the error introduced when the effective dead-time obtained for a particular phantom is employed to correct dead-time for another phantom with different SCR, that is, when the single-parameter method is employed, comparing the results with the ones obtained correcting with effective dead-times estimated with the SCR-based method.

Besides simulations, the relationship between τ and SCR for the rPET scanner was explored also with real data. The *Water (SC)* and *Water (LC)* phantoms were used as calibration acquisitions for the SCR-based method to calculate the calibration parameters, τ_C and τ_S from eq. (49). A further acquisition of a Hot Derenzo phantom (see Appendix A) was employed to compare the τ value obtained from the decaying source method and the one obtained using the computed τ_C and τ_S from eq. (49) (SCR-based method).

4.1.1.2. Activity calibration with reference data (Calibration curve)

Ideally, activity calibration is accomplished by measuring a phantom containing a known, homogeneous activity concentration determined from an external independent measurement, using a well-counter for example [Cherry *et al.*, 2003].

For the activity calibration of the rPET scanner, the *Water (SC)* phantom was used. The acquisition was reconstructed with a 3D-OSEM algorithm [Herraiz *et al.*, 2006a]. Images from all frames were obtained. Several regions of interest (with a size of a few cc to prevent partial volume effects) were chosen at different places in the interior of the cylinder and at different slices and the

mean value and the statistical error were computed for each frame. The counts per cubic centimeter and second (cps/cc) obtained were compared to the known specific activity (uCi/cc) in the inner region of the cylinder and the data were fit to a linear calibration curve, looking for the proportionality constant relating the specific rate measured in the image to the known specific activity for each frame. A linear fit assumes that non-linear effects have been removed.

4.1.2. Results

4.1.2.1. Count rate linearization

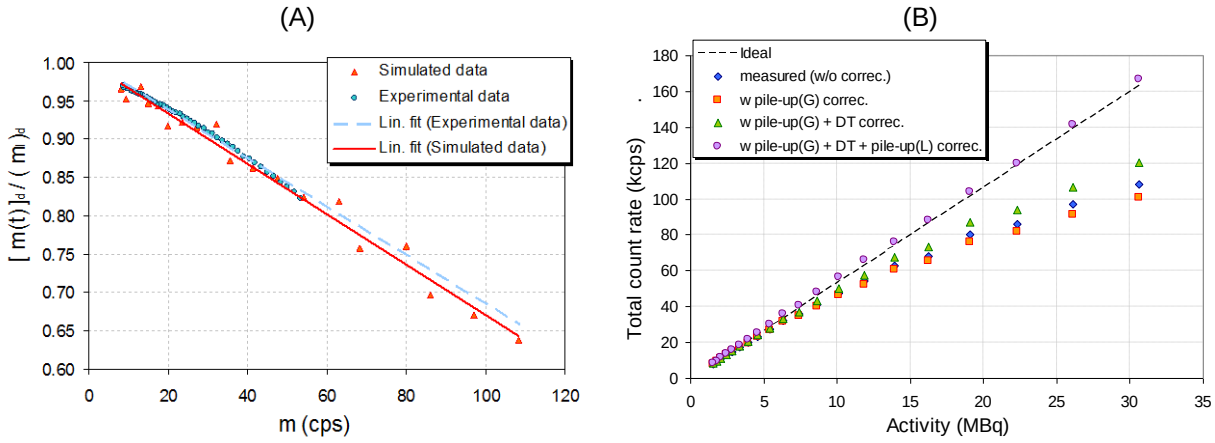

Figure 35. (A)*: Linear fits employed to derive* τ *for the Water (SC) phantom using the rPET scanner with a 400-700 keV energy window. The dead-time correction factor* $[m(t)]_d/[n(t)]_d$ *is plotted against measured count rates, exhibiting an approximate linear behaviour in the range considered. The effective* τ *is obtained from the slope.* ***(B)****: Simulated study showing the different contributions to effective dead-time for the same case shown in (A), as a function of activity in the FOV.*

Figure 35A shows the linear fits where the deacaing source method and the non-paralyzable model were used to estimate the effective dead-time τ of the *Water (SC)* phantom for real and simulated data for rPET scanner. The resulting τ values are reported in Table 21 In the case of the simulation, it is possible to estimate the contributions: dead-time and pile-up losses and gains. Equation (50) was used to yield the total τ and this value is compared with the one obtained from the fit using the deacaing source method. Two main results are worth mentioning:

1) A very good agreement of the value of the fitted effective τ between the simulation and the experimental data is seen.
2) For the simulation, the τ obtained from the fit using the non-paralyzable model and the one computed from the dead-time and pile-up (losses and gains) contributions using Eq. (50) are in good agreement. This result indicates the consistency of the parameters inputted in the simulation and the use of Eq. (50) to compute the total effective dead time.

Figure 35B shows the count rates of the simulated *Water (SC)* phantom in the 400-700 keV energy window and the different corrections applied as a function of actual activity in the FOV. No random correction was applied since, as we can see in Figure 36A, the percentage of random counts is less than 3% for all count rates considered. Figure 35B shows the suitability of the obtained effective τ since the corrected count rates do not show significant differences from the ideal curve for both high and low count rates.

Table 21. *Effective dead-time values for experimental and simulated data of the Water (SC) phantom in the 400-700 keV energy window.*

		τ (μs)	
EXPERIMENTAL DATA	**Fit using the non-paralyzable model**	3.17 ± 0.04	
SIMULATED DATA	**Fit using the non-paralyzable model**	3.3 ± 0.1	
	Pile-up (loss) time	2.31 ± 0.08	3.2 ± 0.1 (using (50))
	Pile-up (gain) time	0.67 ± 0.02	
	Dead-time	1.60 ± 0.01	

Figure 36 shows the relative contribution (in percentage) of the non-linear effects (i.e., pile-up, dead time and random counts) to the total count rates for the case of an energy window of 400-700 keV for the *Water (SC)* (Figure 36A) and the *Water (LC)* (Figure 36B) phantoms. The two phantoms have very different SCR (see Table 22). Empty symbols represent coincidence losses, solid ones are detected coincidences. The most important effect for both cylinders is the loss of coincidences due to pile-up, not being the same percentage for the same acquired count rate in both phantoms. The next major effect is dead-time losses, in this case showing the same percentage in both cylinders for the same count rate. Pile-up gains and random coincidences (solid dots) are much smaller, being random coincidences the smallest contribution.

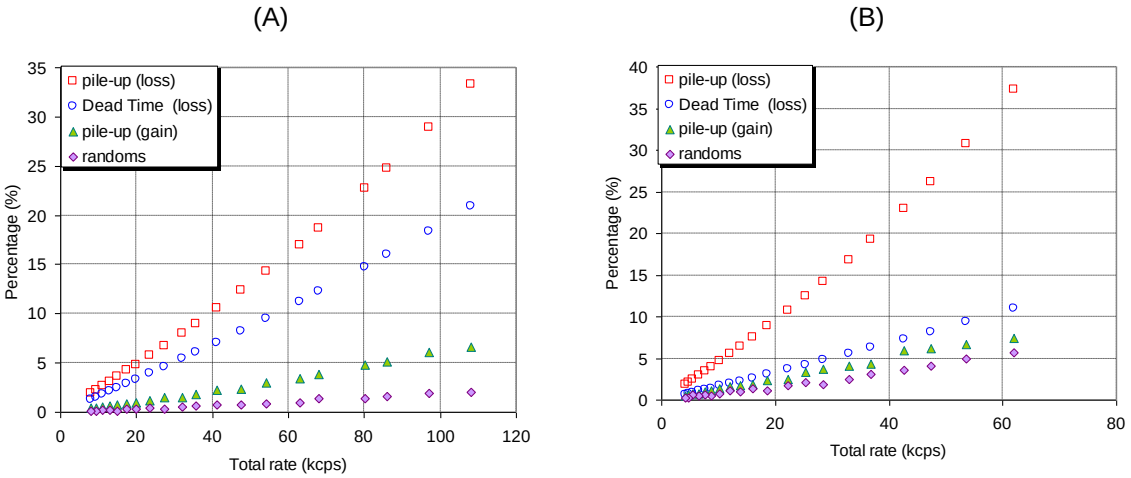

Figure 36. *Relative contributions of non-linear effects to the total count rate for the scanner rPET in an energy window of 400-700 keV.* ***(A)****: Water (SC) phantom (SCR=19),* ***(B)****: Water (LC) phantom (SCR=42).*

Although the percentages of coincidence losses and gains due to pile-up do not show the same dependence on the count rate for phantoms with different *SCR*, it is possible to obtain an effective dead-time for any acquisition, employing only two calibration acquisitions, one with high *SCR* and one with low *SCR*. This procedure works because the effective τ, as it has been shown (Appendix 4.1A), has a linear dependence on *SCR*. The values of the effective dead-time and the *SCR* are reported in Table 22 for the rPET scanner.

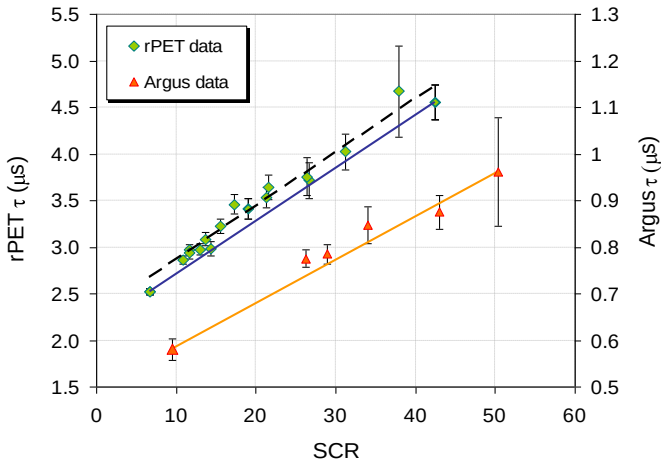

Figure 37. *Effective dead-time τ versus SCR for different acquisitions of rPET (diamonds, left Y axis) and Argus (triangles, right Y axis) scanners (400-700 keV). The dashed line is a linear fit to all rPET points, and the solid line is obtained from the two calibration points of the SCR-based method at the extreme values of SCR, namely PS and Water (LC) phantoms in rPET. A similar line is also shown for the Argus scanner.*

In Figure 37 we plot the effective dead-times obtained from simulations of the decaying phantoms described in Table 20, for the case of the rPET scanner (diamonds), and for the Argus one (triangles), against SCR. As expected, a linear behaviour is seen for both scanners. (Argus data results are discussed at the end of this section). In this figure we also plot with solid lines the relationship between the effective dead-time and the SCR estimated using our proposed SCR-based method using two calibration acquisitions, namely the *PS* and the *Water (LC)* cylinder. These phantoms are representative of both extreme sides of the SCR range. We used these two points to estimate the linear relationship with SCR, although some points are slightly underestimated, because we found that an error in the effective dead-time, $\Delta\tau$, results in a lower error in the corrected count rates, *n(t)*, when $\Delta\tau < 0$ (underestimation) than $\Delta\tau > 0$ (overestimation). (For more details see Appendix 4.1B). The calibration-estimated line lies slightly below the linear fit using all rPET phantoms (dashed line), but with similar slope. The relative error between their intercept values is 6%. Despite this error in the intercept, we found that using the SCR-based calibration method to compute each effective τ, the error in the corrected count rate is less than 7%, even for high count rates, for all phantoms considered. An example of this is shown in Figure 38.

Table 22. *Singles-to-coincidence ratio (SCR) and effective dead-time (τ) in the 400-700 keV energy window for the simulated phantoms described in Table 20 for rPET scanner.*

Phantom Name	SCR	τ (μs)	Phantom Name	SCR	τ (μs)
PS	6.7 ± 0.1	2.52 ± 0.03	***Water (SL&C3.0)***	14.3 ± 0.2	2.98 ± 0.07
Water (SC)	19.0 ± 0.3	3.4 ± 0.1	***Water (SL&C4.0)***	15.5 ± 0.3	3.22 ± 0.08
Al (SC)	21.3 ±0.3	3.5 ± 0.1	***Water (SL&C5.0)***	17.0 ± 0.2	3.19 ± 0.07
GSO (SC)	26.7 ± 0.6	3.7 ± 0.2	***Al (SL&C0.4)***	11.6 ± 0.2	2.93 ± 0.06
Pb (SC)	37 ± 1	4.7 ± 0.5	***Al (SL&C1.0)***	13.7 ± 0.2	3.09 ± 0.07
Water (LC)	42.4 ± 0.7	4.6 ± 0.2	***Al (SL&C2.0)***	17.3 ± 0.3	3.5 ± 0.1
Water (SL&C0.4)	10.9 ± 0.2	2.86 ± 0.05	***Al (SL&C3.0)***	21.6 ± 0.4	3.6 ± 0.1
Water (SL&C1.0)	11.7± 0.2	2.97 ± 0.05	***Al (SL&C4.0)***	26.4 ± 0.7	3.8 ± 0.2
Water (SL&C2.0)	13.0 ± 0.2	2.98 ± 0.06	***Al (SL&C5.0)***	31.2 ± 0.7	4.0 ± 0.2

We show in Figure 38 a comparison between the single-parameter method (1-param. correction) and the one proposed in this work (SCR-based method), for the rPET scanner in the 400-700 keV energy window. For the single-parameter method, we used the *Water (SC)* phantom to get the fixed τ value. In the figure we plot the ratios of corrected over ideal count rates for two situations: a point source (*PS*) and the small cylinder of lead (*Pb (SC)*). The *PS* was chosen to show the magnitude of the error in the corrected count rates when the effective dead-time is overestimated, as it happens when using the dead-time obtained with the single-parameter method from the *Water (SC)* to correct the count rates of the *PS* acquisition. The second example, *Pb (SC)*, was selected because this is the point with the worse fit to the calibration-estimated line for rPET scanner in the SCR-based method (see Figure 37, point: (37, 4.7)). We can see that in both cases the SCR-based method provides more accurate results, with a relative error smaller than 7% for the *Pb (SC)* phantom and less than 6% for the *PS*, compared to deviations of 10% for the *Pb (SC)* phantom and even up to 100% (*PS*) when the 1-parameter correction is employed. This example shows that the 1-parameter correction introduces a bias in the corrected count rates. This error is large if the τ used for the correction overestimates the one of the acquisition and will be more significant for large detector blocks, so the SCR-based method would be highly recommended for clinical dedicated-breast PET scanners (or PEM cameras) as for example the ones described in [Wang *et al.*, 2006a, Wu *et al.*, 2009] or for high sensitivity preclinical PET scanners with detectors particularly close as, for example the ones described in [Seidel *et al.*, 2010, Zhang *et al.*, 2011].

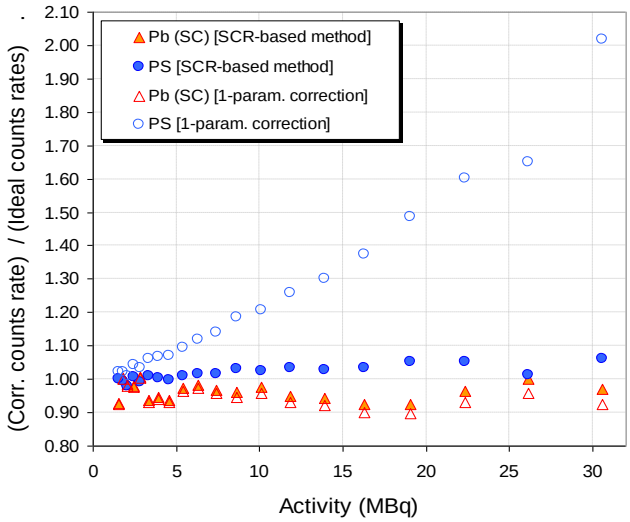

Figure 38. *Comparison of the ratio of corrected over ideal rates for the SCR-based method (solid points) and the single-parameter method which uses only one value for the effective dead-time (1-param. correction, empty points) for the PS and the Pb (SC) phantoms. It can be observed that in both cases the SCR-based method provides more accurate results, with a relative error smaller than 7% for the Pb (SC) phantom and 6% for the PS one.*

The linear behavior between τ and SCR was also studied for other two energy windows of the rPET scanner, 100-700 keV and 250-700 keV, finding a good estimation of the dead-time as well. In Table 23 we compare the parameters of the linear fits (intercept τ_C and slope $2\tau_S$) for three different energy windows. Several phantoms were used to determine the parameters of the fits.

We can see in the table an almost constant slope (column 3) in all the cases for the rPET scanner. This is due to the fact that the slope depends on the effective dead-time for singles and no energy window was applied to the singles measurements. We can also observe that the coincidences-only dead-time (intercepts) approaches the conversion time of the ADC of the scanner (τC = 1.6 μs as we mentioned before) for the wider energy window, and increases with narrower energy windows. This is due to the way the rPET system works. Events that are identified as part of a coincidence are integrated, converted and further processed. It is after conversion when the energy window is applied.

For the narrower energy windows some events are integrated and afterwards discarded because they fall outside the energy window. Thus, there are counts keeping the acquisition electronics busy, contributing to dead-time, but they will not remain in the acquired data. The effective coincidence dead-time increases approximately as the inverse of the fraction of counts that survives the energy window.

Table 23. *Linear fits to get the effective dead-time as a function of the SCR for three energy windows using simulated data (rPET scanner).*

Energy window (keV)	Linear fit parameters	
	Intercept: τ_C (μs)	Slope: $2\tau_S$ (μs)
100-700	1.66 ± 0.09	0,048 ± 0.009
250-700	2.05 ± 0.07	0.046 ± 0.006
400-700	2.20 ± 0.09	0.059 ± 0.008

Besides simulations, the relationship between τ and SCR for the rPET scanner was explored also with real data. Table 24 shows the parameters τ (calculated using the decaying source method) and *SCR* from the *Water (SC)* and the *Water (LC)* phantoms in the 400-700 keV energy window. These are the two acquisitions employed in the calibration phase of the SCR-based method. The effective τ obtained from the *Derenzo* decaying experiment and the one estimated from the SCR-based method differ about 3%. Also, the experimental values of the effective dead-time for these rPET acquisitions are within 8% of the ones of the simulations, presented in Table 23.

Table 24. *SCR (measured at low activity) and effective dead-time from real acquisitions of the rPET scanner in the 400-700 keV energy window. The Water (SC) and Water (LC) phantoms were used to calibrate (intercept τ_C and slope $2\tau_S$) the SCR-based method.*

Phantom name	SCR	τ (μs)	τ fit (μs)
Water (SC)	20	3.17 ± 0.04	$\tau = 0.053 \cdot SCR + 2.11$
Water (LC)	43	4.4 ± 0.2	
Derenzo	36	3.9 ± 0.2	4.0 (Relative error: 3%)

Further, as we showed in Figure 37, the procedure is illustrated with simulated data from another PET scanner with more conventional geometry, the Sedecal Argus scanner [Wang *et al.*, 2006b]. Simulations of several phantoms listed in Table 20 were used. It is important to remark that, contrarily to what it was found for the rPET scanner, the random counts fraction in Argus scanner is not negligible in comparison with the other non-linear effects. Thus, it was necessary to apply a previous random correction to the data before computing τ. This does not mean a loss of generality, because most PET scanners have procedures to remove or correct for random counts in the acquisition. This result shows that the method can be applied to different PET scanners provided that a random correction is performed to the coincidences rates when the random counts fraction is not negligible in comparison with other non-linear effects.

4.1.2.2. Activity calibration with reference data (Calibration curve)

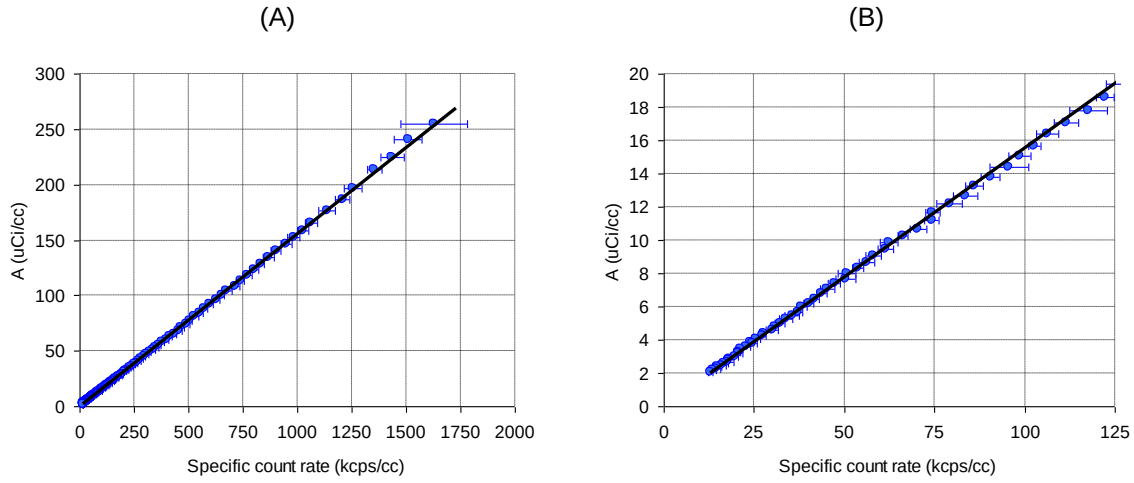

Figure 39. *Specific count rates (kcps/cc) in the image vs. activity concentration (calibration curve).* ***(A)****: Whole range data.* ***(B)*** *Zoom-in region.*

Figure 39 shows the calibration curve which relates the experimental specific count rate measured in the image to the actual specific activity for different activity levels for the *Water (SC)* phantom. The obtained fit is:

$$Y = A_1 \cdot X = \left[(1553 \pm 2) \cdot 10^{-4} (\mu\text{Ci/kcps})\right] \cdot X$$

where: [X] = (cps/cc),
[Y] = (μCi/cc).

We can state that a linear calibration (transformation from cps/cc measured in the image to a specific activity in the FOV) is achievable, for both high and low levels of activity, verifying that the linearization in the total count rates acquired works fine.

4.1.3. Conclusions

This work proposes a simple method to identify the effective dead-time (τ) needed to restore the correct linear relationship between activity in the FOV and count rate measured by the scanner, getting rid of non linear effects due to dead-time and pile-up losses and pile-up gains. This method fully deals with the fact that each acquisition exhibits a different effective τ since pile-up effects depend on the material, object size and source distribution (inside/outside the FOV). The standard procedure that uses the same effective dead-time τ to correct every acquisition, introduces a bias in the corrected count rates, especially in situations when the effective τ of the correction overestimates the actual value τ of the acquisition, with errors sometimes up to 100% for high activities.

Our SCR-based method requires only two calibration acquisitions and is based on the linear relationship between τ and the Singles-to-Coincidences ratio (SCR). The simulations show that the error in the corrected count rates is below 7%, even when high activities are present in the FOV. Even smaller errors could be attained employing more than two phantoms to calibrate the method.

We have verified with experimental and simulated data that the SCR-based method performs well for two commercial preclinical PET scanners with very different architectures: rPET [Vaquero *et al.*, 2005a], a small-animal PET scanner with four rotating large-area detectors without pile-up

rejection in the electronics, for which pile-up is relatively important, and the Argus scanner [Wang *et al.*, 2006b], a small-animal PET with more conventional geometry (two full rings) and small-area detectors. The SCR-based method might be applied to any other scanner, including clinical scanners, with higher interest in scanners with large detector blocks, as for instance clinical dedicated-breast PET scanners (or PEM cameras) [Wang *et al.*, 2006a, Wu *et al.*, 2009] or high sensitivity preclinical PET scanners with close-up detectors [Seidel *et al.*, 2010, Zhang *et al.*, 2011].

4.1.4. Appendix 4.1A. Linear relationship between τ and SCR

In the limit of low rates, the fraction of coincidences that are free of pile-up and dead-time, f_c, can be written as [Knoll, 2000]:

$$f_c \cong 1 - n\tau \quad \textbf{(51)}$$

where n is the incident coincidences rate and τ the effective dead-time for coincidences. Quite generally in any scanner we can consider a dead-time component (possibly including pile-up effects) which affects every single event recorded by the scanner. This would be characterized by the 'singles' dead-time τ_S. Further, there may be additional dead-time contributions coming from the further processing of events identified as being part of a coincidence event. This would be an 'only-coincidences' dead-time τ_C. For instance, in a scanner working in singles mode, for which every single event detected is converted, processed and stored in disk, τ_c would be negligible and the effective dead-time seen in the recorded coincidences would be just due to the loss of single events. On the other extreme, there may be scanners working in 'coincidence only' mode, which would convert and store just the events that are identified as being part of a valid coincidence event. In the limit of low rates, the fraction of coincidences which remains free from dead-time (and pile-up) is related to the fraction of singles free of dead-time (and pile-up), 1- n_s τ_s, as follows:

$$f_c = 1 - n\tau = (1 - n_s\tau_s)^2 \cdot (1 - n\tau_C) \quad \textbf{(52)}$$

where n_s is the incident singles rate. This equation just indicates that, in order to record a coincidence, both single events belonging to it must survive to singles dead-time effects and, further, the resulting coincidence must survive any coincidence-only dead-time effects. If we work out Eq. (52) to find the value of τ, we get in the limit of low count rates (disregarding the terms of second and higher order in τ_C and τ_s):

$$\tau = 2 \cdot \tau_s \cdot \frac{n_s}{n} + \tau_C \quad \textbf{(53)}$$

We define the Singles-to-Coincidences (SCR) ratio for the incident rates (n) as $SCR=n_s/n$ so that Eq. (53) reads:

$$\tau = 2 \cdot \tau_s \cdot SCR + \tau_C \quad \textbf{(54)}$$

Eq. (54) has been derived here in the limit of low count rates ($n_s\tau_s << 1$ and $n\tau_C << 1$) and in this limit it is valid for both the paralyzable and non-paralyzable models. It is straightforward to show that it is also exactly valid (that is, for any rate) in the case of paralyzable dead-time systems, being the deviations from (54) relatively small (of logarithmic order) for the case of non-paralyzable dead-time systems.

Eq. (54) shows that under rather general grounds, a linear relationship between the effective dead-time seen in the acquired coincidences and SCR emerges. It also shows that the slope and intercept of a linear fit of the effective τ against SCR will estimate the effective singles dead-time, which may include pile-up effects, and the coincidences-only dead-time, respectively.

4.1.5. Appendix 4.1B. Relative error in the corrected count rates as a function of the error in the effective dead-time

Let *n* be the count rates corrected by the true value of the effective dead-time, τ, for one acquisition and *n'* the count rates corrected by the estimated effective dead-time, (τ +Δτ), being Δτ the error in the effective dead-time. We can write:

$$n = \frac{m}{1 - m\tau} \quad \text{and} \quad n' = \frac{m}{1 - m(\tau + \Delta\tau)} \tag{55}$$

where these two count rates are related by:

$$n' = \frac{n}{1 - n\Delta\tau} \tag{56}$$

So the relative error of the corrected count rates is:

$$E_r = \left| \frac{n' - n}{n} \right| = \left| \frac{n\Delta\tau}{1 - n\Delta\tau} \right| \tag{57}$$

Equation (57) shows that the relative error increases much faster with n when τ is overestimated ($\Delta\tau > 0$) than when it is underestimated ($\Delta\tau < 0$).

4.2. Measurement of misalignments in small-animal PET scanners based on rotating planar detectors and parallel-beam geometry

The increasing number of animal models of human diseases used in translational research makes small-animal imaging an essential tool to assess biological functions. This approach makes it possible to carry out new types of studies, such as monitoring of transgenic expression in genetically modified mice or *in vivo* monitoring of tumor response to therapy [Lewis and Achilefu, 2002, Pomper, 2001, Massoud and Gambhir, 2003]. In these systems, the dimensions of the structures whose biochemical functions we want to analyze impose additional system requirements not shared by clinical scanners [Lecomte, 2004]. To address the same biological questions that are already being investigated in humans, both systems must provide similar relation between spatial resolution and size of the organ under study, which is know as 'image equivalence' [Jagoda *et al.*, 2004]. This suggests that a small-animal system would have to reconstruct images with a resolution below 1 mm in all directions, whereas systems for imaging human tissue typically have a resolution of ~4-10 mm. Therefore, exact geometric characterization is critical in small-animal scanners, as even submillimetric misalignments of the detectors may result in noticeable degraded image resolution and artifacts. Figure 40 illustrates this effect with a rat study affected by a detector misalignment in the range of half the crystal pitch size (one detector was misplaced by 0.8 mm). Acquired data were reconstructed with FBP with a sinogram bow-tie filtering scheme [Abella *et al.*, 2009].

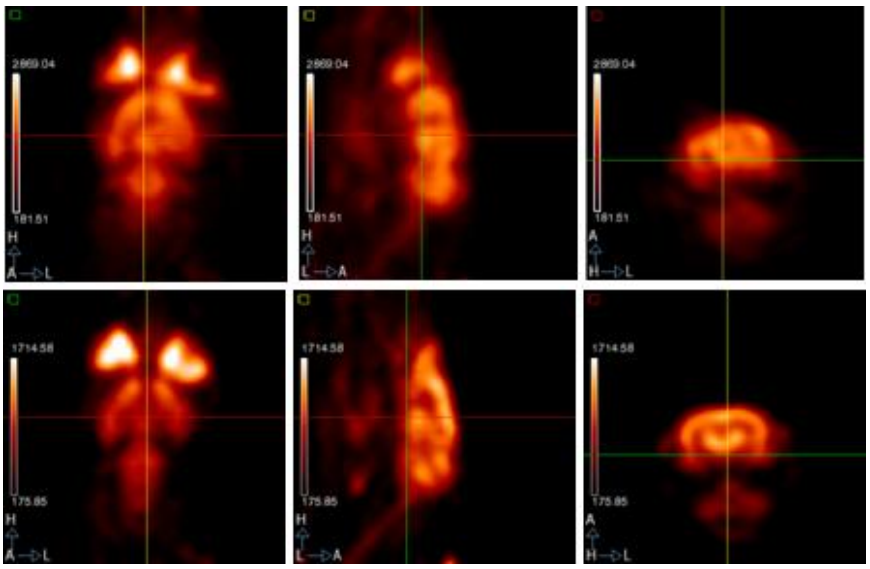

Figure 40. *Coronal, sagittal, and axial views of an FDG rat study acquired with the rPET scanner and reconstructed with FBP with a bow-tie filtering scheme. Reconstructed volume was 55x55x55 with isotropic 0.8 mm pixel size. Result before (top) and after (bottom) correcting for misalignments in the range of half the crystal pitch size (one detector was misplaced by 0.8 mm).*

Methods for estimating geometrical parameters of tomography scanners have been investigated since 1987, mainly for CT and SPECT systems based on fan-beam geometry [Hsieh, 1992, Gullberg *et al.*, 1987] and cone-beam geometry [Gullberg *et al.*, 1990, Noo *et al.*, 2000, Beque *et al.*, 2003, Sun *et al.*, 2007]. Systems based on parallel-beam geometry have received little attention. In [Azevedo *et al.*, 1990] the authors studied methods for estimating the center of rotation (COR) in CT using sinogram data; [Busemann-Sokole, 1987] proposed a method for the determination of collimator hole angulations in SPECT scanners, and, more recently, [Donath *et al.*, 2006] presented an iterative procedure for the determination of the position of the optimum COR intended for any tomography system. Few contributions have been made on the specific case of rotating PET systems, except for a

preliminary study of the effect of misalignments by our group [Abella *et al.*, 2006]. More recently, Pierce *et al.* proposed a new calibration method to determine block positions in a system based on a ring of PET detectors [Pierce *et al.*, 2009]. To the best of our knowledge, there are no systematic studies of the effect of all possible misalignments in a tomography system based on rotating planar detectors.

Calibration techniques are usually based on analytical expressions applicable to the acquisition of ad-hoc phantoms, which sometimes require precise positioning in the field of view (FOV). In our experience, these analytic algorithms should only be used to provide an initial appraisal of misalignment parameters, as most of them make assumptions of ideal or negligible conditions that may not hold in real scanners, and usually require further fine tuning.

We analyzed misalignment effects in PET systems based on rotating detectors with parallel-beam geometry and defined a robust and easy-to-implement protocol for geometric characterization [Abella *et al.*, 2012]. The result of the calibration step can then be used to generate the correct 3D-sinogram from the acquired list-mode data. Section 4.2.1 presents a description of the simulations used. Section 4.2.2 describes the misalignments considered in this work and provides a theoretical study of the effects of these misalignments on projection data and of the tolerance of the system to each one, in order to define an easy way for detection and calibration. Section 4.2.3 proposes the algorithm to measure these misalignments in a real scanner. Finally, section 4.2.4 presents an evaluation of the calibration tool proposed.

4.2.1. Monte Carlo simulations using PeneloPET

In order to study and quantify the effects of the different geometrical misalignments and to evaluate the proposed algorithm, we used the simulation package PeneloPET (see chapter 2, section 2.3). In the simulations, detector blocks can be displaced from their regular positions in order to build non-regular complex geometries or to introduce misalignments of detectors [España *et al.*, 2009].

Simulations were done based on the high-resolution animal rPET scanner (see chapter 2, section 2.1). In this system, 3D data approximate line integrals of the radioactive tracer distribution along lines of response (LOR) that are not restricted to transaxial planes. Data measured by each detector pair are rearranged into a set of direct 2D sinograms, which only include LORs from transaxial slices, and oblique 2D sinograms, which traverse several slices, thus conforming a 3D sinogram as a function of three variables (ρ, θ, s). ρ is the distance between the LOR and the COR (ranging from 0 to R (radius of the FOV)), θ is the azimuthal angle between the LOR and the Y_0-axis (ranging from 0 to 180 degrees (Figure 41, left), and s is an integer variable which accounts for the different 2D sinograms (ranging from 0 to 28^2). These sinograms cover all the possible combinations formed by the events registered by detector elements on different rows.

Data for angles over 360 degrees are reallocated at the corresponding 2D sinogram position in the range 0-180 degrees, as derived from the symmetry property

$$p(\rho,\theta+\pi) = p(-\rho,\theta) \quad \textbf{(58)}$$

where $p(\rho,\theta)$ is the data measured in an LOR defined by the pair (ρ,θ) for a given s. As a result, there is a region where the extra 14 degrees from the first and last position of the detectors overlap (Figure 41, right). Each 2D sinogram has 55 radial and 120 angular bins, resulting in a spacing of 0.8 mm and 1.5 degrees in the radial and angular directions, respectively.

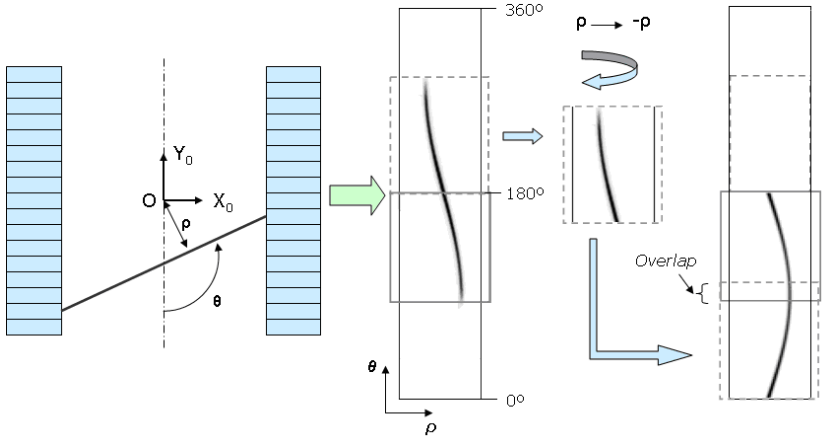

Figure 41. *Left: Transaxial view showing the 2D sinogram variables ρ and θ used to parameterize the LORs. Right: Rearrangement of the data, from a 360-degree 2D sinogram into a 180-degree 2D sinogram.*

Two point source studies with different misalignment configurations were simulated: one located at the center of the FOV and the other one at 10 mm from the center of the FOV, both in the central axial slice. The point source consisted of a sphere (0.5 mm of diameter) of ^{18}F of 30 uCi in a cubic phantom ($1\times1\times1$ cm^3) of water. We chose an acquisition time of 320 s, which provided a total number of acquired coincidences of around $7\cdot10^6$ (center) and $6\cdot10^6$ (1 cm off-center).

Finally, a Hot Derenzo Phantom (see Appendix A) acquisition was simulated with and without misalignments to evaluate the effect of the remaining misalignments within the tolerance of the presented method on the corrected image quality. The initial activity was 11.2 MBq (300 μCi) and the acquisition time 560 s (total number of acquired coincidences: $3\cdot10^7$). The misalignments used in this simulation are listed below:

$$\Delta x_1 = 0.0,\ \Delta x_2 = 5.0,\ \Delta x_3 = 2.5,\ \Delta x_4 = -2.5,$$
$$\Delta y_1 = 0.0,\ \Delta y_2 = 1.6,\ \Delta y_3 = 0.8,\ \Delta y_4 = -0.8,$$
$$\Delta z_1 = 0.0,\ \Delta z_2 = 0.0,\ \Delta z_3 = 0.0,\ \Delta z_4 = 0.0,$$
$$\Phi_{offset} = 88.0$$

4.2.2. Study of the effect of misalignments

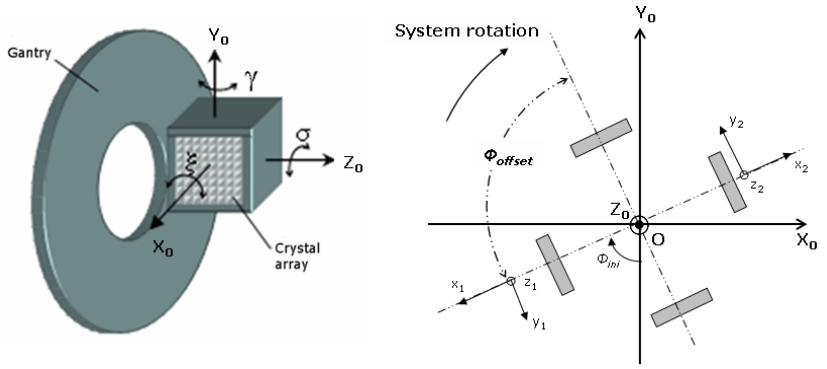

Figure 42. *Left: Detector attached to the rotating gantry showing the three possible sources of angular errors in the detector position in relation to the gantry: σ, γ, and ξ. Right: Axial view of the system showing the coordinate systems used: X_0, Y_0, and Z_0 are absolute coordinates and (x_1,y_1,z_1) and (x_2,y_2,z_2) are coordinates relative to detectors 1 and 2, respectively.*

This section presents a study of the effect of different geometrical misalignments on a detector pair: linear shifts of the detectors (*x*, *y*, and *z* in Figure 42, right) and angles between the detector and the gantry (ξ, skew; σ, tilt; γ, slant in Figure 42, left).

For each type of misalignment, we study its effect on the positioning of the LORs, the 3D sinogram, and the reconstructed image. We also calculate the tolerance of the system to each type of misalignment. These effects can be classified according to the schema shown in Figure 43:

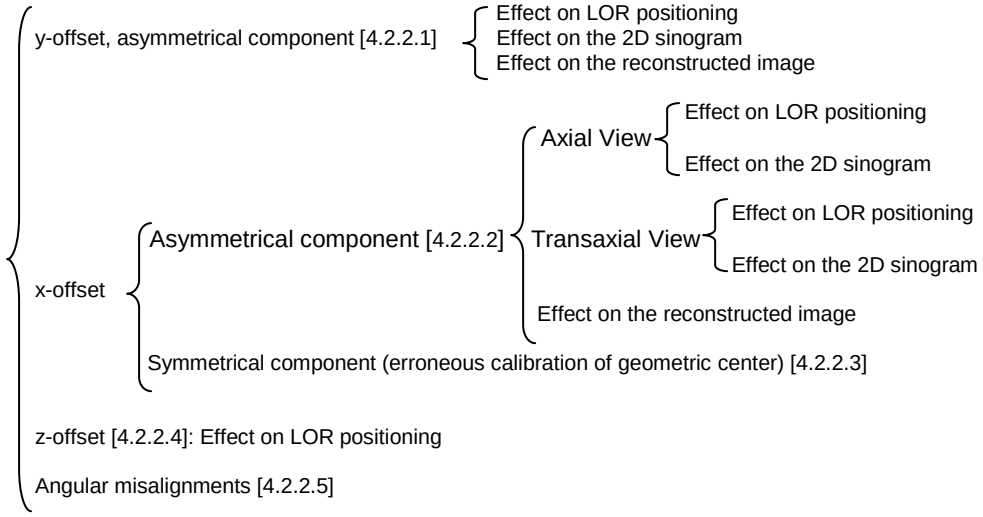

Figure 43. *Classification of the effects considered. Numbers in brackets indicate the subsection where that effect is analyzed.*

4.2.2.1. Misalignment along the y-axis

In a rotating PET scanner, a misalignment along the *y*-axis, hereafter referred to as '*y*-offset', produces two types of effects. The first effect ('asymmetrical component') derives from a differential misalignment between opposite detectors and leads to a mismatch between the geometrical center and the COR. The second effect ('symmetrical component') produces an error in the θ parameter when positioning the LORs, although this will only result in a loss of resolution. This section describes the former asymmetrical component.

Effect on LOR positioning

Figure 44 illustrates the effect of the asymmetrical component of a *y*-offset, which alters the position of the geometrical center, on the apparent position of the LORs. The two gantry positions shown in the figure (corresponding to 0 and 180 degrees of rotation) should theoretically generate equivalent LORs. However, if an asymmetrical *y*-offset is ignored, the counts corresponding to the indicated LORs will be assigned to erroneous bins in the corresponding 2D sinogram.

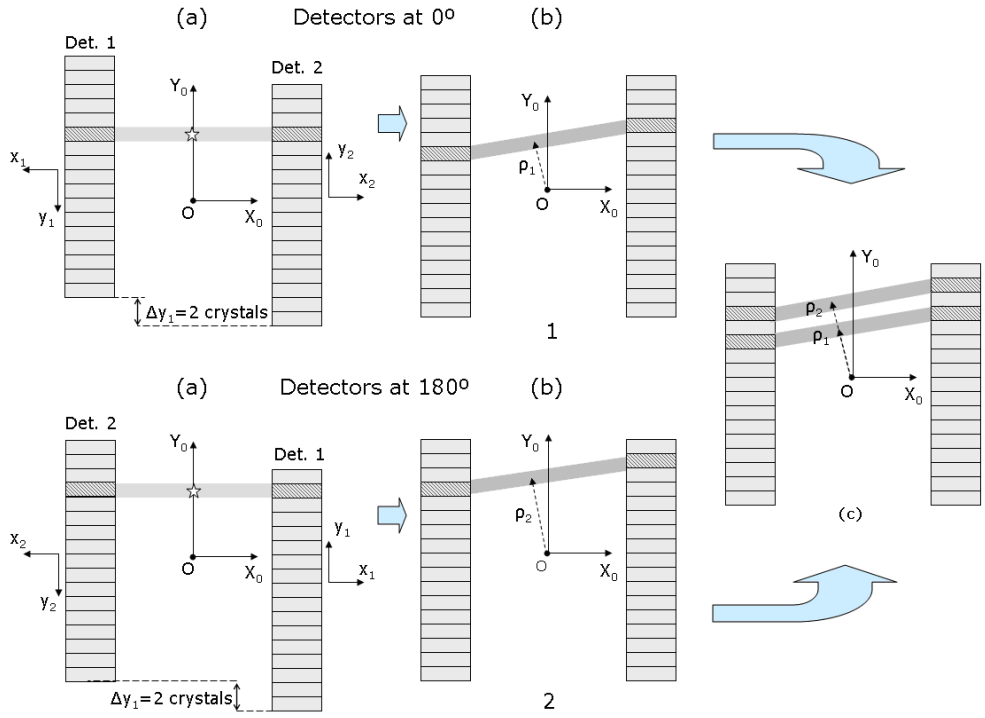

Figure 44. *Drawing of a detector pair in two gantry positions that should theoretically generate coincident LORs. The star represents an annihilation event. Detector 1 has a y-offset of Δy1 = -3.2 mm (two-crystal widths). The panels labeled* ***(a)*** *show the LOR in the real position of the detectors, while the panels labeled* ***(b)*** *show the apparent LOR that would be obtained if the offset were ignored. Panel* ***(c)*** *shows the shift quantification.* ρ_1 *is the radial coordinate in the 2D sinogram corresponding to the apparent LOR when the detectors are at 0 degrees and* ρ_2 *corresponds to the apparent LOR with the detectors at 180 degrees.*

Effect on the 2D sinogram

Figure 45 shows the consequence of this type of LOR positioning error on the 180-degree 2D sinogram in our experimental setup: the region of overlap (zoomed-in view in Figure 45 (a)) shows a discontinuity that we refer to as 'radial gap' in the bins corresponding to gantry positions with 180 degrees of difference. This gap is only visible in the 14-degree sector, which is scanned twice in one rotation, as explained above. Data at the left side of the radial gap (1 in Figure 45 (a)) correspond to events read while the detectors were at the 0-degree gantry position, and data to the right of the radial gap (2 in Figure 45 (a)) were acquired with the detectors at 180 degrees. The *y*-offset, Δy, is directly related to the number of radial bins, *n*, in the sinogram spanned by the discontinuity, according to:

$$\Delta y = nb \qquad \textbf{(59)}$$

where *b* is the radial bin size in mm and Δy is the *y*-offset. Due to the binning in the sinogram, *n* is an integer value, and it can be seen from equation Figure 45 that the estimate for Δy will be discredited (size of the radial bin, *b*). The value *n* only depends on the amount of mismatch between the geometric center and the COR, which is a function of the relative displacement between detectors. The 'sign' of the radial gap is related to the direction of the mismatch between the geometric center and the COR.

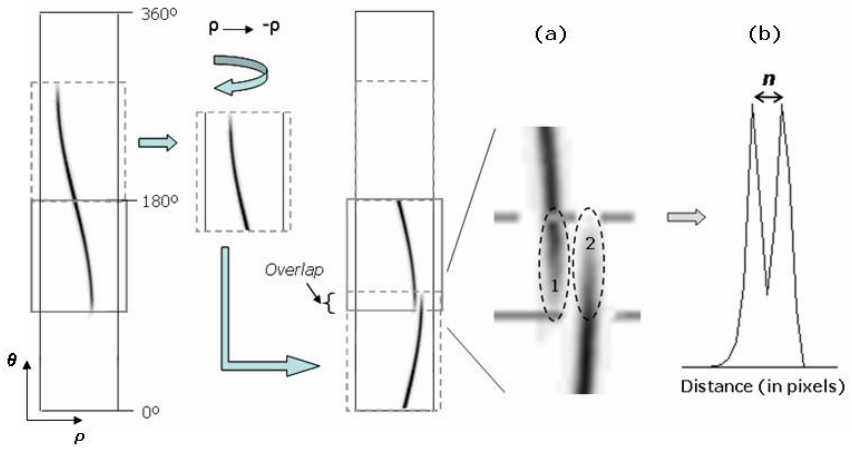

Figure 45. *Example of a y-offset with an asymmetrical component (mismatch between the geometrical center and the COR).* ***(a)*** *Zoomed-in view of the overlap region, showing the radial gap. Labels 1 and 2 identify data acquired at positions 1 (detectors at 0 degrees) and 2 (detectors at 180 degrees) in Figure 44.* ***(b)*** *Radial profile across the gap region.*

Effect on the reconstructed image

Figure 46 shows the effect of a mismatch between the COR and the geometric center on the reconstructed image of a point source, which is a 'crescent' shape of the image that deteriorates resolution. The simulation corresponds to a point source located at 10 mm from the center of the FOV in the central slice.

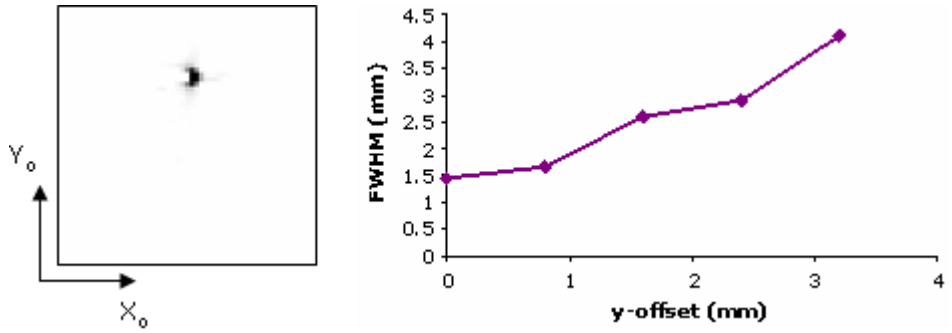

Figure 46. *Effect of a y-offset on the reconstructed image resolution. Left: transaxial view of a simulated point source for a y-offset of 1.6 mm showing a 'crescent' shape. Right: FWHM of profiles drawn along the Y_o-axis for different values of the y-offset.*

A summary of the effects and tolerance for the *y*-offset is presented in Table 25 (rows 1 and 2).

4.2.2.2. Misalignment along the x-axis with mismatch between geometric center and COR

The misalignment along the *x*-axis, hereafter referred to as '*x*-offset', may also lead to two types of effect. The first one derives from a differential misalignment between opposite detectors and leads to a mismatch between the geometrical center and the COR ('asymmetrical component'). The second one occurs when both detectors are misplaced the same amount in opposite directions and leads to erroneous calibration of the distance between detectors (see section 4.2.2.3). This section describes the asymmetrical component.

An *x*-offset that produces a change in the geometrical center induces LOR mispositioning in both the *x* and *z* coordinates (axial and transaxial views), which will be studied separately.

Effect on LOR positioning in the z coordinate (axial view)

Figure 47 shows an example of an *x*-offset, Δx, in detector 2. Gantry positions at 0 and 180 degrees would show equivalent LORs if there were no offset (Δx=0).

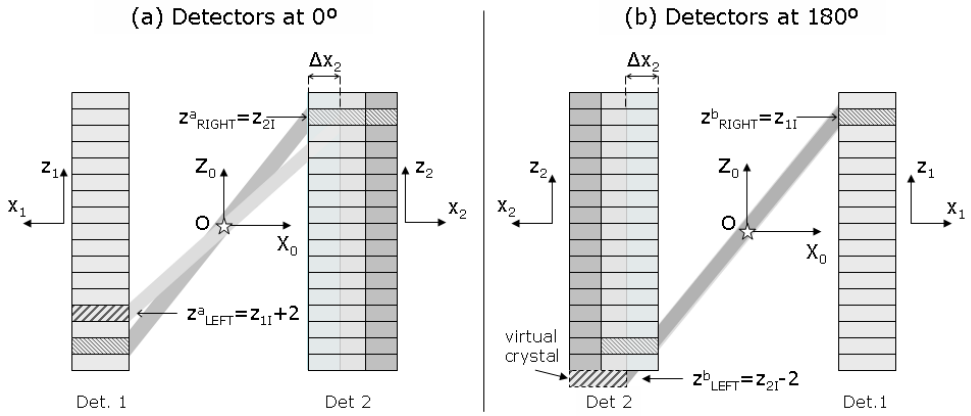

Figure 47. *Axial view of a detector pair at 0 degrees* ***(a)*** *and 180 degrees* ***(b)*** *when there is an x-offset in detector 2. The ideal detectors (without misalignment) are depicted in light gray and the real detector (with misalignment) in dark gray. The star represents an annihilation event. The apparent LOR is depicted in light gray while the real LOR is depicted in dark gray. For a given LOR, z_{1I} and z_{2I} are the apparent axial positions of the crystals that form the LOR in detectors 1 and 2 respectively. For a given axial position on the right detector, z^a_{RIGHT}, the left detector crystals that define the equivalent LORs at gantry positions 0 and 180º, z^b_{LEFT}, have different axial positions.*

Effect on the z coordinate of the sinogram (axial view)

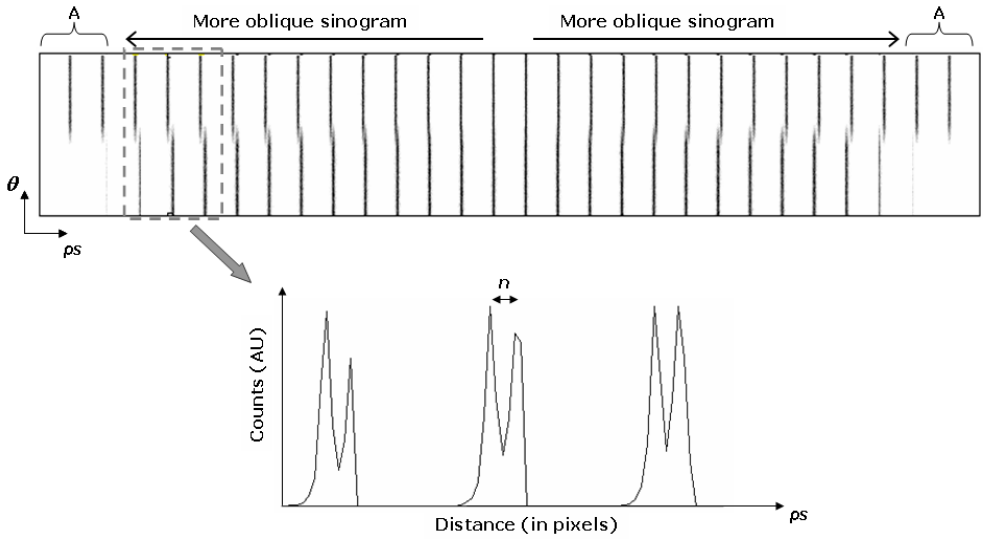

Figure 48. *Top: Plot of a 3D sinogram of a point source placed at the center of the FOV. Coordinates are (θ, ρs). Bottom: Profiles along the s axis corresponding to the highlighted area in the sinogram. Due to the x-offset, the gap increases for more oblique 2D sinograms.*

Figure 48 shows a plot of a 3D sinogram for coordinates θ (120 bins) and ρs (55×28^2 bins). Note that the most oblique 2D sinograms containing the point source (A in Figure 48) lack half of the angular positions. This is because that there is no opposite crystal to conform the LOR in those extreme positions (Figure 47b).

Since the size of these discontinuities in the sinogram is directly related to the *x*-offset, it is possible to estimate this offset from the axial gaps measured on the sinograms. Figure 49 shows a zoomed-in picture of the top half of one detector, depicting the real and apparent detector positions.

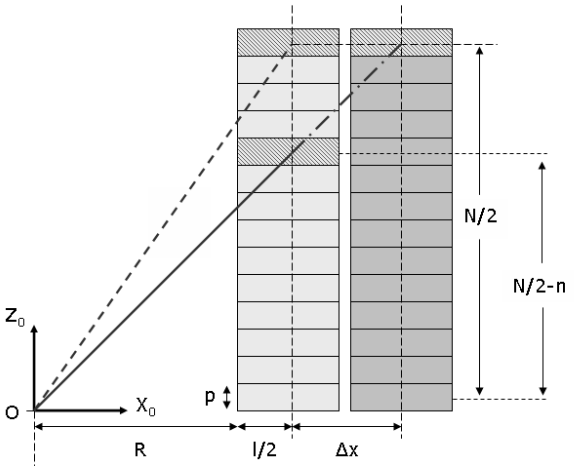

Figure 49. *Diagram of the top half of one detector showing the rationale for the estimation of the x-offset. In light gray we have The detector in the ideal position is shown in light gray and the detector in the real position (with misalignment) is shown in dark gray. R is the radius of rotation, p the pitch size, N the number of crystals in the axial direction, l the crystal thickness, and Δx the x-offset of the detector.*

The value of Δx can be obtained from simple trigonometric relations. For the upper crystal row of the detector we have:

$$\frac{p\cdot(N/2-0.5)}{R+l/2+\Delta x}=\frac{p\cdot(N/2-0.5-n)}{R+l/2} \qquad \textbf{(60)}$$

where R is the radius of rotation, N is the number of crystals in the detector along the *z*-axis, l is the crystal thickness, p is the pitch size, and n is the number of crystals by which the LOR is misplaced (equal to half the axial gap in sinogram bins). Thus, the value of Δx can be calculated as

$$\Delta x=(R+l/2)\left[\frac{n}{\left(N/2-0.5-n\right)}\right] \qquad \textbf{(61)}$$

This effect will appear in the 3D sinogram if there is a minimum change of one crystal in the position of the LORs, i. e. n=1. Equation (61) shows that the minimum value for the calculated *x*-offset, Δx, to have an effect is about 7 mm.

Knowledge of the position of the detectors along the *x*-axis enables a software correction that will lead to correct positioning of the counts in the sinogram. Thus, good quality images can be reconstructed despite the physical mismatch between the geometrical center and the COR. The gap size can be used to obtain a rough estimate of the asymmetrical component of an *x*-offset, as explained above. In order to refine this estimate we can use the effect on the 'transaxial view' (see following section).

Effect on LOR positioning in the x coordinate (transaxial view)

In the case of an asymmetrical *x*-offset, the LORs corresponding to the initial and final rotating positions (gantry at 0 and 180 degrees), which should be equivalent, will show the same θ value but a different ρ value in the 2D sinogram (Figure 50c).

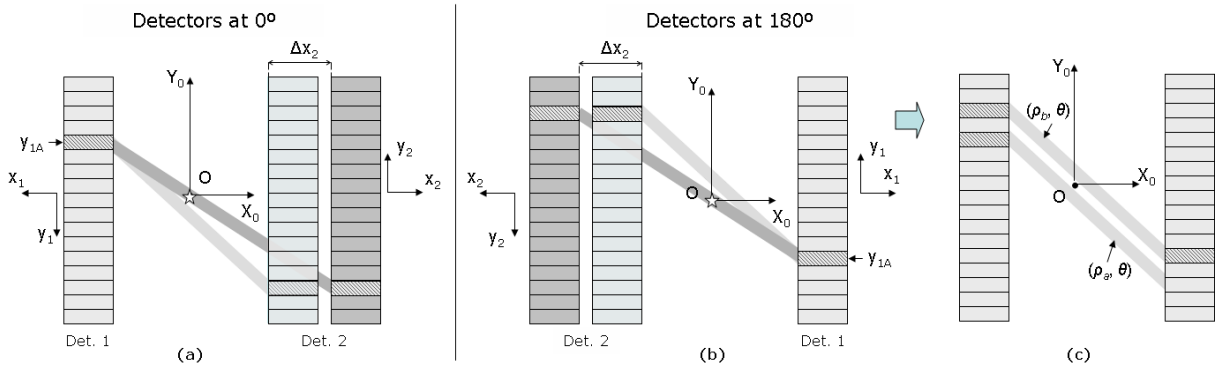

Figure 50. *Axial view of a detector pair at gantry positions corresponding to 0 degrees (a) and 180 degrees (b). The real detector (with misalignment) is depicted in dark gray while the ideal one is depicted in light gray. The star represents an annihilation event. For a given crystal position in detector 1, y1A, and a given angle, θ, the real LOR is depicted in dark gray and the apparent LOR if the x-offset were ignored is depicted in light gray. In (c), we see that the apparent LORs read at 0 and 180 degrees that should coincide show the same angle but different ρ value.*

Effect on the 3D sinogram in the x coordinate (axial view)

The error in the LOR positioning explained above results in a widening of the 2D sinogram. In our experimental setup, due to the arrangement in a 180-degree sinogram, the sinogram area corresponding to the initial and final gantry positions shows a characteristic shape (gray dotted square in Figure 51, left). The right panel of Figure 51 shows that the trajectory followed by the center of mass along the ρ-coordinate presents a deviation from the expected profile at the overlap area. The amount of deviation corresponds to half the differential *x*-offset of the system. This value also reflects the difference between the COR and center of the FOV.

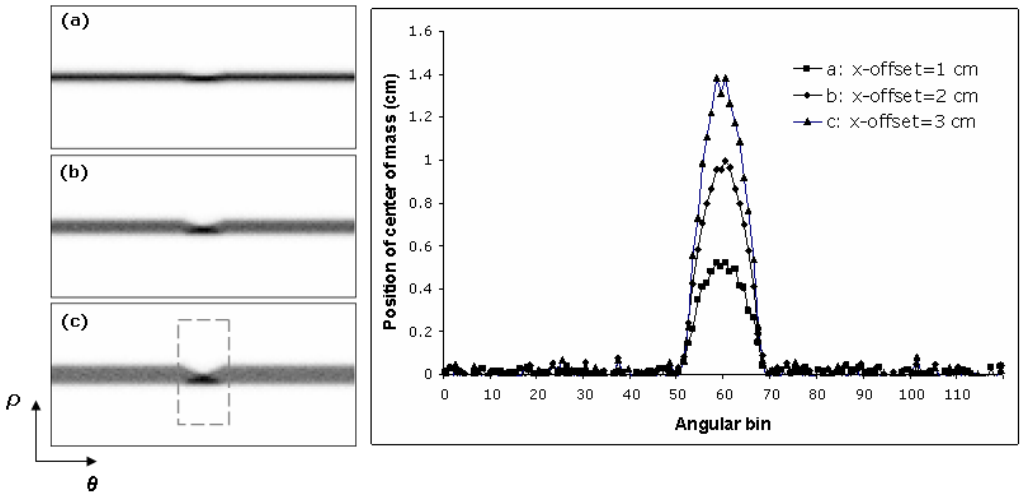

Figure 51. *Left: Sum of all oblique 2D sinograms for different x-offset values {1, 2, 3 cm}. Right: Center of mass vector for each 2D sinogram on the left.*

Effect on the reconstructed image

The visual effect on the reconstructed image of a point source is similar to that produced by a *y*-offset (a 'crescent' shape). The sign of the axial gap is also associated with the direction of the mismatch between the geometric center and the COR, and it produces the same effect irrespective of whether only one or both detectors are actually misaligned.

4.2.2.3. Effects of erroneous calibration of the distance between detectors

To study the effect of erroneous calibration of the distance between detectors, we considered the particular situation which arises when both detectors are misplaced by the same distance in opposite directions on the *x*-axis, that is, with no change in the geometrical center (symmetrical offset). In this case, an erroneous value for the distance between detectors leads to changes in the resolution of the reconstructed image.

This change in resolution is easily explained by considering that closer detectors subtend a larger solid angle for a point source. Figure 52 provides a transaxial view of a detector pair for two different values of the distance between detectors, showing that more tubes of response (TOR) intersect the point source when the detectors are closer. Therefore, if the actual distance between detectors is lower than the nominal one, the source activity that impinges on the same number of crystals would be larger, thus showing a wider point spread function (PSF).

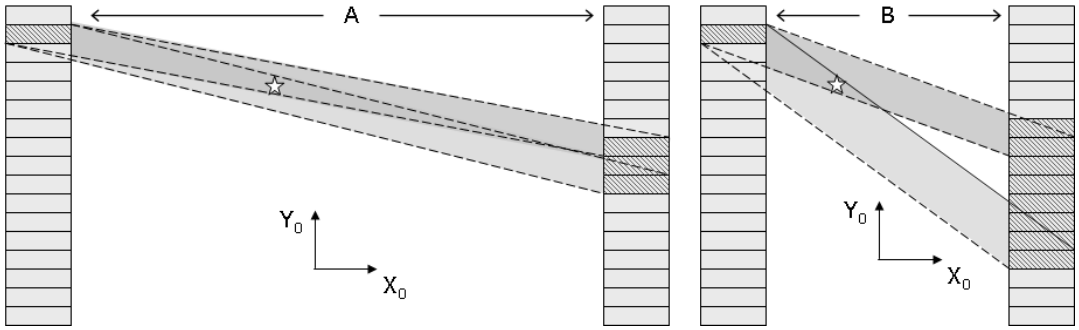

Figure 52. *Transaxial view of one pair of detectors at different distances. Given an annihilation event (star), the dotted lines show the first and last tubes of response (TOR) corresponding to a single crystal (shadowed) in the left detector that would 'see' the point source. The dark gray TOR corresponds to the uppermost crystal and the light gray one to the lowest crystal. When the distance between detectors is A, this number of TORs is three (left panel) whereas for a distance of B the number of TORs is eight (right panel).*

Figure 53 shows the effect of erroneous calibration on the resolution of the reconstructed image, for three different distances between detectors (symmetrical misalignment, no COR mismatch). The simulation corresponds to a point source located at 10 mm from the center of the FOV in the central slice. The PSF increases when the actual distance between detectors is underestimated (b and c in Figure 52).

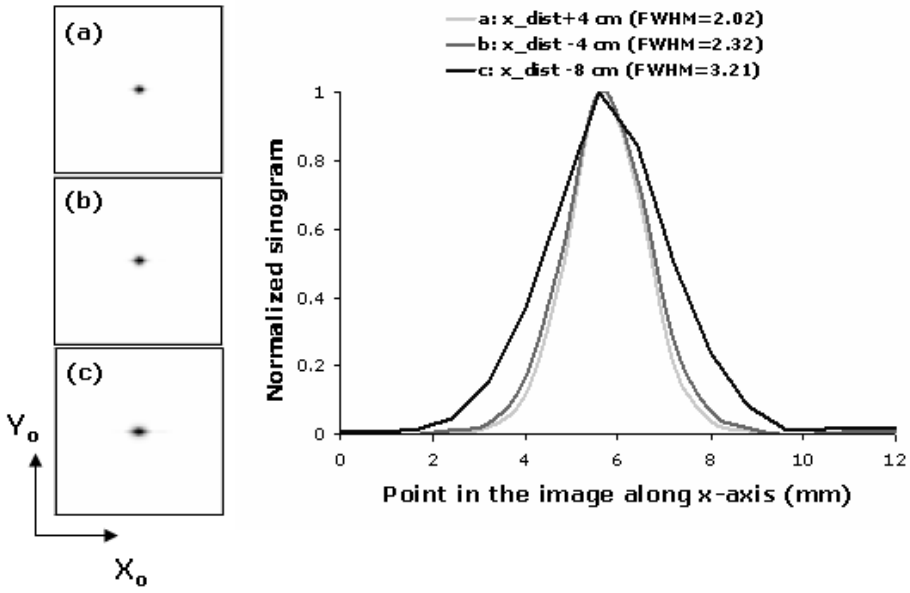

Figure 53. *Effect of an erroneous calibration of the distance between detectors on the resolution of the reconstructed image. Left: Coronal view of a simulated point source for error in the distance between detectors of 4, -4, and -8 cm. Right: Profiles drawn in the reconstructed images along the Xo-axis.*

A summary of the effects and tolerance for the *x*-offset is presented in Table 25 (rows 3 and 4).

4.2.2.4. Misalignment along the z-axis

The effect of erroneous calibration of the position of the detectors along the *z*-axis ('*z*-offset') is an erroneous positioning of the LORs in the axial direction that assigns the counts to an erroneous oblique 2D sinogram. This effect can be observed by tracking the trajectory followed by the planar projection of a point source after rebinning the sinogram data with single-slice rebinning algorithm (SSRB) (span 2). Ideally, the point source should appear at the same position along the *s'*-axis. Thus, the result of adding up all the projections should be a horizontal straight line.

Effect on LOR positioning

To show the effect of this offset, we simulated a complete set of projections of a point source located 24 mm away from the center of the FOV for an ideal system with a detector pixel of 0.4 mm width, for different values of z-offset (Figure 54).

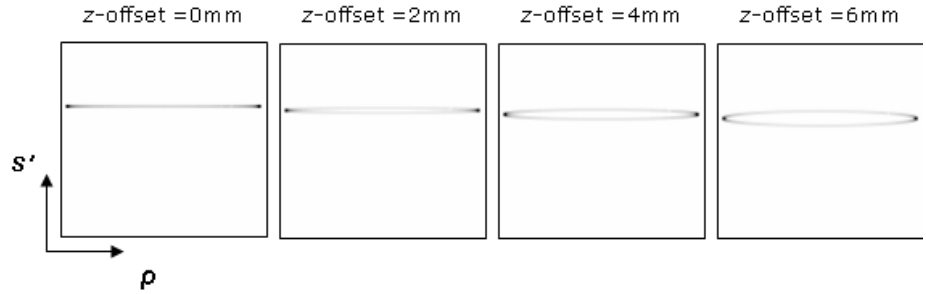

Figure 54. *Sum of projection angles covering 360 degrees for four different z-offsets: note the ellipsoidal trajectory.*

Figure 55 shows that an annihilation event close to the detector will generate projections at 0 and 180 degrees with an axial difference equal to the *z*-offset.

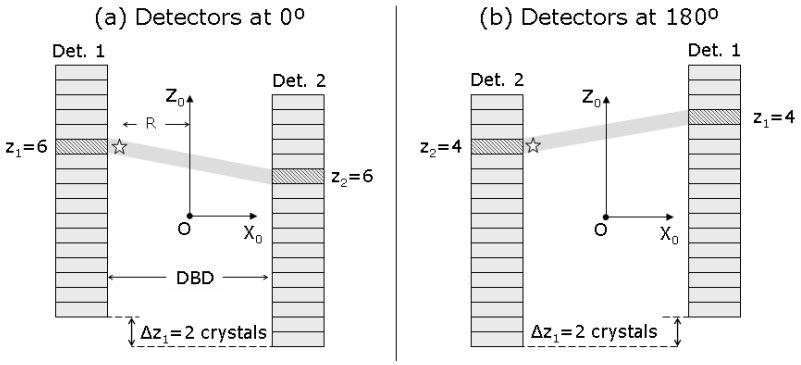

Figure 55. *Axial view of a detector pair at 0 degrees* ***(a)*** *and 180 degrees* ***(b)*** *when there is a z-offset of Δz1 in detector 1. The star represents an annihilation event. When the gantry is at the starting position (a), the 'direct' LOR that contains the event is different from the one at 180 degrees. For this reason, projection at different angles will show the point source at different axial positions.*

For annihilation events originated at a distance *R* from the axis of rotation, we can derive a formula to estimate the *z*-offset, by applying simple trigonometric relations, as follows:

$$\frac{z-offset}{DBD} = \frac{axialdiff}{\left(\frac{DBD}{2}+R\right)} \Rightarrow z-offset = DBD * \frac{axialdiff}{\left(\frac{DBD}{2}+R\right)} \quad \textbf{(62)}$$

where *DBD* is the distance between detectors, *R* is the distance to the COR, and *axialdiff* is the length of the short axis of the ellipsoidal trajectory.

Since the achievable resolution in the projections with the scanner under study is only about 0.8 mm, the ellipsoidal shape of the trajectory is barely visible. Thus, the effect of a *z*-offset in practice will appear as an increase in the FWHM of the profile along the *z*-axis. This increase will only be visible when there is a change in the axial positions of the LORs that requires a z-offset higher than the crystal pitch. A summary of the effects and tolerance for the *z*-offset is presented in Table 25 (row 5).

4.2.2.5. Angular misalignments

As shown in the left panel of Figure 42, the detector may have angular misalignments around the three axes, X_o, Y_o, Z_o.

Effect of slant and tilt

Both slant and tilt, (angular rotations around Y_o and around Z_o), produce the same effect in a system with planar detectors. From Figure 56 we can see that the minimum value of σ that would generate a noticeable effect, i.e. that would change the identification of the crystals involved in the LOR, is given by the equation:

$$\tan(\theta_{\min}) = \frac{pitch}{l/2} \quad \textbf{(63)}$$

where *pitch* is the distance between the center of two adjacent crystals and *l* is the crystal length.

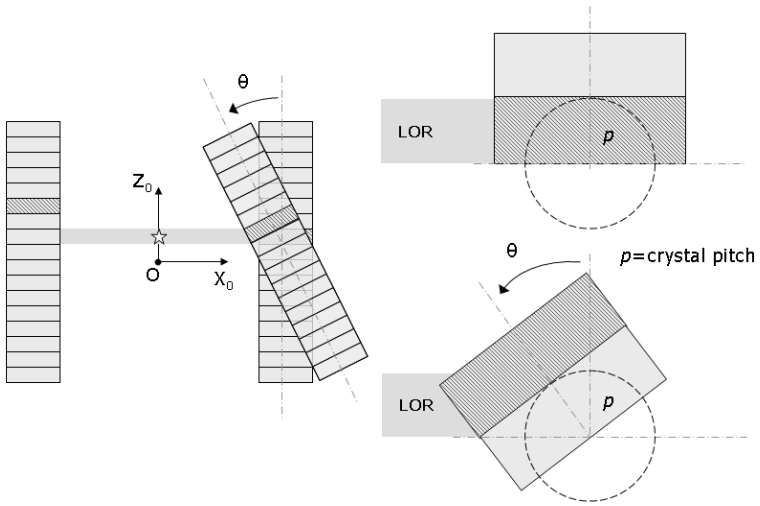

Figure 56. *Minimum detector tilt required to produce a noticeable effect (change in LOR). Left: Axial view of a detector pair with misalignment in σ. The star represents an annihilation event. Right: Zoomed-in view of one detector showing the crystal that detects an annihilation event (shaded) in the ideal position (top) and the real position with misalignment (bottom).*

For the scanner under study, with a crystal pitch of 1.6 mm and l=12 mm, we obtain θ_{min}= 14.9º. Such a large angular error is highly unlikely to be found in real equipment after manufacturing controls.

Effect of skew

In the case of detector skew (rotation around the *x*-axis, ξ in Figure 42), an erroneous pixel assignment results in a loss in *z*-resolution and a visual effect similar to that described for a mismatch of the COR and the geometric center (‘crescent’ shape).

As shown in Figure 57, the effect becomes more severe for peripheral points in the FOV. For the detector pixel shadowed in Figure 57, we can see that the angle that will cause a change in the crystal assignment of the LOR, given by equation (64), is about 4 degrees:

$$\xi_{\min} = \arcsin\left(\frac{pitch}{R - pitch/2}\right) = \arcsin\left(\frac{1.6}{21.9}\right) = 4.2^{o} \qquad \textbf{(64)}$$

Due to the way the detector is attached to the gantry (Figure 42, left), the only angulation that may be relevant in practice is the one around the *z*-axis, which is guaranteed to be much smaller than the calculated $\theta_{\min}$ (14.9 degrees) after the mechanical calibration. Misalignment in the other angles would only be due to the looseness of the crystal matrix inside the detector box, an effect that can be considered negligible (definitely below the minimum values calculated previously). For this reason, angular misalignments of the detector are not taken into account in the calibration algorithm. A summary of the effects and tolerance for the angular misalignments is presented in Table 25 (rows 6, 7, and 8).

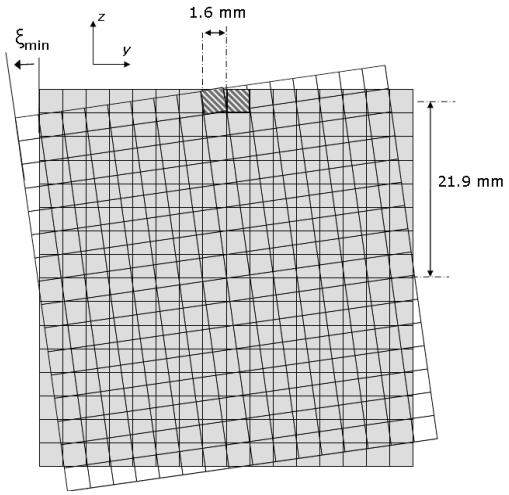

Figure 57. *Rotation of one detector around the x-coordinate.*

4.2.2.6. Summary

Table 25 summarizes our results, indicating the formula for the minimum value necessary to produce a visible effect (what we call 'tolerance') and the value for the particular case of the rPET system studied.

Table 25. *Summary of the study of misalignments. For each misalignment type the table indicates the simulation study used to assess its effect on the sinogram and on the reconstructed image, the tolerance formula (minimum value to produce a noticeable effect) and its value for the particular case of the rPET system.*

Misalignment	Acquisition	Effect on sinogram	Effect on image	Tolerance	Value for the rPET system
y-offset, affecting COR (asymmetrical)	Non-centered point source	Radial gap	Crescent shape	Half pitch size	0.8 mm
y-offset, not affecting COR (symmetrical)	Non-centered point source	Higher FWHM in coronal view	Transaxial resolution loss	Not considered	Not considered
x-offset, affecting COR (asymmetrical)	Centered-FOV point source	Axial gap Center of mass modified Higher FWHM in coronal view	Crescent shape	$\Delta x = \left(R + l/2\right)\left[\frac{1}{\left(N/2 - 1.5\right)}\right]$	7 mm
x-offset, not affecting COR (symmetrical)	Non-centered point source	Higher FWHM in coronal view	Axial and transaxial resolution loss	Not considered	Not considered
z-offset	Any point source	Higher FWHM in sagittal view	Axial resolution loss	Pitch size	1.6 mm
Tilt (along *y*-axis)	Non centered point source	Radial gap	Axial resolution loss	$\theta_{\min} = \arctan\frac{pitch}{(l/2)}$	14.9º
Slant (along *z*-axis)	Any known point source location	Higher FWHM in sagittal view	Crescent shape	$\theta_{\min} = \arctan\frac{pitch}{(l/2)}$	14.9º
Skew	Non-centered point source (both in x-y and z)	Radial gap and higher FWHM in axial view	Transaxial and axial resolution loss	$\xi_{\min} = \arcsin\left(\frac{pitch}{R - pitch/2}\right)$	4.2º

All the misalignments in Table 25 correspond to a single pair of detectors. In a system with more than one pair of detectors, such as the one under study here, there are two additional calibration

parameters to measure: the *z*-offset between detector pairs and the angle between detector pairs (angle Φ_{offset} in Figure 42, right). We did not perform any simulation of these two misalignments, since the procedure to obtain their values is straightforward (explained below).

4.2.3. Calibration algorithm

The results of the presented study enabled us to develop a calibration algorithm to calculate scanner misalignments. The input data for the algorithm are two acquisitions in coincidence list-mode of a small spherical ^{22}Na point source (in our case, 0.3 mm in diameter, encapsulated in a 1-cm^3 epoxy box. In the first acquisition, the source is placed at the center of the FOV ('*centered* acquisition') and in the second one the source is located 11 mm away from that center in the transaxial plane ('*non-centered* acquisition'). Intermediate reconstructions are generated by means of SSRB with span 1, followed by a 2D filtered back-projection (FBP) with a ramp filter. For the rPET scanner, the voxel size of the resulting image is 0.8 mm isotropic. The result of the calibration algorithm is a file containing the misalignment values. This file is used by subsequent reconstructions to generate a corrected sinogram, in which the position of each LOR is relocated according to the actual misalignments. Figure 58 shows a flowchart of the calibration process and the interface of the calibration tool at the end of the process.

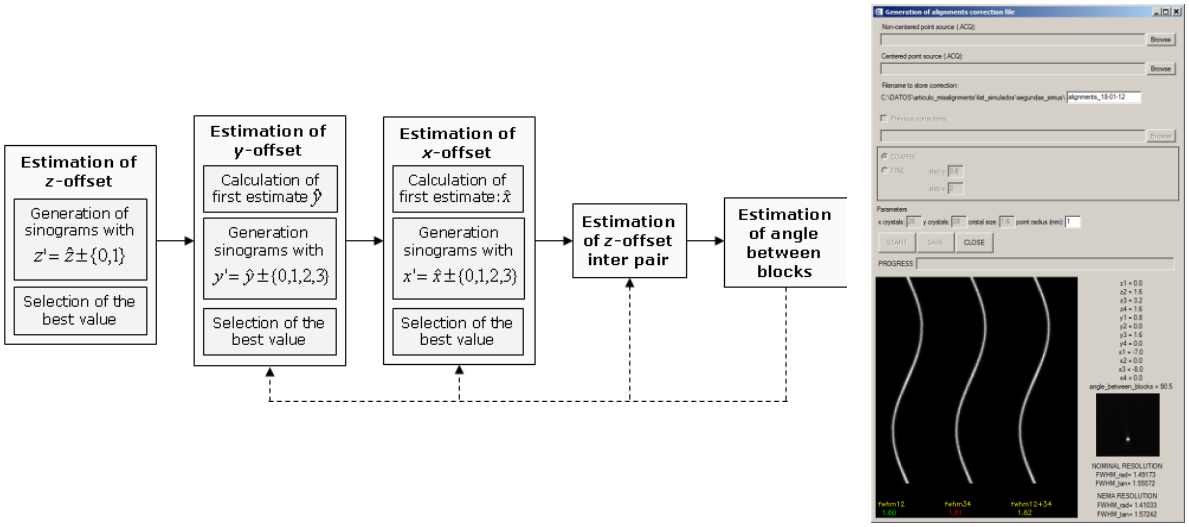

Figure 58. *Flowchart of the calibration algorithm. Dotted lines indicate iterative paths for a fine tuning of the offset values.Left: Interface of the calibration tool at the end of the process showing the sinogram from each pair of detector and the summed sinogram, the misalignment values found, and the resulting resolution.*

For each offset, the program makes a first estimate and guides the user through an interactive tuning procedure. After an initial estimation of all the offsets, in a process called *coarse tuning*, the software offers the user the possibility of performing more iterations of the calibration algorithm using smaller offset values (*fine tuning*) until the result is satisfactory. When this process has finished for all the possible offsets, the final values are stored.

The following subsections present a detailed explanation of the processing performed at each step of the flow chart.

4.2.3.1. Estimation of z-offset

For the measurement of the *z*-offset between the two detectors of a pair, the calibration protocol makes use of the *centered* acquisition and generates sinograms for different values of the detector 1 position along the z-axis, z'_1, as follows:

$$z'_1 = z_1 + a * z\_offset_1 \qquad a = \{0, \pm 1\} \tag{65}$$

where z_1 is the nominal axial position of detector 1 and z_offset_1 is the tentative value for z-offset selected by the user (the default value is the pitch size). The projection data are rebinned into a set of direct sinograms (coordinates (ρ, θ, s')) using SSRB with span 1, and the planar projections for each angle are added together to form an image of 55 × 55 pixels. The optimum $z\text{-offset}_1$ is obtained as the one that yields the lowest FWHM along both the s'-axis and the θ-axis of the rebinned sinogram (Figure 59).

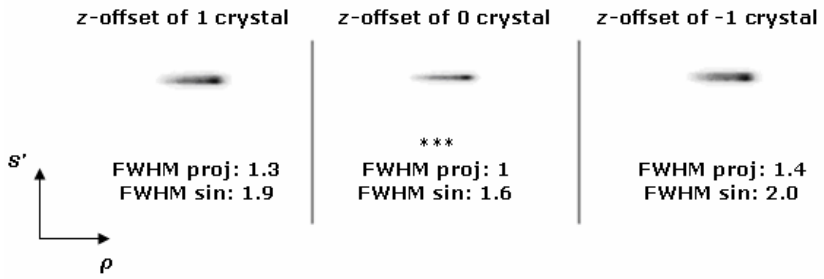

Figure 59. *Images obtained for different of z-offset values in the first detector when adding together the planar projections for every angle of one detector pair*

4.2.3.2. Estimation of y-offset

The *y*-offset was estimated using data from the *non-centered* acquisition. The algorithm generates a first sinogram considering that all offsets but the z-offset, calculated in the previous step, are equal to zero and measures the sinogram radial gap using a procedure explained below for the *gap size* parameter. A first estimation of the *y*-offset is then calculated from this value according to equation (59), and the nominal value is corrected (obtaining $\hat{y}_i$). At this point, the algorithm generates sinograms corresponding to seven different positions of the detectors along the *y*-axis, y'_1 and y'_2, with:

$$y'_i = \hat{y}_i \pm a * step, \qquad a = \{0,1,2,3\} \qquad i = \{1,2\} \tag{66}$$

where the step is chosen by the user (default value is a quarter of the pitch). We define three quality parameters (figures of merit) to guide the selection of the *y*-offset: the *sinogram FWHM*, the *sinusoid fitting score*, and the *gap size*. To obtain the *sinogram FWHM*, the algorithm adds up all the rows in the sinogram (each row represents data at one angle bin, θ) with their center of mass aligned and fits the resulting profile to a Gaussian function. The *sinusoid fitting score* is computed as the mean root square error between the normalized profile given by the trajectory of the center of mass at each θ and an ideal sinusoid. Finally, the algorithm computes the position of the maximum for each angular bin and calculates the distance between the positions of the maximum value for every two consecutive angular bins, obtaining the *gap size* as the mean value of all the distances that are higher than one radial bin (this will correspond to the overlap area in Figure 45a). The most appropriate *y*-offset is selected by the user based on the simultaneous visual inspection of the sinogram and the reconstructed image, as well as on the total of the three values of the figures of merit (Figure 60).

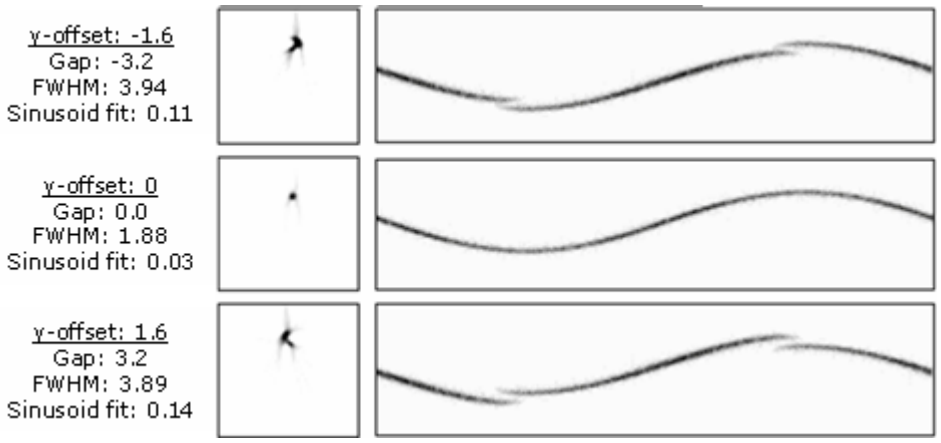

Figure 60. *Estimation of the y-offset. Example of calculated values for 'gap size', 'sinogram FWHM', and 'sinusoid fitting score' (left), reconstructed image (middle), and sinograms (right) for different values of y-offset.*

4.2.3.3. Estimation of x-offset

The calibration protocol estimates the *x*-offset using the *centered* acquisition data. The algorithm generates a sinogram corrected for the offsets already estimated (*z*- and *y*-offset) and provides an initial estimation of the *x*-offset according to equation (61) and the axial *gap size* in the sinogram.

The algorithm then generates sinograms corresponding to seven different positions of detector 1 along the x-axis, x'_1, assuming that position of detector 2 along the *x*-axis is correct (thus, ignoring the symmetrical component), as follows:

$$x'_1 = \hat{x}_1 \pm a * step, \qquad a = \{0,1,2,3\} \qquad i = \{1,2\} \tag{67}$$

where $\hat{x}_1$ is the ideal value corrected with the initial estimate of *x*-offset and the step is chosen by the user (default value is 2 mm).

For each sinogram, the algorithm calculates two figures of merit: the *sinogram FWHM*, explained above, and the deviation of the center of mass shown in Figure 51, right. The selection of the appropriate *x*-offset is made by the user based on the visual inspection of the sinogram, the reconstructed image, and the figures of merit defined, for each tested value.

4.2.3.4. Estimation of z-offset between detector pairs

Once each pair of detectors is corrected for *x*- and *y*-offsets, the calibration algorithm determines the *z*-offset between detector pairs. For each detector pair, the algorithm generates an image by adding up the planar projections for every angle. The z-offset between detector pairs is calculated as the difference between the center of mass along the *z*-axis for each image, as shown in Figure 61.

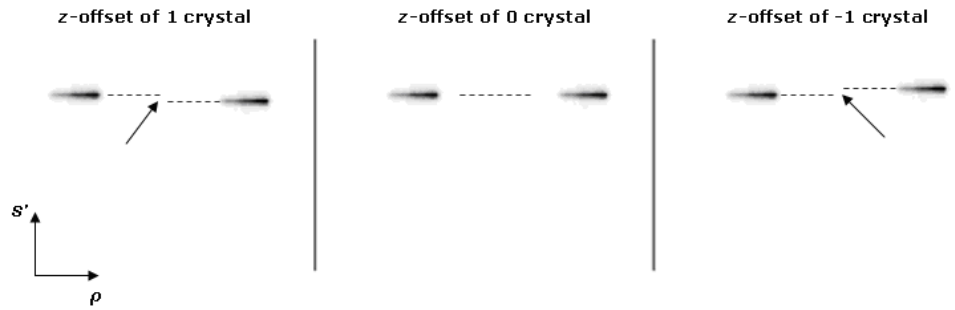

Figure 61. *Images obtained by adding-up the planar projection for every angle of the two detector pairs, for different values of z-offset between detectors.*

4.2.3.5. Estimation of the angle between blocks

The last step is to determine the angle between detector pairs, which theoretically is 90 degrees (angle Φ_{offset} in Figure 42, right). To this end, the algorithm compares the trajectory drawn by the center of mass for every angle bin (θ dimension) of one detector pair with that obtained from other detector pair with different shift values, θ_{shift}. The shift value that leads to the least error (first column in Figure 62), two coincident trajectories (second column in Figure 62), and two coincident sinograms (third column in Figure 62) is selected as the Φ_{offset}.

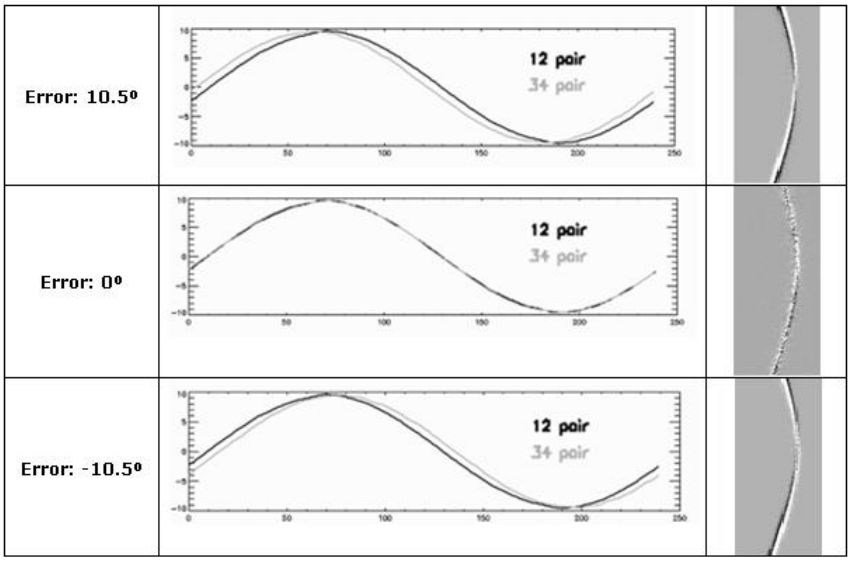

Figure 62. *Center of mass trajectory for each detector pair and difference image of both sinograms. The central row shows the optimum value.*

4.2.4. Evaluation

As mentioned above, the method proposed only detects absolute misalignments, without discriminating if it was produced by one or both detectors within the pair. We estimated the effect of the uncertainty provided by the method on the relative misalignment of each single detector by using the Hot Derenzo Phantom simulation described before (with and without misalignments). The simulation cases are described in Table 26. All the misalignments were properly corrected except

those listed in column 3. For each case we computed the root mean square error (RMSE) inside the FOV relative to the maximum value of the image without misalignments. The analysis was performed by adding up 45 slices of the reconstructed image.

Table 26. *Results on reconstructed images from the Hot Derenzo Phantom simulation. For each case the table indicates a brief description of the analyzed image, the estimated misalignment values used in the reconstruction, and the computed MSE relative to the image without misalignments.*

Study name	Description	Estimated misalignments (mm)	Relative MSE (%)
Without misalignments	No misalignments were simulated	---	0.0
Without any correction	None of the misalignments were corrected	No corrections	11.2
No x-y correction (pair 1)	Misalignments in detector pair 1 (detectors 1 and 2) were not corrected	No correction in pair 1: $\Delta x_1 = 0.0$, $\Delta x_2 = 0.0$, $\Delta y_1 = 0.0$, $\Delta y_2 = 0.0$	7
Misalignments corrected	All the misalignments were corrected	---	2.4
x corrected – y (opt 1)	Equivalent correction (option 1) for Δy_1 and Δy_2 (pair 1)	Equivalent correction (opt 1): $\Delta y_1 = -0.8$, $\Delta y_2 = 0.8$	2.6
x corrected - y (opt 2)	Equivalent correction (option 2) for Δy_1 and Δy_2 (pair 1)	Equivalent correction (opt 2): $\Delta y_1 = 0.0$, $\Delta y_2 = -1.6$	2.9
y corrected - x (opt 1)	Equivalent correction (option 1) for Δx_1 and Δx_2 (pair 1)	Equivalent correction (opt 1): $\Delta x_1 = -2.5$, $\Delta x_2 = 2.5$	2.4
y corrected - x (opt 2)	Equivalent correction (option 2) for Δx_1 and Δx_2 (pair 1)	Equivalent correction (opt 2): $\Delta x_1 = -5.0$, $\Delta x_2 = 0.0$	2.4
x (opt 1) - y (opt 1)	Equivalent correction (option 1) for Δx_1, Δx_2, Δy_1 and Δy_2 (pair 1)	Equivalent correction (opt 1): $\Delta x_1 = -2.5$, $\Delta x_2 = 2.5$ $\Delta y_1 = -0.8$, $\Delta y_2 = 0.8$	2.7

We can see that the relative RMSE decreases when the exact correction of the misalignments is applied, with no significant changes between the different equivalent corrections in x and y coordinates (or both of them) and the exact one. The highest deviations obtained were at the edge of the transaxial FOV because the misalignments can change the ideal FOV hindering the correct visualization of some structures at the edge. However, these errors are not so critical in pre-clinical studies in which usually no important structures are placed at the edge of the FOV. These results show that an equivalent correction in x and y coordinates does not affect to the final quality of the image. Nevertheles, we can see important differences in the case where the misalignments were not corrected.

The same effect is observed when studying image profiles along a row of rods of 1.6 mm on the Hot Derenzo Phantom images, plotted in Figure 63. Important differences are present when the misalignments are not corrected (as expected, as more misalignments uncorrected, the greater the error) and no significant differences between all the equivalent cases studied.

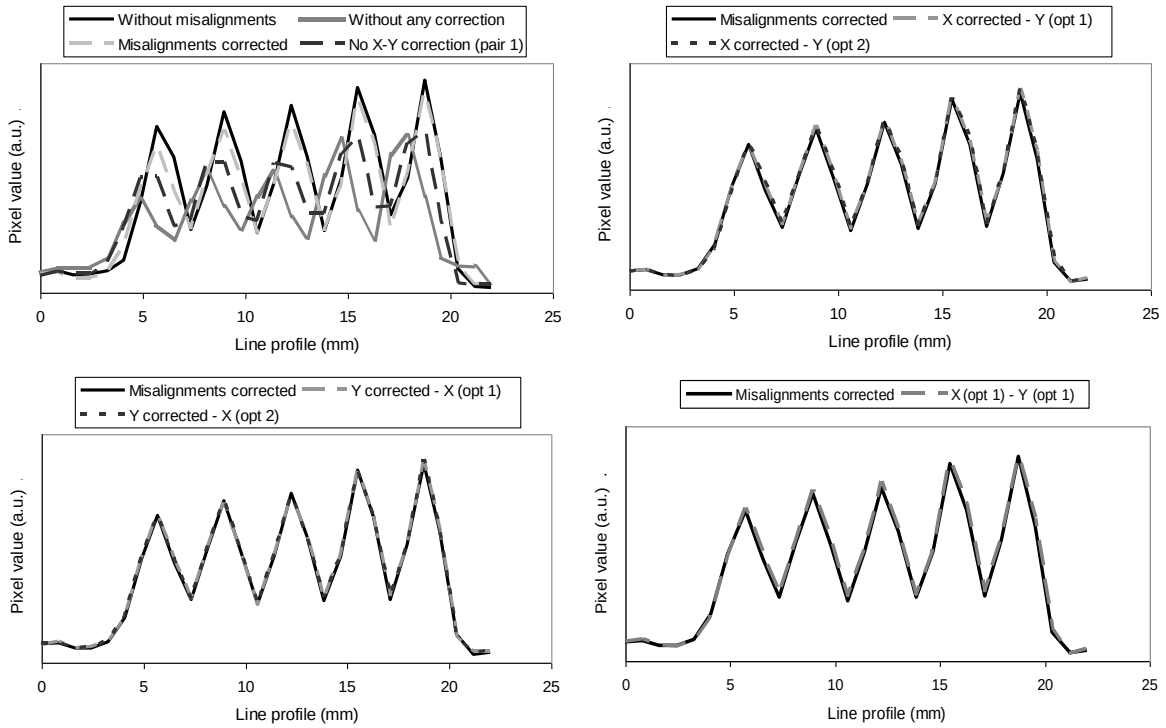

Figure 63. *Profiles along a row of rods of 1.6 mm on the Hot Derenzo Phantom images with different corrections.*

To evaluate the performance of the proposed tool four users performed the calibration of three simulated situations, described by the misalignments given in Table 27.

Table 27. *Misalignment values for the three cases simulated to evaluate the performance of the proposed tool. Each case consists of two studies, one is non-centered point source and the other one is a point source in the center of the field of view.*

Misalignment	Case 1	Case 2	Case 3
offset_tube1_y (mm)	1.0	0.0	0.0
offset_tube2_y (mm)	0.0	2.0	1.6
offset_tube3_y (mm)	0.8	1.8	0.8
offset_tube4_y (mm)	-0.8	-0.8	-0.8
offset_tube1_z (mm)	0.0	0.0	0.0
offset_tube2_z (mm)	1.6	-2.0	0.0
offset_tube3_z (mm)	3.2	3.0	0.0
offset_tube4_z (mm)	1.6	0.0	0.0
offset_tube1_x (mm)	0.0	-10.0	0.0
offset_tube2_x (mm)	7.0	0.0	5.0
offset_tube3_x (mm)	-3.0	5.0	2.5
offset_tube4_x (mm)	5.0	-5.0	-2.5
angle_between_blocks (degrees)	88.0	91.0	88.0

The results showed an absolute error of under the tolerance value for each parameter when using only one iteration of the algorithm. The complete results are given in Table 28.

Table 28. *Mean error for each parameter in each case given in table 3 and total mean and standard deviation of the errors*

Misalignment	Case 1	Case 2	Case 3	Mean error	Std. Dev.
y-error (mm)	0,15	0,57	0,48	0,40	0,22
x-error (mm)	0,38	0,83	2,00	1,07	1,06
z-error (mm)	0,00	0,90	0,00	0,30	0,49
angle_between_blocks (degrees)	0,5	0,5	0,25	0,42	0,3

4.2.5. Conclusions

We have presented a detailed study of the effect on the image and data quality of mechanical misalignments in PET scanners based on rotating planar detectors. Our results enabled us to propose a robust, easy-to-perform calibration protocol that makes use of simple phantoms to measure misalignments. Although numerous works analyze this problem for CT and SPECT systems, information on parallel-beam geometry is scant and only aimed at obtaining the COR.

We have analyzed the effect on reconstructed image quality of the six main misalignment parameters that can exist in a real scanner and conclude that only the linear misalignments along the three axes of the scanner have a relevant effect in practice. This is due to the fact that the minimum tilt errors that would produce any effect in the image are clearly larger than those that would reasonably remain after manufacture. We have developed a software tool to generate an offset error file, which can be used during subsequent reconstructions to correct the misalignments. Although an iterative reconstruction algorithm could be used, since the calibration process includes several reconstructions, we use FBP to optimize timing. We do not expect to find differences in the calibration with the proposed method since it is mainly based on sinogram measurements. The evaluation of the proposed calibration tool has shown small errors, well under acceptable tolerances in each geometrical parameter.

The procedure has been incorporated into the software of the commercial rPET system [Vaquero *et al.*, 2005a]. The method can be easily adapted to similar geometries, as Yap-PET [Del Guerra *et al.*, 1998] and ClearPET [Mosset *et al.*, 2004, Khodaverdi *et al.*, 2005] scanners. We demonstrated its versatility in [Lage *et al.*, 2009].

Our results highlight the importance of the characterization of detector misalignment: an error of 0.8 mm in the assumed position of a detector results in an increase of 14% in the tangential FWHM of a point source at the center of the FOV. Besides loss of resolution, misalignment errors also produce artifacts that result in severe degradation of the reconstructed image.

4.3. Attenuation correction of PET images using CT data in the small animal PET scanner Argus PET/CT

Attenuation correction is an important correction required for quantitative analysis of PET. Although the magnitude of this correction for small animal subjects is much smaller than in humans [Chow *et al.*, 2002], it is important to correct the data for quantitative analysis of the tracer distribution [Kinahan *et al.*, 2003].

There are several methods to correct for attenuation in PET [Kinahan *et al.*, 2003, Zaidi *et al.*, 2004]. The material properties of the object/subject can be obtained using transmission images, which can be acquired either with a PET or an x-ray CT scanner. For PET transmission, the source is usually a gamma-emitter isotope (^{137}Cs for example) while for CT transmission, the source is an X-ray tube.

Even though the transmission image obtained using ^{137}Cs source provides a good overview of the structure, the quality of the attenuation correction obtained can be improved further by using an image obtained from a CT scanner [Chow *et al.*, 2002]. The potential benefits of using CT based attenuation correction method over the PET based method include: (a) Lower statistical noise in transmission images acquired on CT versus PET, since the photon flux is higher; (b) availability of high quality anatomical information; (c) faster acquisitions; (d) less background due to the radioactivity injected to the patient; (e) transmission scan using PET scanner requires handling of radioactive source. On the other hand, using CT images to correct the attenuation in PET requires an energy scaling since the attenuation depends on the photon energy besides on the material properties of the object/subject [Valk *et al.*, 2006, Kinahan *et al.*, 1998].

In this section we describe a procedure to correct the attenuation based on a CT image for the SEDECAL Argus PET/CT scanner described in chapter 2, section 2.2. The images are reconstructed using FIRST code (see chapter 2, section 2.4), but the correction can be used with any other reconstruction method [Vicente *et al.*, 2010b].

4.3.1. Materials & Methods

4.3.1.1. Mathematical description of the attenuation

The transmission of the photons through the matter can be characterized with the linear attenuation coefficient, μ. This coefficient depends on the photon energy E and the atomic number of the material. A well-collimated mono-energetic beam with an input intensity of I_0 passing through a length of material along any desired line of response (LOR) has an output intensity I of [Valk *et al.*, 2006]:

$$I = I_0 \cdot e^{-\int_{LOR} \mu(x,E)dx} \quad \textbf{(68)}$$

It can be seen from eq. (68) that the photon fraction transmitted through a tissue depends on its attenuation coefficient and the length of the trajectory.

For PET scanning of homogenous material (μ), the detection probability ($P = I/I_0$) of coincidental photon pair is:

$$P = e^{-\mu x} \cdot e^{-\mu(D-x)} = e^{-\mu D} \quad \textbf{(69)}$$

where D is the material thickness. Note that the probability that both photons will reach the detector is independent of the source location along the line of response (Figure 64).

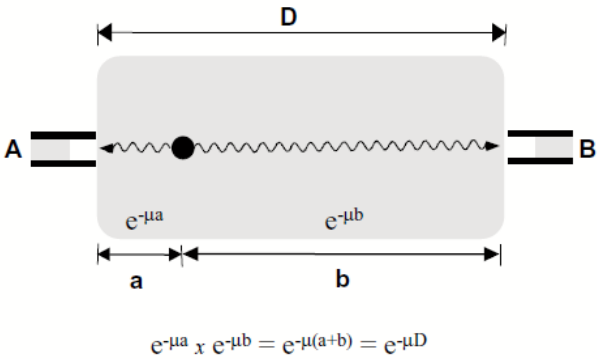

Figure 64. *Probability that both photons of a PET coincidence will reach the detectors (A and B), separated a distance D.*

4.3.1.2. Attenuation correction based on a CT image

CT image is a map of the effective linear attenuation coefficient, μ(E), at each point in the body, and represented as CT numbers in Hounsfield units (HU)

$$HU = \left(\frac{\mu(E)}{\mu_{H_2O}(E)} - 1 \right) \cdot 1000 \qquad \textbf{(70)}$$

The transformation of the CT attenuation coefficient μ(CT) (energies of tens of keV) to μ(PET) (511 keV) is not completely straightforward. This is because the mechanism of attenuation is different for energies around 511 keV (with higher probability of Compton) and low energies (where, besides the Compton scatter, photoelectric absorption and Rayleigh scatter are important contributions as well) [Valk *et al.*, 2006].

There are several methods to perform this transformation, from the simplest based on a linear transformation using the attenuation coefficient of water (similar to soft tissue) to the most elaborate using a detailed segmentation of different tissue types.

In this work we have computed the transformation with a bilinear approximation from the HU values of air, water and bone (cortical) and the corresponding linear attenuation coefficients (μ) for photons of 511 keV (Kinahan et al., 1998). The attenuation value for any other material is estimated using this bilinear transformation and its corresponding HU value (Figure 65).

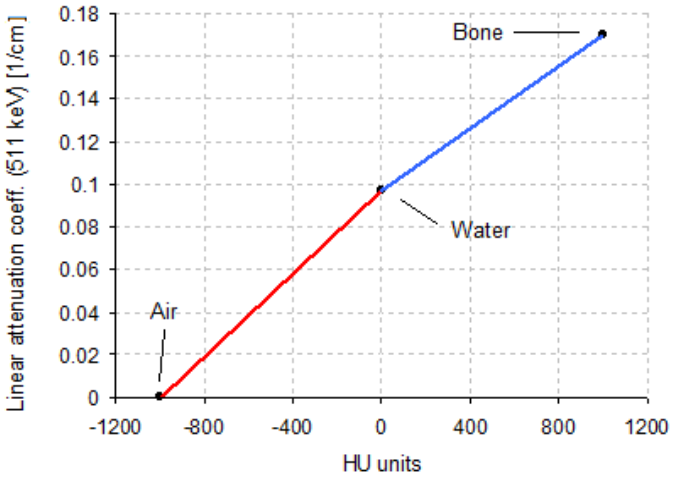

Figure 65. *Bilinear approximation to compute the linear attenuation coefficients.*

4.3.1.3. Application of the attenuation correction

The attenuation correction is applied to data before reconstructing the PET images. To carry out the correction, the attenuation map is forward projected to get the attenuation correction factor (ACF) for each LOR:

$$ACF = e^{\int_{LOR} \mu(x,E)dx} \tag{71}$$

The correction is accomplished by multiplying by the ACF of each LOR the data on the same LOR.

4.3.1.4. Data acquisition and processing

Both acquisitions, PET and CT, were performed using the multimodality scanner Sedecal Argus PET/CT [Wang *et al.*, 2006b, Vaquero *et al.*, 2008] described in chapter 2, section 2.2. Figure 66 shows a simplified workflow with the necessary steps to correct attenuation in the Argus scanner using CT images.

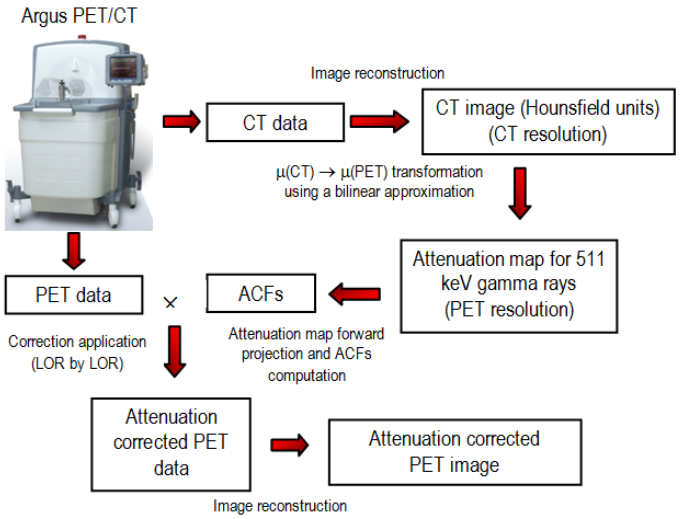

Figure 66. *Workflow for the attenuation correction using CT images for the SEDECAL Argus PET/CT.*

Several phantom studies were performed for validation purposes. In this work we show, as an example, an acquisition of the NEMA Image quality phantom (more details of the phantom can be found in Appendix A). The phantom was filled with ^{18}F except for two small cylindrical cavities (diameter: 8 mm). One of them was filled with water, and the second one remained empty. The reconstruction was carried out with FIRST [Herraiz *et al.*, 2006a] with 1 iteration and 50 subsets.

For the Argus scanner, FIRST code includes an attenuation correction of a FOV-sized water cylinder by default. This default correction is an initial approximation since it does not take into account the different materials and their distribution in the FOV. In this work we compare the results of this default correction with the one that we get with a more accurate correction based on a CT image.

The χ^2 is a useful parameter in order to verify if the applied corrections or improvement in a reconstruction algorithm allow for a better description of the data. This quantity is defined as:

$$\chi^2 = \frac{1}{(N_L - N_V)} \sum_{i=1}^{N_L} \frac{(Y_i - y_i)^2}{Y_i} \qquad \textbf{(72)}$$

where N_L is the number of LORs (independent data acquired), N_V is the number of voxels in the image, being (N_L - N_V) the degrees of freedom, Y_i is the number of counts per LOR, and y_i represents the estimated data, that is, the projection of the object recovered by the reconstruction. High values of χ^2 imply a disagreement between the estimation and the data and point out inaccuracies in the system model, failures in the system (a detector not working properly, for instance) and/or some effects not considered in the reconstruction [Herraiz *et al.*, 2006a].

4.3.2. Results

Figure 67 (top-left) shows the attenuation map for the NEMA Image quality phantom that we got using the CT image. This map was used to get the ACFs. The second image in Figure 67 is the PET image with the default attenuation correction, and the next one (top-right) shows the PET image with the attenuation correction based on the CT image.

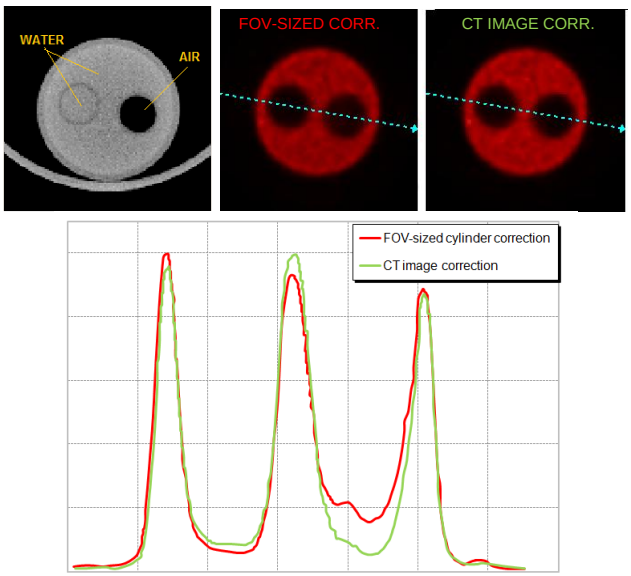

Figure 67. *NEMA QC phantom analysis. Top, from left to right: Attenuation map obtained from the CT image, PET image with attenuation correction based on a FOV-sized water cylinder, and PET image with attenuation correction based on the CT image. Bottom: Normalized profiles through the blue line drawn in the PET images.*

The two PET images do not seem to differ significantly to the naked eye, but we can see in a profile (Figure 67, bottom) through the two small cylindrical cavities (blue dashed line on the PET images) that there are differences in the air region. If the attenuation correction does not take into account the different materials in the phantom (as the default correction does, when no CT image is available), the result is an excess of counts in the air region. The attenuation correction based on the CT image corrects this problem and after applying it, the two cold regions have a similar number of counts.

Figure 68 plots the χ^2 evolution with the number of image updates (number of subsets). We can see that the attenuation correction based on the CT image reduces sizeably the χ^2 parameter. This indicates that the attenuation correction improves the consistency between the reconstructed image and the acquired data.

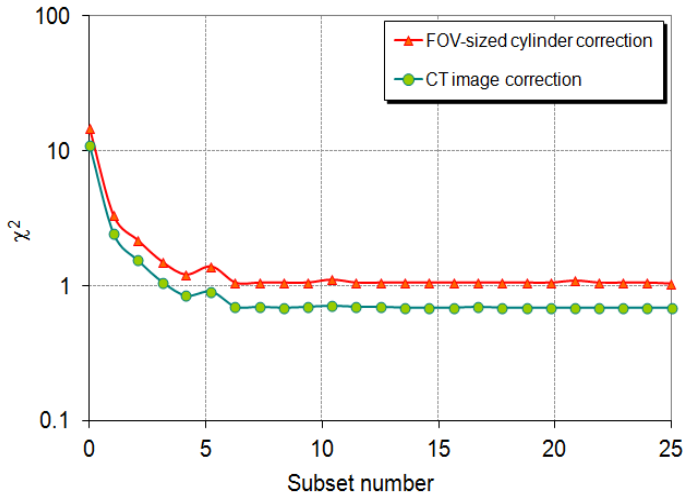

Figure 68. *χ^2 evolution with the number of image updates.*

Finally, since the procedure has been incorporated into the software of the commercial Argus PET/CT system, we present in Figure 69 a few screenshots of the 3D-OSEM user console to show how easy is to perform the correction for a final user. First of all, the user needs to select, in the 'upload' menu (Figure 69A), the acquisition file using the 'browse' button. (Figure 69B, 'Acquisition file to be reconstructed' label). After that, the user has to select the attenuation map using the 'browse' button (Figure 69C, 'Attenuation file map' label). If no attenuation map is selected, the default correction (FOV-sized water cylinder) will be applied.

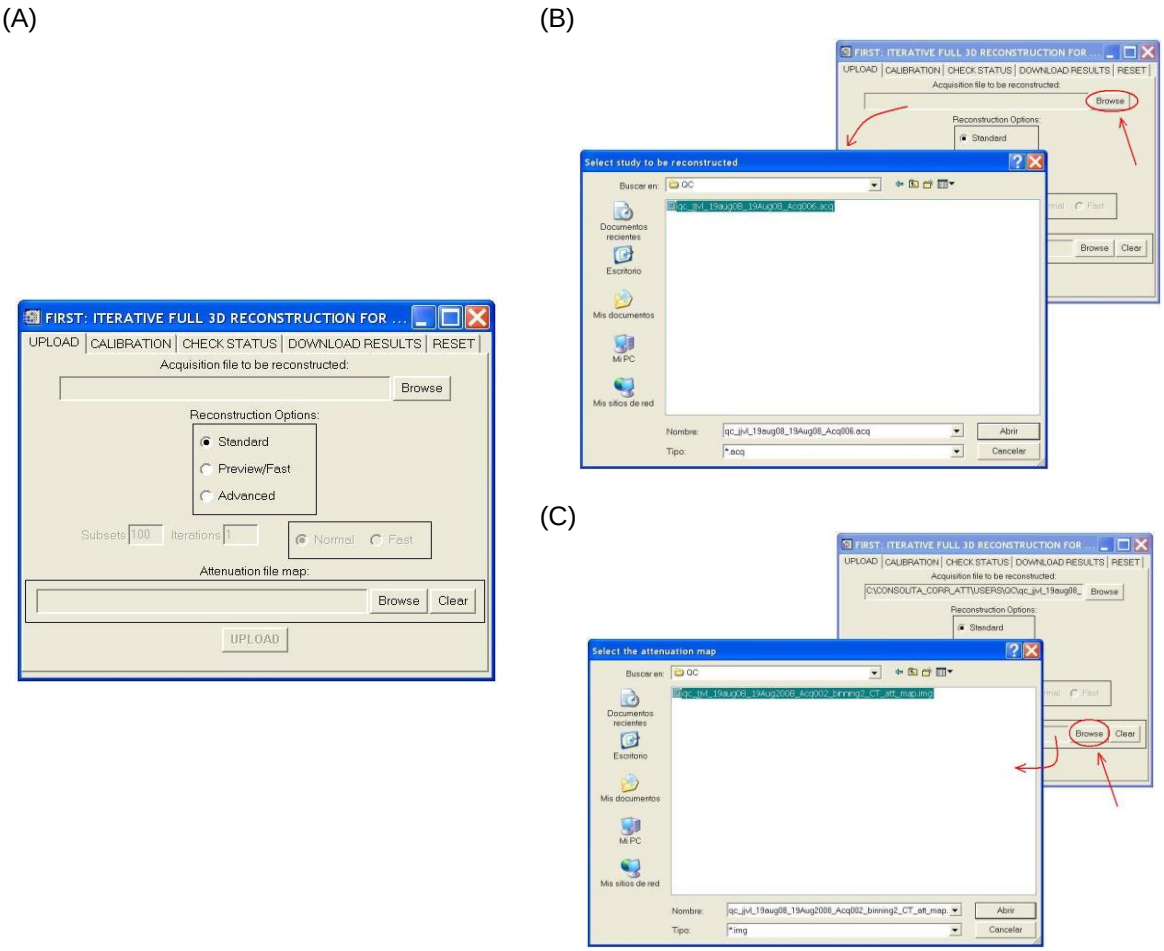

Figure 69. *Screenshots of the 3D-OSEM user console incorporated in the commercial Argus PET/CT*

4.3.3. Conclusions

PET data are affected by attenuation which reduces the number of photons detected in each line of response (LOR). Nowadays, attenuation correction based on CT images is the most practical method due to the availability of high quality CT images with the low acquisition time.

In this work we have compared a simple attenuation correction method based on a FOV-sized water cylinder with a more accurate method based on CT images. The attenuation correction based on CT images not only provides a better quantification, but also reduces the χ^2 parameter, what means a better consistency between the reconstructed image and the acquired data. The procedure has been incorporated into the software of the commercial Argus PET/CT system.

4.4. References

Abella, M., Vaquero, J., Soto-Montenegro, M., Lage, E. & Desco, M. 2009. Sinogram Bow-Tie Filtering in FBP PET Reconstruction. *Med. Phys.,* 36**,** 1663-71.

Abella, M., Vaquero, J. J., Vicente, E., Álvarez, J., Lage, E. & Desco, M. 2006. Effect of misalignments in small animal PET scanners based on rotating planar detectors. *Mol. Ima. Biol.,* 8**,** 75-6.

Abella, M., Vicente, E., Rodríguez-Ruano, A., España, S., Lage, E., Desco, M., Udias, J. M. & Vaquero, J. J. 2012. Misalignments calibration in small-animal PET scanners based on rotating planar detectors and parallel-beam geometry. *Phys Med Biol (Submitted)*.

Azevedo, S. G., Schneberk, D. J., Fitch, J. P. & Martz, H. E. 1990. Calculation of the rotational centers in computed tomography sinograms. *Nuclear Science, IEEE Transactions on,* 37**,** 1525-1540.

Badawi, R. D. & Marsden, P. K. 1999b. Self-normalization of emission data in 3D PET. *IEEE Transactions on Nuclear Science,* 46**,** 709-712.

Badawi, R. D., Miller, M. P., Bailey, D. L. & Marsden, P. K. 1999. Randoms variance reduction in 3D PET. *Phys Med Biol,* 44**,** 941-54.

Bendriem, B. & Townsend, D. W. 1998. The theory and practice of 3D PET. Kluwer Academic.

Beque, D., Nuyts, J., Bormans, G., Suetens, P. & Dupont, P. 2003. Characterization of pinhole SPECT acquisition geometry. *IEEE Trans. Med. Imaging,* 22**,** 599–612.

Brasse, D., Kinahan, P. E., Lartizien, C., Comtat, C., Casey, M. & Michel, C. 2005. Correction methods for random coincidences in fully 3D whole-body PET: impact on data and image quality. *J Nucl Med,* 46**,** 859-67.

Busemann-Sokole, E. 1987. Measurement of collimator hole angulation and camera head tilt for slant and parallel-hole collimators used in SPECT. *J. Nucl. Med.,* 28**,** 1592–8.

Casey, M. E. & Hoffman, E. J. 1986. Quantitation in positron emission computed tomography: 7. A technique to reduce noise in accidental coincidence measurements and coincidence efficiency calibration. *J Comput Assist Tomogr,* 10**,** 845-50.

Cherry, S. R., Sorenson, J. A. & Phelps, M. E. 2003. *Physics in nuclear medicine,* Saunders.

Chow, P. L., Rannou, R. & Chatziioannou, A. 2002. Attenuation correction for a 3D small animal PET tomograph, using x-ray microCT. *Mol. Imag. Biol.,* 4**,** S17–S18.

Daube-Witherspoon, M. E. & Carson, R. E. 1991. Unified deadtime correction model for PET. *IEEE Trans Med Imaging,* 10**,** 267-75.

Del Guerra, A., Di Domenico, G., Scandola, M. & Zavattini, G. 1998. YAP-PET: first results of a small animal positron emission tomograph based on YAP:Ce finger crystals. *Nuclear Science, IEEE Transactions on,* 45**,** 3105-3108.

Donath, T., Beckmann, F. & Schreyer, A. 2006. Automated determination of the center of rotation in tomography data. *J. Opt. Soc. Am.,* 23**,** 1048-1057.

Eriksson, L., Wienhard, K. & Dahlbom, M. 1994 A simple data loss model for positron camera systems. *IEEE Transactions on Nuclear Science,* 41**,** 1566 - 1570

España, S., Herraiz, J. L., Vicente, E., Vaquero, J. J., Desco, M. & Udias, J. M. 2009. PeneloPET, a Monte Carlo PET simulation tool based on PENELOPE: features and validation. *Phys Med Biol,* 54**,** 1723-42.

Furrer, M., Gostely, J. J. & Lerch, P. 1984. Timing problems due to pile-up in coincidence counting. *Nuclear Instruments and Methods in Physics Research Section A: Accelerators, Spectrometers, Detectors and Associated Equipment,* 226**,** 455-462.

Germano, G. & Hoffman, E. J. 1988. Investigation of count rate and deadtime characteristics of a high resolution PET system. *J Comput Assist Tomogr,* 12**,** 836-46.

Germano, G. & Hoffman, E. J. 1990. *A study of data loss and mispositioning due to pileup in 2-D detectors in PET.*

Germano, G. & Hoffman, E. J. 1991. An investigation of methods of pileup rejection for 2-D array detectors employed in high resolution PET. *IEEE Trans Med Imaging,* 10**,** 223-7.

Gullberg, G. T., Tsui, B. M. W., Crawford, C. R., Ballard, J. G. & Hagius, J. T. 1990. Estimation of geometrical parameters and collimator evaluation for cone beam tomography. *Med. Phys.,* 17**,** 264–72.

Gullberg, G. T., Tsui, B. M. W., Crawford, C. R. & Edgerton, E. 1987. Estimation of geometrical parameters for fan-beam tomography. *Phys. Med. Biol.,* 32**,** 1581–94.

Herraiz, J. L., Espana, S., Vaquero, J. J., Desco, M. & Udias, J. M. 2006a. FIRST: Fast Iterative Reconstruction Software for (PET) tomography. *Phys Med Biol,* 51**,** 4547-65.

Hoffman, E. J., Phelps, M. E. & Huang, S. C. 1983. Performance evaluation of a positron tomograph designed for brain imaging. *J Nucl Med,* 24**,** 245-57.

Hsieh, Y.-L. 1992. *Calibration of fan-beam geometry for single photon emission computed tomography.* University of Utah.

Imperiale, C. & Imperiale, A. 2001. On nuclear spectrometry pulses digital shaping and processing. *Measurement,* 30**,** 49-73.

Jagoda, E. M., Vaquero, J. J., Seidel, J., Green, M. V. & Eckelman, W. C. 2004. Experiment assessment of mass effects in the rat: implications for small animal PET imaging. *Nuclear Medicine and Biology,* 31**,** 771-9.

Khodaverdi, M., Weber, S., Streun, M., Parl, C., Larue, H., Brandenburg, G., Bauer, A., Dehnhardt, M., Auffray, E., Boutemeur, M., Bruyndonckx, P., Choi, Y., D'Asseler, Y., Devroede, O., Dujardin, C., Fedorov, A., Heinrichs, U., Janier, M., Jung, J. H., Korjik, M., Krieguer, M., Largeron, G., Lartizien, C., Lecoq, P., Lemaitre, C., Leonard, S., Loude, J. F., Morel, C., Mosset, J. B., Pedrini, C., Petrosyan, A. G., Rey, M., Sappey-Marinier, D., Roldan, P. S., Simon, L., Song, T. Y., Staelens, S., Tavernier, S., Trummer, J., Van Holen, R., Vieira, J. M., Wieers, E., Wisniewska, M., Wisniewski, D., Wu, Y., Pietrzyk, U. & Ziemons, K. 2005. High resolution imaging with ClearPET™ Neuro - first animal images. *In:* Nuclear Science Symposium Conference Record, 2005 IEEE,

23-29 Oct. 2005 2005. 4 pp.
Kinahan, P. E., Hasegawa, B. H. & Beyer, T. 2003. X-ray-based attenuation correction for positron emission tomography/computed tomography scanners. *Semin Nucl Med,* 33**,** 166-79.
Kinahan, P. E., Townsend, D. W., Beyer, T. & Sashin, D. 1998. Attenuation correction for a combined 3D PET/CT scanner. *Med Phys,* 25**,** 2046-53.
Knoll, G. F. 2000. *Radiation detection and measurement / Glenn F. Knoll,* New York :, Wiley.
Lage, E., Vaquero, J. J., Sisniega, A., Espana, S., Tapias, G., Abella, M., Rodriguez-Ruano, A., Ortuno, J. E., Udias, A. & Desco, M. 2009. Design and performance evaluation of a coplanar multimodality scanner for rodent imaging. *Phys Med Biol,* 54**,** 5427-41.
Lecomte, R. 2004. Technology challenges in small animal PET imaging. *Nucl. Instrum. Meth. Phys. Res. A,* 527**,** 157-165.
Lewis, J. S. & Achilefu, S. 2002. Small Animal Imaging: Current Technology and Perpectives for Oncological Imaging. *Eur. J. Cancer,* 38**,** 2173-88.
Mankoff, D. A., Muehllehner, G. & Karp, J. S. 1989. The high count rate performance of a two-dimensionally position-sensitive detector for positron emission tomography. *Phys Med Biol,* 34**,** 437-56.
Massoud, T. F. & Gambhir, S. S. 2003. Molecular imaging in living subjects: seeing fundamental biological processes in a new light. *Gene. Dev.,* 17**,** 545-80.
Mazoyer, B. M., Roos, M. S. & Huesman, R. H. 1985. Dead time correction and counting statistics for positron tomography. *Phys Med Biol,* 30**,** 385-99.
Mosset, J. B., Devroede, O., Krieguer, M., Rey, M., Vieira, J. M., Jung, J. H., Kuntner, C., Streun, M., Ziemons, K., Auffray, E., Sempere-Roldan, P., Lecoq, P., Bruyndonckx, P., Loude, J. F., Tavernier, S. & Morel, C. 2004. Development of an optimised LSO/LuYAP phoswich detector head for the ClearPET camera. *In:* Nuclear Science Symposium Conference Record, 2004 IEEE, 16-22 Oct. 2004 2004. 2439-2443 Vol. 4.
Noo, F., Clackdoyle, R., Mennessier, C., White, T. A. & Roney, T. J. 2000. An analytic method based on identification of ellipse parameters for scanner calibration in conebeam tomography. *Phys. Med. Biol.,* 45**,** 3489-3508.
Pierce, L., Miyaoka, R., Lewellen, T., Alessio, A. & Kinahan, P. 2009. Determining Block Detector Positions for PET Scanners. *IEEE Nucl. Sci. Symp. Conf. Rec.*
Pomper, M. G. 2001. Molecular Imaging: and Overview. *Acad. Radiol.,* 8**,** 1141-53.
Seidel, J., Wenze, X., Kakareka, J. W., Pohida, T. J., Green, M. V. & Choyke, P. L. 2010. A positron projection imager for whole-body mouse imaging. *In:* Nuclear Science Symposium Conference Record (NSS/MIC), 2010 IEEE, Oct. 30 2010-Nov. 6 2010 2010. 2206-2209.
Sjöland, K. A. & Kristiansson, P. 1994. Pile-up and defective pulse rejection by pulse shape discrimination in surface barrier detectors. *Nuclear Instruments and Methods in Physics Research Section B: Beam Interactions with Materials and Atoms,* 94**,** 333-337.
Smith, R. J., Karp, J. S. & Muehllehner, G. 1994. The countrate performance of the volume imaging PENN-PET scanner. *IEEE Trans Med Imaging,* 13**,** 610-8.
Stearns, C. W., Chesler, D. A., Kirsch, J. E. & Brownell, G. L. 1985. Quantitative Imaging with the MGH Analog Ring Positron Tomograph. *IEEE Transactions on Nuclear Science,* 32**,** 898-901.
Stearns, C. W., McDaniel, D. L., Kohlmyer, S. G., Arul, P. R., Geiser, B. P. & Shanmugam, V. 2003. Random coincidence estimation from single event rates on the Discovery ST PET/CT scanner. *In:* Nuclear Science Symposium Conference Record, 2003 IEEE, 19-25 Oct. 2003 2003. 3067-3069 Vol.5.
Sun, Y., Hou, Y. & Hu, J. 2007. Reduction of Artifacts Induced by Misaligned Geometry in Cone-Beam CT. *IEEE Trans. Bio. Eng.,* 54**,** 1461-71.
Thompson, C. J. & Meyer, E. 1987. *The effect of live time in components of a positron tomograph on image quantification*.
Valk, P. E., Delbeke, D. & Bailey, D. L. 2006. *Positron emission tomography: clinical practice*, Springer.
Vaquero, J. J., Lage, E., Ricon, L., Abella, M., Vicente, E. & Desco, M. 2005a. rPET detectors design and data processing. *In:* Nuclear Science Symposium Conference Record, 2005 IEEE, 23-29 Oct. 2005 2005a. 2885-2889.
Vaquero, J. J., Lage, E., Ricón, L., Abella, M., Vicente, E. & Desco, M. 2005b. rPET Detectors Design and Data Processing. *IEEE Nuclear Science Symposium Conference Record*.
Vaquero, J. J., Redondo, S., Lage, E., Abella, M., Sisniega, A., Tapias, G., Montenegro, M. L. S. & Desco, M. 2008. Assessment of a New High-Performance Small-Animal X-Ray Tomograph. *Nuclear Science, IEEE Transactions on,* 55**,** 898-905.
Vicente, E., Espana, S., Lopez Herraiz, J., Herranz, E., Desco, M., Vaquero, J. J. & Udias, J. M. 2008. Nonlinear effect of pile-up in the quantification of a small animal PET scanner. *In:* Nuclear Science Symposium Conference Record, 2008. NSS '08. IEEE, 19-25 Oct. 2008 2008. 5391-5395.
Vicente, E., Herraiz, J. L., Espana, S., Herranz, E., Desco, M., Vaquero, J. J. & Udias, J. M. 2011. Deadtime and pile-up correction method based on the singles to coincidences ratio for PET. *In:* Nuclear Science Symposium and Medical Imaging Conference (NSS/MIC), 2011 IEEE, 23-29 Oct. 2011 2011. 2933-2935.
Vicente, E., Herraiz, J. L., España, S., Herranz, E., Desco, M., Vaquero, J. J. & Udías, J. M. 2012a. Improved effective dead-time correction for PET scanners: Application to small-animal PET. *Phys Med Biol (Submitted)*.
Vicente, E., Soto-Montenegro, M., España, S., Herraiz, J. L., Herranz, E., Vaquero, J. J., Desco, M. & Udias, J. M. 2007. Influence of random, pile-up and scatter corrections in the quantification properties of small-animal PET scanners. *In:* Nuclear Science Symposium Conference Record, 2007. NSS '07. IEEE, Oct. 26 2007-Nov. 3 2007 2007. 3964-3968.
Vicente, E., Udías, A. L., Herraiz, J. L., Desco, M., Vaquero, J. J. & Udías, J. M. 2010b. Corrección de atenuación de imágenes PET usando datos de TAC en el escáner para animales pequeños Argus PET/CT. *Libro de Actas, CASEIB 2010.*
Wang, G. C., Huber, J. S., Moses, W. W., Qi, J. & Choong, W. S. 2006a. Characterization of the LBNL PEM camera.

Nuclear Science, IEEE Transactions on, 53**,** 1129-1135.
Wang, Y., Seidel, J., Tsui, B. M., Vaquero, J. J. & Pomper, M. G. 2006b. Performance evaluation of the GE healthcare eXplore VISTA dual-ring small-animal PET scanner. *J Nucl Med,* 47**,** 1891-900.
Williams, C. W., Crabtree, M. C. & Burgiss, S. G. 1979. Design and Performance Characteristics of a Positron Emission Computed Axial Tomograph--ECATÂ®-II. *Nuclear Science, IEEE Transactions on,* 26**,** 619-627.
Wu, Y., Bowen, S. L., Yang, K., Packard, N., Fu, L., Burkett, G., Qi, J., Boone, J. M., Cherry, S. R. & Badawi, R. D. 2009. PET characteristics of a dedicated breast PET/CT scanner prototype. *Phys Med Biol,* 54**,** 4273-87.
Yamamoto, S., Amano, M., Miura, S., Iida, H. & Kanno, I. 1986. Deadtime correction method using random coincidence for PET. *J Nucl Med,* 27**,** 1925-8.
Zaidi, H., Montandon, M. L. & Slosman, D. O. 2004. Attenuation compensation in cerebral 3D PET: effect of the attenuation map on absolute and relative quantitation. *Eur J Nucl Med Mol Imaging,* 31**,** 52-63.
Zhang, H., Bao, Q., Vu, N. T., Silverman, R. W., Taschereau, R., Berry-Pusey, B. N., Douraghy, A., Rannou, F. R., Stout, D. B. & Chatziioannou, A. F. 2011. Performance evaluation of PETbox: a low cost bench top preclinical PET scanner. *Mol Imaging Biol,* 13**,** 949-61.

5. Design of Small Animal PET Prototypes

Small animal PET tomographs play an important role in biology [Myers, 2001, Herschman, 2003] and studies of in vivo tracer pharmacokinetics and metabolism [Wang and Maurer, 2005, Sossi and Ruth, 2005, Toyama *et al.*, 2005, Kenanova *et al.*, 2007]. Pavlopoulos and Tzanakos [Pavlopoulos and Tzanakos, 1993, 1996] were among the first to suggest, in 1992, a small animal PET with highly segmented detector blocks [Tzanakos and Pavlopoulos, 1993], based on BGO and a new position sensitive photomultiplier (PSPMT), the Hamamatsu R2487. Theirs was a computer aided design made possible by the use of a newly developed Monte Carlo package [Tzanakos and Pavlopoulos, 1991], which simulated the individual blocks as well as the whole PET system. Other Monte Carlo packages designed for special studies in PET appeared in the literature at the same time [Thompson *et al.*, 1992a]. Soon, the first realization of a small animal PET scanner by Watanabe *et al.* was published in [Watanabe *et al.*, 1992].

Ever since this first small animal PET system appeared, small animal PET scanners are in continuous development. New systems are produced with higher sensitivity, spatial resolution, and count rate capabilities [Wang *et al.*, 2006b, Bao *et al.*, 2009a]. The design of a new small animal PET scanner is a very complex process that requires taking decisions of several natures. Monte Carlo simulation have turned into an invaluable tool for all the stages of the PET scanners design, allowing for exhaustive studies which take into account all the elements of the scanner [Heinrichs *et al.*, 2003].

A considerable number of Monte Carlo packages with different characteristics are available nowadays, suitable for the simulation of either PET or SPECT physical processes, with different detail level [Rogers, 1984, Briesmeister, 1993, Baró *et al.*, 1995, Agostinelli, 2003, Harrison *et al.*, 1993, Jan *et al.*, 2004b, Zaidi and Scheurer, 1999, Thompson *et al.*, 1992b, España *et al.*, 2009]. Although most of these packages are very flexible, it is virtually impossible that they cover every conceivable variation of design of a PET scanner. Thus it is often necessary to introduce extensions in the MC codes to make them able of simulating non-standard geometries of some prototypes.

Besides the simulation of raw data, it is necessary to develop appropriate reconstruction methods to process this data in order to evaluate the performance of the system, such as the spatial resolution, and to assess the quality of the final images. To this end, existing reconstruction methods have to be modified and extended to adapt the existing codes to the non-conventional geometry of some designs.

Examples of these modifications on simulation and reconstruction codes to suit particularly creative or non-standard geometries are presented in this chapter whose purpose is the study, by means of Monte Carlo simulations, of the main features and fine tune of design of two new small animal PET prototypes under development in two different centers where the author of this thesis was working as a part of an internship program. The two studied prototypes are:

- **Zoom-in PET system** (section 5.1), proposed and designed by the Department of Biomedical Engineering, University of California, (Davis, CA, USA) [Zhou and Qi, 2009, 2010, 2011, Qi *et al.*, 2011]. The system incorporates a high-resolution detector into an existing PET scanner to obtain high-resolution images of a region of interest.

- **NIH PPI system** (section 5.2**)** developed at the National Institutes of Health (NIH), Bethesda, MD, USA (Molecular Imaging Program, National Cancer Institute) [Seidel et al., 2010]. It is a low cost bench top preclinical PET scanner dedicated to mouse studies which employs a non-rotating compact dual-head geometry similar to those of positron emission mammography (PEM) systems.

5.1. Zoom-in PET scanner

Small animal PET systems have been improved significantly in terms of spatial resolution and sensitivity since their first development in the mid 1990s. Images with higher resolution can improve our capability of studying human diseases using animal models. For instance, sub-millimeter resolution is required in order to detect small metastases or study brain function in mice. This explain the never ending quest for improved resolution in small animal PET scanners.

Most current systems use scintillator-based detectors because of their ability to achieve high performance with a relatively compact geometry and at an acceptable cost [Chatziioannou, 2002]. Some research systems have reported sub-millimeter spatial resolutions in animal studies using arrays of small scintillator elements [Tai *et al.*, 2003, Rouze *et al.*, 2004, Miyaoka *et al.*, 2005]. However, the resolution of these systems is still mainly limited by the physical size of the scintillator elements and the intrinsic spatial resolution of the detectors [Stickel and Cherry, 2005]. Using smaller scintillator elements in close proximity to the object is useful to obtain both higher spatial resolution and sensitivity, but one has to keep in mind that these two performance goals (high resolution and high sensitivity) are in competency. Simulations help to decide the best tradeoff between resolution and sensitivity. Successful instances have been presented where high-resolution detectors are either inserted into an existing whole body PET scanner [Janecek *et al.*, 2006, Wu *et al.*, 2008c] or a small-animal PET device prepared to be as close as possible to the object being imaged [Clinthorne *et al.*, 2003, Park *et al.*, 2007, Wu *et al.*, 2008b] to improve the system performance in a smaller field of view (FOV). The effect of high-resolution inserts on system resolution was analyzed by [Tai *et al.*, 2008]. Related work on modeling of a half-ring PET insert was presented in [Keesing *et al.*, 2008].

While these approaches have been successful, there is clearly room for improvement. First, most PET-inserts require a large number of high-resolution detectors (either partial or full ring) to be placed within the gantry of an existing system, which significantly increases the complexity of the system (e.g., number of electronic channels) and the cost. Second, most existing PET inserts use short scintillation crystals (e.g., 3.75 mm for the micro-insert described in [Wu *et al.*, 2008b]) to avoid the depth of interaction (DOI) effect, yielding a fairly low sensitivity for the high-resolution detector, which limits the potential gain of using the insert. In addition, high-resolution detectors are usually placed in a ring at a fixed radius, so it may not be possible to position the animal right up against the high-resolution detectors to take full advantage of the resolution available.

In this section we study a new prototype, the 'Zoom-in PET' system (or ZiPET), proposed and designed by the Department of Biomedical Engineering, University of California, (Davis, CA) [Zhou and Qi, 2009, 2010, 2011, Qi *et al.*, 2011], where the author of this thesis was working during the summer of 2010. The system integrates a single high-resolution detector into an existing microPET scanner that acts analogously to a 'magnifying glass' in order to obtain high-resolution data of a small portion of the FOV defined by a region of interest around the face of the insert (see Figure 70). The proposed design can offer a cost-effective solution to obtain high-resolution images for a targeted region without building a full-ring PET system. Such a system can be useful for studying human tumors with animal models where tumors are often grown near the surface of the skin of the animal and therefore they can be placed very close to the high-resolution detector.

In this work we use Monte Carlo simulations with PeneloPET (see chapter 2, section 2.3) to characterize the impact of the insert in the performance of the system. It was necessary to introduce several modifications in the PeneloPET code due to the non-standard geometry of the system with two different sets of block detectors at different radial positions. The improvement in spatial resolution was already studied in previous works using theoretical analysis and basic simulations [Zhou and Qi, 2009], and experimental measurements [Qi *et al.*, 2011].

This section is organized as follows. Section 5.1.1 describes in detail the setup of the ZiPET

system. In section 5.1.2 we review the modifications introduced to PeneloPET code to make it able of simulating the geometry of the setup described in section 5.1.1. Sections 5.1.3 and 5.1.4 present the performance characteristics of the system as stems from the simulations with the modified version of PeneloPET.

5.1.1. Setup description

The Zoom-in PET system incorporates a high-resolution detector into an existing PET scanner (microPET II) to obtain high-resolution images of a region of interest. Figure 70 shows a diagram of the setup of the simulated system with the high-resolution detector centered in the axial direction of the FOV of the microPET II scanner [Tai *et al.*, 2003].

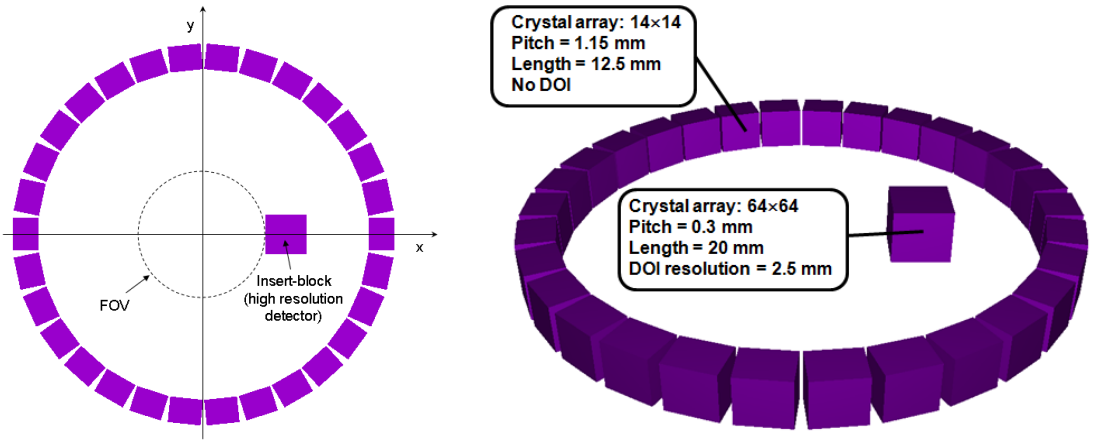

Figure 70. *2D (Transaxial view) [**left**] and 3D [**right**] views of the Zoom-in PET system simulated in this work.*

The microPET II (μPET in what follows) scanner consists of three axial rings of detectors with a diameter of 160 mm, each formed by 30 detector modules. However, in this work we only consider one of the three axial rings for the simulations. Each μPET detector module consists of a 14×14 array of 1.0×1.0×12.5 mm^3 lutetium oxyorthosilicate (LSO) crystals. The performance of the standard microPET II scanner has been previously characterized by [Tai *et al.*, 2003] and [Yang *et al.*, 2004].

The high-resolution detector (insert in what follows) is made of a 64×64 array of 0.3×0.3×20 mm^3 LSO crystals and can provide depth-of-interaction (DOI) information to reduce parallax errors. DOI information is obtained by means of dual-ended readout detectors. The light generated by the array of scintillation crystals is read out by two position sensitive avalanche photodiodes (PSAPDs) one at the front and the other at the back end of the detector [Yang *et al.*, 2006]. The DOI value is calculated by taking the ratio of the signals from the two PSAPDs providing a continuous measure of DOI for each recorded event.

Similar hardware configurations of high-resolution detector inserts have been investigated by other groups. One approach proposed by Wu *et al*. [2008a] had a high-resolution detector insert rotating inside a microPET scanner and acquired coincidence data between the high-resolution insert and the microPET detectors. Huh *et al*. [2008] presented a PET imaging probe where a high-resolution detector is used in coincidence with an arc of low-resolution detectors to perform limited angle tomography of a region of interest. Compared with their designs, our system collects not only coincidence data between the high-resolution insert and the detectors in the μPET scanner (which we refer to as High-resolution data), but also the usual coincidence data between μPET detectors (which we refer to as Low-resolution data). The combination of the High-resolution and Low-resolution data provides high-sensitivity and a full angular coverage of any point inside the FOV.

Table 29 reports the main ZiPET configuration parameters employed for the simulations. Columns 3 and 4 show the parameters for two configurations proposed. For the 1-ring configuration we simulated one axial block-ring of μPET detectors (14×14 LSO crystals) and the entire block for the insert (64× 64 LSO crystals). The 1-row configuration comprises only one row of crystals for each type of detector in the simulation. Note that the axial size of the insert crystals is different from the one used in the 1-ring simulation but it is the same as the axial size of the μPET crystals. Both configurations were simulated for two radial positions of the insert-block, 15 mm and 30 mm from the center of the μPET ring.

Table 29. *Zoom-in PET parameters employed for the simulations. The computed DOI value for the insert was discretized into 8 'effective layers' (8 virtual layers made of the same material) being the output of the simulation process the effective layer correspondent to the DOI value of each particular interaction. This fact is emphasized by the star placed next to the parameter in the table.*

	Parameter	value	
		1-ring simulation	1-row simulation
General parameters	coincidence time window	10 ns	
	integration time	220 ns	
	coincidences dead-time	1200 ns	
μPET detectors	number of blocks per ring	30	30
	number of blocks in coincidence	9	9
	crystal array	14×14	14×1
	number of layers	1 (LSO)	1(LSO)
	crystal size	1×1×12.5 mm^3	1×1×12.5 mm^3
	reflector thickness	0.15 mm	0.15 mm
	energy resolution	42%	42%
	detector radius	80 mm	80 mm
insert-block	number of blocks per ring	1	1
	number of blocks in coincidence	15 (μPET blocks)	15 (μPET blocks)
	crystal array	64×64	64×1
	number of layers	8 (LSO) [*]	8 (LSO) [*]
	crystal size	0.25×0.25×20 mm^3	0.25×1×20 mm^3
	reflector thickness	0.05 mm	0.05 mm
	Energy resolution	42%	42%
	detector radius	15 mm / 30 mm	15 mm / 30 mm

5.1.2. Main modifications to PeneloPET to consider the Zoom-in PET system

Due to the non-standard geometry of the ZiPET system, it was necessary to modify the PeneloPET code to expand the simulation setup. These modifications allow simulating not only the ZiPET system, but also a wider range of types of scanners with different sets of block detectors. This section describes the changes introduced in PeneloPET.

5.1.2.1. Scanner Geometry

In the standard version of PeneloPET [España *et al.*, 2009], the geometrical parameters defining the system are gathered in a configuration file. Some examples of the format of this geometry file are shown in Table 30. Every body included in the simulation must be defined giving their limiting surfaces. This way, all the surfaces are defined first and the bodies are later constructed by combining groups of surfaces. PeneloPET reads the geometrical information from the 'scanner.inp' file (see Table 7, chapter 2) and generates the file 'scanner.geo' (see Table 30) with the specific format of PENELOPE.

Table 30. *Examples of different parts of the file 'scanner.geo', the PENELOPE input file (generated by PeneloPET) needed to define the scanner geometry for the simulation*

0000000000000000000000000000000000000000000000000000 SURFACE (1) INDICES=(0, 0, 0, 1, 0) Z-SHIFT=(-0.797500000000000E+00, 0) 0000000000000000000000000000000000000000000000000000	**Example of Surface definition**
0000000000000000000000000000000000000000000000000000 MODULE (1) MATERIAL(1) SURFACE (1), SIDE POINTER=(+1) SURFACE (2), SIDE POINTER=(-1) SURFACE (3), SIDE POINTER=(+1) SURFACE (4), SIDE POINTER=(-1) SURFACE (5), SIDE POINTER=(+1) SURFACE (6), SIDE POINTER=(-1) 0000000000000000000000000000000000000000000000000000	**Example of Body definition**
0000000000000000000000000000000000000000000000000000 CLONE (2) MODULE (1) 1111111111111111111111111111111111111111111111111111 OMEGA=(0.120000000000000E+02, 0) DEG 0000000000000000000000000000000000000000000000000000	**Example of how to clone a body**

Since the ZiPET geometry requires the definition of two kinds of detector modules, it was necessary to modify the generation process of the 'scanner.geo' file in PeneloPET. The new version of PeneloPET makes use of two input files each one containing the information for one of the detector types:

- scanner_d1.inp (for MicroPET II ring)
- scanner_d2.inp (for the insert block)

PeneloPET reads the geometry information from both files and generates the file 'scanner.geo'.

5.1.2.2. Explicit definition of the coincidence matrix

In a standard scanner configuration, the number of detectors in coincidence (number of detectors that can generate coincidence events with each single detector) is defined by the second parameter of the 'scanner.inp' file (see Table 7, chapter 2). However, when simulating non-conventional configurations, like ZiPET, it is necessary to define explicitly the coincidence matrix. To this end, PeneloPET offers the possibility of using an extra input file, 'coinc_matrix.inp', where the coincidence matrix is defined. To enable this option, the first parameter of the fourth line ('Read coinc_matrix.inp') in the 'main.inp' file has to be set to 'T' (true) (see Table 7, chapter 2).

Examples on how to define the coincidence matrix for the first block (block 0 in PeneloPET numeration) of μPET and for the insert-block (block 30) in the 'coinc_matrix.inp' file are shown in Table 31. Each line of the file indicates a pair of blocks that are connected in coincidence and,

therefore, can generate coincidence events. One block can be in coincidence with as many blocks as desired. It is important to remark that, once the coincidence matrix option has been enabled, only the detectors specified in the file will be connected in coincidence, ignoring all other possible connections.

Table 31. *Examples of coincidence matrix definition for the first block (block 0) of μPET and for the insert-block (block 30) in the 'coinc_matrix.inp' file (first column of the table). Second column of the table shows a graphic example of the pair of blocks in coincidence (red lines) defined in the first column.*

0 0 0 11 0 0 0 12 0 0 0 13 0 0 0 14 0 0 0 15 0 0 0 16 0 0 0 17 0 0 0 18 0 0 0 19 Ring1 Block1 Ring2 Block2	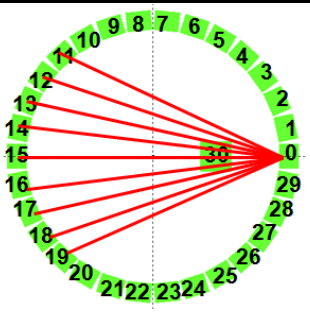 Coincidences pairs for the block 0
0 30 0 8 0 30 0 9 0 30 0 10 0 30 0 11 0 30 0 12 0 30 0 13 0 30 0 14 0 30 0 15 0 30 0 16 0 30 0 17 0 30 0 18 0 30 0 19 0 30 0 20 0 30 0 21 0 30 0 22 Ring1 Block1 Ring2 Block2	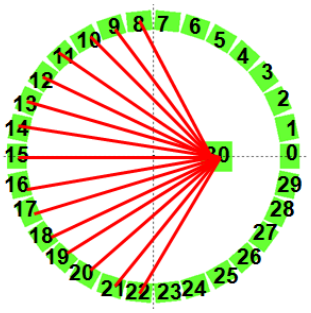 Coincidences for the block 30 (insert)

5.1.2.3. Dynamic loading of detector parameters for each single detection

In the standard version of PeneloPET, detector parameters are treated as global variables which are used in all the computations involving radiation interaction in the detectors. Since ZiPET has two kinds of detectors, it was necessary to dynamically detect the type of detector involved in the interaction and load the appropriate parameters every time a photon interacted with a detector block. A flowchart of the procedure is shown in Figure 71:

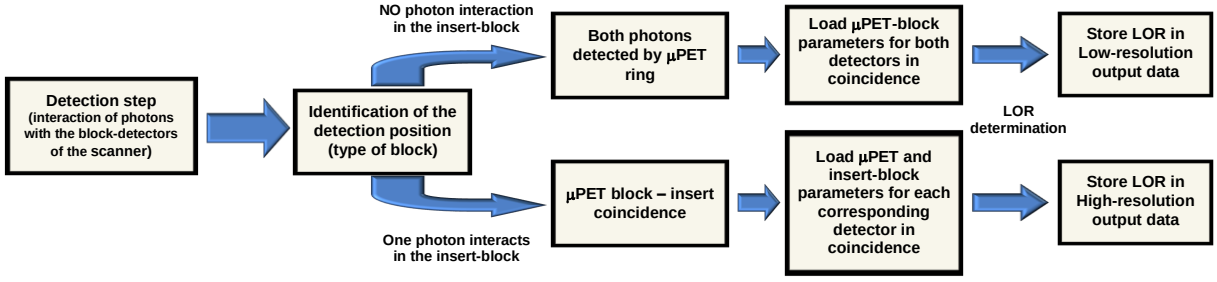

Figure 71. *Flowchart of the new procedure of identifying the type of block-detector and loading its parameters.*

5.1.2.4. DOI modeling

To model the effect of DOI as estimated in the insert-block, the depth of interaction inside the insert of each event was blurred using a convolution with a Gaussian kernel..The use of a Gaussian kernel is justified based on measurements of DOI distributions from experimental detectors [James *et al.*, 2009, Yang *et al.*, 2006]. For an actual DOI *Z* (obtained from PENELOPE) in the crystal, the blurred depth *Z'* is given by:

$$Z' = Z + \Delta Z \tag{73}$$

where ΔZ is obtained from a zero-mean normal distribution with standard deviation, σ, chosen to match the FWHM of the Gaussian distribution to the DOI resolution. This yields:

$$\sigma = \frac{\text{DOI resolution (mm)}}{2\sqrt{2\ln 2}}. \tag{74}$$

The resulting depth in the detector, *Z'*, must be limited to the physical length of the scintillation crystals (20 mm), thus events that after DOI blurring would be located outside of the crystal are placed at 0 or 20 mm depth, as appropriate.

In our simulations, the DOI resolution employed to shift the original estimation of DOI in PeneloPET was 2.5 mm. Having this value and given the crystal length, the value of *Z'* for each interaction was binned into 8 'effective layers', being the output of the simulation process the effective layer correspondent to the *Z'* value of every interaction.

5.1.2.5. New output files for High and Low resolution data

The ZiPET system collects the coincidence data between the high-resolution detector and the detectors in the μPET scanner (High-resolution data), and also the projection data between μPET detectors (Low-resolution data). For this reason, to provide a detailed analysis of the data and get high-resolution reconstructed images, different output files with separated High/Low resolution data were added to the default output files.

5.1.3. Simulated study of the performance of the scanner

In order to study the potential of the ZiPET system, we evaluate three key performance characteristics for the different configurations in Table 29, namely the sensitivity, the DOI capability of the insert-block and the noise equivalent count (NEC) rate.

5.1.3.1. Sensitivity

The sensitivity of the system was estimated from simulations of point sources placed at different positions within the FOV. First we evaluated the absolute central point sensitivity (ACS) for the configurations described in Table 29 to investigate the increase in sensitivity provided by the use of the insert compared to the sole μPET ring and the improvement when using the whole ring as compared to a single row of crystals. The statistic of coincidence event types (trues, scatter, randoms, pile-up, etc.) was also studied.

In order to study in more detail the improvement in sensitivity due to the insert, we simulated point sources at several positions distributed along the X direction (red arrow in Figure 72) for the radial position of the insert of 1.5 cm. This setup was selected to mimic the conditions used to measure

the spatial resolution in the work published by [Zhou and Qi, 2009].

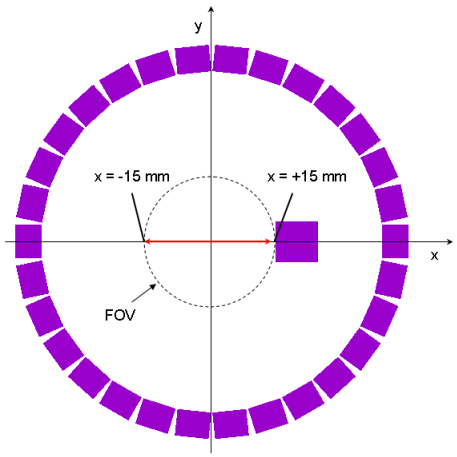

Figure 72. *Transaxial view of the Zoom-in PET system. The red arrow marks the direction for which the sensitivity was evaluated, from x = -15 mm to the insert front face (x = +15 mm) for the 15-mm-radial-position configuration of the insert.*

5.1.3.2. Depth of interaction (DOI)

In order to study the DOI capability of the insert, we first performed a qualitative study of the distribution of coincidences in the insert crystals array for each effective layer using a simulation of a point source placed at the center of the FOV. A quantitative study was also performed to analyze the coincidence sensitivity as a function of the effective layer. Coincidence sensitivity curves were used to determine the crystal length that achieves good resolution without compromising too much the sensitivity of the insert.

5.1.3.3. Noise equivalent count (NEC) rates

The NEC curve of the system was estimated using the method described in chapter 3 (section 3.1.1.4) from simulated data of the mouse-sized phantom (see Appendix A). Figure 73 sketches the simulation.

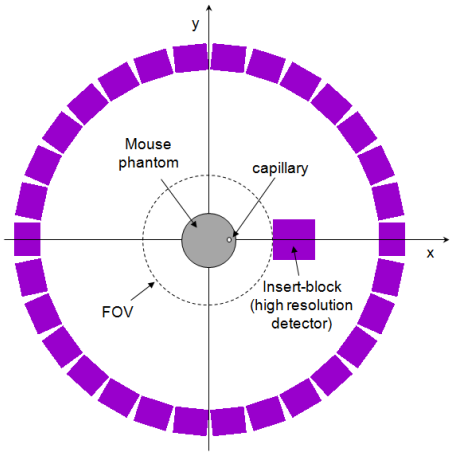

Figure 73. *Transaxial view of the Zoom-in PET system with the mouse-sized phantom placed at the center of the FOV.*

5.1.4. Results

5.1.4.1. Sensitivity

ACS results for the 100-700 keV energy window are reported in Table 32 along with the statistics of the different coincidence types, for all the configurations listed in Table 29. As expected, the ACS value is higher for the ZiPET configuration than for the μPET system both for the 1-row and 1-ring simulations. However, the sensitivity improvement is smaller for the 1-ring case ($ZiPET(r=1.5cm)/\mu PET=1.22$) than for the 1-row one ($ZiPET(r=1.5cm)/\mu PET=1.44$). The apparent loss of sensitivity in the 1-ring case is explained by the smaller solid angle sustained by the insert, where the sensitivity increases a factor of 2 per row in the 1-ring case compared to the 1-row case, while for μPET data (Low-resolution data) it increases by a factor of 3.

Table 32. *Sensitivity and coincidence type statistics for ZiPET and μPET (100-700 keV).*

		1-row simulation			1-ring simulation		
		ZiPET (r=1.5cm)	ZiPET (r=3cm)	μPET	ZiPET (r=1.5cm)	ZiP ET (r=3cm)	μPET
TOTAL SINGLES	SINGLES RATE (cps)	18560	12967	10488	344209	263117	224817
	SENSITIVITY (%)	0.5	0.4	0.3	9.3	7.1	6.0
TOTAL COINCIDENCES	COINCIDENCES RATE (cps)	915	784	635	32188	29636	26456
	SENSITIVITY (%)	0.05	0.04	0.03	1.7	1.6	1.4
	TRUES (%)	99.6	99.8	99.9	96.1	98.6	99.4
	RANDOMS (%)	0.05	0.01	0.02	0.3	0.1	0.04
	SCATTER (%)	0.01	0.03	0.01	0.2	0.1	0.06
	PILE-UP (%)	0.2	0.03	0.02	1.4	0.4	0.2
	SELF-COINC (%)	0.2	0.1	0.04	2.0	0.7	0.3
HIGH-RESOLUTION DATA	COINCIDENCES RATE (cps)	416	224	--	10795	6371	--
	SENSITIVITY	0.02	0.01	--	0.6	0.3	--
	$COINC._{HIGH\text{-}RES}$ / TOTAL COINC. (%)	45.5	28.5	--	33.5	21.5	--
	TRUES (%)	99.1	99.6	--	89.5	95.6	--
	RANDOMS (%)	0.1	0.03	--	0.6	0.3	--
	SCATTER (%)	0.02	0.06	--	0.35	0.2	--
	PILE-UP (%)	0.4	0.06	--	3.9	1.4	--
	SELF-COINC (%)	0.4	0.2	--	5.68	2.5	--
LOW-RESO. DATA	COINCIDENCES RATE (cps)	499	561	635	21392	23264	26456
	$COINC._{LOW\ RESO}$ / TOTAL COINC. (%)	54	71	100	66	78	100

From the analysis of the statistics of the different coincidence types, it can be observed that the insert improves the total sensitivity of the system, increasing both true and the non-desirable

coincidences. Part of this increase is due to the higher sensitivity presented by the insert to single events, whose rate is higher than for coincidences. This effect will be more important in situations when the source or a part of it is placed outside the FOV as stated below, in the NEC analysis (section 5.1.4.3).

A more detailed study on the sensitivity is shown in Figure 74 for the ZiPET system with the insert at the radial position of 1.5 cm. The plots show the variation in sensitivity when the point source is moved along the X direction, toward the insert. In Figure 74 A and B the sensitivity value achieved by the ZiPET system is compared to the one of μPET for the 1-row and 1-ring configurations respectively. The sensitivity value when considering only the High-resolution data is shown in the green curve, providing an estimation of the sensitivity obtained by the insert.

An increase in the sensitivity of the High-resolution data is observed for both configurations (1-ring and 1-row) when the source moves closer to the insert along the X direction. The same trend is observed for the two configurations, but the ratio ZiPET/μPET is higher for the 1-row case, as shown in Figure 74C. The difference increases as the point source is moved towards the insert. Figure 74D compares ZiPET sensitivity for three energy windows, 100-700 keV, 250-700 keV, and 400-700 keV.

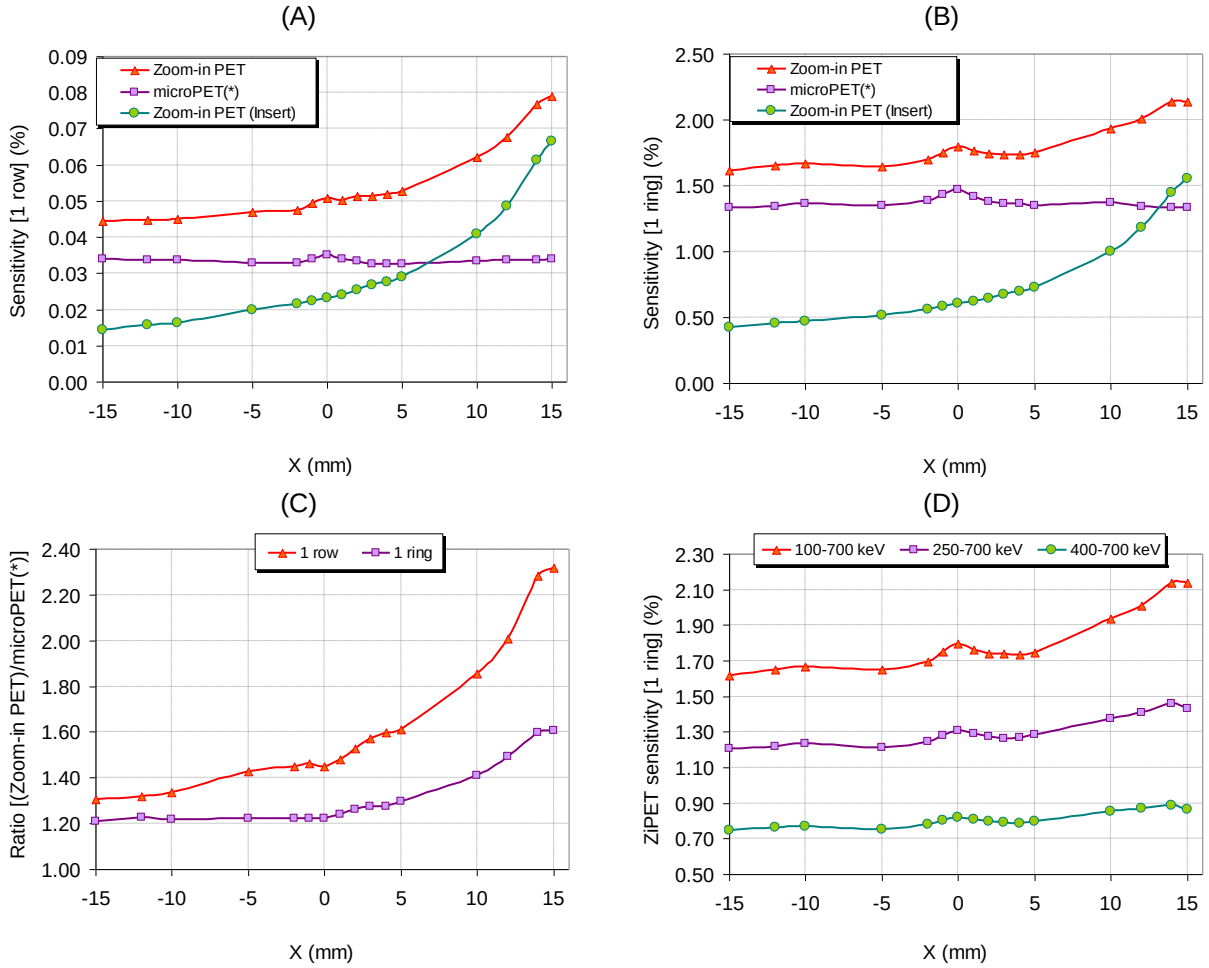

Figure 74. *Sensitivity profiles along X axis for μPET and ZiPET systems, with the insert at the radial position of 1.5 cm.* ***(A)*** *and* ***(B)****: Comparison between both scanners for 1-row and 1-ring configurations respectively (100-700 keV).* ***(C)****: ZiPET/μPET sensitivity ratio for 1-row and 1-ring configurations (100-700 keV).* ***(D)****: ZiPET sensitivity for three energy windows. The star in the microPET legend is used to remind that this results are not for the commercial system (with 3 axial rings) but for a 1-row or 1-ring configurations, respectively.*

5.1.4.2. *Depth of interaction (DOI)*

Figure 75 shows the distribution of coincidences among effective layers for ZiPET with the insert at the two radial positions (1.5 cm [left] and 3 cm [right]) with two μPET blocks in coincidence with the insert. Each set of 8 images for each configuration was independently normalized. The upper images correspond to the coincidences between the insert and the opposite μPET detector (block 15 in the picture), while the lower images are for a more oblique combination (insert and the block 13). As expected, the distribution of coincidences for the 1.5 cm radial position of the insert is more concentrated around the central crystals because the insert in this case is closer to the point source.

Due to the asymmetric position of the center of the FOV with respect to the insert and the μPET detectors, the coincidences detected by each pair of detectors do not illuminate all the insert crystals. An example of this is shown in Figure 76 for the ZiPET system with the insert placed at the radial position of 3 cm. The figure analyzes the coincidences between the insert and the opposite μPET detector (block 15) and shows the distribution of coincidences for first and last effective layers. Note that each image is normalized independently to show the distribution, but as it can be seen in Figure 75, the number of coincidences in the last layer is clearly lower than in the first one. Using geometric relationships, the number of illuminated crystals (reddish area within green boundary in these figures) can be easily computed. In addition to the predicted illuminated crystals, a surrounding area is observed in the coincidences images (bluish region) due to scatter of gamma-rays in the crystal array. It can be also seen that, for solid angle reasons, the number of illuminated crystals is higher for deeper layers, being the scattered area larger as well.

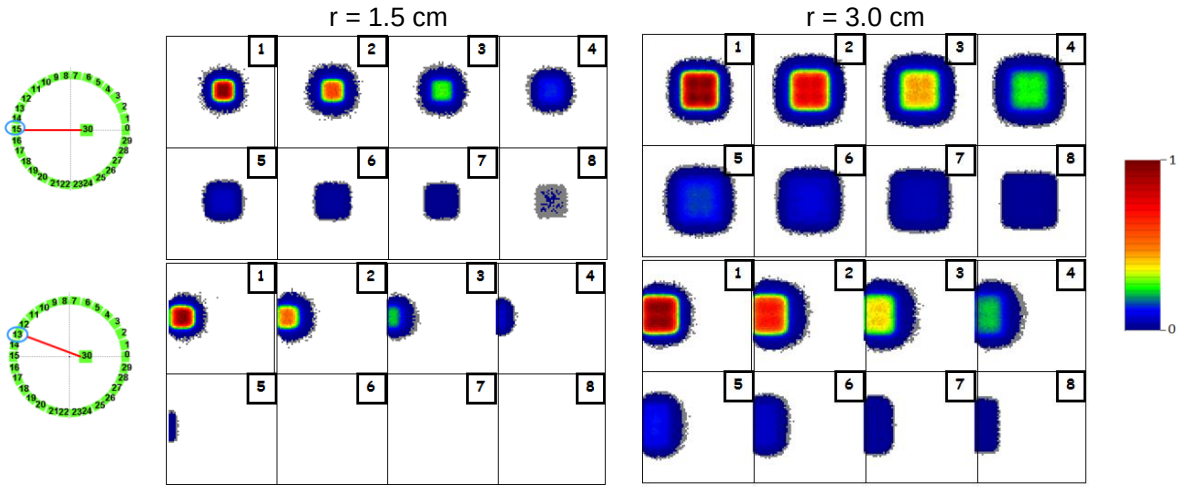

Figure 75. *Distribution of coincidences for the ZiPET system with the insert at two radial positions (1.5 cm [left] and 3 cm [right]) for two μPET blocks in coincidence with the insert. The numbers on the insert crystals arrays indicate the effective layer.*

Quantitative results for the number of coincidences per effective layer for the system with the insert in the radial position of 1.5 cm are shown in Figure 77 for three different energy windows. Data from four μPET blocks (see Figure 77A) in coincidence with the insert were evaluated (due to the decrease in solid angle as the detectors move away from the front side of the insert, only these four blocks and their symmetrical partners have a significant number of coincidences for an acquisition of a centered point source). The plots were normalized dividing the number of coincidences in each layer by the maximum number of coincidences in all the blocks studied, for each energy window. The length of crystal representing the best tradeoff between resolution and sensitivity can be inferred from the curves in Figure 77. For example, the number of coincidences for all the blocks (in the three energy windows) detected by the two last layers is less than half the one detected in the layer with more counts, suggesting that only minor sensitivity increase is provided by those layers, whereas they degrade resolution and thus a shorter crystal can be used to enhance resolution with acceptable degradation in sensitivity.

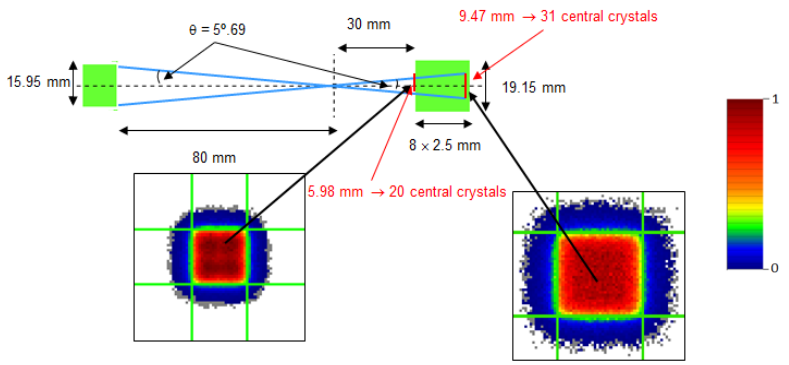

Figure 76. *Description of the experimental setup for the DOI analysis of the insert and microPET block 15 and distribution of coincidences at the insert crystal array (64×64) for the first/last effective layers of the insert. The radial position of the insert is 3 cm.*

Due to the method used to determine the DOI (*Z'*) in the simulations (see section 5.1.3.2), and in the real scanner (see section 5.1.1), the trend shown by the curves in Figure 77 slightly departs from the theoretical law $e^{-\lambda z}$ governing the absorption inside the crystal. This law predicts a maximum of sensitivity at the first effective layer with an exponential drop in subsequent layers; however, as we can see in Figure 77, the maximum of sensitivity is reached at the second effective layer for the detectors closer to the front side of the insert (blocks 14 and 15). This result is an example of the importance of using realistic simulation models of the system in order to take crucial decisions for system design.

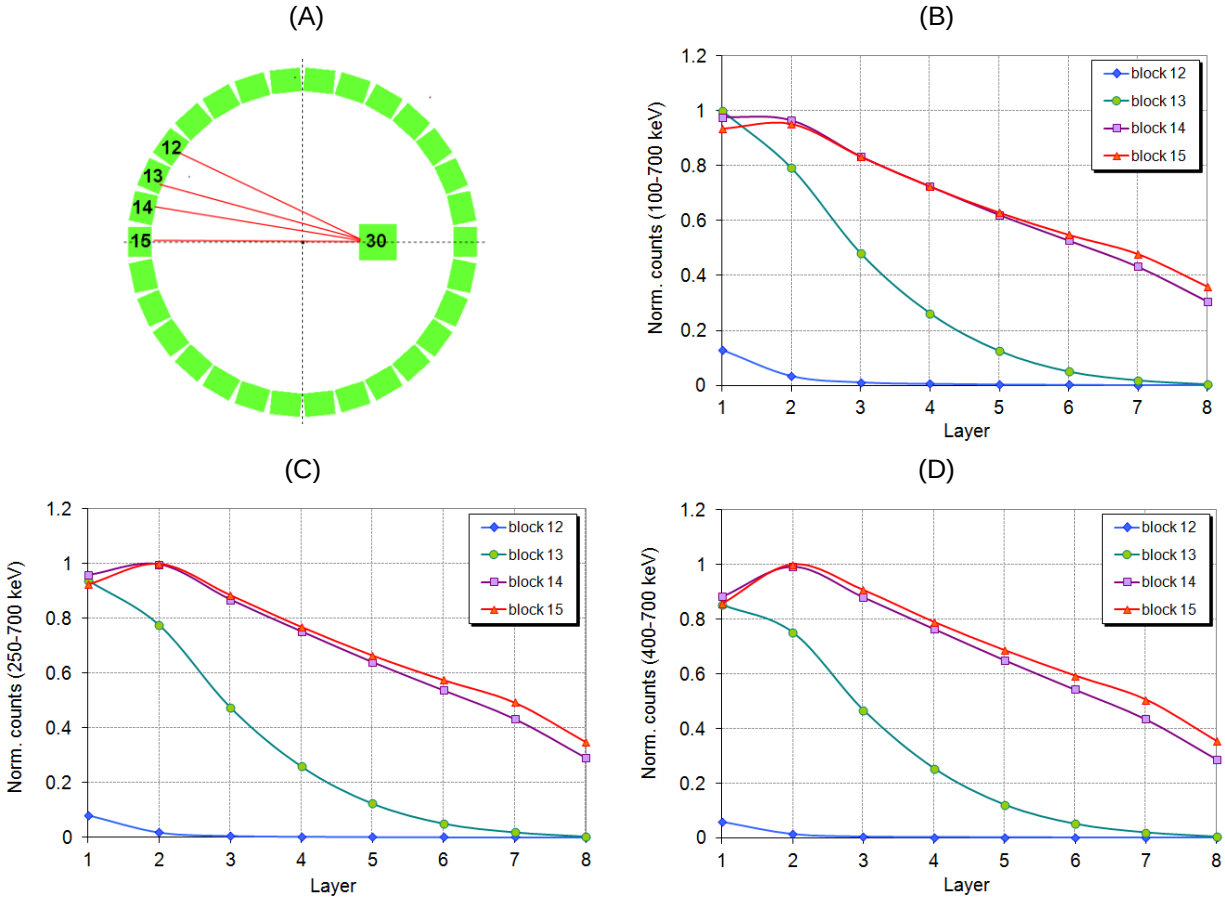

Figure 77. *Coincidences per effective layer for the ZiPET system with the insert at the radial position of 1.5 cm for three different energy windows.*

5.1.4.3. Noise equivalent count (NEC) rates

Figure 78 plots the NEC curves for the μPET and ZiPET systems (r = 1.5 cm) for the 1-ring configuration. As expected, the NEC sensitivity is higher for the ZiPET system, however this trend is inverted at 5 MBq approximately, when the high count rates of the ZiPET system saturate the acquisition system.

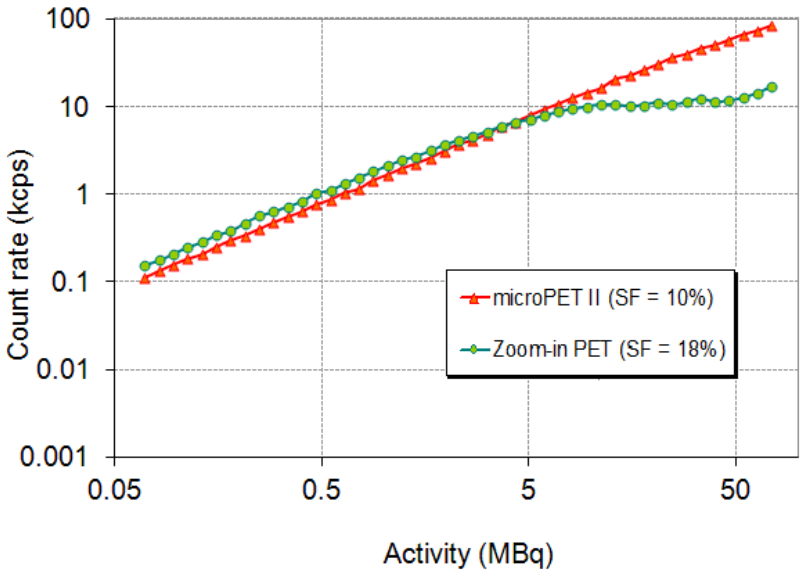

Figure 78. *NEC vs. activity for microPET II and Zoom-in PET (radial position of the insert: 1.5 cm) in the 100-700 keV energy window. Both axes of the plot are in logarithmic scale.*

In order to analyze the behavior observed in the NEC curve, we plot in Figure 79 count rates for the different types of coincidence events. We can see in Figure 79A that the prompt rate is higher for the ZiPET system for all activity values. However, the curve of scatter + random coincidences increases very fast with activity, reducing the fraction of true coincidences. A more detailed analysis of scatter and random coincidences is shown in Figure 79B where we can observe that random coincidences are the main responsible for the worsening of the NEC curve. We already saw in section 5.1.4.1 that the number of non-desirable coincidences slightly increased in the ZiPET system when a point source is placed at the center of the FOV, but the situation gets worse when part of the source distribution is outside the FOV like in this case for which the axial length of the capillary source is 6 cm, while the axial sizes of the μPET and ZiPET detectors are 1.6 cm and 1.9 cm, respectively.

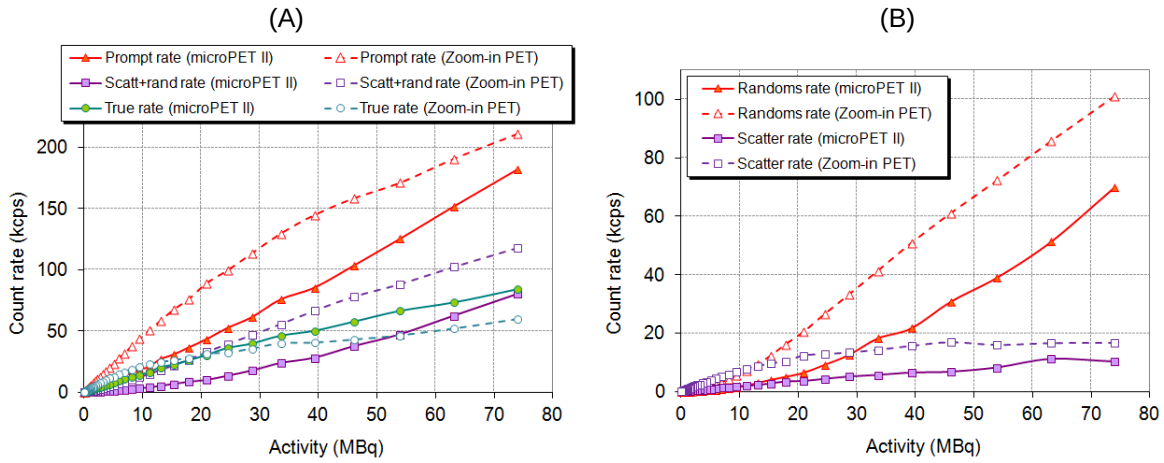

Figure 79. *Count rates vs. activity for microPET II and Zoom-inPET systems (radial position of the insert: 1.5 cm) in the 100-700 keV energy window for each type of coincidence event.*

5.1.5. Conclusions

We have studied the 'Zoom-in PET' system, a high-resolution detector centered in the axial field of view of the microPET II scanner with only one axial ring. The study has been performed using Monte Carlo simulations with an extended version of PeneloPET. This extended version supports non-standard geometries having two blocks of detectors at different radial positions, can deal with two types of detectors with different features inside a single system and includes statistical blurring of the depth of interaction distribution.

Since the spatial resolution was measured in previous works [Zhou and Qi, 2009, Qi *et al.*, 2011] proving its improvement, the performance evaluation of the system has been focused on sensitivity, DOI capability of the insert and noise equivalent count rate. From the results we can state that there is an evident improvement of sensitivity when the insert is included in the system. However, there is room for improvement, given the fact that the current design with only one axial μPET ring and the size proposed for the insert does not provide optimal performance, since non-desirable coincidences, such as pile-up, randoms, self-coincidences and scatter, increase very significantly when the insert is present.

This section shows how simulations can guide the design of scanner prototypes, analyzing the advantages and drawbacks before making final decisions. Our study suggest modifications in the geometry of the system including, for example, more axial rings in the microPET II system and shielding the insert from single events coming from outside the axial FOV.

5.2. NIH PPI scanner

Many radionuclide molecular imaging studies do not, in practice, require tomographic images of biological structures. In the early development of tumor-seeking agents, for example, it is common to perform projection imaging studies in large groups of mice where the tumor can be grown at a location favorable to projection imaging, e.g. the flank, and to observe the accumulation and elimination of the agent from these tumors (and body) over extended periods of time, e.g. hours to tens of days. Since many animals must be imaged many times, the imaging process must be as efficient as possible in order to reduce the time needed to take the image to a minimum. Projection imaging of the tumor and the whole body is an efficient way to provide these data: total tumor tracer content can be determined with an accuracy that is not significantly different from tomographic measurements if the tumor is located on the animal periphery, data processing time is reduced because image reconstruction is eliminated and only a single region of interest is required to outline the tumor in each projection image, etc. Importantly, projection imaging systems can be substantially less expensive than tomographic systems of similar technology. All these reasons led to the design, assembly and test of the positron projection imager (PPI) [Seidel *et al.*, 2010].

The PPI system is a low cost bench top preclinical PET scanner dedicated to mouse studies. The scanner employs compact dual-head geometry, similar to those of positron emission mammography (PEM) systems [Murthy *et al.*, 2000] or a high-sensitivity small-animal PET system based on High-Resolution Research Tomograph detector technology [Kao *et al.*, 2009]. The prototype system was developed at the National Institutes of Health (NIH), Bethesda, MD (Molecular Imaging Program, National Cancer Institute) where the author of this thesis was working on the summer 2011. It consists of two large detectors placed facing each other with three possible face-to-face detector separations: 39, 29 and 19 mm. The system was specifically designed to work at a much lower radioactivity concentration than current scanners, in order to reduce the dose delivered to mice, what is particularly important in the case of longitudinal studies involving multiple PET procedures on the same animal.

In this work, PeneloPET Monte Carlo simulations were performed to provide a quantitative analysis of system performance in terms of sensitivity, resolution and image quality. Although the scanner was initially designed for projection imaging, in this work we explore the 3D imaging potential of the system, analyzing spatial resolution and 3D image reconstruction possibilities. To this end it was necessary to develop new methods of reconstruction adapting the existing algorithms to the non-conventional geometry of the PPI system.

5.2.1. Setup description

The prototype consists of two opposed pixelated LYSO detector modules (Omega Piezo Technology Inc., State College, PA) in time coincidence, mounted in a fixture that allows the face-to-face separation between modules to be varied among 39, 29 and 19 mm (see Figure 80). The object to be imaged is placed on a plastic plate located between the detectors faces such that the mid-plane of the object can be made to coincide with the image plane which is always located exactly midway between the detector faces. The detectors are kept stationary during the scan, making PPI a limited angle tomography system. The FOV of the detectors is large enough to image the whole body of a mouse in a single scan.

The individual LYSO crystals in each detector module are $1.5\times1.5\times12$ mm^3 with a pitch of 1.6 mm. Each crystal is polished on all sides and five of the sides are coated with a highly reflective specular reflector. The exit surface of the 26×59 array is covered by a 3.5 mm thick optical glass window that is coupled with silicon grease to a pair of side-by-side Hamamatsu H8500C position-sensitive photo-multiplier tubes (PSPMTs, Hamamatsu Corp., Bridgewater, NJ). These components are shown in Figure 81. A 511 keV field flood image of this detector module is shown in Figure 82.

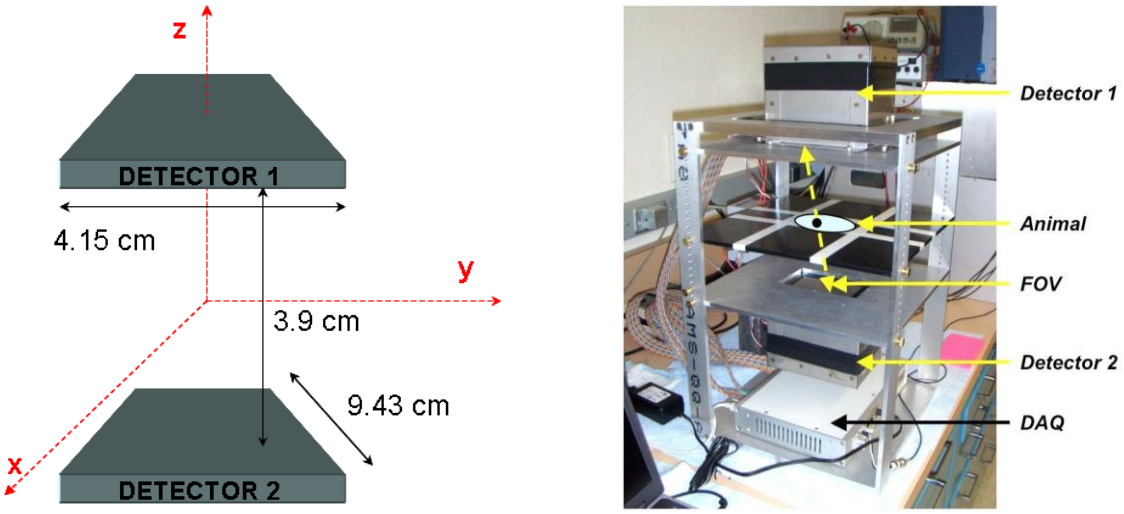

***Figure 80. Left**: Conceptual drawing of the PPI. **Right**: picture of the prototype. It features a 64-channel DAQ [Seidel et al., 2010].*

The anodes of each H8500C PSPMT are combined by resistive division to yield eight row and eight column signals for a total of 16 signals/PSPMT, 32 signals/module and 64 signals for the entire system. These signals are acquired by a 64-channel data acquisition system (DAQ, Adaptive I/O Technologies Inc., Blacksburg, VA) shown in Figure 80 (right). Digitization of these signals occurs if the summed dynode signals of the two PSPMTs in one detector module are in time coincidence with the summed dynode signals of the opposite module.

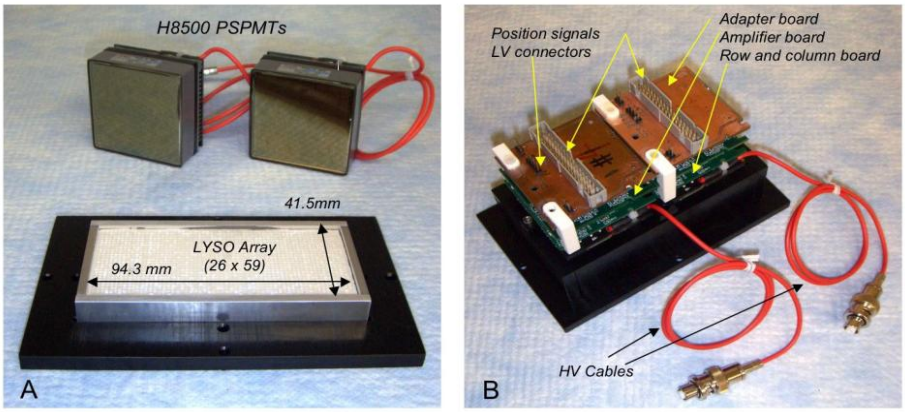

***Figure 81. (A)**: disassembled PPI detector module; **(B)**: assembled module with signal processing boards attached [Seidel et al., 2010].*

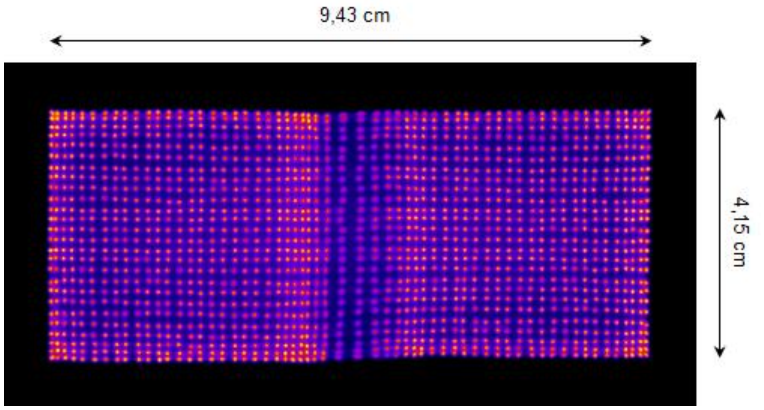

Figure 82. *511 keV field flood image of the detector module shown in Figure 81. All 1534 individual crystals can be identified [Seidel et al., 2010].*

Table 33 reports the main PPI features employed in the simulations. Three different detector separations: 39, 29 and 19 mm were simulated. To distinguish each configuration, we call them PPI_{39mm}, PPI_{29mm} and PPI_{19mm}, respectively.

Table 33. *PPI parameters employed in the simulations.*

	parameter	Value
general parameters	coincidence time window	10 ns
	iIntegration time	400 ns
	coincidences dead-time	1200 ns
PPI detectors	number of blocks per ring	2
	number of blocks in coincidence	1
	crystal array	26×59
	number of layers	1 (LYSO)
	crystal size	1.5×1.5×12 mm^3
	reflector thickness	0.1 mm
	energy resolution	14%
	detector radius (separation between detectors)	39 mm / 29 mm / 19 mm

5.2.2. Image Reconstruction for the PPI

In order to characterize the system in terms of spatial resolution and image quality it is necessary to reconstruct the PET data. Due to the non-conventional geometry of the PPI scanner, new methods for image reconstruction had to be implemented [Vicente *et al.*, 2012b].

5.2.2.1. Parallel imaging

As a first approximation, a parallel imaging algorithm was implemented. The projection image is formed on the image plane midway between the two detector faces by backward projecting the counts measured in the accepted LORs. Accepted LORs are those within a small, user-specified cone angle, almost perpendicular to the image plane. Events occurring outside this cone angle are ignored. The

conceptual basis for the projection image formation is shown in Figure 83. This parallel imaging method provides a planar 2D image without information along the direction between detectors.

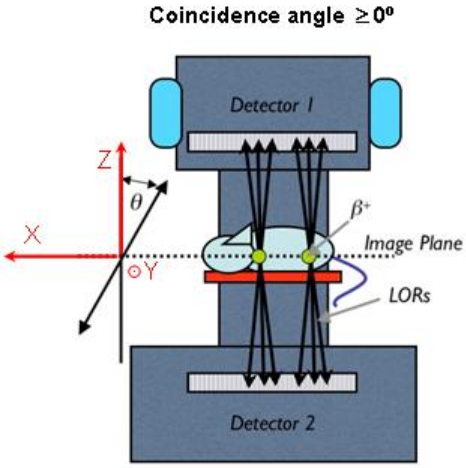

Figure 83. *2D-Image formation in the PPI [Seidel et al., 2010].*

5.2.2.2. 3D iterative reconstruction without resolution recovery (noRR-GFIRST)

We developed a 3D-mode reconstruction[10] based on the GFIRST code (see chapter 2, section 2.4.2). This code uses ML-EM (Maximum Likelihood-Expectation Maximization) algorithm [Shepp and Vardi, 1982] extended to incorporate subsets (OSEM) [Hudson and Larkin, 1994, Herraiz *et al.*, 2006a]. In this iterative reconstruction method the update equation is given by:

$$x^{it+1}(j) = x^{it}(j) \frac{\sum_{i \in Subsets} A(i,j) \frac{y(i)}{\sum_{j'} A(i,j') x^{it}(j')}}{\sum_{i \in Subsets} A(i,j)} \qquad \textbf{(75)}$$

where $x^{it}(j)$ is the expected value of voxel j at iteration it, $A(i,j)$ is the probability of an emission from voxel j being detected along LOR i, and $y(i)$ is the projection from the object measured at LOR i (experimental data).

For this 3D-mode reconstruction method, we used a simplified version of the probability matrix A, taking the value of each element $A(i,j)$ as the distance of LOR i to the center of voxel j, together with a calibration factor for each LOR. In that way, we can write the matrix of probabilities as:

$$A = WL \qquad \textbf{(76)}$$

where $W = W(i)_I$ is the calibration vector which takes into account geometric sensitivity variations (normalization correction) and $L = L(i,j)_{I \times J}$ is the matrix of intersection lengths. This L matrix can be computed online.

With these approximations, all resolution effects (positron range, photon non-collinearity and intrinsic detector resolution) are neglected. For that reason, there is not resolution recovery and the quality of the resulting images is comparable to FBP reconstructions in terms of spatial resolution.

[10] No angular limitation was applied to 3D-mode methods.

5.2.2.3. 3D iterative reconstruction with resolution recovery (RR-GFIRST)

The second 3D-mode method implemented was also based on GFIRST code. In this method, we used a more realistic probability matrix to account for resolution effects, which can be measured and considered known. To this end, the matrix of probabilities $A = A(i,j)_{I\times J}$ can be factorized as [Kupinski and Barrett, 2005]:

$$A = WLH \tag{77}$$

The matrix $H = H(j,j')_{J\times J}$ accounts for finite resolution effects, $L = L(i,j)_{I\times J}$ is the matrix of intersection lengths, and $W = W(i)_I$ is the calibration vector as mentioned above. Then, the algorithm becomes:

$$x^{it+1}(j) = x^{it}(j)\frac{\sum_{j'} H(j',j)\sum_{i\in Subsets} L(i,j')\dfrac{y(i)}{\sum_{j''} L(i,j'')\sum_{j'''} H(j'',j''')x^{it}(j''')}}{\sum_{j'} H(j',j)\sum_{i\in Subsets} W(i)L(i,j')} \tag{78}$$

The expression (78) can be rewritten in vector form:

$$\vec{x}^{it+1} = \vec{x}^{it}\times\vec{s}\times\vec{c}^{it} \tag{79}$$

where × denotes an element-by-element multiplication of vectors, $\vec{x}^{it+1}$ and $\vec{x}^{it}$ contain the new and old image estimates, and $\vec{s}$ contains the sensitivity correction factors of the denominator of eq. (78). $\vec{c}^{it}$ contains the multiplicative image correction values given by:

$$\vec{c}^{it} = H^T\left[\sum_{i\in Subset}\overrightarrow{BP_i}\left(\frac{\vec{y}}{FP_i(H\vec{x}^{it})}\right)\right] \tag{80}$$

where FP_i is an operator based on matrix L which forward projects vector $H\vec{x}^{it}$ along LOR i to give a scalar value, and $\overrightarrow{BP_i}$ is an operator which back projects a scalar value along LOR i into a 3D image based on matrix L.

To simplify the computation in (80) and speed up the reconstruction, we consider the system as shift-invariant. In this situation, the blurring component H can be taken as a shift-invariant kernel ρ ($H\vec{x}^{it} = H^T\vec{x}^{it} = \vec{x}^{it}\otimes\rho$). Then, the algorithm becomes:

$$\vec{x}^{it+1} = \vec{x}^{it}\times\vec{s}\times\left(\left[\sum_{i\in Subset}\overrightarrow{BP_i}\left(\frac{\vec{y}}{FP_i(\vec{x}^{it}\otimes\rho)}\right)\right]\otimes\rho\right) \tag{81}$$

The kernel ρ can be defined as an effective point spread function (PSF) that takes into account the aforementioned resolution effects. In order to obtain a realistic estimation of the kernel ρ, we used point sources at different positions of the FOV and reconstructed the images using the 3D-mode reconstruction method without resolution recovery explained above. From these images, the point spread function (PSF) in the three directions was obtained. Since the PSF value is not shift-invariant in this system, we selected a mean value of the PSF for each direction in order to apply the approximation (81). We will investigate a non shift-invariant kernel in future works using the algorithm form (80).

As a further improvement of this reconstruction method, we used an unmatched forward-/back-projector pair, which was initially proposed by Zeng *et al.* [2000] to increase the convergence rate of the algorithm. To this end, we used the previously estimated PSF in the forward-projector kernel ($\rho_{FP} = PSF$) and a narrower PSF, $\rho_{BP} = (3/4)PSF$, for the back-projector kernel, which was empirically selected as the best option to remove ring artifacts and assure a good convergence. With this unmatched forward-/back-projector pair, the algorithm becomes:

$$\vec{x}^{it+1} = \vec{x}^{it} \times \vec{s} \times \left(\left[\sum_{i \in Subset} \overrightarrow{BP}_i \left(\frac{\vec{y}}{FP_i(\vec{x}^{it} \otimes \rho_{FP})} \right) \right] \otimes \rho_{BP} \right) \quad \textbf{(82)}$$

A flowchart of this implementation of RR-GFIRST is shown in Figure 84.

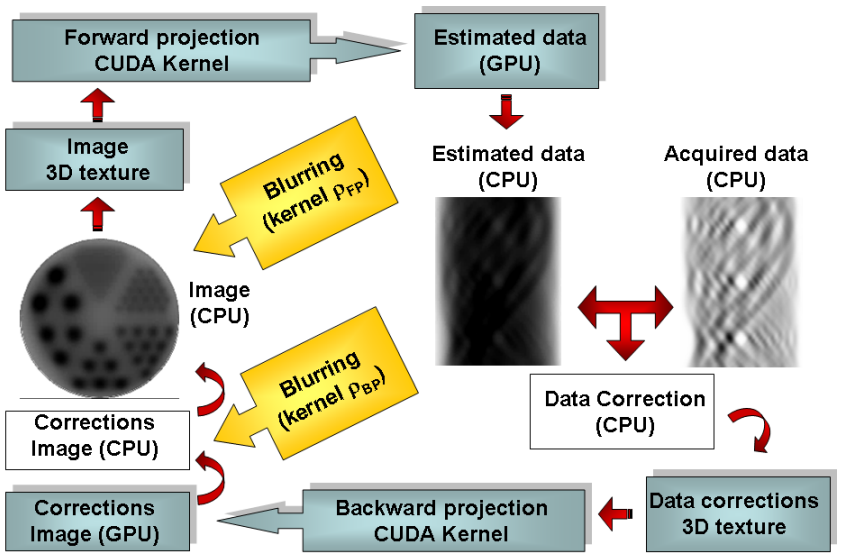

Figure 84. *Flowchart of the implementation of the RR-GFIRST code.*

5.2.2.4. 3D iterative reconstruction with resolution recovery and regularization (RRr-GFIRST)

The main problem for obtaining a 3D-mode reconstructed image in this system is the limited angle θ of the measured data due to the system geometry. The missing data results in poor resolution in the Z direction (separation between detectors), being more than three times worse the X or Y resolutions. This fact makes the convergence in the *Z* direction much slower than in *X* or *Y*. That means that, using an algorithm like (82), the image will reach the optimal resolution in *X* and *Y* directions for a determined number of iterations, while the convergence in *Z* direction will not have been achieved yet. Increasing the number of iterations to optimize the convergence in Z is not a good solution either because it overiterates the image in the other two directions, causing chessboard artifacts [Dai *et al.*, 2007]. This is mainly because the reconstruction problem is ill-posed and requires some regularization to converge to images with the desired properties.

In order to avoid these convergence problems, we developed a 3D-mode reconstruction method based on the one explained in the previous section (5.2.2.3), but with an extra blurring component [Vicente *et al.*, 2012b]. The main idea of this method is to slow down the *X* and *Y* convergence for a number of initial iterations, allowing for a normal convergence in *Z*. When the *Z* resolution value is similar to *X* and *Y* ones, the condition for reducing *X* and *Y* convergence is removed and the algorithm becomes the one described by (82). This was implemented including an extra blurring component in X

and Y in the backprojector:

$$\vec{x}^{it+1} = \vec{x}^{it} \times \vec{s} \times \left[\left(\left[\sum_{i \in Subset} \overrightarrow{BP}_i \left(\frac{\vec{y}}{FP_i(\vec{x}^{it} \otimes \rho_{FP})} \right) \right] \otimes \rho_{BP} \right) \otimes \rho_{Reg(X,Y)} \right]_{it \le N-R} \quad \textbf{(83)}$$

where $\rho_{Reg(X,Y)}$ is the additional blurring kernel for *X* and *Y* directions, *N* is the total number of iterations and *R* is the number of the final iterations when the algorithm becomes the one described by (82). Since the convolution of two Gaussians is another Gaussian, we can rewrite (83) with the kernel ρ_{BP} in its *X*, *Y* and *Z* components as follows:

$$\vec{x}^{it+1} = \vec{x}^{it} \times \vec{s} \times \left(\left[\sum_{i \in Subset} \overrightarrow{BP}_i \left(\frac{\vec{y}}{FP_i(\vec{x}^{it} \otimes \rho_{FP})} \right) \right] \otimes \left[\rho'_{BP(X)}, \rho'_{BP(Y)}, \rho_{BP(Z)} \right] \right) \quad \textbf{(84)}$$

where $\begin{cases} \rho'_{BP(X,Y)} = \rho_{BP(X,Y)} \otimes \rho_{Reg(X,Y)} & if\ it \in [1, N-R] \\ \rho'_{BP(X,Y)} = \rho_{BP(X,Y)} & if\ it \in (N-R, N] \end{cases}$

The selected kernel $\rho'_{BP(X,Y)}$, when $it \le (N\text{-}R)$, is wider than the $\rho_{FP(XY)}$ in order to control the convergence of the image in each actualization. The value chosen for the kernel $\rho'_{BP(X,Y)}$.was $PSF'(X,Y) = 3PSF(X,Y)$

The value of the PSF of the kernel $\rho_{Reg(X,Y)}$ and the number of iterations was selected based on the difference in the convergence in *Z* direction compared to *X* and *Y*. These values were obtained after several tests.

5.2.3. Simulated study of the performance of the scanner

We evaluated sensitivity and resolution in different positions within the FOV. Initial imaging studies were also performed to demonstrate the imaging capabilities of the PPI system.

5.2.3.1. Sensitivity

The sensitivity of the system was measured at different positions within the FOV. For each position we simulated a point source consisting of a sphere (0.2 mm diameter) of ^{18}F of 30 μCi in a cubic phantom (1×1×1 cm^3) of water, computing the number of detected coincidence over the actual number of positron annihilations. The three detector distances explained above were evaluated in the 400-650 keV energy window. Additional measurements were performed for the separation of 39 mm in two more energy windows (100-650 keV and 250-650 keV).

The point source simulations for each scanner configuration (i.e. distance between the detectors) were variable depending of the FOV dimension in *Z* direction. The step of the point source shift was 2 mm in the three directions. A summary of the positions of the point sources for each configuration is reported in Table 34.

Table 34. *Summary of the number of point source simulations performed for each system configuration (i.e. separation between detectors) to get the 3D-sensitivity profiles.*

Separation between detectors (mm)	# of X positions	# of Y positions	# of Z positions	# of simulations
39	24 ∈ [0,46 mm]	10 ∈ [0,18 mm]	10 ∈ [0,18 mm]	2400
29	24 ∈ [0,46 mm]	10 ∈ [0,18 mm]	8 ∈ [0,14 mm]	1920
19	24 ∈ [0,46 mm]	10 ∈ [0,18 mm]	5 ∈ [0,8 mm]	1200

As we can see in the table, the number of point sources simulated for each configuration only cover an eighth of the total FOV. The rest of the FOV was completed taking advantage of system symmetries.

In order to validate the simulated results, the absolute central sensitivity (ACS) was also measured experimentally using a point source similar to the one employed in the simulations.

5.2.3.2. Spatial resolution

To measure the spatial resolution of the system we simulated point sources (same size than in the previous section) at different positions within the FOV. Each point source simulation was reconstructed and activity profiles were drawn in the image in three directions and fitted to Gaussians to calculate the FWHM. Since this system does not have cylindrical symmetry as standard PET scanners, the resolution was measured along *X, Y* and *Z* directions. The resolution was evaluated for the PPI system with the detectors separation of 39 mm (PPI_{39mm}).

The image reconstruction was performed using two 3D-mode reconstruction methods: with and without resolution recovery. The method without resolution recovery (noRR-GFIRST, section 5.2.2.2) was employed to study what we call in this work 'intrinsic resolution'. Intrinsic resolution in this context means the system resolution without employing any resolution recovery procedure, as the FBP algorithm, which is the standard reconstruction method employed to characterize the systems in term of spatial resolution. We set the number of iterations to 5 as more than 5 iterations without including resolution effects in the reconstruction produced Gibb's artifacts. The method with resolution recovery (RR-GFIRST, section 5.2.2.3) was used to explore the resolution limits of the system using a shift-invariant kernel ρ, that is, the same PSF value for all the positions within the FOV. The number of iterations was set to 200. It is straight forward to see that, since the resolution is measured using isolated point sources, these measurements correspond to the maximum resolution achieved under ideal conditions. Note that no regularization was applied in the recovery reconstruction method since there is no problem with chessboard artifacts when reconstructing isolated point sources.

To evaluate the resolution, we first simulated a point source placed at the center of the FOV of the PPI scanner including continuous rotation (4.5 degrees per second) of its detectors to provide a full tomographic acquisition. Figure 85 shows a conceptual drawing of the PPI system with rotation. The spatial resolution obtained with this system was compared with the one obtained with the standard PPI_{39mm} using the noRR-GFIRST method for the reconstruction.

Secondly, we studied the resolution variation within the FOV for the standard PPI_{39mm} (without rotation). To this end, we simulated point sources at different positions within the FOV. The step of the point source shift was 4.5 mm in the three directions. A total of 176 simulations ({11 ($X \in$ [0,40 mm])} × {4 ($Y \in$ [0,13 mm])} × {4 ($Z \in$ [0,13 mm])}) was performed covering approximately an eighth of the total FOV. The rest of the FOV was completed taking advantage of system symmetries. The resulting 3D profiles were used to evaluate the resolution along the 3 axes using both mentioned

reconstruction methods.

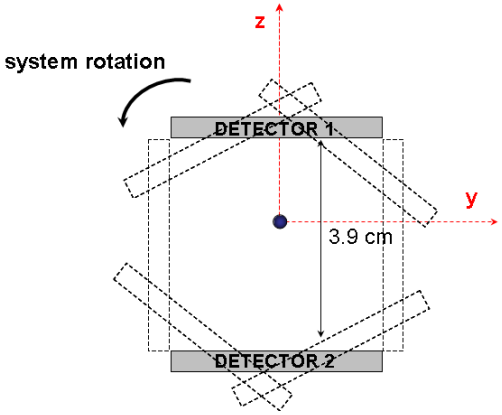

Figure 85. *Diagram of the PPI system with rotation. The dashed-lines represent different detector positions in their continuous rotation movement (speed: 4.5 degrees per second)*

Finally, we compared the resolution obtained from the simulations with the one measured in the real system.

5.2.3.3. Initial imaging studies

Both simulated and real data were reconstructed. No corrections were applied to the data, except normalization. Extra corrections will be included in future works. The system configuration chosen for the imaging studies was the PPI_{39mm}.

A conceptual drawing of the simulated acquisition performed is shown in Figure 86. A (3×3×3) matrix of point sources was placed at the center of the FOV with a 7.5 mm separation between point sources in the three directions. The acquired list-mode data were then histogrammed into a sinogram, after applying an energy window of 100-650 keV. Images were reconstructed using noRR-GFIRST and RR-GFIRST. The number of iterations without resolution recovery was set to 5 (to avoid Gibb's artifacts). Using resolution recovery the number of iterations could be set to 200.

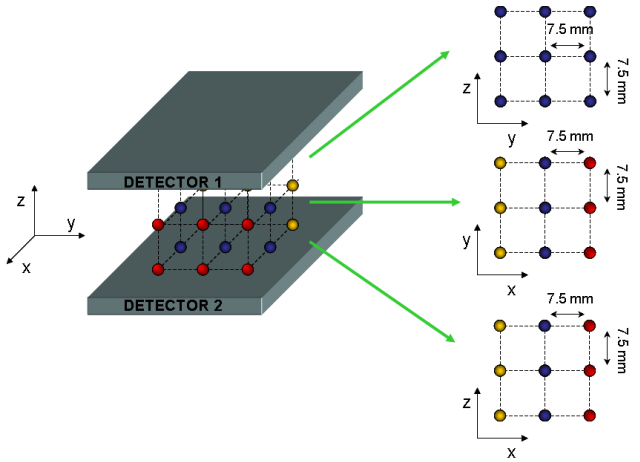

Figure 86. *Diagram of the (3×3×3) matrix of point sources.*

An initial imaging study using experimental data was performed with a 20 g dead mouse bone scan study. We chose a mouse bone scan since it is the biological acquisition most likely to clearly show spatial variations of resolution over the imaging volume. The mouse was injected with 100 μCi

of unbound fluoride (^{18}F) and following a 2 hours uptake period it was scanned for 3 hours, for an initial activity of 35 μCi. The mouse was centered in the *XY* plane between the detectors. The acquired list-mode data were then histogrammed into a sinogram with an energy window of 400-650 keV. Images were reconstructed using the parallel imaging method (cone angle of 5.0 degrees) and the RR-GFIRST with and without regularization. The number of iterations without regularization was set to 20 as more than 20 iterations produced chessboard artifacts. Using the regularization, the number of iterations could be set to 200, employing regularization for the first 150.

5.2.4. Results

5.2.4.1. Sensitivity

Figure 87 shows a qualitative analysis of the *X-Z* sensitivity profiles along the Y axis for the PPI_{39mm} in the 400-650 keV energy window. All the images of the sequence have the same color map. As expected, the maximum value is reached at the center of the FOV and it drops for positions away from the center.

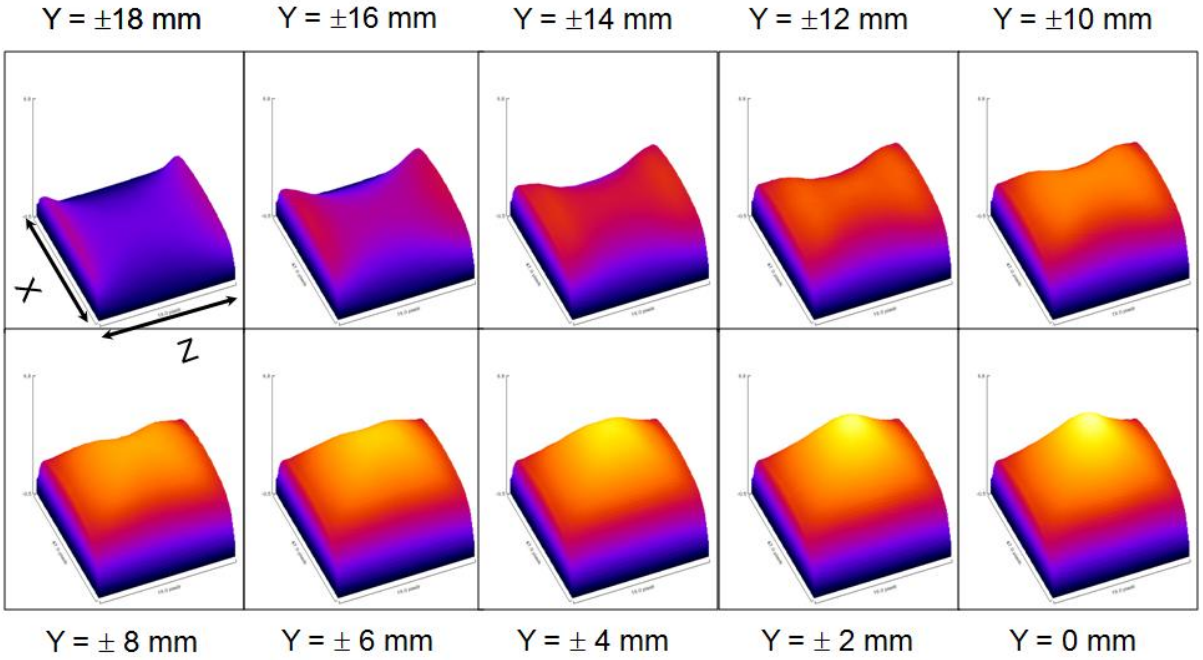

Figure 87. *X-Z sensitivity profiles at different Y positions for the PPI_{39mm} system in the 400-650 keV energy window.*

A quantitative study is shown in Figure 88 where one-dimensional profiles along both *X*- (A and C) and *Z*-axis (B and D) are plotted. The upper plots present the sensitivity variation along both axes for the PPI_{39mm} in three energy windows, while the lower ones depict the variation for the three detectors separations in the 400-650 keV energy window. We observe in all the plots that the peak absolute sensitivity of the system is reached at the center of the FOV and it falls away from the center, with faster reduction in the *Z* direction.

(A) (B)

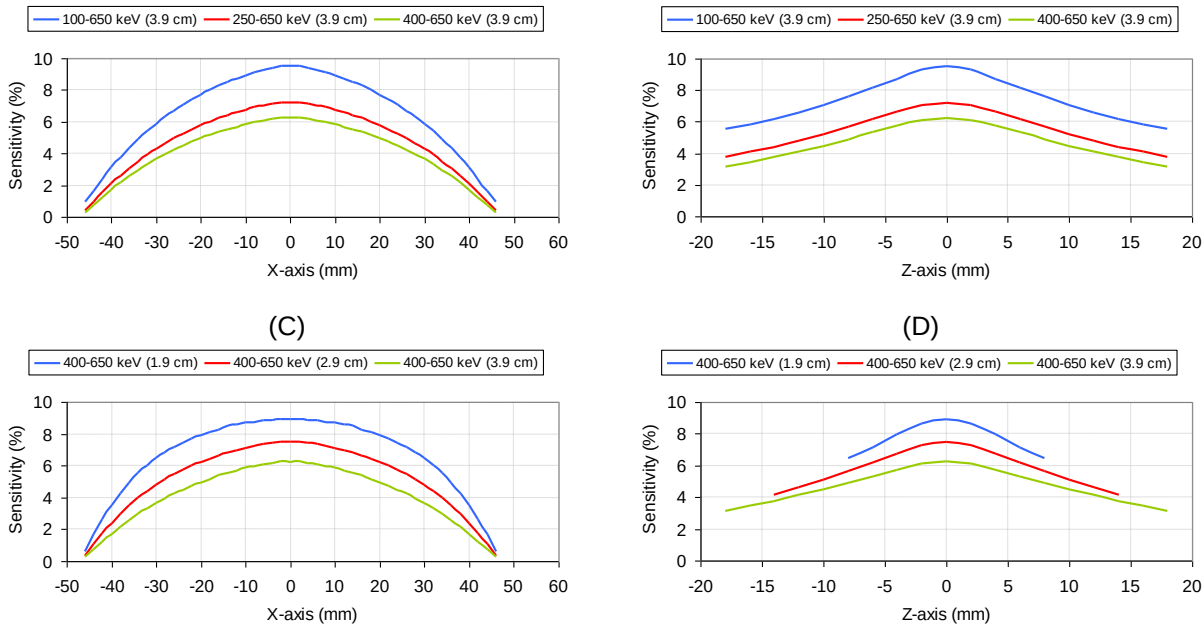

Figure 88. *One-dimensional sensitivity profiles along both X- (**A** and **C**) and Z-axis (**B** and **D**) for the PPI_{39mm} system in three energy windows (upper plots) and the three PPI configurations (i.e. detectors separation) in 400-650 keV (lower plots).*

Experimental values of the ACS are reported in Table 35 for the PPI_{39mm}. We see a good agreement between simulations and experimental values in both the 100-650 keV and 250-650 keV energy windows with relative errors less than 5% and 8% respectively. However a high discrepancy is observed for the sensitivity value obtained in the 400-700 keV energy window. This is most likely due to energy calibration errors in the real scanner.

Table 35. *Absolute central point sensitivity (ACS) comparison among different small animal PET scanners. Results from simulations and experimental data are reported for the PPI_{39mm}*

System	Reference	Energy Window (keV)	ACS (%)
PPI_{39mm} (simulations)	---	100-650	9.5
		250-650	7.2
		400-650	6.2
PPI_{39mm} (experimental data)	---	100-650	10.0
		250-650	6.7
		400-650	4.5
PETbox	[Zhang *et al.*, 2011]	100-650	4.6
		250-650	2.8
Argus	[Wang *et al.*, 2006b] (see chapter 3, section 3.1.2.1)	100-700	6.8
		250-700	4.3
		400-700	2.3
microPET P4	[Tai *et al.*, 2001]	250-750	2.3
microPET R4	[Knoess *et al.*, 2003]	250-750	4.4
Mosaic HP	[Surti *et al.*, 2005]	250-665	3.6
Inveon	[Visser *et al.*, 2009]	350-650	6.8
LabPET 12	[Bergeron *et al.*, 2009]	250-650	5.4

From these results we can state that, due to the small distance between the detectors and its large

size, the PPI system has a very competitive sensitivity value, improving the sensitivity of the PETbox system [Zhang *et al.*, 2011], a small animal PET scanner with similar characteristics (detector sensitive area: 5×10 cm^2, detectors separation: 5 cm) and improving most of the sensitivity values of full-ring scanners. Table 35 reports an ACS comparison among several small animal PET scanners and the simulated and experimental values for the PPI_{39mm} system. .

5.2.4.2. Spatial resolution

Table 36. *Spatial resolution at the center of the FOV for the PPI_{39mm} without rotation vs. rotation. The point sources images were reconstructed using the noRR-GFIRST method.*

	cFOV FWHM (mm)		
	X	**Y**	**Z**
Without rotation	1.2	1.2	5.4
With rotation	1.5	1.4	1.4

Table 36 shows a resolution comparison between the PPI_{39mm} and the same system with rotation as it was explained above. As commented, the incomplete LOR collection due to the system geometry results in degradation in the *Z* resolution. System rotation recovers the missing data yielding very similar resolution values in the three directions.

A more detailed study of the PPI_{39mm} resolution (without rotation) is presented in Figure 89, where resolution is plotted along the 3 axes for the reconstruction method without resolution recovery (no RR, Figure 89A) and with resolution recovery (RR, Figure 89B). The study of the resolution without resolution recovery shows the system intrinsic resolution with values mostly above 6 mm for the *Z* direction and under 1.8 mm for the other two directions. These differences are reduced using the PSF in the reconstruction. Although the *Z* resolution is still the worse value, in this case it is well under 1.8 mm.

We compare in Table 37 the resolution measured in a point source placed at the center of the FOV. It shows good agreement of simulations and experiment for both reconstruction methods. The same good agreement is observed in Figure 90, where activity profiles along the *Z* direction are plotted for the noRR-GFIRST (Figure 90A) and the RR-GFIRST (Figure 90B) methods. In Figure 90C we also compare the experimental activity profile with and without resolution recovery, in order to see the effect of including resolution effects.

(A) (B)

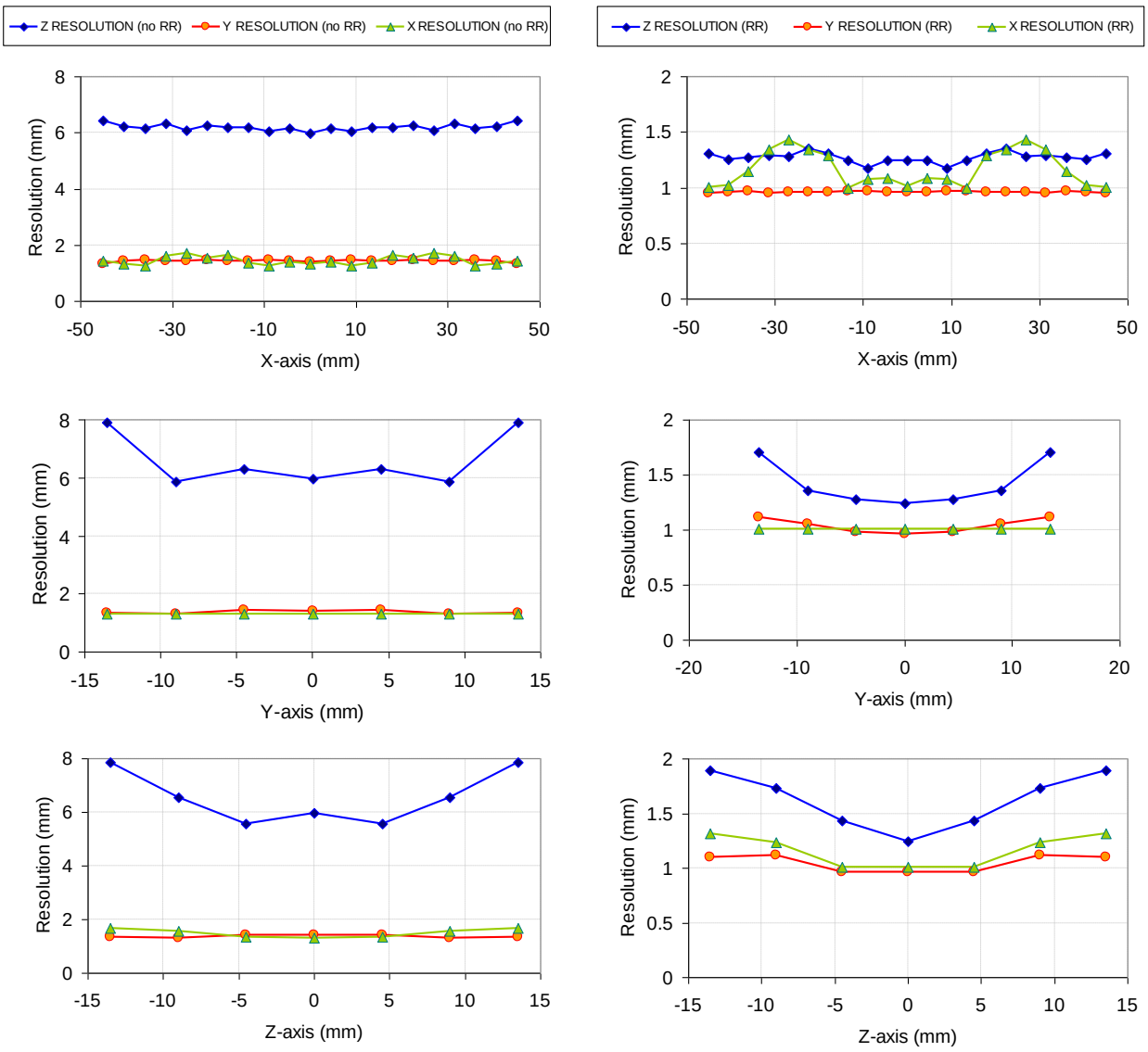

Figure 89. *Resolution profiles along the 3 axes. Left (**A**, **B** and **C**): Reconstruction without resolution recovery (no RR). Right (**D**, **E** and **F**): Reconstruction with resolution recovery (RR).*

Table 37. *Experimental vs. simulated resolution for a point source at the center of the FOV.*

		cFOV FWHM (mm)		
		X	**Y**	**Z**
No PSF	**Simulated data**	1.2	1.2	5.4
	Measured data	1.2	1.2	5.5
PSF info	**Simulated data**	0.8	0.8	1.1
	Measured data	0.9	0.8	1.2

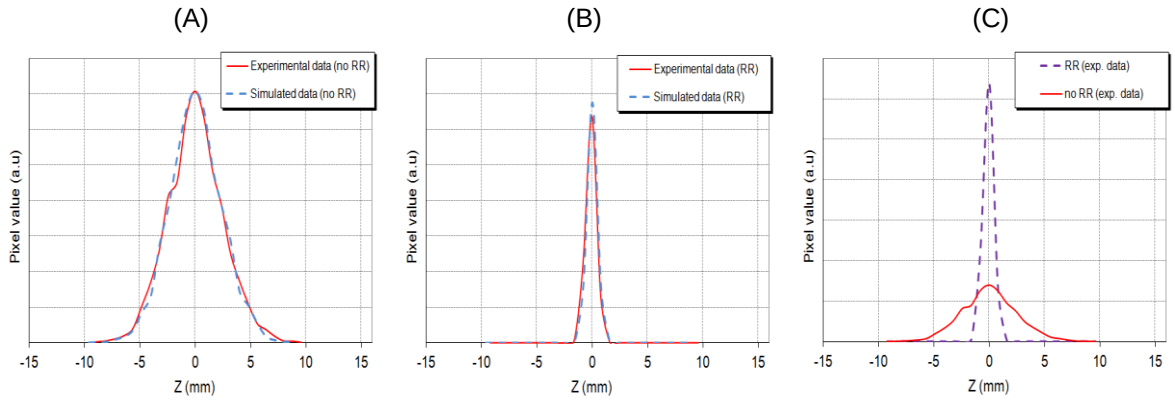

Figure 90. *Experimental vs. simulated data comparison for a point source placed at the center of the FOV.* ***(A)****: Reconstruction without PSF information.* ***(B)****: Reconstruction with PSF information*

Finally, we compare in Table 38 resolution values at several *Z* positions (with *X*=0 and *Y*=0) for the PPI_{39mm} with the values reported in [Zhang *et al.*, 2011] for the PETbox system. The PPI_{39mm} resolution values were obtained using the resolution recovery method (RR-GFIRST) since the PETbox values were obtained using an iterative reconstruction method based on ML-EM algorithm with the incorporation of a system probability matrix (P-matrix) [Bao *et al.*, 2009b]. We observe that the resolution of the PPI system is better in the three directions. This is because the individual crystal elements of the PPI system have smaller cross-section size (PPI: 1.5×1.5 mm^2, PETbox: 2×2 mm^2) and the block detectors are closer in the PPI system (3.9 cm for the PPI vs 5 cm for the PETbox) resulting in a less incomplete LOR collection in comparison with the PETbox.

Table 38. *Spatial resolution at different Z positions (with X=0 and Y=0) for the PPI_{39mm} and the PETbox systems.*

System	Z position (mm)	FWHM (mm) at (0,0,*Z*)		
		X	Y	Z
PPI_{39mm} (simulated data)	**0**	1.0	1.0	1.2
	4.5	1.0	1.0	1.4
	9	1.2	1.1	1.7
PETbox [Zhang *et al.*, 2011]	**0**	1.6	1.5	2.6
	6	1.5	1.4	2.7

5.2.4.3. Initial imaging studies

Figure 91 shows the reconstructed images from the initial simulated imaging study described in Figure 86. The upper figures show three views of the image obtained without resolution recovery (left) and with resolution recovery (right). We can observe how resolution is recovered in *Z* direction when the shift-invariant blurring component, defined as an effective PSF, is included in the reconstruction. This improvement in resolution can also be seen in the profile drawn along the Z direction (Figure 91, down). However there remains room for improvement in the reconstruction method, for instance, we can see that the point sources at the edges of the matrix in *Y* direction have less intensity than the central ones and the regularization presented above did not improve the result.

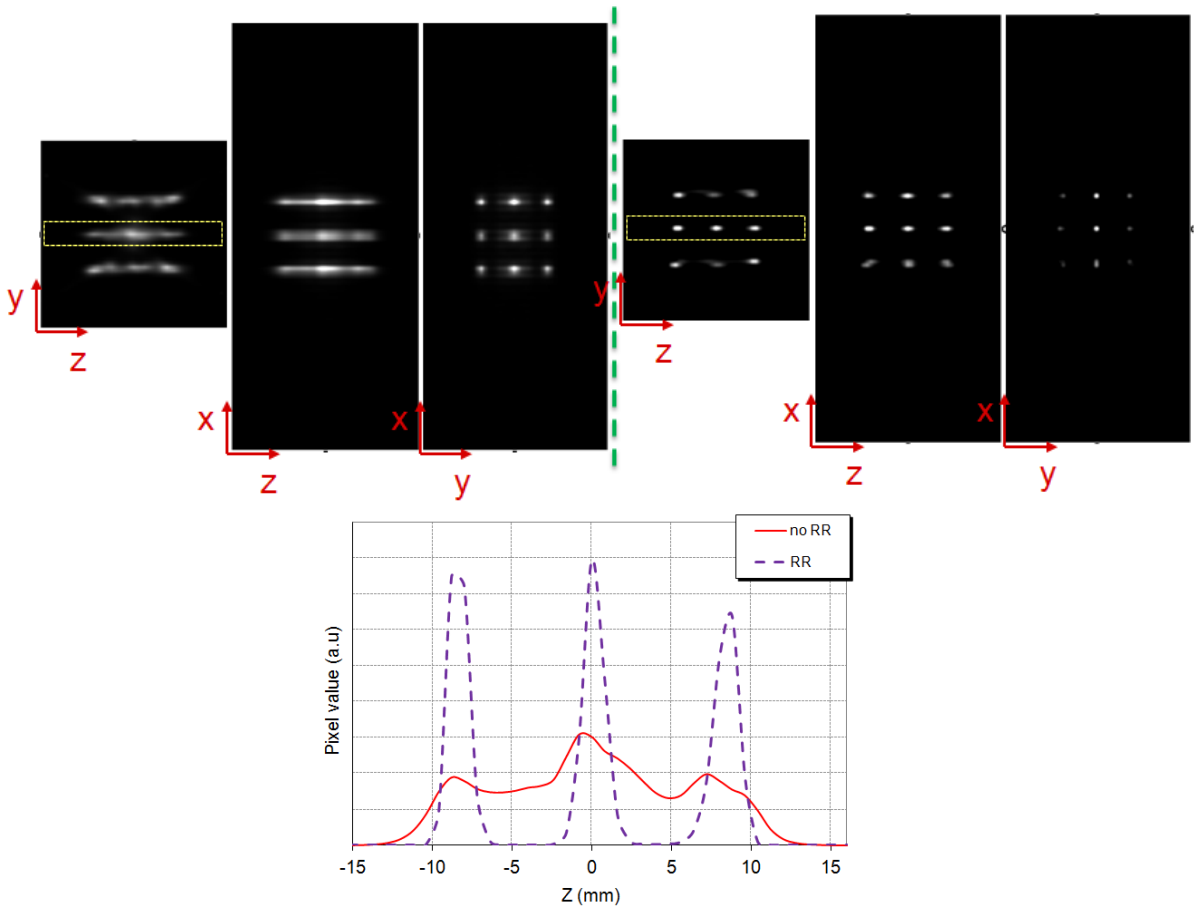

Figure 91. *Reconstruction of a simulated (3×3×3) matrix of point sources for the PPI_{39mm} configuration in the 100-650 keV energy window. Upper row shows the image reconstructed with the noRR-GFIRST code (left, 5 iterations) and the RR-GFIRST one (right, 200 iterations). Lower row shows an activity profile along Z axis as it is marked (dashed lines) in the upper images.*

Figure 92 shows a comparison of the parallel imaging method (cone angle of 5.0 degrees) and the RR-GFIRST with and without regularization. The two 3D images were 2D-projected (average intensity) in order to compare with the parallel imaging method. The first image in Figure 92 (left) corresponds to the parallel imaging method, the next one (center) is the 3D reconstruction with resolution recovery (20 iterations) and the third one is the 3D reconstruction with resolution recovery and regularization (200 iterations, applying regularization in the first 150). We can observe that the parallel imaging method is already a good estimation of the distribution of the ^{18}F in the mouse. The 3D methods get better results largely improving the resolution, even allowing distinguishing small structures as, for example, ribs, bowels and the peculiar shape of the mouse elbow. An evident improvement in image quality for the reconstruction (right) with regularization is also observed.

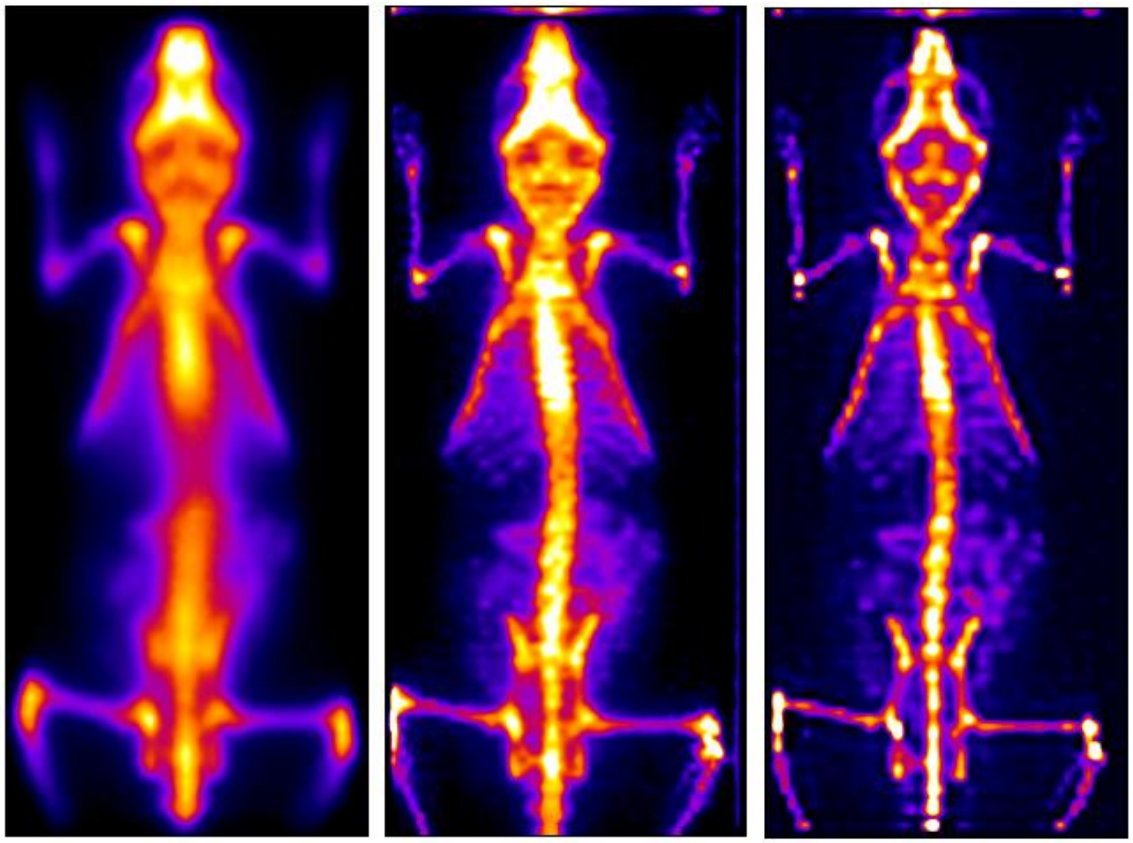

Figure 92. *2D-projection of the mouse bone scan acquisition.* ***Left****: parallel imaging method;* ***center****: RR-GFISRT method (20 iterations);* ***right****: RRr-GFIRST (200 iterations, applying regularization in the first 150). The two 3D images (center and right) were 2D-projected (average intensity) in order to compare with the parallel imaging method.*

Figure 93 shows an example of the chessboard artifact in the XY plane when no regularization is applied in the reconstruction and the number of iterations is increased from 20 to 100.

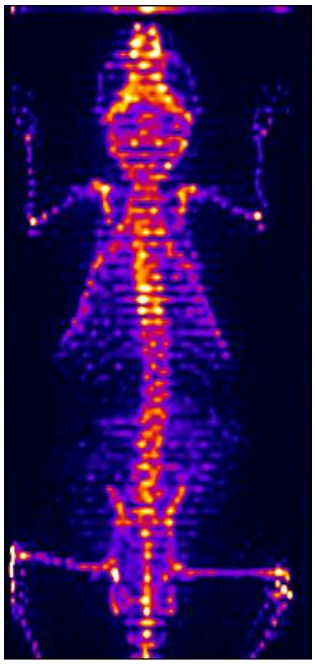

Figure 93. *Example of the chessboard artifact in XY plane when no regularization is applied in the reconstruction. The image is a 2D-projection of the mouse bone scan acquisition reconstructed using the GFIRST with resolution recovery with 100 iterations.*

However the interesting improvement here is in *Z* direction. In order to show the resolution increase when regularization is applied to control convergence in the *XY* plane, we present in Figure 94 and Figure 95 an image sequence of a volume render for each reconstruction method (without and with regularization respectively). The image sequence is a set of 18 images of a 180º rotation of the mouse.

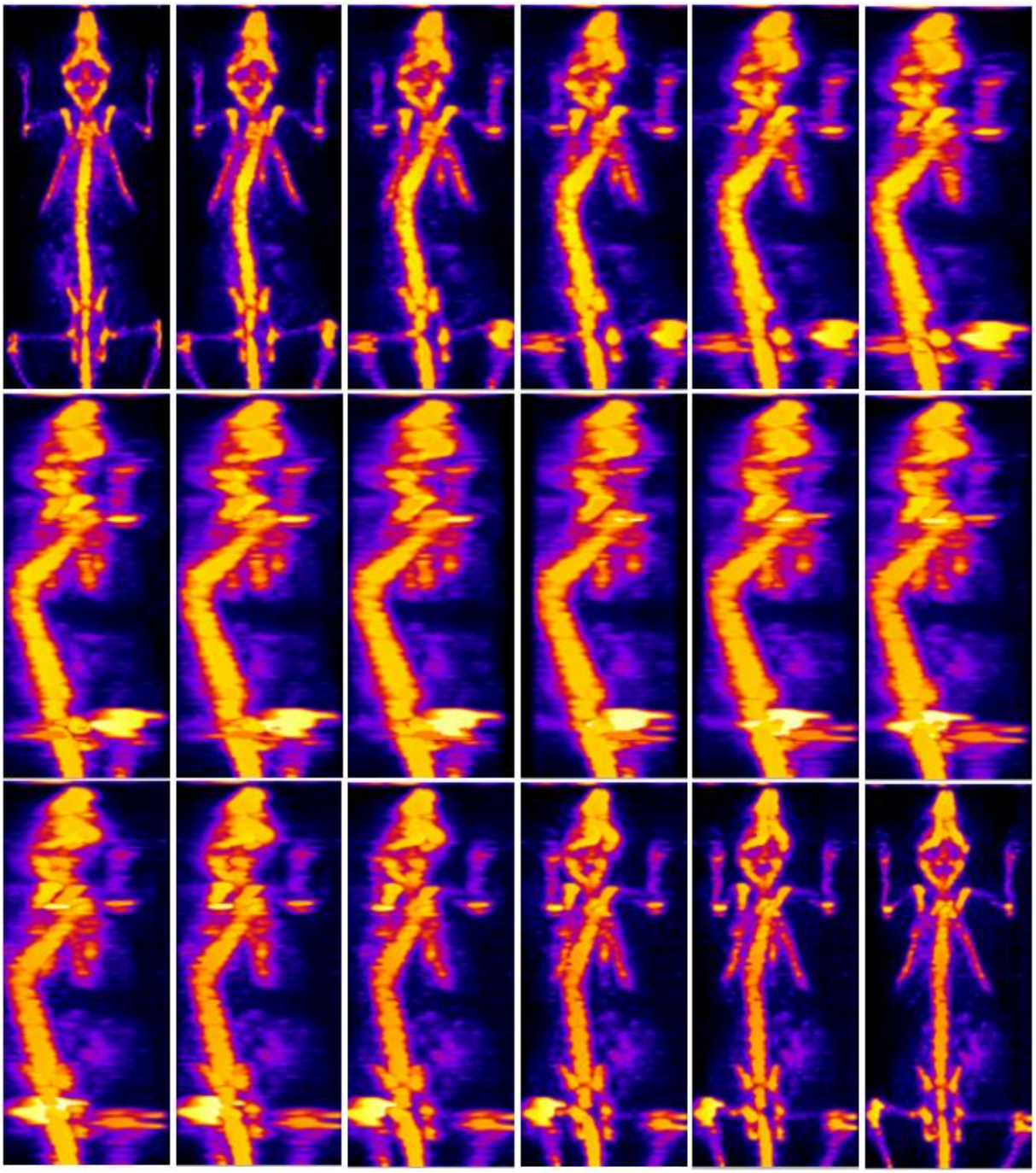

Figure 94. *Image sequence of a volume render of the mouse bone scan reconstructed with the RR-GFIRST. The sequence is a set of 18 images showing the 180º rotation of the mouse. The number of iterations was set to 20 in order to avoid chessboard artifacts in the XY plane.*

Figure 94 (3D reconstruction without regularization) shows a good estimation of the ^{18}F activity in the mouse for *XY* plane, which is deteriorated in *Z* direction with resolutions more than double the *XY* ones. Regularization, as it was explained in section 5.2.2.4, allows to increase the number of iterations from 20 (Figure 94) to 200 (Figure 95), controlling the convergence in *XY* in the first 150. The resulting image has still better resolution in *XY* plane than in *Z* direction, but the *Z* resolution improves vastly.

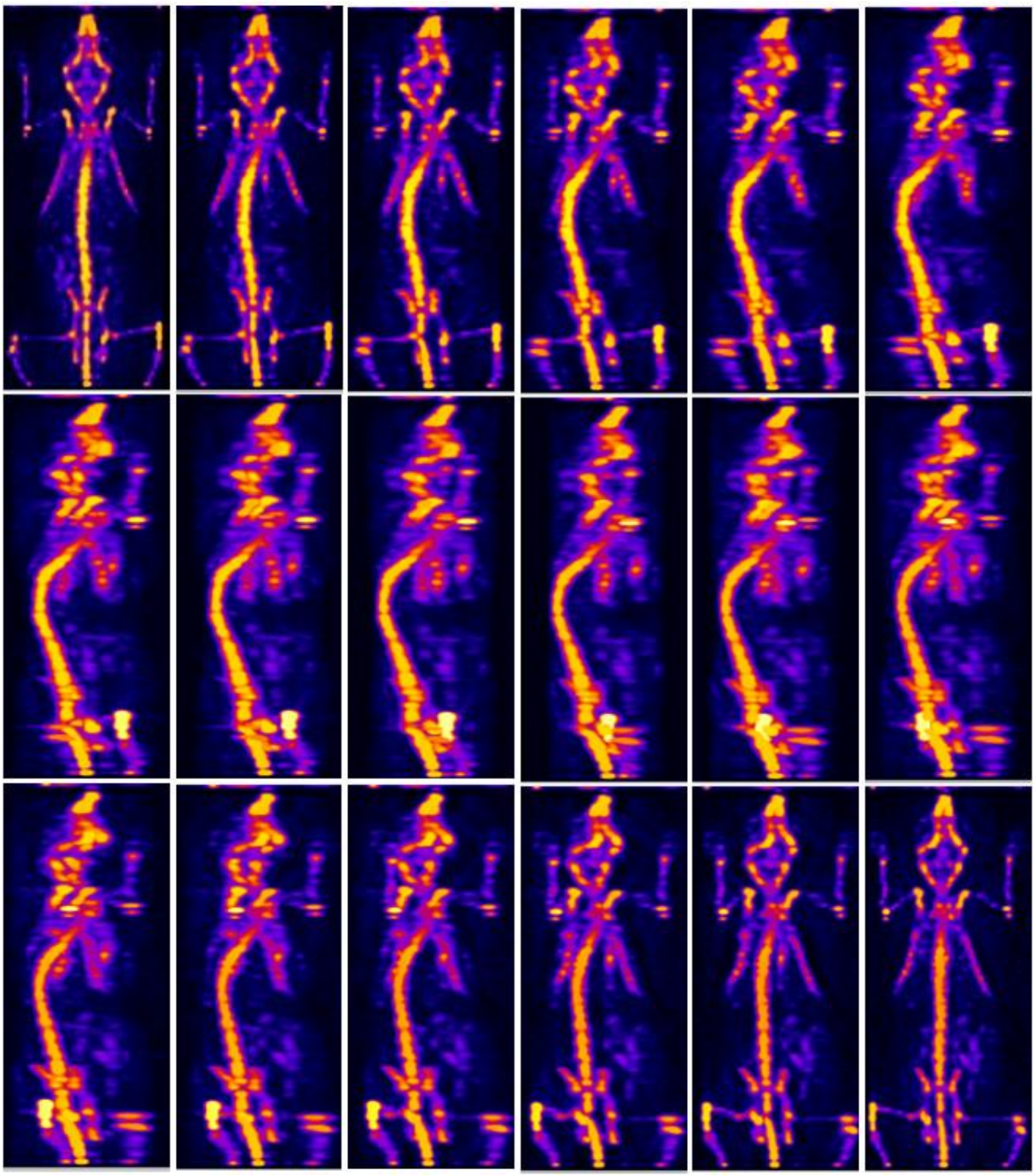

Figure 95. *Image sequence of a volume render of the mouse bone scan reconstructed with the RRr-GFIRST. The sequence is a set of 18 images showing the 180º rotation of the mouse. The number of iterations was set to 200, applying regularization in X and Y directions in the first 150.*

5.2.5. Conclusions

The PPI system was designed as low cost option for studies in mice. Compared with commercially available small animal PET scanners, the bench top configuration of this system greatly reduces the cost as well as the space needed for researchers to access PET imaging technology. While a very high performance scanner was not the goal of the PPI design, the key performance metrics for the system were chosen to satisfy typical resolution and sensitivity requirements. This section demonstrates that the prototype system meets the design specifications.

Due to the dual-head geometry, the PPI system provides a limited angle tomography along the direction between detectors (*Z* direction). Image reconstruction for such geometry depends on the accurate system modeling [Moses and Qi, 2003]. In this work, different approaches and new reconstruction methods has been implemented from a parallel imaging method which provides planar 2D images without information of the *Z* direction, to more accurate 3D-mode reconstructions based on GFIRST [Herraiz *et al.*, 2011] with three different approximations. In the first one, we used a simplified version of the probability matrix, disregarding resolution effects. This method was employed to measure the spatial resolution of the system since the quality of the resulting images is comparable, in terms of spatial resolution, to a FBP reconstruction, the standard reconstruction method to measure the spatial resolution in PET scanners. In the second 3D-mode method, we included resolution effects by means of a shift-invariant blurring component defined as an effective point spread function (PSF) and an unmatched forward-/back-projector pair to increase the convergence rate of the algorithm. Finally, a novel method was implemented, improving the latter method with an extra blurring component to regularize the convergence in *X* and *Y* directions.

This work has shown that the PPI system has very competitive sensitivities values, being some experimental ACS values, for example: 10% at 100-650 keV, 7% at 250-650 keV and 5% at 400-650 keV. These results improve the sensitivity of the PETbox system [Zhang *et al.*, 2010, Zhang *et al.*, 2011], being the PPI sensitivity at 400-650 keV window about the same as the PETbox at 100-650 keV window. The PPI system also improves most of the sensitivity values of full-ring scanners. Regarding to the resolution measurements, the system has high resolution in the *XY* plane with values less than 1.8 mm and practically uniform in all the FOV (which can fits a whole body mouse). However, the incomplete LOR collection due to the system geometry results in degradation of the *Z* resolution, with values mostly above 6 mm when no resolution recovery is applied in the reconstruction. These differences are reduced using PSF information in the reconstruction. Then the *Z* resolution is still the worse value, but reasonably under 1.8 mm in Z direction and under 1.4 mm in the other two directions.

Finally, the initial images showed in this work, using the aforementioned reconstruction methods, have demonstrated the imaging capabilities of the PPI system and the potential of the novel reconstruction method with regularization.

5.3. References

Agostinelli, S. 2003. GEANT4 - a simulation toolkit. *Nucl. Inst. Meth. In Phy. Res. A,* 506**,** 250-303.

Bao, Q., Newport, D., Chen, M., Stout, D. B. & Chatziioannou, A. F. 2009a. Performance evaluation of the inveon dedicated PET preclinical tomograph based on the NEMA NU-4 standards. *J Nucl Med,* 50**,** 401-8.

Bao, Q., Rannou, F. R., Taschereau, R., Stout, D. B. & Chatziioannou, A. F. 2009b. Image reconstruction for PETbox, a benchtop preclinical PET tomograph. *In:* Nuclear Science Symposium Conference Record (NSS/MIC), 2009 IEEE, Oct. 24 2009-Nov. 1 2009 2009b. 2733-2737.

Baró, J., Sempau, J., Fernández-Varea, J. M. & Salvat, F. 1995. PENELOPE: An algorithm for Monte Carlo simulation of the penetration and energy loss of electrons and positrons in matter. *Nucl. Inst. Meth. In Phy. Res. B,* 100**,** 31-46.

Bergeron, M., Cadorette, J., Bureau-Oxton, C., Beaudoin, J. F., Tetrault, M. A., Leroux, J. D., Lepage, M. D., Robert, G., Fontaine, R. & Lecomte, R. 2009. Performance evaluation of the LabPET12, a large axial FOV APD-based digital PET scanner. *In:* Nuclear Science Symposium Conference Record (NSS/MIC), 2009 IEEE, Oct. 24 2009-Nov. 1 2009 2009. 4017-4021.

Briesmeister, J. F. 1993. MNCP 4 A, Monte Carlo N-Particle Transport System. Los Alamos, New Mexico: Los Alamos National Laboratory.

Clinthorne, N. H., Sangjune, P., Rogers, W. L. & Ping-Chun, C. 2003. Multi-resolution image reconstruction for a high-resolution small animal PET device. *In:* Nuclear Science Symposium Conference Record, 2003 IEEE, 19-25 Oct. 2003 2003. 1997-2001 Vol.3.

Chatziioannou, A. F. 2002. PET scanners dedicated to molecular imaging of small animal models. *Mol Imaging Biol,* 4**,** 47-63.

Dai, S., Han, M., Xu, W., Wu, Y. & Gong, Y. 2007. Soft Edge Smoothness Prior for Alpha Channel Super Resolution. *In:* Computer Vision and Pattern Recognition, 2007. CVPR '07. IEEE Conference on, 17-22 June 2007 2007. 1-8.

España, S., Herraiz, J. L., Vicente, E., Vaquero, J. J., Desco, M. & Udias, J. M. 2009. PeneloPET, a Monte Carlo PET simulation tool based on PENELOPE: features and validation. *Phys Med Biol,* 54**,** 1723-42.

Harrison, R. L., Vannoy, S. D., Haynor, D. R., Gillispie, S. B., Kaplan, M. S. & Lewellen, T. K. 1993. Preliminary Experience With The Photon History Generator Module Of A Public-domain Simulation System For Emission Tomography. *In:* Nuclear Science Symposium and Medical Imaging Conference, 1993., 1993 IEEE Conference Record., 31 Oct-6 Nov 1993 1993. 1154-1158.

Heinrichs, U., Pietrzyk, U. & Ziemons, K. 2003. Design optimization of the PMT-ClearPET prototypes based on simulation studies with GEANT3. *Nuclear Science, IEEE Transactions on,* 50**,** 1428-1432.

Herraiz, J. L., Espana, S., Vaquero, J. J., Desco, M. & Udias, J. M. 2006a. FIRST: Fast Iterative Reconstruction Software for (PET) tomography. *Phys Med Biol,* 51**,** 4547-65.

Herraiz, J. L., España, S., Cabido, R., Montemayor, A. S., Desco, M., Vaquero, J. J. & Udias, J. M. 2011. GPU-Based Fast Iterative Reconstruction of Fully 3-D PET Sinograms. *Nuclear Science, IEEE Transactions on,* 58**,** 2257-2263.

Hudson, H. M. & Larkin, R. S. 1994. Accelerated image reconstruction using ordered subsets of projection data. *Medical Imaging, IEEE Transactions on,* 13**,** 601-609.

Huh, S. S., Rogers, W. L. & Clinthorne, N. H. 2008. On-line sliding-window list-mode PET image reconstruction for a surgical pet imaging probe. *In:* Nuclear Science Symposium Conference Record, 2008. NSS '08. IEEE, 19-25 Oct. 2008 2008. 5479-5484.

James, S. S., Yang, Y., Wu, Y., Farrell, R., Dokhale, P., Shah, K. S. & Cherry, S. R. 2009. Experimental characterization and system simulations of depth of interaction PET detectors using 0.5 mm and 0.7 mm LSO arrays. *Phys Med Biol,* 54**,** 4605-19.

Jan, S., Santin, G., Strul, D., Staelens, S., Assie, K., Autret, D., Avner, S., Barbier, R., Bardies, M., Bloomfield, P. M., Brasse, D., Breton, V., Bruyndonckx, P., Buvat, I., Chatziioannou, A. F., Choi, Y., Chung, Y. H., Comtat, C., Donnarieix, D., Ferrer, L., Glick, S. J., Groiselle, C. J., Guez, D., Honore, P. F., Kerhoas-Cavata, S., Kirov, A. S., Kohli, V., Koole, M., Krieguer, M., van der Laan, D. J., Lamare, F., Largeron, G., Lartizien, C., Lazaro, D., Maas, M. C., Maigne, L., Mayet, F., Melot, F., Merheb, C., Pennacchio, E., Perez, J., Pietrzyk, U., Rannou, F. R., Rey, M., Schaart, D. R., Schmidtlein, C. R., Simon, L., Song, T. Y., Vieira, J. M., Visvikis, D., Van de Walle, R., Wieers, E. & Morel, C. 2004b. GATE: a simulation toolkit for PET and SPECT. *Phys Med Biol,* 49**,** 4543-61.

Janecek, M., Heyu, W. & Yuan-Chuan, T. 2006. A simulation study for the design of a prototype insert for whole-body PET scanners. *Nuclear Science, IEEE Transactions on,* 53**,** 1143-1149.

Kao, C.-M., Xie, Q., Dong, Y., Wan, L. & Chen, C.-T. 2009. A High-Sensitivity Small-Animal PET Scanner: Development and Initial Performance Measurements. *Nuclear Science, IEEE Transactions on,* 56**,** 2678-2688.

Keesing, D. B., Pal, D., O'Sullivan, J. A., Komarov, S., Wu, H. & Tai, Y.-C. 2008. System modeling of a DOI-capable half-ring PET insert device for breast cancer imaging. *In:* Nuclear Science Symposium Conference Record,

2008. NSS '08. IEEE, 19-25 Oct. 2008 2008. 4218-4222.

Knoess, C., Siegel, S., Smith, A., Newport, D., Richerzhagen, N., Winkeler, A., Jacobs, A., Goble, R. N., Graf, R., Wienhard, K. & Heiss, W. D. 2003. Performance evaluation of the microPET R4 PET scanner for rodents. *Eur J Nucl Med Mol Imaging,* 30**,** 737-47.

Kupinski, M. A. & Barrett, H. H. 2005. *Small-animal Spect Imaging,* Springer.

Miyaoka, R. S., Janes, M. L., Lee, K., Park, B., Kinahan, P. E. & Lewellen, T. K. 2005. Development of a single detector ring micro crystal element scanner: QuickPET II. *Mol Imaging,* 4**,** 117-27.

Moses, W. W. & Qi, J. 2003. Fundamental limits of positron emission mammography. *Nuclear Instruments and Methods in Physics Research Section A: Accelerators, Spectrometers, Detectors and Associated Equipment,* 497**,** 82-89.

Park, S. J., Rogers, W. L. & Clinthorne, N. H. 2007. Design of a very high-resolution small animal PET scanner using a silicon scatter detector insert. *Phys Med Biol,* 52**,** 4653-77.

Pavlopoulos, S. & Tzanakos, G. 1993. Design and performance evaluation of a high resolution small animal positron tomograph. *In:* Nuclear Science Symposium and Medical Imaging Conference, 1993., 1993 IEEE Conference Record., 31 Oct-6 Nov 1993 1993. 1697-1701 vol.3.

Pavlopoulos, S. & Tzanakos, G. 1996. Design and performance evaluation of a high-resolution small animal positron tomograph. *Nuclear Science, IEEE Transactions on,* 43**,** 3249-3255.

Qi, J., Yang, Y., Zhou, J., Wu, Y. & Cherry, S., R. 2011. Experimental assessment of resolution improvement of a zoom-in PET. *Physics in Medicine and Biology,* 56**,** N165.

Rogers, D. W. O. 1984. Low energy electron transport with EGS. *Nucl. Inst. Meth. In Phy. Res. A,* 227**,** 535-48.

Rouze, N. C., Schmand, M., Siegel, S. & Hutchins, G. D. 2004. Design of a small animal PET imaging system with 1 microliter volume resolution. *Nuclear Science, IEEE Transactions on,* 51**,** 757-763.

Seidel, J., Wenze, X., Kakareka, J. W., Pohida, T. J., Green, M. V. & Choyke, P. L. 2010. A positron projection imager for whole-body mouse imaging. *In:* Nuclear Science Symposium Conference Record (NSS/MIC), 2010 IEEE, Oct. 30 2010-Nov. 6 2010 2010. 2206-2209.

Shepp, L. A. & Vardi, Y. 1982. Maximum Likelihood Reconstruction for Emission Tomography. *Medical Imaging, IEEE Transactions on,* 1**,** 113-122.

Stickel, J. R. & Cherry, S. R. 2005. High-resolution PET detector design: modelling components of intrinsic spatial resolution. *Phys Med Biol,* 50**,** 179-95.

Tai, C., Chatziioannou, A., Siegel, S., Young, J., Newport, D., Goble, R. N., Nutt, R. E. & Cherry, S. R. 2001. Performance evaluation of the microPET P4: a PET system dedicated to animal imaging. *Phys Med Biol,* 46**,** 1845-62.

Tai, Y. C., Chatziioannou, A. F., Yang, Y., Silverman, R. W., Meadors, K., Siegel, S., Newport, D. F., Stickel, J. R. & Cherry, S. R. 2003. MicroPET II: design, development and initial performance of an improved microPET scanner for small-animal imaging. *Phys Med Biol,* 48**,** 1519-37.

Tai, Y. C., Wu, H., Pal, D. & O'Sullivan, J. A. 2008. Virtual-pinhole PET. *J Nucl Med,* 49**,** 471-9.

Thompson, C. J., Moreno-Cantu, J. & Picard, Y. 1992a. PETSIM: Monte Carlo simulation of all sensitivity and resolution parameters of cylindrical positron imaging systems. *Physics in Medicine and Biology,* 37**,** 731.

Thompson, C. J., Moreno-Cantu, J. & Picard, Y. 1992b. PETSIM: Monte Carlo simulation of all sensitivity and resolution parameters of cylindrical positron imaging systems. *Phys Med Biol,* 37**,** 731-49.

Tzanakos, G. & Pavlopoulos, S. 1991. Modeling and simulation of a PET scanner. *In:* Nuclear Science Symposium and Medical Imaging Conference, 1991., Conference Record of the 1991 IEEE, 2-9 Nov. 1991 1991. 1689-1694 vol.3.

Tzanakos, G. & Pavlopoulos, S. 1993. Design and performance evaluation of a new high resolution detector array module for PET. *In:* Nuclear Science Symposium and Medical Imaging Conference, 1993., 1993 IEEE Conference Record., 31 Oct-6 Nov 1993 1993. 1842-1846 vol.3.

Urosevic, J., Sauzeau, V., Soto-Montenegro, M. L., Reig, S., Desco, M., Burkitt Wright, E. M., Cañamero, M., Mulero, F., Ortega, S., Bustelo, X. R. & Barbacid, M. 2011. Constitutive activation of B-Raf in the mouse germ line provides a model for human cardio-facio-cutaneous syndrome. *P Natl Acad Sci USA,* 108**,** 5015-5020.

Vicente, E., Herraiz, J. L., Seidel, J., Green, M. V., Desco, M., Vaquero, J. J. & Udias, J. M. 2012b. Regularization of 3D Iterative Reconstruction for a Limited-Angle PET Tomograph. *In:* Nuclear Science Symposium Conference Record (NSS/MIC), 2012 IEEE (*Accepted*), 2012b.

Visser, E. P., Disselhorst, J. A., Brom, M., Laverman, P., Gotthardt, M., Oyen, W. J. & Boerman, O. C. 2009. Spatial resolution and sensitivity of the Inveon small-animal PET scanner. *J Nucl Med,* 50**,** 139-47.

Wang, Y., Seidel, J., Tsui, B. M., Vaquero, J. J. & Pomper, M. G. 2006b. Performance evaluation of the GE healthcare eXplore VISTA dual-ring small-animal PET scanner. *J Nucl Med,* 47**,** 1891-900.

Watanabe, M., Uchida, H., Okada, H., Shimizu, K., Satoh, N., Yoshikawa, E., Ohmura, T., Yamashita, T. & Tanaka, E. 1992. A high resolution PET for animal studies. *Medical Imaging, IEEE Transactions on,* 11**,** 577-580.

Wu, H., Pal, D., O'Sullivan, J. A. & Tai, Y. C. 2008a. A feasibility study of a prototype PET insert device to convert a general-purpose animal PET scanner to higher resolution. *J Nucl Med,* 49**,** 79-87.

Wu, H., Pal, D., Song, T. Y., O'Sullivan, J. A. & Tai, Y. C. 2008b. Micro insert: a prototype full-ring PET device for improving the image resolution of a small-animal PET scanner. *J Nucl Med,* 49**,** 1668-76.

Wu, H., Song, T. Y., Pal, D., Keesing, D. B., Komarov, S., O Sullivan, J. A. & Tai, Y.-C. 2008c. A high resolution PET insert system for clinical PET/CT scanners. *In:* Nuclear Science Symposium Conference Record, 2008. NSS '08. IEEE, 19-25 Oct. 2008 2008c. 5442-5444.

Yang, Y., Dokhale, P. A., Silverman, R. W., Shah, K. S., McClish, M. A., Farrell, R., Entine, G. & Cherry, S. R. 2006. Depth of interaction resolution measurements for a high resolution PET detector using position sensitive avalanche photodiodes. *Phys Med Biol,* 51**,** 2131-42.

Yang, Y., Tai, Y. C., Siegel, S., Newport, D. F., Bai, B., Li, Q., Leahy, R. M. & Cherry, S. R. 2004. Optimization and performance evaluation of the microPET II scanner for in vivo small-animal imaging. *Phys Med Biol,* 49**,** 2527-45.

Zaidi, H. & Scheurer, C. 1999. An object-oriented Monte Carlo simulator for 3D cylindrical positron tomographs. *Comput. Methods Programs Biomed.,* 58**,** 133-45.

Zeng, G. L. & Gullberg, G. T. 2000. Unmatched projector/backprojector pairs in an iterative reconstruction algorithm. *Medical Imaging, IEEE Transactions on,* 19**,** 548-555.

Zhang, H., Bao, Q., Vu, N. T., Silverman, R. W., Taschereau, R., Berry-Pusey, B. N., Douraghy, A., Rannou, F. R., Stout, D. B. & Chatziioannou, A. F. 2011. Performance evaluation of PETbox: a low cost bench top preclinical PET scanner. *Mol Imaging Biol,* 13**,** 949-61.

Zhou, J. & Qi, J. 2009. Theoretical analysis and simulation study of a high-resolution zoom-in PET system. *Physics in Medicine and Biology,* 54**,** 5193.

Zhou, J. & Qi, J. 2010. Efficient system modeling of a high-resolution zoom-in PET scanner. *In:* Nuclear Science Symposium Conference Record (NSS/MIC), 2010 IEEE, Oct. 30 2010-Nov. 6 2010 2010. 3501-3505.

Zhou, J. & Qi, J. 2011. Adaptive Imaging for Lesion Detection Using a Zoom-in PET System. *Medical Imaging, IEEE Transactions on,* 30**,** 119-130.

Conclusions of this Thesis

Small-animal PET is a complex technique, which has gained increasing impact in recent years due to the development of dedicated systems. There remain many challenges regarding instrumentation, data evaluation and experimentation, which need to be overcome in order to achieve reliable and valuable small animal PET data.

This thesis has presented original contributions to the study of the sources of error that limit the quality of PET images providing new methods and algorithms to compensate them, and improvements in Monte Carlo simulations and existing reconstruction codes to extend them to the non-conventional geometry of new modern designs.

The main contributions of this thesis are:

1. A detailed performance evaluation of two dedicated small-animal scanners with very different geometries and features, the SEDECAL rPET and the SEDECAL Argus systems, showing the importance of standardized protocols to assess the performance. A critical comparison between these two scanners and to other preclinical PET systems available on the market has been also briefly presented, showing that both scanners have very competitive features improving in some parameters the performance of other commercial systems.

2. It has also been shown that the protocols to assess the scanner performance are not flawless, analyzing in detail some examples and, with the help of very detailed and realistic simulations, we have proposed improvements on some procedures. An example of these proposals is a way to upgrade the NEMA protocol to measure scatter fraction to make it isotope range-independent. This extension to the NEMA protocol includes a deconvolution of the radial sinogram profiles using a one-dimensional distribution of the positron range in order to remove range effects from sinogram profiles. The improved protocol has been tested for ^{68}Ga, a radionuclide with large positron range, yielding the same results than using ^{18}F, the isotope proposed by NEMA.

3. From the limitations observed in the scanners evaluated, new correction methods and algorithms have been developed. They are relevant not only for these particular scanners, but easily adaptable to different architectures provided they comply with certain common design constraints. Namely:

   3.1. A new method to linearize the total count rates getting rid of non linear effects due to dead-time losses and pile-up losses and gains within the selected energy window. The method is based on the linear relationship between the effective dead-time (which takes into account dead-time and pile-up effects) τ, and the Singles-to-Coincidences ratio (SCR). Results have shown that, using the proposed method, corrected count rates are accurate within 7%, even when high activities are present in the FOV, avoiding the bias that appears when using a single-parameter procedure. We have verified the method using experimental and simulated data from rPET and Argus systems, demonstrating its applicability.

   3.2. A novel calibration protocol developed and implemented in a software tool, to compensate the effect of small mechanical misalignments in rotating PET systems with planar detectors. This calibration tool determines the misalignments within acceptable tolerance in each geometrical parameter. The results highlight the importance of the characterization of detector misalignment whose effect, if they are not properly corrected, may result in loss of resolution and artifacts with severe degradation of the reconstructed image.

   3.3. An attenuation correction based on Computed Tomography (CT) images. PET images

corrected with the tool presented in this thesis have demonstrated to exhibit better quantification and more consistency between the reconstructed image and the acquired data than the ones obtained with simpler methods, as for example an attenuation correction based on a FOV-sized water cylinder.

4. Making use of all the experience gained during the characterization of the scanners and the study of the sources of error that limit the quality of the images, Monte Carlo simulation tools have been developed and extended to guide in the design of new prototypes, performing as well the necessary modifications in the available reconstruction methods to adapt the existing codes to the non-conventional geometry of the new designs. Two different new designs have been studied:

   4.1. Zoom-in PET scanner: a high-resolution detector centered in the axial field of view of the microPET II scanner with only one axial ring. Monte Carlo simulation studies were performed with a modified version of the PeneloPET package. This modification was required in order to support the non-standard geometrical configuration of this scanner. This study is an example of how simulated data can help to guide the design of new prototypes, analyzing all the advantages and drawbacks before taking the final decision on the construction. The results obtained suggested to modify the geometry of the system, for example, by adding more axial rings to the microPET II system and further trying to shield the insert to avoid single events from outside the axial FOV to reach the insert.

   4.2. NIH PPI: a low-cost high-sensitivity bench-top preclinical PET system consisting of a compact dual stationary head geometry. This system is a limited angle tomography system, with very poor sampling in the direction perpendicular to the detectors. Due to this poor sampling in one direction, it has been necessary to develop new approaches for the reconstruction, such as a new regularization procedure for a 3D reconstruction algorithm which employs variable, direction-dependent filtering between iterations, allowing for the convergence speed to be more isotropic. The performance evaluation presented has demonstrated that the prototype system meets the intended design specifications. The initial images have shown the imaging capabilities of the PPI system and the potential of the novel reconstruction method with regularization.

As a summarizing conclusion, this thesis shows the power of detailed MC simulations in the improvement of existing scanners and performance assessment protocols and in the design of new scanners.

The results described in conclusions 3.2 and 3.3 have been transferred to the industry and an implementation is integrated on the small-animal, high-resolution molecular imaging systems manufactured by SEDECAL (Madrid, Spain) and distributed world-wide.

Publications Derived from this Thesis

Papers Published in International Journals

1. A. L. Goertzen, Q. Bao, M. Bergeron, E. Blankemeyer, S. Blinder, M. Cañadas, A. F. Chatziioannou, K. Dinelle, E. Elhami, H.-S. Jans, E. Lage, R. Lecomte, V. Sossi, S. Surti, Y.-C. Tai, J. J. Vaquero, **E. Vicente**, D. A. Williams, and R. Laforest, "*NEMA NU 4-2008 Comparison of Preclinical PET Imaging Systems*," *The Journal of Nuclear Medicine (Accepted)*, 2012.
2. J Cal-González, JL Herraiz, S España, **E Vicente**, E Herranz, M Desco, JJ Vaquero, JM Udías. *"Study of CT-based positron range correction in high resolution 3D PET imaging"*. Nucl Instrum Meth A, S172-S175, 2011.
3. S España, JL Herraiz, **E Vicente**, JJ Vaquero, M Desco, JM Udías. *"PeneloPET, a Monte Carlo PET simulation tool based on PENELOPE: features and validation"*. Phys Med Biol, 54(6): 1723-1742, 2009.
4. JL Herráiz, S España, **E Vicente**, JJ Vaquero, M Desco, JM Udías. *"Noise and physical limits to maximum resolution of PET images"*. Nucl Instrum Meth A, 580(2): 934-937, 2007.

Papers Submitted to International Journals

1. **E. Vicente**, J. L. Herraiz, S. España, E. Herranz, M. Desco, J. J. Vaquero, and J. M. Udías, "*Improved effective dead-time correction for PET scanners: Application to small-animal PET*," *Phys Med Biol (Submitted)*, 2012.
2. M. Abella[§], **E. Vicente**[§], A. Rodríguez-Ruano, S. España, E. Lage, M. Desco, J. M. Udias, and J. J. Vaquero, "*Misalignments calibration in small-animal PET scanners based on rotating planar detectors and parallel-beam geometry*," *Phys Med Biol (Submitted)*, 2012.

[§] These authors contributed equally to this work.

Conference Proceedings

1. **E. Vicente**, J. L. Herraiz, J. Seidel, M. V. Green, M. Desco, J. J. Vaquero, and J. M. Udias, "*Regularization of 3D Iterative Reconstruction for a Limited-Angle PET Tomograph*," in *Nuclear Science Symposium Conference Record (NSS/MIC), 2012 IEEE (Accepted)*, 2012.
2. E Herranz, JL Herraiz, **E Vicente**, S España, M Desco, JJ Vaquero, JM Udías. *"Quantification limits of iterative PET reconstruction algorithms and improved estimation of kinetic constants"*. 2011 IEEE International Symposium on Biomedical Imaging, 1766-1769, 2011.
3. **E. Vicente**, J. L. Herraiz, S. Espana, E. Herranz, M. Desco, J. J. Vaquero, and J. M. Udias, "*Deadtime and pile-up correction method based on the singles to coincidences ratio for PET*," in *Nuclear Science Symposium and Medical Imaging Conference (NSS/MIC), 2011 IEEE*, 2011, pp. 2933-2935.
4. E. Herranz, J. L. Herraiz, **E. Vicente**, S. Espana, M. Desco, J. J. Vaquero, and J. M. Udias, "*Quantification limits of iterative PET reconstruction algorithms and improved estimation of kinetic constants*," in *Nuclear Science Symposium and Medical Imaging Conference (NSS/MIC), 2011 IEEE*, 2011, pp. 2968-2972.

5. K. M. Abushab, J. L. Herraiz, **E. Vicente**, S. Espana, J. J. Vaquero, B. W. Jakoby, and J. M. Udias, "*PeneloPET simulations of the Biograph ToF clinical PET scanner*," in *Nuclear Science Symposium and Medical Imaging Conference (NSS/MIC), 2011 IEEE*, 2011, pp. 4420-4428
6. P. M. G. Corzo, J. Cal-Gonzalez, E. Picado, S. Espana, J. L. Herraiz, E. Herranz, **E. Vicente**, J. M. Udias, J. J. Vaquero, A. Munoz-Martin, and L. M. Fraile, "*Measurement of activity produced by low energy proton beam in metals using off-line PET imaging*," in *Nuclear Science Symposium and Medical Imaging Conference (NSS/MIC), 2011 IEEE*, 2011, pp. 3514-3517
7. **E Vicente Torrico**, A Udías Moinelo, J López Herraiz, M Desco Menéndez, JJ Vaquero López, JM Udías Moinelo. *"Corrección de atenuación de imágenes PET usando datos de TAC en el escáner para animales pequeños Argus PET/CT"*. Proceedings del XXVIII Congreso Anual de la Sociedad Española de Ingeniería Biomédica (CASEIB), s.p., 2010.
8. JJ Vaquero, S España, E Picado, J Cal-González, LM Fraile, JL Herraiz, **E Vicente**, M Desco, JM Udías. *"Viabilidad del uso de fotodetectores SiPM en sistemas PET/IRM"*. Proceedings del XXVIII Congreso Anual de la Sociedad Española de Ingeniería Biomédica (CASEIB), s.p., 2010.
9. KM Abushab, J López Herraiz, **E Vicente Torrico**, S España Palomares, JJ Vaquero López, JM Udías Moinelo. *"Validation of peneloPET simulations of the Biograph PET/CT scanner with TOF capabilities"*. Proceedings del XXVIII Congreso Anual de la Sociedad Española de Ingeniería Biomédica (CASEIB), s.p., 2010.
10. **E Vicente**, JL Herraiz, M Cañadas, J Cal-González, S España, M Desco, JJ Vaquero, JM Udías. *"Validation of NEMA NU4-2008 Scatter Fraction estimation with 18F and 68Ga for the ARGUS small-animal PET Scanner"*. Proceeding of the 2010 IEEE Nuclear Science Symposium Conference Record, 3553-3557, 2010.
11. M Cañadas, E Romero Sanz, M Oteo Vives, JJ Vaquero, M Desco, **E Vicente**, JM Udías, L Romero. *"Performance Evaluation for 68Ga and 18F of the ARGUS Small-Animal PET Scanner Based on the NEMA NU-4 Standard"*. Proceeding of the 2010 IEEE Nuclear Science Symposium Conference Record, 3454-3457, 2010.
12. S España, J Cal-González, LM Fraile, E Picado, JL Herraiz, **E Vicente**, JM Udías, M Desco, JJ Vaquero. *"Performance Evaluation of SiPM Photosensors in the Presence of Magnetic Fields"*. La Rábida 2009: International Scientific Meeting on Nuclear Physics - Basic Concepts in Nuclear Physics: Theory, Experiments, and Applications, 1231: 171-172, 2010
13. S España, LM Fraile, JL Herraiz, **E Vicente**, JM Udías, M Desco, JJ Vaquero. *"Performance evaluation of SIPM photosensors for PET imaging in the presence of magnetic fields"*. Abstract book of European Society for Molecular Imaging (ESMI), 163, 2009
14. E Herranz, JL Herraiz, JJ Vaquero, **E Vicente**, S España, M Desco, JM Udías. *"Non-invasive estimate of input function from PET images of small mice"*. Abstract book of European Society for Molecular Imaging (ESMI), 179, 2009
15. S España, G Tapias, LM Fraile, JL Herraiz, **E Vicente**, J Udías, M Desco, JJ Vaquero. *"Performance Evaluation of SiPM Detectors for PET Imaging in the Presence of Magnetic Fields"*. 2008 IEEE Nuclear Science Symposium Conference Record, 3591-3595, 2008.
16. J López Herraiz, S España, **E Vicente**, E Herranz, M Desco, JJ Vaquero, J Udías. *"Frequency Selective Signal Extrapolation for Compensation of Missing Data in Sinograms"*. 2008 IEEE Nuclear Science Symposium Conference Record, 4299-4302, 2008.
17. **E Vicente**, S España, JL Herraiz, E Herranz, M Desco, JJ Vaquero, JM Udías. *"Nonlinear Effect of Pile-up in the Quantification of a Small Animal PET Scanner"*. 2008 IEEE Nuclear Science Symposium Conference Record, 5391-5395, 2008.
18. A Sisniega, JJ Vaquero, E Lage, M Abella, A Rodríguez, V García, A Udías, J Pascau, ML Soto-Montenegro, **E Vicente**, M Desco. *"PET/CT coplanar para imagen de pequeños animales"*. Libro de actas, CASEIB 2007, 130-133, 2007.
19. S España, JL Herraiz, **E Vicente**, E Herranz, JJ Vaquero, M Desco, JM Udías. *"Improved Image Reconstruction in Small Animal PET Using a Priori Estimates of Single-Pixel Events"*. 2007 IEEE Nuclear Science Symposium Conference Record, 3876-3880, 2007.

20. **E Vicente**, M Soto-Montenegro, S España, JL Herraiz, E Herranz, JJ Vaquero, M Desco, JM Udías. *"Influence of Random, Pile-up and Scatter Corrections in the Quantification Properties of Small-Animal PET Scanners"*. 2007 IEEE Nuclear Science Symposium Conference Record, 3964-3968, 2007.
21. JL Herraiz, S España, **E Vicente**, E Herranz, JJ Vaquero, M Desco, JM Udías. *"Revised Consistency Conditions for PET Data"*. 2007 IEEE Nuclear Science Symposium Conference Record, 3865-3870, 2007.
22. S España, JL Herraiz, **E Vicente**, E Herranz, JJ Vaquero, M Desco, JM Udías. *"Validation of PeneloPET Against Two Small Animal PET Scanners"*. 2007 IEEE Nuclear Science Symposium Conference Record, 3640-3643, 2007.
23. M Abella, J Vaquero, **E Vicente**, J Sánchez, M Desco. *"Effect of sinogram filtering in the quality of positron emission tomography reconstructions"*. Molecular Imaging and Biology, 8(2): 75, 2006.
24. M Abella, J Vaquero, **E Vicente**, J Álvarez, E Lage, M Desco. *"Effect of misalignments in small animal positron emission tomography scanners based on rotating planar detectors"*. Molecular Imaging and Biology, 8(2): 75-76, 2006.
25. M Abella, J Vaquero, **E Vicente**, J Sánchez, S Redondo, M Desco. *"Issues in the quantitative reconstruction of positron emission tomography studies"*. Molecular Imaging and Biology, 8(2): 76, 2006.
26. S España, JL Herráiz, **E Vicente**, JJ Vaquero, M Desco, J Udías. *"Resolution improvement of small animal positron emission tomography images using a step and shoot rotating scanner"*. Molecular Imaging and Biology, 8(2): 84, 2006.
27. JL Herráiz, S España, **E Vicente**, JJ Vaquero, M Desco, JM Udías. *"Iterative vs analytic reconstruction methods for positron emission tomography's: combining the best of both approaches"*. Molecular Imaging and Biology, 8(2): 87, 2006.
28. JL Herráiz, S España, **E Vicente**, JJ Vaquero, M Desco, JM Udías. *"Small animal positron emission tomography scanners design optimized for statistical reconstruction methods"*. Molecular Imaging and Biology, 8(2): 87, 2006.
29. J Sánchez-González, JJ Vaquero, S España, M Abella, **E Vicente**, M Desco. *"A new technique for reconstructing positron emission tomography datasets from rotating scanners"*. Molecular Imaging and Biology, 8(2): 100, 2006.
30. J Vaquero, E Lage, S Redondo, M Abella, **E Vicente**, M Desco. *"Initial results of a positron emission tomography/computed tomography small-animal imaging device with co-planar geometry"*. Molecular Imaging and Biology, 8(2): 107, 2006.
31. J Pascau, J Vaquero, M Abella, **E Vicente**, M Soto, A Santos, M Desco. *"One click alignment after small animal illpositioned acquisition"*. Molecular Imaging and Biology, 8(2): 97, 2006.
32. **E Vicente**, JJ Vaquero, E Lage, G Tapias, M Abella, JL Herráiz, S España, JM Udías, M Desco. *"Caracterización del Tomógrafo de Animales rPET"*. Libro de Actas, CASEIB 2006, 395-398, 2006.
33. **E Vicente**, JJ Vaquero, S España, JL Herráiz, JM Udías, M Desco. *"Normalization in 3D PET: Dependence on the Activity Distribution of the Source"*. 2006 IEEE Nuclear Science Symposium Conference Record, 2206-2209, 2006.
34. JL Herráiz, S España, **E Vicente**, JJ Vaquero, M Desco, JM Udías. *"Optimal and Robust PET Data Sinogram Restoration Based on the Response of the System"*. 2006 IEEE Nuclear Science Symposium Conference Record, 3404-3407, 2006.
35. S España, JL Herráiz, **E Vicente**, JJ Vaquero, M Desco, JM Udías. *"PeneloPET, a Monte Carlo PET simulation toolkit based on PENELOPE: Features and Validation"*. 2006 IEEE Nuclear Science Symposium Conference Record, 2597-2601, 2006.
36. **E Vicente**, JJ Vaquero, E Lage, G Tapias, M Abella, J López, S España, JM Udías, M Desco. *"Caracterización del Tomógrafo de Animales rPET"*. Libro de Resúmenes del CASEIB 2006, 111, 2006.
37. J.J. Vaquero, E. Lage, L. Ricón, M. Abella, **E. Vicente**, M. Desco. *"rPET Detectors Design and Data Processing"*. 2005 IEEE Nuclear Science Symposium Conference Record (CD-ROM), 2885-2889, 2005.

38. J.J. Vaquero, E. Lage, S. Redondo, M. Abella, J. Pascau, J. Sánchez, **E. Vicente**, M. Soto-Montenegro, M. Desco. *"Co-Planar PET/CT for Small Animal Imaging"*. 2005 IEEE Nuclear Science Symposium Conference Record (CD-ROM), 1748-1751, 2005.

List of figures

List of tables

Appendix A. -Description of the phantoms

NEMA NU 4 Mouse/Rat sized phantoms

The mouse-like phantom is made of a solid, right circular cylinder composed of high density polyethylene (density 0.96 ± 0.1 g/cm^3), 70 ± 0.5 mm long and 25 ± 0.5 mm in diameter. A cylindrical hole (3.2 mm diameter) is drilled parallel to the central axis at the radial distance of 10 mm.

The rat-like phantom has similar geometry but with larger dimensions: a cylinder with a diameter of 50 ± 0.5 mm and length of 150 ± 0.5 mm. A cylindrical hole (3.2mm diameter) is drilled parallel to the central axis at a radial distance of 17.5 mm.

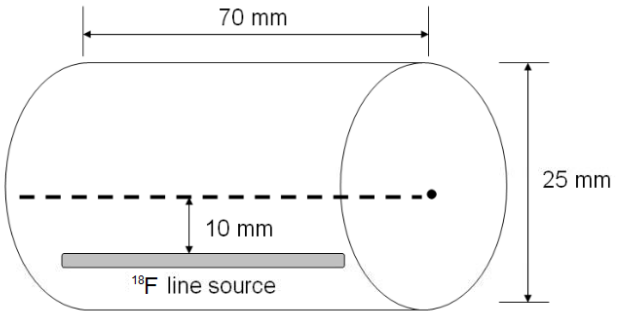

Figure A.1. *NEMA NU 4 mouse sized phantom diagram. The rat sized phantom has similar geometry but with larger dimensions.*

The test phantom line source insert is clear flexible tubing with a fillable section 10 mm shorter than the cylindrical phantoms with an outside diameter which fits the 3.2 mm hole. The tubing is threaded through the hole in the test phantom.

NEMA NU4 Image Quality Phantom

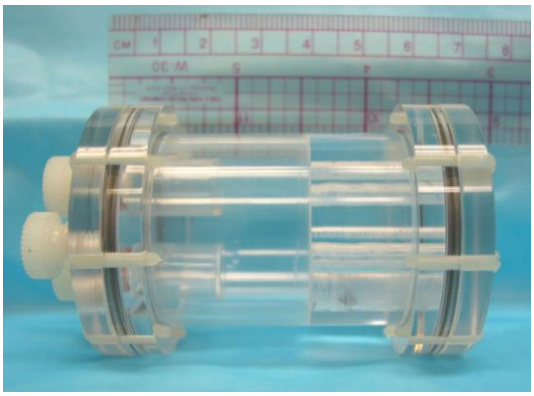

Figure A.2. *NEMA NU 4 Image quality phantom.*

The phantom is made from PMMA (polymethyl methacrylate) and offers a large fillable cylindrical cavity with 30 mm diameter and 30 mm length. This large chamber houses two smaller cavities with 8 mm diameter, 15 mm length. (see Figure A.3, left). The second half of the cylinder houses five smaller cavities with diameters of 1, 2, 3, 4, and 5 mm, respectively, radially aligned around the phantom length axis (see Figure A.3, right) and provides an interconnection to the first half cavity.

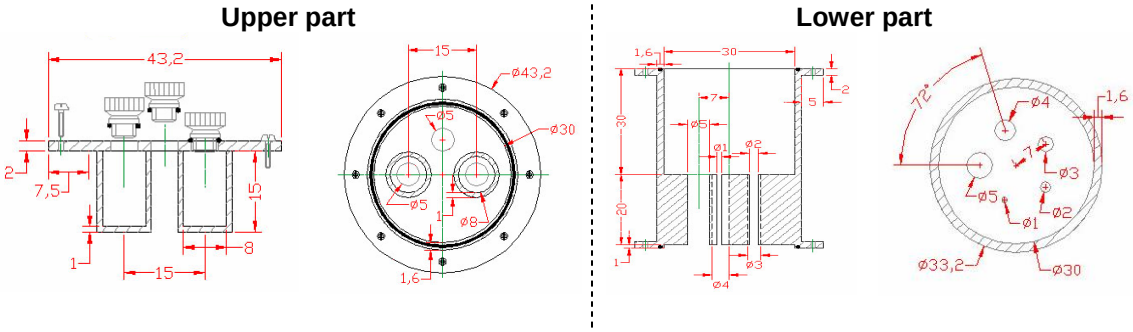

Figure A.3. *Coronal and transverse cross sections of the two parts of the NEMA NU 4 Image quality phantom.*

Derenzo-like phantom

This phantom consists of five sectors, each one containing radioactive rods with different diameters (1.2, 1.5, 2.0, 2.5, and 3.0 mm), being the distance between sources twice their diameter. The sources are distributed within a disk of 36 mm diameter.

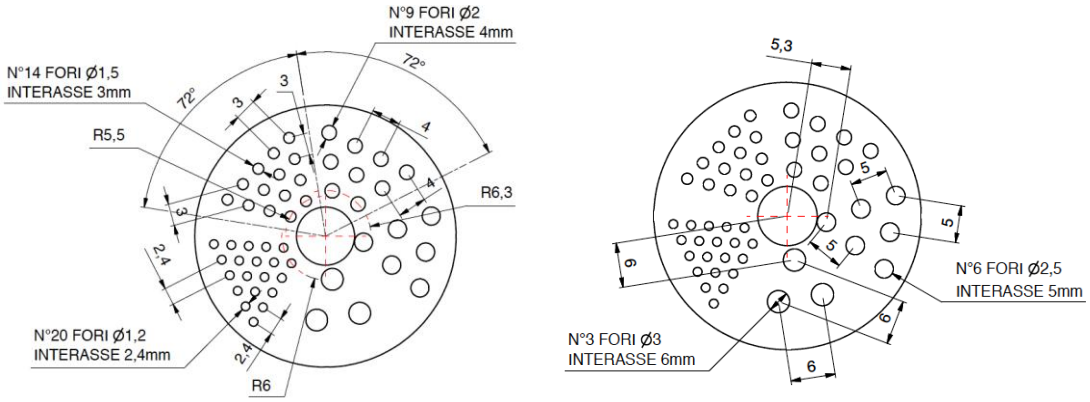

Figure A.4.*Derenzo-like phantom diagrams.*

Bibliography

Abella, M., Vaquero, J., Soto-Montenegro, M., Lage, E. & Desco, M. 2009. Sinogram Bow-Tie Filtering in FBP PET Reconstruction. *Med. Phys.,* 36**,** 1663-71.

Abella, M., Vaquero, J. J., Vicente, E., Álvarez, J., Lage, E. & Desco, M. 2006. Effect of misalignments in small animal PET scanners based on rotating planar detectors. *Mol. Ima. Biol.,* 8**,** 75-6.

Abella, M., Vicente, E., Rodríguez-Ruano, A., España, S., Lage, E., Desco, M., Udias, J. M. & Vaquero, J. J. 2012. Misalignments calibration in small-animal PET scanners based on rotating planar detectors and parallel-beam geometry. *Phys Med Biol (Submitted)*.

Agostinelli, S. 2003. GEANT4 - a simulation toolkit. *Nucl. Inst. Meth. In Phy. Res. A,* 506**,** 250-303.

Alessio, A., Sauer, K. & Bouman, C. A. 2003. MAP reconstruction from spatially correlated PET data. *Nuclear Science, IEEE Transactions on,* 50**,** 1445-1451.

Allemand, R., Gresset, C. & Vacher, J. 1980. Potential advantages of a Cesium Floride scintillator for time-of-flight positron camera. *J. Nucl. Med.,* 21**,** 153-5.

Andreo, P. 1991. Monte Carlo techniques in medical radiation physics. *Physics in Medicine and Biology,* 36**,** 861.

Anger, H. O. 1969. Scintillation Camera and Multiplane Tomographic Scanner. *Kaku Igaku,* 62**,** 125-48.

Arce, P., Rato, P., Canadas, M. & Lagares, J. I. 2008. GAMOS: A Geant4-based easy and flexible framework for nuclear medicine applications. *In:* Nuclear Science Symposium Conference Record, 2008. NSS '08. IEEE, 19-25 Oct. 2008 2008. 3162-3168.

Azevedo, S. G., Schneberk, D. J., Fitch, J. P. & Martz, H. E. 1990. Calculation of the rotational centers in computed tomography sinograms. *Nuclear Science, IEEE Transactions on,* 37**,** 1525-1540.

Badawi, R. D., Kohlmyer, S. G., Harrison, R. L., Vannoy, S. D. & Lewellen, T. K. 2000. The effect of camera geometry on singles flux, scatter fraction and trues and randoms sensitivity for cylindrical 3D PET-a simulation study. *Nuclear Science, IEEE Transactions on,* 47**,** 1228-1232.

Badawi, R. D. & Marsden, P. K. 1999a. Developments in component-based normalization for 3D PET. *Physics in Medicine and Biology,* 44**,** 571.

Badawi, R. D. & Marsden, P. K. 1999b. Self-normalization of emission data in 3D PET. *IEEE Transactions on Nuclear Science,* 46**,** 709-712.

Badawi, R. D., Miller, M. P., Bailey, D. L. & Marsden, P. K. 1999. Randoms variance reduction in 3D PET. *Phys Med Biol,* 44**,** 941-54.

Bai, B., Li, Q., Holdsworth, C. H., Asma, E., Tai, Y. C., Chatziioannou, A. & Leahy, R. M. 2002. Model-based normalization for iterative 3D PET image reconstruction. *Physics in Medicine and Biology,* 47**,** 2773.

Bailey, D. L. 2005. *Positron emission tomography: basic sciences,* Springer.

Bailey, D. L., Jones, T., Spinks, T. J., Gilardi, M.-C. & Townsend, D. W. 1991. Noise equivalent count measurements in a neuro-PET scanner with retractable septa. *IEEE Trans. Med. Imaging,* 10**,** 256-60.

Bao, Q., Newport, D., Chen, M., Stout, D. B. & Chatziioannou, A. F. 2009a. Performance evaluation of the inveon dedicated PET preclinical tomograph based on the NEMA NU-4 standards. *J Nucl Med,* 50**,** 401-8.

Bao, Q., Rannou, F. R., Taschereau, R., Stout, D. B. & Chatziioannou, A. F. 2009b. Image reconstruction for PETbox, a benchtop preclinical PET tomograph. *In:* Nuclear Science Symposium Conference Record (NSS/MIC), 2009 IEEE, Oct. 24 2009-Nov. 1 2009 2009b. 2733-2737.

Baró, J., Sempau, J., Fernández-Varea, J. M. & Salvat, F. 1995. PENELOPE: An algorithm for Monte Carlo simulation of the penetration and energy loss of electrons and positrons in matter. *Nucl. Inst. Meth. In Phy. Res. B,* 100**,** 31-46.

Barret, O., Carpenter, T. A., Clark, J. C., Ansorge, R. E. & Fryer, T. D. 2005. Monte Carlo simulation and scatter correction of the GE Advance PET scanner with SimSET and Geant4. *Phys. Med. Biol.,* 50**,** 4823-40.

Bendriem, B. & Townsend, D. W. 1998. The theory and practice of 3D PET. Kluwer Academic.

Beque, D., Nuyts, J., Bormans, G., Suetens, P. & Dupont, P. 2003. Characterization of pinhole SPECT acquisition geometry. *IEEE Trans. Med. Imaging,* 22**,** 599–612.

Bergeron, M., Cadorette, J., Bureau-Oxton, C., Beaudoin, J. F., Tetrault, M. A., Leroux, J. D., Lepage, M. D., Robert, G., Fontaine, R. & Lecomte, R. 2009. Performance evaluation of the LabPET12, a large axial FOV APD-based digital PET scanner. *In:* Nuclear Science Symposium Conference Record (NSS/MIC), 2009 IEEE, Oct. 24 2009-Nov. 1 2009 2009. 4017-4021.

Bettinardi, V., Pagani, E., Gilardi, M. C., Alenius, S., Thielemans, K., Teras, M. & Fazio, F. 2002. Implementation and evaluation of a 3D one-step late reconstruction algorithm for 3D positron emission tomography brain studies using median root prior. *Eur. J. Nucl. Med. Mol. Imaging,* 29**,** 7-18.

Biemond, J., Lagendijk, R. & Mersereau, R. 1990. Iterative methods for image deblurring *In:* IEEE NSS-MIC, 1990. 856-883.

Bloomfield, P. M., Rajeswaran, S., Spinks, T. J., Hume, S. P., Myers, R., Ashworth, S., Clifford, K. M., Jones, W. F., Byars, L. G., Young, J. & et al. 1995. The design and physical characteristics of a small animal positron emission tomograph. *Phys Med Biol,* 40**,** 1105-26.

Brasse, D., Kinahan, P. E., Lartizien, C., Comtat, C., Casey, M. & Michel, C. 2005. Correction methods for random coincidences in fully 3D whole-body PET: impact on data and image quality. *J Nucl Med,* 46**,** 859-67.

Briesmeister, J. F. 1993. MNCP 4 A, Monte Carlo N-Particle Transport System. Los Alamos, New Mexico: Los Alamos National Laboratory.

Brownell, G. L., Burnham, C. A., Wilensky, S., Aronow, S., Kazemi, H. & Streider , D. 1969. New developments in positron

scintigraphy and the application of cyclotron produced positron emitters. *In:* Medical Radioisotope Scintigraphy, 1969 Vienna, Austria. International Atomic Energy Agency, 163–176.

Brun, R. & Rademakers, F. 1997. ROOT - An object oriented data analysis framework. *Nucl. Inst. & Meth. in Phys. Res. A,* 389**,** 81-86.

Burnham, C. A. & Brownell, G. L. 1972. A Multi-Crystal Positron Camera. *Nuclear Science, IEEE Transactions on,* 19**,** 201-205.

Busemann-Sokole, E. 1987. Measurement of collimator hole angulation and camera head tilt for slant and parallel-hole collimators used in SPECT. *J. Nucl. Med.,* 28**,** 1592–8.

Buvat, I. & Castiglioni, I. 2002. Monte carlo simulations in spet and pet. *The quarterly journal of nuclear medicine,* 46**,** 48–61.

Buvat, I. & Lazaro, D. 2006. Monte Carlo simulations in emission tomography and GATE: An overview. *Nucl. Inst. Meth. In Phy. Res. A,* 569**,** 323-29.

Byme, C. L. 2001. Likelihood maximization for list-mode emission tomographyc image reconstruction. *IEEE Trans. Med. Imaging,* 20**,** 1084-92.

Carrier, C., Martel, C., Schmitt, D. & Lecomte, R. 1988. Design of a high resolution positron emission tomograph using solid state scintillation detectors. *Nuclear Science, IEEE Transactions on,* 35**,** 685-690.

Casey, M. E., Gadagkar, H. & Newport, D. 1996. A component based method for normalization in volume PET. *In:* GRANGEAT, P. & AMANS, J. L., eds. Three-Dimensional Image Reconstruction in Radiology and Nuclear Medicine, 1996 Aix-Les-Bains, France. Kluwer Academic, 66-71.

Casey, M. E. & Hoffman, E. J. 1986. Quantitation in positron emission computed tomography: 7. A technique to reduce noise in accidental coincidence measurements and coincidence efficiency calibration. *J Comput Assist Tomogr,* 10**,** 845-50.

Casey, M. E. & Nutt, R. 1986. A Multicrystal Two Dimensional BGO Detector System for Positron Emission Tomography. *IEEE Trans. Nuc. Sci.,* 33**,** 460-463.

Clinthorne, N. H., Sangjune, P., Rogers, W. L. & Ping-Chun, C. 2003. Multi-resolution image reconstruction for a high-resolution small animal PET device. *In:* Nuclear Science Symposium Conference Record, 2003 IEEE, 19-25 Oct. 2003 2003. 1997-2001 Vol.3.

Cooke, B. E., Evans, A. C., Fanthome, E. O., Alarie, R. & Sendyk, A. M. 1984. Performance Figures and Images from the Therascan 3128 Positron Emission Tomograph. *Nuclear Science, IEEE Transactions on,* 31**,** 640-644.

Cooper, R., Turk, G., Boston, A., Boston, H., Cresswell, J., Mather, A., Nolan, P., Hall, C., Lazarus, I. & Simpson, J. 2007. Position sensitivity of the first SmartPET HPGe detector. *Nuclear Instruments and Methods in Physics Research Section A: Accelerators, Spectrometers, Detectors and Associated Equipment,* 573**,** 72-75.

Chatziioannou, A. F. 2002. PET scanners dedicated to molecular imaging of small animal models. *Mol Imaging Biol,* 4**,** 47-63.

Chen, Y., Liu, B., O'Connor, M., Didier, C. S. & Glick, S. J. 2006. Comparison of Scatter/Primary Measurements with GATE Simulations for X-Ray Spectra in Cone Beam CT Mammography. *In:* IEEE NSS-MIC, 2006 San Diego. USA, 3909-14.

Cherry, S. R., Sorenson, J. A. & Phelps, M. E. 2003. *Physics in nuclear medicine,* Saunders.

Chow, P. L., Rannou, R. & Chatziioannou, A. 2002. Attenuation correction for a 3D small animal PET tomograph, using x-ray microCT. *Mol. Imag. Biol.,* 4**,** S17–S18.

Dahlbom, M., MacDonald, L. R., Eriksson, L., Paulus, M., Andreaco, M., Casey, M. E. & Moyers, C. 1997. Performance of a YSO/LSO phoswich detector for use in a PET/SPECT system. *Nuclear Science, IEEE Transactions on,* 44**,** 1114-1119.

Dahlbom, M., MacDonald, L. R., Schmand, M., Eriksson, L., Andreaco, M. & Williams, C. 1998. A YSO/LSO phoswich array detector for single and coincidence photon imaging. *Nuclear Science, IEEE Transactions on,* 45**,** 1128-1132.

Dai, S., Han, M., Xu, W., Wu, Y. & Gong, Y. 2007. Soft Edge Smoothness Prior for Alpha Channel Super Resolution. *In:* Computer Vision and Pattern Recognition, 2007. CVPR '07. IEEE Conference on, 17-22 June 2007 2007. 1-8.

Daube-Witherspoon, M. E. & Carson, R. E. 1991. Unified deadtime correction model for PET. *IEEE Trans Med Imaging,* 10**,** 267-75.

Daube-Witherspoon, M. E. & Muehllehner, G. 1987. Treatment of axial data in three-dimensional PET. *J Nucl Med,* 28**,** 1717-24.

DeBenedetti, S., Cowan, C. E., Konneker, W. R. & Primakoff, H. 1950. On the angular distribution of two-photon annihilation radiation. *Physical Review,* 77**,** 205-212.

Defrise, M., Kinahan, P. E., Townsend, D. W., Michel, C., Sibomana, M. & Newport, D. F. 1997. Exact and approximate rebinning algorithms for 3-D PET data. *Medical Imaging, IEEE Transactions on,* 16**,** 145-158.

Defrise, M., Townsend, D. & Clack, R. 1991a. Favor: a fast reconstruction algorithm for volume imaging in PET. *In:* Nuclear Science Symposium and Medical Imaging Conference, 1991., Conference Record of the 1991 IEEE, 2-9 Nov 1991 1991a. 1919-1923 vol.3.

Defrise, M., Townsend, D. W., Bailey, D., Geissbuhler, A. M. C. & Jones, T. 1991b. A normalization technique for 3D PET data. *Physics in Medicine and Biology,* 36**,** 939.

Del Guerra, A., Bartoli, A., Belcari, N., Herbert, D., Motta, A., Vaiano, A., Di Domenico, G., Sabba, N., Moretti, E., Zavattini, G., Lazzarotti, M., Sensi, L., Larobina, M. & Uccelli, L. 2006. Performance evaluation of the fully engineered YAP-(S)PET scanner for small animal imaging. *Nuclear Science, IEEE Transactions on,* 53**,** 1078-1083.

Del Guerra, A., Di Domenico, G., Scandola, M. & Zavattini, G. 1998. YAP-PET: first results of a small animal positron emission tomograph based on YAP:Ce finger crystals. *Nuclear Science, IEEE Transactions on,* 45**,** 3105-3108.

Derenzo, S. E. 1979. Precision measurement of annihilation point spread distributions for medically important positron

emitters. *In:* 5th Int. Conf. of Positron Annihilation, 1979 Lake Yamanaka, Japan. 819–23.
Desco, M. Cursos 97-98, 98-99, 00-01. Asignatura "Bioestadística" (Especialidad de Laboratorio). Escuela Técnico Profesional de la Salud de la Comunidad de Madrid. Hospital General Universitario Gregorio Marañón.
Donath, T., Beckmann, F. & Schreyer, A. 2006. Automated determination of the center of rotation in tomography data. *J. Opt. Soc. Am.,* 23**,** 1048-1057.
Du, Y., Frey, E. C., Wang, W. T., Tocharoenchai, C., Baird, W. H. & Tsui, B. M. W. 2002. Combination of MCNP and SimSET for Monte Carlo simulation of SPECT with medium- and high-energy photons. *IEEE Trans. Nuc. Sci.,* 49**,** 668-74.
Eijk, C. W. E. v. 2002. Inorganic scintillators in medical imaging. *Physics in Medicine and Biology,* 47**,** R85.
Engels, R., Clemens, U., Kemmerling, G. & Schelten, J. 2003. High spatial resolution scintillation detector based on the H8500 photomultiplier. *In:* Nuclear Science Symposium Conference Record, 2003 IEEE, 19-25 Oct. 2003 2003. 692-695 Vol.1.
Eriksson, L., Wienhard, K. & Dahlbom, M. 1994 A simple data loss model for positron camera systems. *IEEE Transactions on Nuclear Science,* 41**,** 1566 - 1570
España, S., Fraile, L. M., Herraiz, J. L., Udías, J. M., Desco, M. & Vaquero, J. J. 2010. Performance evaluation of SiPM photodetectors for PET imaging in the presence of magnetic fields. *Nuclear Instruments and Methods in Physics Research Section A: Accelerators, Spectrometers, Detectors and Associated Equipment,* 613**,** 308-316.
España, S., Herraiz, J. L., Vicente, E., Vaquero, J. J., Desco, M. & Udias, J. M. 2009. PeneloPET, a Monte Carlo PET simulation tool based on PENELOPE: features and validation. *Phys Med Biol,* 54**,** 1723-42.
España, S., Tapias, G., Fraile, L. M., Herraiz, J. L., Vicente, E., Udias, J., Desco, M. & Vaquero, J. J. 2008. Performance evaluation of SiPM detectors for PET imaging in the presence of magnetic fields. *In:* Nuclear Science Symposium Conference Record, 2008. NSS '08. IEEE, 19-25 Oct. 2008 2008. 3591-3595.
Fahey, F. H. 2002. Data acquisition in PET imaging. *J Nucl Med Technol,* 30**,** 39-49.
Fessler, J. A. 2008. Iterative Methods for Image Reconstruction (ISBI Tutorial).
Frese, T., Rouze, N. C., Bouman, C. A., Sauer, K. & Hutchins, G. D. 2001. Quantitative comparison of FBP, EM, and Bayesian reconstruction algorithms, including the impact of accurate system modeling, for the IndyPET scanner. *In:* Nuclear Science Symposium Conference Record, 2001 IEEE, 2001 2001. 1806-1810.
Furrer, M., Gostely, J. J. & Lerch, P. 1984. Timing problems due to pile-up in coincidence counting. *Nuclear Instruments and Methods in Physics Research Section A: Accelerators, Spectrometers, Detectors and Associated Equipment,* 226**,** 455-462.
General-Purpose Computing on Graphics Processing Units repository [Online]. Available: www.gpgpu.org. [September 2010].
Germano, G. & Hoffman, E. J. 1988. Investigation of count rate and deadtime characteristics of a high resolution PET system. *J Comput Assist Tomogr,* 12**,** 836-46.
Germano, G. & Hoffman, E. J. 1990. *A study of data loss and mispositioning due to pileup in 2-D detectors in PET.*
Germano, G. & Hoffman, E. J. 1991. An investigation of methods of pileup rejection for 2-D array detectors employed in high resolution PET. *IEEE Trans Med Imaging,* 10**,** 223-7.
Goertzen, A. L., Bao, Q., Bergeron, M., Blankemeyer, E., Blinder, S., Cañadas, M., Chatziioannou, A. F., Dinelle, K., Elhami, E., Jans, H.-S., Lage, E., Lecomte, R., Sossi, V., Surti, S., Tai, Y.-C., Vaquero, J. J., Vicente, E., Williams, D. A. & Laforest, R. 2012. NEMA NU 4-2008 Comparison of Preclinical PET Imaging Systems. *The Journal of Nuclear Medicine (Accepted).*
Green, P. J. 1990. Bayesian reconstructions from emission tomography data using a modified EM algorithm. *Medical Imaging, IEEE Transactions on,* 9**,** 84-93.
Gropp, W., Lusk, E. & Skjellum, A. 1999. *Using MPI: portable parallel programming with the message-passing interface*, MIT Press.
Gullberg, G. T., Tsui, B. M. W., Crawford, C. R., Ballard, J. G. & Hagius, J. T. 1990. Estimation of geometrical parameters and collimator evaluation for cone beam tomography. *Med. Phys.,* 17**,** 264–72.
Gullberg, G. T., Tsui, B. M. W., Crawford, C. R. & Edgerton, E. 1987. Estimation of geometrical parameters for fan-beam tomography. *Phys. Med. Biol.,* 32**,** 1581–94.
Harrison, R. L., Vannoy, S. D., Haynor, D. R., Gillispie, S. B., Kaplan, M. S. & Lewellen, T. K. 1993. Preliminary Experience With The Photon History Generator Module Of A Public-domain Simulation System For Emission Tomography. *In:* Nuclear Science Symposium and Medical Imaging Conference, 1993., 1993 IEEE Conference Record., 31 Oct-6 Nov 1993 1993. 1154-1158.
Heinrichs, U., Pietrzyk, U. & Ziemons, K. 2003. Design optimization of the PMT-ClearPET prototypes based on simulation studies with GEANT3. *Nuclear Science, IEEE Transactions on,* 50**,** 1428-1432.
Henkin, R. E., Bova, D., Dillehay, G. L. & Karesh, S. M. 2006. *Nuclear medicine,* Philadelphia, Elsevier Health Sciences.
Herman, G. T. 1980. *Image reconstruction from projections: the fundamentals of computerized tomography,* Academic Press.
Hermansen, F., Spinks, T. J., Camici, P. G. & Lammertsma, A. A. 1997. Calculation of single detector efficiencies and extension of the normalization sinogram in PET. *Phys Med Biol,* 42**,** 1143-54.
Herraiz, J. L., Espana, S., Vaquero, J. J., Desco, M. & Udias, J. M. 2006a. FIRST: Fast Iterative Reconstruction Software for (PET) tomography. *Phys Med Biol,* 51**,** 4547-65.
Herraiz, J. L., España, S., Cabido, R., Montemayor, A. S., Desco, M., Vaquero, J. J. & Udias, J. M. 2011. GPU-Based Fast Iterative Reconstruction of Fully 3-D PET Sinograms. *Nuclear Science, IEEE Transactions on,* 58**,** 2257-2263.
Herraiz, J. L., España, S., Vaquero, J. J., Desco, M. & Udias, J. M. 2006b. FIRST: Fast Iterative Reconstruction Software for (PET) tomography. *Phys. Med. Biol.,* 51**,** 4547-4565.
Hoffman, E. J., Guerrero, T. M., Germano, G., Digby, W. M. & Dahlbom, M. 1989. PET system calibrations and corrections for quantitative and spatially accurate images. *Nuclear Science, IEEE Transactions on,* 36**,** 1108-1112.

Hoffman, E. J., Phelps, M. E. & Huang, S. C. 1983. Performance evaluation of a positron tomograph designed for brain imaging. *J Nucl Med,* 24**,** 245-57.

Hong, I. K., Chung, S. T., Kim, H. K., Kim, Y. B., Son, Y. D. & Cho, Z. H. 2007. Ultra Fast Symmetry and SIMD-Based Projection-Backprojection (SSP) Algorithm for 3-D PET Image Reconstruction. *Medical Imaging, IEEE Transactions on,* 26**,** 789-803.

Hsieh, Y.-L. 1992. *Calibration of fan-beam geometry for single photon emission computed tomography.* University of Utah.

Huang, S. C., Hoffman, E. J., Phelps, M. E. & Kuhl, D. E. 1979. Quantitation in positron emission computed tomography: 2. Effects of inaccurate attenuation correction. *J Comput Assist Tomogr,* 3**,** 804-14.

Hudson, H. M. & Larkin, R. S. 1994. Accelerated image reconstruction using ordered subsets of projection data. *Medical Imaging, IEEE Transactions on,* 13**,** 601-609.

Huh, S. S., Rogers, W. L. & Clinthorne, N. H. 2008. On-line sliding-window list-mode PET image reconstruction for a surgical pet imaging probe. *In:* Nuclear Science Symposium Conference Record, 2008. NSS '08. IEEE, 19-25 Oct. 2008 2008. 5479-5484.

Imperiale, C. & Imperiale, A. 2001. On nuclear spectrometry pulses digital shaping and processing. *Measurement,* 30**,** 49-73.

Inadama, N., Murayama, H., Watanabe, M., Omura, T., Yamashita, T., Kawai, H., Umehara, T., Kasahara, T., Orita, N. & Tsuda, T. 2004. Performance of a PET detector with a 256ch flat panel PS-PMT. *Nuclear Science, IEEE Transactions on,* 51**,** 58-62.

Jagoda, E. M., Vaquero, J. J., Seidel, J., Green, M. V. & Eckelman, W. C. 2004. Experiment assessment of mass effects in the rat: implications for small animal PET imaging. *Nuclear Medicine and Biology,* 31**,** 771-9.

Jakoby, B. W., Bercier, Y., Conti, M., Casey, M. E., Bendriem, B. & Townsend, D. W. 2011. Physical and clinical performance of the mCT time-of-flight PET/CT scanner. *Phys Med Biol,* 56**,** 2375-89.

James, S. S., Yang, Y., Wu, Y., Farrell, R., Dokhale, P., Shah, K. S. & Cherry, S. R. 2009. Experimental characterization and system simulations of depth of interaction PET detectors using 0.5 mm and 0.7 mm LSO arrays. *Phys Med Biol,* 54**,** 4605-19.

Jan, S., Santin, G., Strul, D., Staelens, S., Assié, K., Autret, D. & Avner, S. 2004a. GATE: a simulation toolkit for PET and SPECT. *Phys. Med. Biol.,* 49**,** 4543-4561.

Jan, S., Santin, G., Strul, D., Staelens, S., Assie, K., Autret, D., Avner, S., Barbier, R., Bardies, M., Bloomfield, P. M., Brasse, D., Breton, V., Bruyndonckx, P., Buvat, I., Chatziioannou, A. F., Choi, Y., Chung, Y. H., Comtat, C., Donnarieix, D., Ferrer, L., Glick, S. J., Groiselle, C. J., Guez, D., Honore, P. F., Kerhoas-Cavata, S., Kirov, A. S., Kohli, V., Koole, M., Krieguer, M., van der Laan, D. J., Lamare, F., Largeron, G., Lartizien, C., Lazaro, D., Maas, M. C., Maigne, L., Mayet, F., Melot, F., Merheb, C., Pennacchio, E., Perez, J., Pietrzyk, U., Rannou, F. R., Rey, M., Schaart, D. R., Schmidtlein, C. R., Simon, L., Song, T. Y., Vieira, J. M., Visvikis, D., Van de Walle, R., Wieers, E. & Morel, C. 2004b. GATE: a simulation toolkit for PET and SPECT. *Phys Med Biol,* 49**,** 4543-61.

Janecek, M., Heyu, W. & Yuan-Chuan, T. 2006. A simulation study for the design of a prototype insert for whole-body PET scanners. *Nuclear Science, IEEE Transactions on,* 53**,** 1143-1149.

Johnson, C. A., Seidel, J., Carson, R. E., Gandler, W. R., Sofer, A., Green, M. V. & Daube-Witherspoon, M. E. 1997. Evaluation of 3D reconstruction algorithms for a small animal PET camera. *IEEE Trans. Nuc. Sci.,* 44**,** 1303-1308.

Johnson, V. E. 1987. A note on stopping rules in EM-ML reconstructions of ECT images. *IEEE Trans. Med. Imaging,* 13**,** 569-71.

Jones, M. D. & Yao, R. 2004. Parallel programming for OSEM reconstruction with MPI, OpenMP, and hybrid MPI-OpenMP. *In:* Nuclear Science Symposium Conference Record, 2004 IEEE, 16-22 Oct. 2004 2004. 3036-3042.

Joung, J., Miyaoka, R. S. & Lewellen, T. K. 2001. cMiCE:a high resolution animal PET using continuous LSO with a statistics based positioning scheme. *In:* IEEE NSS-MIC, 2001. 1137-1141 vol.2.

Kadrmas, D. J. 2004. LOR-OSEM: statistical PET reconstruction from raw line-of-response histograms. *Phys. Med. Biol.,* 49**,** 4731-4744.

Kak, A. C. & Slaney, M. 1988. *Principles of Computerized Tomographic Imaging,* New York, Society for Industrial Mathematics.

Kalos, M. H. & Whitlock, P. A. 1986. *Monte Carlo Methods, vol. 1,* New York, Wiley.

Kao, C.-M., Xie, Q., Dong, Y., Wan, L. & Chen, C.-T. 2009. A High-Sensitivity Small-Animal PET Scanner: Development and Initial Performance Measurements. *Nuclear Science, IEEE Transactions on,* 56**,** 2678-2688.

Kawrakow, I. & Bielajew, A. F. 1998. On the condensed history technique for electron transport. *Nucl. Inst. Meth. In Phy. Res. B,* 142**,** 253-280.

Keesing, D. B., Pal, D., O'Sullivan, J. A., Komarov, S., Wu, H. & Tai, Y.-C. 2008. System modeling of a DOI-capable half-ring PET insert device for breast cancer imaging. *In:* Nuclear Science Symposium Conference Record, 2008. NSS '08. IEEE, 19-25 Oct. 2008 2008. 4218-4222.

Khodaverdi, M., Weber, S., Streun, M., Parl, C., Larue, H., Brandenburg, G., Bauer, A., Dehnhardt, M., Auffray, E., Boutemeur, M., Bruyndonckx, P., Choi, Y., D'Asseler, Y., Devroede, O., Dujardin, C., Fedorov, A., Heinrichs, U., Janier, M., Jung, J. H., Korjik, M., Krieguer, M., Largeron, G., Lartizien, C., Lecoq, P., Lemaitre, C., Leonard, S., Loude, J. F., Morel, C., Mosset, J. B., Pedrini, C., Petrosyan, A. G., Rey, M., Sappey-Marinier, D., Roldan, P. S., Simon, L., Song, T. Y., Staelens, S., Tavernier, S., Trummer, J., Van Holen, R., Vieira, J. M., Wieers, E., Wisniewska, M., Wisniewski, D., Wu, Y., Pietrzyk, U. & Ziemons, K. 2005. High resolution imaging with ClearPET™ Neuro - first animal images. *In:* Nuclear Science Symposium Conference Record, 2005 IEEE, 23-29 Oct. 2005 2005. 4 pp.

Kinahan, P. E., Hasegawa, B. H. & Beyer, T. 2003. X-ray-based attenuation correction for positron emission tomography/computed tomography scanners. *Semin Nucl Med,* 33**,** 166-79.

Kinahan, P. E., Townsend, D. W., Beyer, T. & Sashin, D. 1998. Attenuation correction for a combined 3D PET/CT scanner. *Med Phys,* 25**,** 2046-53.

Kisung, L., Kinahan, P. E., Miyaoka, R. S., Jae-Seung, K. & Lewellen, T. K. 2004. Impact of system design parameters on image figures of merit for a mouse PET scanner. *Nuclear Science, IEEE Transactions on,* 51**,** 27-33.

Knoess, C., Siegel, S., Smith, A., Newport, D., Richerzhagen, N., Winkeler, A., Jacobs, A., Goble, R. N., Graf, R., Wienhard, K. & Heiss, W. D. 2003. Performance evaluation of the microPET R4 PET scanner for rodents. *Eur J Nucl Med Mol Imaging,* 30**,** 737-47.

Knoll, G. F. 2000. *Radiation detection and measurement / Glenn F. Knoll,* New York :, Wiley.

Krane, K. S. 1987. *Introductory Nuclear Physics,* New York, Wiley.

Kupinski, M. A. & Barrett, H. H. 2005. *Small-animal Spect Imaging,* Springer.

L'Ecuyer, P. 1988. Efficient and portable combined random number generators. *In:* ACM, 1988 New York. ACM, 742-51.

Lage, E., Tapias, G., Villena, J., Desco, M. & Vaquero, J. J. 2010. Data acquisition electronics for gamma ray emission tomography using width-modulated leading-edge discriminators. *Physics in Medicine and Biology,* 55**,** 4291.

Lage, E., Vaquero, J. J., Sisniega, A., Espana, S., Tapias, G., Abella, M., Rodriguez-Ruano, A., Ortuno, J. E., Udias, A. & Desco, M. 2009. Design and performance evaluation of a coplanar multimodality scanner for rodent imaging. *Phys Med Biol,* 54**,** 5427-41.

Lazaro, D., Buvat, I., Loudos, G., Strul, D., Santin, G., Giokaris, N. & Donnarieix, D. 2004. Validation of the GATE Monte Carlo simulation platform for modelling a CsI(Tl) scintillation camera dedicated to small-animal imaging. *Phys. Med. Biol.,* 49**,** 271-285.

Lecomte, R. 2004. Technology challenges in small animal PET imaging. *Nucl. Instrum. Meth. Phys. Res. A,* 527**,** 157-165.

Lee, J., Vaquero, J. J., Barbosa, F. J., Seidel, J. & Green, M. V. 2000. High performance phoswich detector module for small animal PET. *J. Nucl. Med.,* 41.

Lerche, C. W., Benlloch, J. M., Sanchez, F., Pavon, N., Escat, B., Gimenez, E. N., Fernandez, M., Torres, I., Gimenez, M., Sebastia, A. & Martinez, J. 2005. Depth of γ-ray interaction within continuous crystals from the width of its scintillation light-distribution. *Nuclear Science, IEEE Transactions on,* 52**,** 560-572.

Levin, C. S., Foudray, A. M. K. & Habte, F. 2006. Impact of high energy resolution detectors on the performance of a PET system dedicated to breast cancer imaging. *Physica Medica,* 21**,** 28-34.

Levin, C. S. & Hoffman, E. J. 1999. Calculation of positron range and its effect on the fundamental limit of positron emission tomography system spatial resolution. *Phys. Med. Biol.,* 44**,** 781-799.

Lewellen, T. K. 2008. Recent developments in PET detector technology. *Phys Med Biol,* 53**,** R287-317.

Lewellen, T. K., Laymon, C. M., Miyaoka, R. S., Ki Sung, L. & Kinahan, P. E. 2001. Design of a Firewire based data acquisition system for use in animal PET scanners. *In:* Nuclear Science Symposium Conference Record, 2001 IEEE, 2001 2001. 1974-1978.

Lewis, J. S. & Achilefu, S. 2002. Small Animal Imaging: Current Technology and Perpectives for Oncological Imaging. *Eur. J. Cancer,* 38**,** 2173-88.

Lewitt, R. M. & Matej, S. 2003. Overview of methods for image reconstruction from projections in emission computed tomography. *In:* IEEE NSS-MIC, 2003. 1588-1611.

Lewittt, R. M., Muehllehner, G. & Karpt, J. S. 1994. Three-dimensional image reconstruction for PET by multi-slice rebinning and axial image filtering. *Phys Med Biol,* 39**,** 321-39.

Liow, J. S. & Strother, S. C. 1991. Practical tradeoffs between noise, resolution and quantitation, and number of iterationsfor maximum likelihood reconstructions. *IEEE Trans. Med. Imag.,* 10**,** 563-571.

Ljungberg, M., Strand, S. E. & King, M. A. 1998. *Monte Carlo calculations in nuclear medicine: applications in diagnostic imaging,* Institute of Physics Pub.

Lois, C., Jakoby, B. W., Long, M. J., Hubner, K. F., Barker, D. W., Casey, M. E., Conti, M., Panin, V. Y., Kadrmas, D. J. & Townsend, D. W. 2010. An assessment of the impact of incorporating time-of-flight information into clinical PET/CT imaging. *J Nucl Med,* 51**,** 237-45.

MacManus, M., Nestle, U., Rosenzweig, K. E., Carrio, I., Messa, C., Belohlavek, O., Danna, M., Inoue, T., Deniaud-Alexandre, E., Schipani, S., Watanabe, N., Dondi, M. & Jeremic, B. 2009. Use of PET and PET/CT for radiation therapy planning: IAEA expert report 2006-2007. *Radiother Oncol,* 91**,** 85-94.

Mair, B. A., Carroll, R. B. & Anderson, J. M. M. 1996. Filter banks and the EM algorithm. *In:* Nuclear Science Symposium, 1996. Conference Record., 1996 IEEE, 2-9 Nov 1996 1996. 1747-1751 vol.3.

Majewski, S., Kieper, D., Curran, E., Keppel, C., Kross, B., Palumbo, A., Popov, V., Wisenberger, A. G., Welch, B., Wojcik, R., Williams, M. B., Goode, A. R., More, M. & Zhang, G. 2001. Optimization of dedicated scintimammography procedure using detector prototypes and compressible phantoms. *Nuclear Science, IEEE Transactions on,* 48**,** 822-829.

Mankoff, D. A., Muehllehner, G. & Karp, J. S. 1989. The high count rate performance of a two-dimensionally position-sensitive detector for positron emission tomography. *Phys Med Biol,* 34**,** 437-56.

Massoud, T. F. & Gambhir, S. S. 2003. Molecular imaging in living subjects: seeing fundamental biological processes in a new light. *Gene. Dev.,* 17**,** 545-80.

Mazoyer, B. M., Roos, M. S. & Huesman, R. H. 1985. Dead time correction and counting statistics for positron tomography. *Phys Med Biol,* 30**,** 385-99.

Melcher, C. L. 2000. Scintillation crystals for PET. *J Nucl Med,* 41**,** 1051-5.

Melcher, C. L. & Schweitzer, J. S. 1992. Cerium-doped lutetium oxyorthosilicate: a fast, efficient new scintillator. *Nuclear Science, IEEE Transactions on,* 39**,** 502-505.

Miyaoka, R. S., Janes, M. L., Lee, K., Park, B., Kinahan, P. E. & Lewellen, T. K. 2005. Development of a single detector ring micro crystal element scanner: QuickPET II. *Mol Imaging,* 4**,** 117-27.

Miyaoka, R. S., Kohlmyer, S. G., Jinhun, J. & Lewellen, T. K. 2001. Performance characteristics of a second generation micro crystal element (MiCE2) detector. *In:* Nuclear Science Symposium Conference Record, 2001 IEEE, 4-10 Nov. 2001 2001. 1124-1127 vol.2.

Moses, W. W. & Qi, J. 2003. Fundamental limits of positron emission mammography. *Nuclear Instruments and Methods in Physics Research Section A: Accelerators, Spectrometers, Detectors and Associated Equipment,* 497**,** 82-89.

Mosset, J. B., Devroede, O., Krieguer, M., Rey, M., Vieira, J. M., Jung, J. H., Kuntner, C., Streun, M., Ziemons, K., Auffray, E., Sempere-Roldan, P., Lecoq, P., Bruyndonckx, P., Loude, J. F., Tavernier, S. & Morel, C. 2004. Development of an optimised LSO/LuYAP phoswich detector head for the ClearPET camera. *In:* Nuclear Science Symposium Conference Record, 2004 IEEE, 16-22 Oct. 2004 2004. 2439-2443 Vol. 4.

Moszynski, M., Kapusta, M., Nassalski, A., Szczesniak, T., Wolski, D., Eriksson, L. & Melcher, C. L. 2006. New Prospects for Time-of-Flight PET with LSO Scintillators. *IEEE Trans. Nuc. Sci.,* 53**,** 2484-8.

Mullani, N. A., Ficke, D. C., Hartz, R., Markham, J. & Wong, G. 1981. System design of a fast PET scanner utilizing time-of-flight. *IEEE Trans. Nuc. Sci.,* NS-28**,** 104-7.

Mumcuoglu, E. U., Leahy, R. M. & Cherry, S. R. 1996. Bayesian reconstruction of PET images: methodology and performance analysis. *Phys Med Biol,* 41**,** 1777-807.

National Electrical Manufacturers Association (NEMA). 1994. Performance Measurements of Positron Emission Tomographs. NEMA Standards Publication NU2-1994. Rosslyn, VA. National Electrical Manufacturers Association

National Electrical Manufacturers Association (NEMA). 2001. Performance Measurements of Positron Emission Tomographs. NEMA Standards Publication NU2-2001. Rosslyn, VA. National Electrical Manufacturers Association

National Electrical Manufacturers Association (NEMA). 2008. Performance Measurements of Small Animal Positron Emission Tomographs. NEMA Standards Publication NU4-2008. Rosslyn, VA. National Electrical Manufacturers Association

Noo, F., Clackdoyle, R., Mennessier, C., White, T. A. & Roney, T. J. 2000. An analytic method based on identification of ellipse parameters for scanner calibration in conebeam tomography. *Phys. Med. Biol.,* 45**,** 3489-3508.

Nuyts, J. & Fessler, J. A. 2003. A penalized-likelihood image reconstruction method for emission tomography compared to postsmoothed maximum-likelihood with matched spatial resolution. *IEEE Trans Med Imaging,* 1042-1052.

NVIDIA CUDA Programming Guide v.2.5.0 [Online]. Available: http://developer.nvidia.com/object/gpu_programming_guide.html. [September 2010].

Olcott, P. D., Talcott, J. A., Levin, C. S., Habte, F. & Foudray, A. M. K. 2003. Compact readout electronics for position sensitive photomultiplier tubes. *In:* Nuclear Science Symposium Conference Record, 2003 IEEE, 19-25 Oct. 2003 2003. 1962-1966 Vol.3.

Oliver, J. F. & Rafecas, M. 2008. Revisiting the singles rate method for modeling accidental coincidences in PET. *In:* Nuclear Science Symposium Conference Record, 2008. NSS '08. IEEE, 19-25 Oct. 2008 2008. 4288-4291.

Otte, A. N., Barral, J., Dogolshein, B., Hose, J., Klemin, S., Lorenz, E., Mirzoyan, R., Popova, E. & Teshima, M. 2005. A Test of Silicon Photomultipliers as Readout for PET. *Nucl.Instrum.Meth.A,* 705-715.

Panettieri, V., Wennberg, B., Gagliardi, G., Duch, M. A., Ginjaume, M. & Lax, I. 2007. SBRT of lung tumours: Monte Carlo simulation with PENELOPE of dose distributions including respiratory motion and comparison with different treatment planning systems. *Phys Med Biol,* 52**,** 4265-81.

Pani, R., Pellegrini, R., Cinti, M. N., Trotta, C., Trotta, G., Garibaldi, F., Scafè, R. & Del Guerra, A. 2003. Flat Panel PMT for photon emission imaging. *Nuclear Instruments and Methods in Physics Research Section A: Accelerators, Spectrometers, Detectors and Associated Equipment,* 505**,** 590-594.

Papathanassiou, D., Bruna-Muraille, C., Liehn, J. C., Nguyen, T. D. & Cure, H. 2009. Positron Emission Tomography in oncology: present and future of PET and PET/CT. *Crit Rev Oncol Hematol,* 72**,** 239-54.

Park, S. J., Rogers, W. L. & Clinthorne, N. H. 2007. Design of a very high-resolution small animal PET scanner using a silicon scatter detector insert. *Phys Med Biol,* 52**,** 4653-77.

Parra, L. & Barrett, H. H. 1998. List-mode likelihood: EM algorithm and image quality estimation demonstrated on 2D PET. *IEEE Trans. Med. Imag.,* 17**,** 228-35.

Pavlopoulos, S. & Tzanakos, G. 1993. Design and performance evaluation of a high resolution small animal positron tomograph. *In:* Nuclear Science Symposium and Medical Imaging Conference, 1993., 1993 IEEE Conference Record., 31 Oct-6 Nov 1993 1993. 1697-1701 vol.3.

Pavlopoulos, S. & Tzanakos, G. 1996. Design and performance evaluation of a high-resolution small animal positron tomograph. *Nuclear Science, IEEE Transactions on,* 43**,** 3249-3255.

Phelps, M. E., Hoffman, E. J., Mullani, N. A. & Ter-Pogossian, M. M. 1975. Application of annihilation coincidence detection to transaxial reconstruction tomography. *J Nucl Med,* 16**,** 210-24.

Pichler, B., Lorenz, E., Mirzoyan, R., Pimpl, W., Roder, F., Schwaiger, M. & Ziegler, S. I. 1997. Performance test of a LSO-APD PET module in a 9.4 Tesla magnet. *In:* Nuclear Science Symposium, 1997. IEEE, 9-15 Nov 1997 1997. 1237-1239 vol.2.

Pierce, L., Miyaoka, R., Lewellen, T., Alessio, A. & Kinahan, P. 2009. Determining Block Detector Positions for PET Scanners. *IEEE Nucl. Sci. Symp. Conf. Rec.*

Pomper, M. G. 2001. Molecular Imaging: and Overview. *Acad. Radiol.,* 8**,** 1141-53.

Popov, V., Majewski, S. & Weisenberger, A. G. 2003. Readout electronics for multianode photomultiplier tubes with pad matrix anode layout. *In:* Nuclear Science Symposium Conference Record, 2003 IEEE, 19-25 Oct. 2003 2003. 2156-2159 Vol.3.

Powsner, R. & Powsner, E. 2006. *Essential Nuclear Medicine Physics,* Haryana, Blackwell Publishing.

Pratx, G., Chinn, G., Olcott, P. D. & Levin, C. S. 2009. Fast, Accurate and Shift-Varying Line Projections for Iterative Reconstruction Using the GPU. *Medical Imaging, IEEE Transactions on,* 28**,** 435-445.

Qi, J., Leahy, R. M., Cherry, S. R., Chatziioannou, A. & Farquhar, T. H. 1998. High-resolution 3D Bayesian image reconstruction using the microPET small-animal scanner. *Phys Med Biol,* 43**,** 1001-13.

Qi, J., Yang, Y., Zhou, J., Wu, Y. & Cherry, S., R. 2011. Experimental assessment of resolution improvement of a zoom-in PET. *Physics in Medicine and Biology,* 56**,** N165.

Rafecas, M., Mosler, B., Dietz, M., Pogl, M., Stamatakis, A., McElroy, D. P. & Ziegler, S. I. 2004. Use of a Monte Carlo-based probability matrix for 3-D iterative reconstruction of MADPET-II data. *Nuclear Science, IEEE Transactions on,* 51**,** 2597-2605.

Raichle, M. E. 1983. Positron Emission Tomography. *Ann. Rev. Neurosci.,* 6**,** 249-267.

Reader, A. J., Ally, S., Bakatselos, F., Manavaki, R., Walledge, R. J., Jeavons, A. P., Julyan, P. J., Sha, Z., Hastings, D. L. & Zweit, J. 2002. One-pass list-mode EM algorithm for high-resolution 3-D PET image reconstruction into large arrays. *Nuclear Science, IEEE Transactions on,* 49**,** 693-699.

Riboldi, S., Seidel, J., Green, M., Monaldo, J., Kakareka, J. & Pohida, T. 2003. Investigation of signal readout methods for the Hamamatsu R8500 flat panel PSPMT. *In:* Nuclear Science Symposium Conference Record, 2003 IEEE, 19-25 Oct. 2003 2003. 2452-2456 Vol.4.

Rogers, D. W. 2006. Fifty years of Monte Carlo simulations for medical physics. *Phys Med Biol,* 51**,** R287-301.

Rogers, D. W. O. 1984. Low energy electron transport with EGS. *Nucl. Inst. Meth. In Phy. Res. A,* 227**,** 535-48.

Rouze, N. C., Schmand, M., Siegel, S. & Hutchins, G. D. 2004. Design of a small animal PET imaging system with 1 microliter volume resolution. *Nuclear Science, IEEE Transactions on,* 51**,** 757-763.

Salvat, F., Fernández-Varea, J. M. & Sempau, J. 2006. *PENELOPE-2006: A Code System for Monte Carlo Simulation of Electron and Photon Transport,* France, NEA.

Sanders, J. & Kandrot, E. 2010 *CUDA by Example: An Introduction to General-Purpose GPU Programming,* Addison-Wesley.

Seidel, J., Vaquero, J. J. & Green, M. V. 2003. Resolution uniformity and sensitivity of the NIH ATLAS small animal PET scanner: Comparison to simulated LSO scanners without depth-of-interaction capability. *Nuclear Science, IEEE Transactions on,* 50**,** 1347-1350.

Seidel, J., Vaquero, J. J., Siegel, S., Gandler, W. R. & Green, M. V. 1999. Depth identification accuracy of a three layer phoswich PET detector module. *Nuclear Science, IEEE Transactions on,* 46**,** 485-490.

Seidel, J., Wenze, X., Kakareka, J. W., Pohida, T. J., Green, M. V. & Choyke, P. L. 2010. A positron projection imager for whole-body mouse imaging. *In:* Nuclear Science Symposium Conference Record (NSS/MIC), 2010 IEEE, Oct. 30 2010-Nov. 6 2010 2010. 2206-2209.

Sempau, J. & Andreo, P. 2006. Configuration of the electron transport algorithm of PENELOPE to simulate ion chambers. *Phys Med Biol,* 51**,** 3533-48.

Sempau, J., Fernández-Varea, J. M., Acosta, E. & Salvat, F. 2003a. Experimental benchmarks of the Monte Carlo code penelope. *Nuclear Instruments and Methods in Physics Research Section B: Beam Interactions with Materials and Atoms,* 207**,** 107-123.

Sempau, J., Fernández-Varea, J. M., Acosta, E. & Salvat, F. 2003b. Experimental benchmarks of the Monte Carlo code PENELOPE. *Nucl. Inst. Meth. In Phy. Res. B,* 207**,** 107-123.

Shepp, L. A. & Vardi, Y. 1982. Maximum Likelihood Reconstruction for Emission Tomography. *Medical Imaging, IEEE Transactions on,* 1**,** 113-122.

Siegel, S., Silverman, R. W., Yiping, S. & Cherry, S. R. 1996. Simple charge division readouts for imaging scintillator arrays using a multi-channel PMT. *Nuclear Science, IEEE Transactions on,* 43**,** 1634-1641.

Sjöland, K. A. & Kristiansson, P. 1994. Pile-up and defective pulse rejection by pulse shape discrimination in surface barrier detectors. *Nuclear Instruments and Methods in Physics Research Section B: Beam Interactions with Materials and Atoms,* 94**,** 333-337.

Slijpen, E. T. P. & Beekman, F. J. 1999. Comparison of post-filtering and filtering between iterations for SPECT reconstruction. *Nuclear Science, IEEE Transactions on,* 46**,** 2233-2238.

Smith, R. J., Karp, J. S. & Muehllehner, G. 1994. The countrate performance of the volume imaging PENN-PET scanner. *IEEE Trans Med Imaging,* 13**,** 610-8.

Snyder, D. L., Miller, M. I., L. J. Thomas, J. & Politte, D. G. 1987. Noise and edge artifacts in maximum-likelihood reconstruction for emission tomography. *IEEE Trans. Nuc. Sci.,* MI-6**,** 228-238.

Sorenson, J. A. & Phelps, M. E. 1987. *Physics in nuclear medicine,* Grune & Stratton.

Stayman, W. & Fessler, J. A. 2001. Nonnegative Definite Quadratic Penalty Design for Penalized-Likelihood Reconstruction. *In:* IEEE Nuc. Sci. Symp., 2001.

Stearns, C. W., Chesler, D. A., Kirsch, J. E. & Brownell, G. L. 1985. Quantitative Imaging with the MGH Analog Ring Positron Tomograph. *IEEE Transactions on Nuclear Science,* 32**,** 898-901.

Stearns, C. W., McDaniel, D. L., Kohlmyer, S. G., Arul, P. R., Geiser, B. P. & Shanmugam, V. 2003. Random coincidence estimation from single event rates on the Discovery ST PET/CT scanner. *In:* Nuclear Science Symposium Conference Record, 2003 IEEE, 19-25 Oct. 2003 2003. 3067-3069 Vol.5.

Stickel, J. R. & Cherry, S. R. 2005. High-resolution PET detector design: modelling components of intrinsic spatial resolution. *Phys Med Biol,* 50**,** 179-95.

Stöcklin, G. & Pike, V. W. 1993. *Radiopharmaceuticals for positron emission tomography: methodological aspects*, Kluwer Academic Publishers.

Strother, S. C., Casey, M. E. & Hoffman, E. J. 1990. Measuring PET scanner sensitivity: relating countrates to image signal-to-noise ratios using noise equivalents counts. *Nuclear Science, IEEE Transactions on,* 37**,** 783-788.

Sun, Y., Hou, Y. & Hu, J. 2007. Reduction of Artifacts Induced by Misaligned Geometry in Cone-Beam CT. *IEEE Trans. Bio. Eng.,* 54**,** 1461-71.

Surti, S., Karp, J. S., Perkins, A. E., Cardi, C. A., Daube-Witherspoon, M. E., Kuhn, A. & Muehllehner, G. 2005. Imaging performance of a-PET: a small animal PET camera. *Medical Imaging, IEEE Transactions on,* 24**,** 844-852.

Sweet, W. H. 1951. The uses of nuclear disintegration in the diagnosis and treatment of brain tumor. *N Engl J Med,* 245**,** 875-

8.
Tai, C., Chatziioannou, A., Siegel, S., Young, J., Newport, D., Goble, R. N., Nutt, R. E. & Cherry, S. R. 2001. Performance evaluation of the microPET P4: a PET system dedicated to animal imaging. *Phys Med Biol,* 46**,** 1845-62.
Tai, Y. C., Chatziioannou, A. F., Yang, Y., Silverman, R. W., Meadors, K., Siegel, S., Newport, D. F., Stickel, J. R. & Cherry, S. R. 2003. MicroPET II: design, development and initial performance of an improved microPET scanner for small-animal imaging. *Phys Med Biol,* 48**,** 1519-37.
Tai, Y. C., Wu, H., Pal, D. & O'Sullivan, J. A. 2008. Virtual-pinhole PET. *J Nucl Med,* 49**,** 471-9.
Tarantola, G., Zito, F. & Gerundini, P. 2003. PET instrumentation and reconstruction algorithms in whole-body applications. *J Nucl Med,* 44**,** 756-69.
Ter-Pogossian, M. M. 1982. Positron emission tomography (PET). *J Med Syst,* 6**,** 569-77.
Ter-Pogossian, M. M., Phelps, M. E., Hoffman, E. J. & Mullani, N. A. 1975. A positron-emission transaxial tomograph for nuclear imaging (PETT). *Radiology,* 114**,** 89-98.
Thompson, C. J. & Meyer, E. 1987. *The effect of live time in components of a positron tomograph on image quantification*.
Thompson, C. J., Moreno-Cantu, J. & Picard, Y. 1992a. PETSIM: Monte Carlo simulation of all sensitivity and resolution parameters of cylindrical positron imaging systems. *Physics in Medicine and Biology,* 37**,** 731.
Thompson, C. J., Moreno-Cantu, J. & Picard, Y. 1992b. PETSIM: Monte Carlo simulation of all sensitivity and resolution parameters of cylindrical positron imaging systems. *Phys Med Biol,* 37**,** 731-49.
Thomson, C. J., Moreno-Cantu, J. & Picard, Y. 1992. PETSIM: Monte Carlo simulation of all sensitivity and resolution parameters of cylindrical positron imaging systems. *Phys. Med. Biol.,* 37**,** 731-749.
Tzanakos, G. & Pavlopoulos, S. 1991. Modeling and simulation of a PET scanner. *In:* Nuclear Science Symposium and Medical Imaging Conference, 1991., Conference Record of the 1991 IEEE, 2-9 Nov. 1991 1991. 1689-1694 vol.3.
Tzanakos, G. & Pavlopoulos, S. 1993. Design and performance evaluation of a new high resolution detector array module for PET. *In:* Nuclear Science Symposium and Medical Imaging Conference, 1993., 1993 IEEE Conference Record., 31 Oct-6 Nov 1993 1993. 1842-1846 vol.3.
Urosevic, J., Sauzeau, V., Soto-Montenegro, M. L., Reig, S., Desco, M., Burkitt Wright, E. M., Cañamero, M., Mulero, F., Ortega, S., Bustelo, X. R. & Barbacid, M. 2011. Constitutive activation of B-Raf in the mouse germ line provides a model for human cardio-facio-cutaneous syndrome. *P Natl Acad Sci USA,* 108**,** 5015-5020.
Valk, P. E., Delbeke, D. & Bailey, D. L. 2006. *Positron emission tomography: clinical practice*, Springer.
Vaquero, J. J. & Desco, M. 2005. Limitaciones tecnológicas de la tomografía por emisión de positrones (PET) para pequeños animales de laboratorio. [Technical limitations of the positron emission tomography (PET) for small laboratory animals]. *Rev Esp Med Nucl,* 24**,** 334-47.
Vaquero, J. J., Lage, E., Ricon, L., Abella, M., Vicente, E. & Desco, M. 2005a. rPET detectors design and data processing. *In:* Nuclear Science Symposium Conference Record, 2005 IEEE, 23-29 Oct. 2005 2005a. 2885-2889.
Vaquero, J. J., Lage, E., Ricón, L., Abella, M., Vicente, E. & Desco, M. 2005b. rPET Detectors Design and Data Processing. *IEEE Nuclear Science Symposium Conference Record*.
Vaquero, J. J., Molins, A., Ortuño, J., Pascau, J. & Desco, M. 2004. Preliminary results of the small animal rotational positron emission tomography scanner. *In:* Mol. Imag. Biol., 2004. 102.
Vaquero, J. J., Redondo, S., Lage, E., Abella, M., Sisniega, A., Tapias, G., Montenegro, M. L. S. & Desco, M. 2008. Assessment of a New High-Performance Small-Animal X-Ray Tomograph. *Nuclear Science, IEEE Transactions on,* 55**,** 898-905.
Vaquero, J. J., Seidel, J., Siegel, S., Gandler, W. R. & Green, M. V. 1998. Performance characteristics of a compact position-sensitive LSO detector module. *Medical Imaging, IEEE Transactions on,* 17**,** 967-978.
Vaska, P., Bolotnikov, A., Carini, G., Camarda, G., Pratte, J. F., Dilmanian, F. A., Park, S. J. & James, R. B. 2005. Studies of CZT for PET applications. *In:* Nuclear Science Symposium Conference Record, 2005 IEEE, 23-29 Oct. 2005 2005. 2799-2802.
Vicente, E., Espana, S., Lopez Herraiz, J., Herranz, E., Desco, M., Vaquero, J. J. & Udias, J. M. 2008. Nonlinear effect of pile-up in the quantification of a small animal PET scanner. *In:* Nuclear Science Symposium Conference Record, 2008. NSS '08. IEEE, 19-25 Oct. 2008 2008. 5391-5395.
Vicente, E., Herraiz, J. L., Canadas, M., Cal-Gonzalez, J., Espana, S., Desco, M., Vaquero, J. J. & Udias, J. M. 2010a. Validation of NEMA NU4-2008 Scatter Fraction estimation with 18F and 68Ga for the ARGUS small-animal PET scanner. *In:* Nuclear Science Symposium Conference Record (NSS/MIC), 2010 IEEE, Oct. 30 2010-Nov. 6 2010 2010a. 3553-3557.
Vicente, E., Herraiz, J. L., Espana, S., Herranz, E., Desco, M., Vaquero, J. J. & Udias, J. M. 2011. Deadtime and pile-up correction method based on the singles to coincidences ratio for PET. *In:* Nuclear Science Symposium and Medical Imaging Conference (NSS/MIC), 2011 IEEE, 23-29 Oct. 2011 2011. 2933-2935.
Vicente, E., Herraiz, J. L., España, S., Herranz, E., Desco, M., Vaquero, J. J. & Udías, J. M. 2012a. Improved effective dead-time correction for PET scanners: Application to small-animal PET. *Phys Med Biol (Submitted)*.
Vicente, E., Herraiz, J. L., Seidel, J., Green, M. V., Desco, M., Vaquero, J. J. & Udias, J. M. 2012b. Regularization of 3D Iterative Reconstruction for a Limited-Angle PET Tomograph. *In:* Nuclear Science Symposium Conference Record (NSS/MIC), 2012 IEEE (Accepted), 2012b.
Vicente, E., Soto-Montenegro, M., España, S., Herraiz, J. L., Herranz, E., Vaquero, J. J., Desco, M. & Udias, J. M. 2007. Influence of random, pile-up and scatter corrections in the quantification properties of small-animal PET scanners. *In:* Nuclear Science Symposium Conference Record, 2007. NSS '07. IEEE, Oct. 26 2007-Nov. 3 2007 2007. 3964-3968.
Vicente, E., Udías, A. L., Herraiz, J. L., Desco, M., Vaquero, J. J. & Udías, J. M. 2010b. Corrección de atenuación de imágenes PET usando datos de TAC en el escáner para animales pequeños Argus PET/CT. *Libro de Actas, CASEIB 2010*.

Vicente, E., Vaquero, J. J., Espana, S., Herraiz, J. L., Udias, J. M. & Desco, M. 2006. Normalization in 3D PET: Dependence on the Activity Distribution of the Source. *In:* Nuclear Science Symposium Conference Record, 2006. IEEE, Oct. 29 2006-Nov. 1 2006 2006. 2206-2209.

Vicente, E., Vaquero, J. J., Lage, E., Tapias, G., Abella, M., Herraiz, J. L., España, S., Udías, J. M. & Desco, M. 2006 Caracterización del Tomógrafo de Animales rPET. *Libro de Actas, CASEIB 2006*.

Vilches, M., García-Pareja, S., Guerrero, R., Anguiano, M. & Lallena, A. M. 2007. Monte Carlo simulation of the electron transport through thin slabs: A comparative study of PENELOPE, GEANT3, GEANT4, EGSnrc and MCNPX. *Nucl. Inst. Meth. In Phy. Res. B,* 254**,** 219-30.

Visser, E. P., Disselhorst, J. A., Brom, M., Laverman, P., Gotthardt, M., Oyen, W. J. & Boerman, O. C. 2009. Spatial resolution and sensitivity of the Inveon small-animal PET scanner. *J Nucl Med,* 50**,** 139-47.

Wang, G. C., Huber, J. S., Moses, W. W., Qi, J. & Choong, W. S. 2006a. Characterization of the LBNL PEM camera. *Nuclear Science, IEEE Transactions on,* 53**,** 1129-1135.

Wang, Y., Seidel, J., Tsui, B. M., Vaquero, J. J. & Pomper, M. G. 2006b. Performance evaluation of the GE healthcare eXplore VISTA dual-ring small-animal PET scanner. *J Nucl Med,* 47**,** 1891-900.

Watanabe, M., Uchida, H., Okada, H., Shimizu, K., Satoh, N., Yoshikawa, E., Ohmura, T., Yamashita, T. & Tanaka, E. 1992. A high resolution PET for animal studies. *Medical Imaging, IEEE Transactions on,* 11**,** 577-580.

Weber, S. & Bauer, A. 2004. Small animal PET: aspects of performance assessment. *Eur J Nucl Med Mol Imaging,* 31**,** 1545-55.

Wernick, M. N. & Aarsvold, J. N. 2004. *Emission tomography: the fundamentals of PET and SPECT*, Elsevier Academic Press.

Williams, C. W., Crabtree, M. C. & Burgiss, S. G. 1979. Design and Performance Characteristics of a Positron Emission Computed Axial Tomograph--ECATÂ®-II. *Nuclear Science, IEEE Transactions on,* 26**,** 619-627.

Wirth, V. 1989. Effective energy resolution and scatter rejection in nuclear medicine. *Phys Med Biol,* 34**,** 85-90.

Wu, H., Pal, D., O'Sullivan, J. A. & Tai, Y. C. 2008a. A feasibility study of a prototype PET insert device to convert a general-purpose animal PET scanner to higher resolution. *J Nucl Med,* 49**,** 79-87.

Wu, H., Pal, D., Song, T. Y., O'Sullivan, J. A. & Tai, Y. C. 2008b. Micro insert: a prototype full-ring PET device for improving the image resolution of a small-animal PET scanner. *J Nucl Med,* 49**,** 1668-76.

Wu, H., Song, T. Y., Pal, D., Keesing, D. B., Komarov, S., O Sullivan, J. A. & Tai, Y.-C. 2008c. A high resolution PET insert system for clinical PET/CT scanners. *In:* Nuclear Science Symposium Conference Record, 2008. NSS '08. IEEE, 19-25 Oct. 2008 2008c. 5442-5444.

Wu, Y., Bowen, S. L., Yang, K., Packard, N., Fu, L., Burkett, G., Qi, J., Boone, J. M., Cherry, S. R. & Badawi, R. D. 2009. PET characteristics of a dedicated breast PET/CT scanner prototype. *Phys Med Biol,* 54**,** 4273-87.

Yamamoto, S., Amano, M., Miura, S., Iida, H. & Kanno, I. 1986. Deadtime correction method using random coincidence for PET. *J Nucl Med,* 27**,** 1925-8.

Yamaya, T., Hagiwara, N., Obi, T., Yamaguchi, M., Kita, K., Ohyama, N., Kitamura, K., Hasegawa, T., Haneishi, H. & Murayama, H. 2003. DOI-PET image reconstruction with accurate system modeling that reduces redundancy of the imaging system. *Nuclear Science, IEEE Transactions on,* 50**,** 1404-1409.

Yang, Y. & Cherry, S. R. 2006. Observations regarding scatter fraction and NEC measurements for small animal PET. *Nuclear Science, IEEE Transactions on,* 53**,** 127-132.

Yang, Y., Dokhale, P. A., Silverman, R. W., Shah, K. S., McClish, M. A., Farrell, R., Entine, G. & Cherry, S. R. 2006. Depth of interaction resolution measurements for a high resolution PET detector using position sensitive avalanche photodiodes. *Phys Med Biol,* 51**,** 2131-42.

Yang, Y., Tai, Y. C., Siegel, S., Newport, D. F., Bai, B., Li, Q., Leahy, R. M. & Cherry, S. R. 2004. Optimization and performance evaluation of the microPET II scanner for in vivo small-animal imaging. *Phys Med Biol,* 49**,** 2527-45.

Yu, D. F. & Fessler, J. A. 2002. Edge-preserving tomographic reconstruction with nonlocal regularization image processing. *IEEE Trans Med Imaging,* 21**,** 159-173.

Zaidi, H. 1999. Relevance of accurate Monte Carlo modeling in nuclear medical imaging. *Med Phys,* 26**,** 574-608.

Zaidi, H. 2006. *Quantitative analysis in nuclear medicine imaging*, Springer.

Zaidi, H., Montandon, M. L. & Slosman, D. O. 2004. Attenuation compensation in cerebral 3D PET: effect of the attenuation map on absolute and relative quantitation. *Eur J Nucl Med Mol Imaging,* 31**,** 52-63.

Zaidi, H. & Scheurer, C. 1999. An object-oriented Monte Carlo simulator for 3D cylindrical positron tomographs. *Comput. Methods Programs Biomed.,* 58**,** 133-45.

Zaidi, H. & Sgouros, G. 2003. *Therapeutic applications of Monte Carlo calculations in nuclear medicine*, IOP, Institute of Physics Pub.

Zeng, G. L. & Gullberg, G. T. 2000. Unmatched projector/backprojector pairs in an iterative reconstruction algorithm. *Medical Imaging, IEEE Transactions on,* 19**,** 548-555.

Zhang, H., Bao, Q., Vu, N. T., Silverman, R. W., Taschereau, R., Berry-Pusey, B. N., Douraghy, A., Rannou, F. R., Stout, D. B. & Chatziioannou, A. F. 2011. Performance evaluation of PETbox: a low cost bench top preclinical PET scanner. *Mol Imaging Biol,* 13**,** 949-61.

Zhou, J. & Qi, J. 2009. Theoretical analysis and simulation study of a high-resolution zoom-in PET system. *Physics in Medicine and Biology,* 54**,** 5193.

Zhou, J. & Qi, J. 2010. Efficient system modeling of a high-resolution zoom-in PET scanner. *In:* Nuclear Science Symposium Conference Record (NSS/MIC), 2010 IEEE, Oct. 30 2010-Nov. 6 2010 2010. 3501-3505.

Zhou, J. & Qi, J. 2011. Adaptive Imaging for Lesion Detection Using a Zoom-in PET System. *Medical Imaging, IEEE Transactions on,* 30**,** 119-130.

Resumen en castellano

Introducción

En 1953, la joven hija de un granjero de Rhode Island fue llevada a Boston para ser diagnosticada de un problema neurológico que la imposibilitaba leer. El neurocirujano del Hospital General de Massachusetts que la atendió fue incapaz de diagnosticar la enfermedad, así que solicitó la ayuda del doctor Gordon L. Brownell. Como contaría un año después la revista Time, el doctor Brownell junto con William H. Sweet desarrollaron un escáner [Sweet, 1951, Burnham and Brownell, 1972, Brownell *et al.*, 1969] que permitió aislar la localización de un tumor (en una región de unos 8.5 mm) que el neurocirujano pudo extraer con éxito del cerebro de la niña. La tecnología que Brownell había inventado asentaría la bases de la tomografía por emisión de positrones (*positron emission tomography*, PET). Unos pocos años después, en 1973, Michael E. Phelps y colaboradores construyeron el primer tomógrafo PET conocido como PETT I [Ter-Pogossian *et al.*, 1975, Phelps *et al.*, 1975]. Phelps fue uno de los primeros en mostrar la activación de diferentes regiones del cerebro en la realización de diferentes tareas mentales.

Desde la aparición de este primer escáner PET, la técnica se ha extendido a diversos campos como oncología, cardiología y neurología. Su extensión a la investigación preclínica ha representado un gran reto desde el desarrollo del primer escáner preclínico a mediados de los años 90 ([Pavlopoulos and Tzanakos, 1993, 1996, Tzanakos and Pavlopoulos, 1993, Watanabe *et al.*, 1992, Bloomfield *et al.*, 1995]), con la consecuente mejora en términos de sensibilidad y resolución principalmente. El interés de esta mejora radica en el hecho de que imágenes con mejor resolución pueden impulsar el estudio de enfermedades humanas empleando modelos animales.

Además de los requisitos de mayor resolución, muchos diseños de sistemas preclínicos presentan nuevas geometrías que también pueden dificultar la aplicación directa de los algoritmos desarrollados inicialmente para los escáneres clínicos. Esto plantea la necesidad de protocolos adaptados a los sistemas de animales pequeños específicos en uso y, al mismo tiempo, conduce a preguntas acerca de cómo las fuentes de error típicas en la escala de escáneres clínicos afectan a estos sistemas.

Los métodos de procesamiento de datos y de imágenes son también un campo de gran interés y desarrollo con el fin de optimizar el uso cuantitativo de las imágenes PET en la práctica clínica y preclínica. La evaluación de estos métodos a menudo se basa en el uso de datos simulados, ya que éstos ofrecen un control de los procesos físicos involucrados en la técnica, desde la emisión del positrón a la detección de los fotones por los detectores. Las métodos de simulación Monte Carlo se han convertido en una herramientas de gran importancia y en un complemento indispensable para una amplia gama de problemas que no podrían ser tratados por métodos experimentales o analíticos [Rogers, 2006].

La simulación en PET usando Monte Carlo permite también la optimización del diseño para nuevos escáneres, el estudio de los factores que afectan a la calidad de la imagen, la validación de métodos de corrección de diferentes efectos tales como el *pile-up* y tiempo muerto, *scatter*, atenuación, volumen parcial, etc, para mejorar la cuantificación de la imagen, así como el desarrollo y la prueba de nuevos algoritmos de reconstrucción de imágenes. Otra ventaja importante de las simulaciones en PET es que permiten estudiar los parámetros que no se pueden medir en la práctica.

El trabajo de esta tesis se ha realizado en una de las líneas de investigación llevadas a cabo por el Grupo de Física Nuclear (GFN) de la Universidad Complutense de Madrid, en estrecha colaboración con el Laboratorio de Imagen Médica (LIM) del Hospital General Universitario Gregorio Marañón, cuyos objetivos son diseñar, desarrollar y evaluar nuevos sistemas de adquisición de datos, procesamiento y reconstrucción de imágenes para aplicaciones en investigación biomédica. En este

contexto, esta tesis presenta contribuciones al estudio y la caracterización de los escáneres PET preclínicos disponibles en el Laboratorio de Imagen Médica, el estudio de las fuentes de error que limitan la calidad de las imágenes junto con la investigación de algoritmos para compensarlos y la búsqueda de nuevos diseños, en colaboración con otros dos centros de investigación (Department of Biomedical Engineering, University of California, (Davis, CA) y the National Institutes of Health (NIH), Bethesda, MD [Molecular Imaging Program, National Cancer Institute]) donde el autor de esta tesis estuvo trabajando como parte del programa de estancias breves de la beca JAEPredoctoral (2008) (Instituto de Estructura de la Materia, Consejo Superior de Investigaciones Científicas (CSIC), Madrid, España).

El objetivo principal de esta tesis es contribuir a la mejora de la calidad de las imágenes de PET para la investigación preclínica con animales pequeños mediante el uso de simulaciones Monte Carlo, ya sea para el estudio de los problemas limitantes de la técnica en los escáneres existentes proporcionando métodos para compensarlos, ya sea para orientar el diseño de nuevos prototipos, analizando las ventajas y desventajas antes de tomar una decisión final. Los objetivos específicos son los siguientes:

1. Evaluar el rendimiento de los sistemas PET preclínicos disponibles en el Laboratorio de Imagen Médica, siguiendo, en la medida de lo posible, una metodología estándar para comparar los sistemas entre sí y con otros sistemas comerciales en las mismas condiciones [Vicente *et al.*, 2006 , Goertzen *et al.*, 2012, Vicente *et al.*, 2010a].

2. Estudiar las fuentes de error que limitan la calidad de las imágenes reconstruidas usando simulaciones Monte Carlo para investigar nuevos métodos y algoritmos para compensarlos [Vicente *et al.*, 2012a, Abella *et al.*, 2012, Vicente *et al.*, 2010b].

3. Utilizar simulaciones Monte Carlo para guiar el diseño de nuevos prototipos, realizando las modificaciones necesarias en el paquete de Monte Carlo empleado (peneloPET, [España *et al.*, 2009]) y en los métodos de reconstrucción existentes (como GFIRST [Herraiz *et al.*, 2011]) para adaptar los códigos existentes a la geometría no convencional de los nuevos diseños [Vicente *et al.*, 2012b].

Todos los algoritmos desarrollados en el contexto de esta tesis no son exclusivos para un escáner en particular, sino que han sido diseñados para ser flexibles y fácilmente adaptables a diferentes arquitecturas que cumplan con ciertas condiciones en cada caso. Sin embargo, dado que este trabajo se beneficia del acceso a datos reales adquiridos por los escáneres disponibles en el Laboratorio de Imagen Médica, el desarrollo de los diferentes métodos se adaptan a la geometría particular de estos sistemas ([Wang *et al.*, 2006b, Vaquero *et al.*, 2005a]).

Como consideración final, decir que una parte significativa de los resultados presentados en esta tesis, además de dar lugar a publicaciones científicas, se pretende que sean incorporados en el software de escáneres preclínicos de alta resolución fabricados por SEDECAL y distribuidos por todo el mundo en virtud de acuerdos de transferencia de tecnología con el Laboratorio de Imagen Médica y el Grupo de Física Nuclear.

Caracterización de escáneres PET preclínicos

En este capítulo presentamos una aplicación de la evaluación estándar de un escáner en la caracterización de dos escáneres preclínicos [Vicente *et al.*, 2006 , Goertzen *et al.*, 2012]: rPET [Vaquero *et al.*, 2005b] y Argus [Wang *et al.*, 2006b], disponibles en el Laboratorio de Imagen Médica (Hospital GU Gregorio Marañón). También presentamos una evaluación detallada del protocolo NEMA para estimar la fracción de dispersión (SF) usando dos tipos de isótopos, ^{18}F, que es el isótopo propuesto por el protocolo y ^{68}Ga, un isótopo cuyo rango de positrón es mucho mayor, proponiendo una mejora del método para poder usar isótopos con rango de positrón no despreciable [Vicente *et al.*, 2010a]

Caracterización de los escáneres rPET y Argus

La caracterización de un tomógrafo consiste en realizar una serie de pruebas necesarias para la determinación de la calidad del prototipo. Para hacer frente a la necesidad de obtener medidas estandarizadas, se publicó en 2008 el protocolo NEMA NU 4 [NEMA-NU4, 2008], una adaptación para escáneres PET preclínicos de los existentes protocolos para escáneres de humanos [NEMA-NU2, 1994, 2001]. Estos protocolos estándar incluyen dos tipos de pruebas, unas encaminadas a estudiar los parámetros intrínsecos del escáner como la resolución espacial o la sensibilidad, otras a estimar la bondad de las correcciones incorporadas en la reconstrucción de las imágenes. Estas pruebas determinan características básicas del escáner como: sensibilidad, resolución espacial, resolución energética, fracción de dispersión (*Scatter fraction*, SF), curva NEC (tasas de conteo) y calidad de imagen. Los resultados obtenidos para los escáneres preclínicos evaluados se presentan a continuación:

Sensibilidad: Los resultados muestran una sensibilidad menor para el escáner rPET (2.2± 0.3 % en 100-700 keV) que para el sistema Argus (6.8 ± 0.8 % en 100-700 keV, 2.3 ± 0.3 % en 400-700 keV). Sin embargo la sensibilidad de rPET mejora la de otros escáneres de características similares como YAP-(S)PET (1.87%) [Del Guerra *et al.*, 2006]. Por su parte, la sensibilidad del Argus tiene un valor muy competido, mejorando la sensibilidad de muchos escáneres con geometría de anillo completo, algunos con campos de visión (FOV) axial mayor.

Resolución espacial: Los valores obtenidos son inferiores a 2.3 mm en todas las direcciones (radial, tangencial y axial) para ambos escáneres. En rPET la mejor resolución se alcanza en la dirección radial, con valores entre 1.5 y 1.8 mm, gracias a su geometría de detectores plano paralelos, que degrada la resolución más despacio a medida que nos alejamos del centro en comparación con escáneres de anillo completo, donde el error de paralaje degrada más rápidamente la resolución en esta dirección. Por otra parte, para el escáner Argus la mejor resolución se alcanza en la dirección tangencial con valores por debajo de 1.7 mm. La resolución radial es algo peor, pero mejora los valores de otros escáneres de anillo completo debido a su capacidad de distinción en la profundidad de interacción (DOI), gracias a las dos capas de cristales que integra (*phoswich*).

Resolución energética: La resolución energética promedio (para todos los cristales de un bloque detector) medida para rPET es de 16.5 % con una desviación estándar de 2%. La peor resolución por cristal medida es de 23.4 %, siendo la mejor de 12.7 %. Para comparar estos valores con los del sistema Argus, utilizamos los publicados por Wang et al. [2006b], ya que no medimos la resolución energética. La resolución promedio medida por estos autores es de 26% en los cristales de LYSO y 33% en los de GSO. (29.6% la resolución promedio contando ambos tipos de cristales). De esta comparación vemos que la resolución energética de rPET es mejor que la del Argus debido a que los bloques detectores de rPET son de mayor tamaño que los de Argus y que la longitud de los cristales es aproximadamente el doble que cada capa del *phoswich* en Argus.

Fracción de dispersión (Scatter fraction [SF]) y curva NEC (Noise equivalent count):, Los valores del pico de la curva NEC obtenidos son mayores para el escáner Argus en toda las ventanas de energía, incluso para 400-700 keV, cuya sensibilidad es similar a la rPET en la ventana de 100-700 keV. Las diferencias entre estas dos últimas curvas se deben principalmente a diferencias en la ventana de coincidencia temporal, tiempo muerto y en el tiempo de integración entre los dos escáneres y porque la posición del capilar con actividad dentro del maniquí empleado (tamaño ratón) está a 1 cm del centro del FOV transaxial, donde la sensibilidad es ligeramente inferior en rPET (100-700 keV) que en Argus (400-700 keV). Sin embargo, el valor de SF (para el maniquí tamaño ratón) para rPET (100-700 keV) es menor que el de Argus para la misma ventana de energía e igual al valor de Argus en la ventana de energía de 250-700 keV. Esto es probablemente debido al hecho de que rPET es un sistema de anillos parcial, de modo que el *scatter* en los blindajes es significativamente menor. Esto es consistente con el trabajo de Yang y Cherry [Yang and Cherry], que mostraron que para el maniquí tamaño ratón en el sistema microPET II, la fuente dominante de scatter proviene de los blindajes. Otro

ejemplo de este hecho se puede encontrar en la siguiente sección de este capítulo, donde se muestra la importancia de la contribución al SF total debido a los blindajes utilizando simulaciones del maniquí tamaño ratón en el sistema de Argus.

Calidad de imagen: Para determinar la calidad de imagen de los escáneres evaluados, utilizamos el maniquí recomendado por el estándar NEMA NU-4 y un análisis propuesto en una versión anterior al documento final, obteniendo los valores de contraste en regiones calientes (con actividad mayor, Q_H) y frías *(*sin actividad, Q_H), la uniformidad de la imagen y los coeficientes de recuperación (*Recovery coefficients, RC)*, que son una medida del efecto de volumen parcial. Es importante hacer notar en esta sección que los resultados obtenidos dependen altamente del algoritmo de reconstrucción empleado y de las correcciones aplicadas a los datos. La variabilidad observada en los resultados de cada sistema muestra que se debe tener cuidado al comparar los resultados de calidad de imagen entre diferentes sistemas. A pesar esta alta dependencia del resultado con el método de reconstrucción, se observa que los contrastes y la uniformidad son ligeramente mejores para el escáner de Argus, así como los RCs, ya que el efecto de volumen parcial está altamente ligado a la resolución espacial del sistema y, como ya hemos visto, la resolución espacial del escáner Argus es superior.

Estimación de la fracción de dispersión (SF) usando fuentes de ^{18}F y ^{68}Ga

En este trabajo presentamos una evaluación del procedimiento propuesto por NEMA para estimar el SF (sección 4 en [NEMA-NU4, 2008]). El análisis se ha hecho mediante simulaciones y datos reales usando dos tipos de isótopos: ^{18}F, isótopo propuesto por NEMA y ^{68}Ga, isótopo de gran interés porque no necesita un ciclotrón para ser obtenido, por lo que puede ser obtenido con un generador de galio directamente en las instalaciones donde se realiza la adquisición, pero que tiene el inconveniente de tener mayor rango de positrón. Este hecho afecta a la determinación del SF en el procedimiento propuesto por NEMA, ya que dicho método analiza perfiles de actividad de capilares en maniquíes (medio que genera la dispersión) y, debido al efecto del rango de positrón, dichos perfiles se ven ensanchados para isótopos con mayor rango, como el ^{68}Ga, como puede verse en la Figura R.1A . En dicha figura se muestra la banda de 14 mm que separa las cuentas de *scatter* (cuando la adquisición se hace a actividades bajas, de manera que las coincidencias aleatorias son despreciables) de las verdaderas, según el método. Podemos observar que la estimación del SF para el Galio es mayor que la del Flúor, cuando debería ser el mismo valor, como demostramos con simulaciones. En la Figura R.1B se presenta una comparación entre datos experimentales y simulados para el ^{18}F, mostrando la estimación de *scatter* (líneas discontinuas) del método propuesto por NEMA y el perfil de *scatter* obtenido de las simulaciones.

A pesar de las diferencias observadas entre los perfiles simulados y los experimentales, debidos muy probablemente a algunos blindajes del escáner no considerados en la simulación, lo que se puede observar es que la distribución de *scatter* no es plana si se tienen en cuenta los blindajes del escáner (simulaciones sin blindajes muestran perfiles de *scatter* planos*)*, apareciendo un pico en la posición del capilar. La estimación del SF de NEMA da un valor intermedio entre el SF proveniente del objeto y el SF total que tiene en cuenta el objeto y los blindajes del escáner, que contribuyen con una parte importante al valor del SF final como ya fue discutido en [Yang and Cherry, 2006].

Sugerencia para mejorar el protocolo NEMA: Con el fin de hacer el procedimiento NEMA isótopo-independiente, proponemos la desconvolución (unidimensional) de los perfiles de actividad radiales en el sinograma utilizados para estimar el *scatter*, para eliminar los efectos del rango del positrón. Para la desconvolución empleamos el perfil unidimensional de la distribución tridimensional del rango del positrón, lo que algunos autores llaman $aPSF_{sin}$ [Blanco, 2006, Cal-Gonzalez *et al.*, 2010] y aplicamos un sencillo EM-ML. Aplicando este método, la estimación del SF con ^{68}Ga es la misma que la obtenida con ^{18}F.

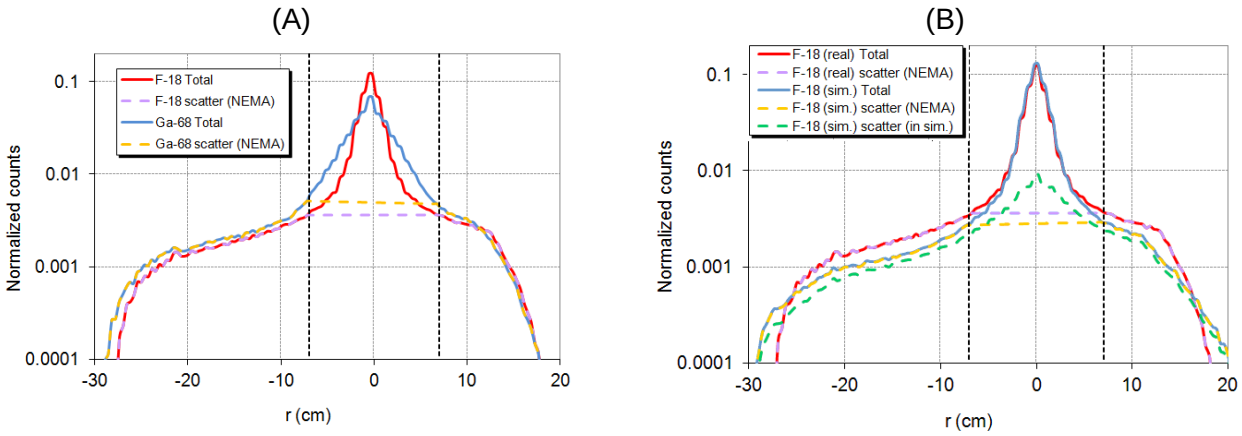

Figura R.1. *Perfiles radiales en el sinograma para estimar el SF según el protocolo NEMA.* ***(A)****: Datos experimentales para los isótopos 18F y 68Ga adquiridos con el escáner Argus.* ***(B)****: Comparación de datos experimentales y simulados (teniendo en cuenta los blindajes del escáner) para el 18F para el escáner Argus.*

Correcciones en escáneres PET preclínicos

En este capítulo estudiamos en detalle algunas de las correcciones necesarias para obtener una cuantificación adecuada en las imágenes. Las correcciones presentadas aquí fueron desarrolladas para los dos escáneres cuya caracterización hemos presentado en el capítulo anterior, pero pueden ser aplicadas a otros sistemas sin grandes cambios.

Modelado de pile-up y tiempo muerto en tomógrafos PET preclínicos

La corrección de pérdida de cuentas debidas al tiempo muerto y *pile-up* deriva normalmente de una combinación de modelos analíticos que describen el comportamiento de los distintos componentes electrónicos y datos experimentales usando adquisiciones largas para permitir el decaimiento de la fuente empleando determinados maniquíes. Normalmente se usa un cilindro de tamaño intermedio para determinar τ y las demás adquisiciones son corregidas empleando este único parámetro, lo que en este trabajo llamamos '*método uniparametral*'. Los modelos para el tiempo muerto normalmente lo separan en dos componentes, paralizable y no paralizable [Knoll, 2000].

Sin embargo, desde nuestra experiencia, no existen protocolos para tener en cuenta el *pile-up* en una adquisición general, ya que depende del material y tamaño del objeto situado en el FOV y de la distribución de la fuente (dentro/fuera del FOV) porque cambia el cociente de singles con respecto a las coincidencias (*Singles-to-Coincidences ratio*, SCR). En el método propuesto por Yamamoto et al [1986] esta dependencia se tiene en cuenta, pero es necesario medir las coincidencias aleatorias '*off-line',* lo que no es siempre posible o práctico.

En este trabajo proponemos un método (método 'SCR-based') para estimar el tiempo efectivo τ (que tiene en cuenta pérdidas por *pile-up* y tiempo muerto y ganancias debidas al *pile-up*) para linealizar las tasas de cuentas adquiridas [Vicente *et al.*, 2012a]. El método requiere sólo dos adquisiciones de calibración (una con bajo SCR, otra con alto SCR) y se basa en la relación lineal existente entre τ y SCR:

$$\tau = 2 \cdot \tau_S \cdot SCR + \tau_C \qquad \textbf{(R.1)}$$

De esta manera, el método propuesto se basa en dos parámetros (τ_C y τ_S), a diferencia del método uniparametral comentado.

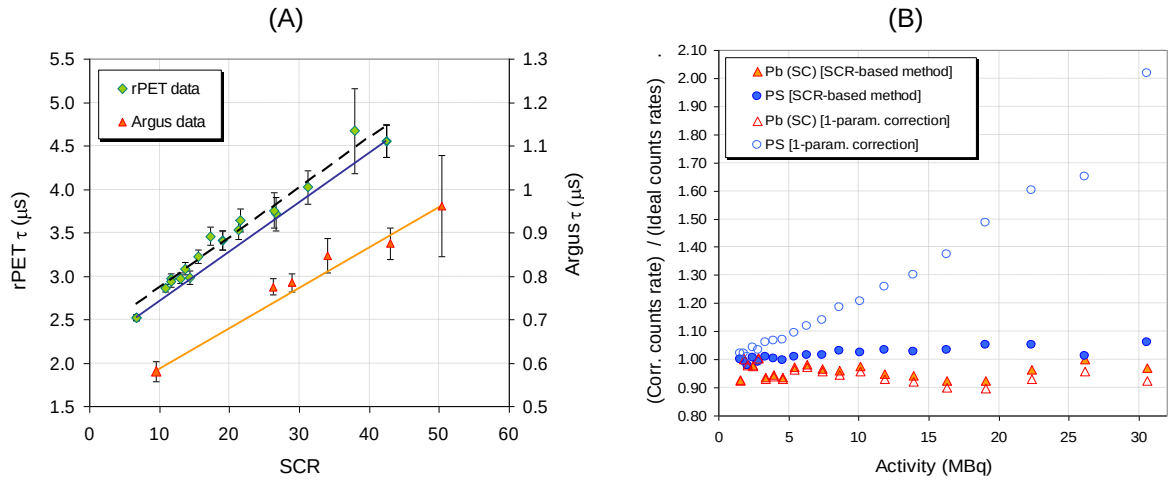

Figura R.2. ***(A):*** *Relación lineal entre el tiempo muerto efectivo τ y el SCR para adquisiciones con diferentes maniquíes simuladas para los escáneres rPET (puntos con forma de diamante, eje Y izquierdo) y Argus (puntos con forma triangular, eje Y derecho) en la ventana de energía de 400-700 keV. La línea discontinua mostrada para rPET representa un ajuste lineal hecho con todos los puntos. Las líneas continuas en ambos escáneres muestran la interpolación propuesta usando los puntos extremos (alto y bajo SCR).* ***(B)****: Comparación entre el método propuesto ('SCR-based method', puntos vacíos) y el uniparametral ('1-param. correction', puntos llenos) para los maniquíes PS y Pb (SC) (datos del escáner rPET). Se muestra el cociente de las tasas corregidas con cada uno de los métodos sobre la tasa ideal en función de la actividad.*

En la Figura R.2A se muestra los tiempos efectivos τ de varias simulaciones (usando PeneloPET [España *et al.*, 2009]) con distinto SCR obtenidos para el escáner rPET (diamantes) y para Argus (triángulos), donde se observa la relación lineal predicha. Cada valor τ se obtuvo con el método uniparametral. Las líneas continuas muestran la estimación (interpolación) de la relación lineal entre τ y SCR empleando dos puntos extremos (con mayor y menor SCR). La línea discontinua mostrada para rPET fue calculada aplicando un ajuste lineal usando todos los puntos mostrados, observando una diferencia del 6% en la ordenada en el origen entre ambas rectas en rPET. A pesar de esta diferencia, en este trabajo mostramos que el método propuesto da un buen resultado en la corrección de las tasas de cualquier adquisición con errores inferiores al 7% para todas las actividades muestreadas, incluso para los puntos que peor se ajustan a la interpolación propuesta. Un ejemplo de esto se muestra en la Figura R.2B, donde el método propuesto ('SCR-based method') se compara con el uniparamentral (*1-param. correction*). El maniquí empleado para el método uniparametral fue el cilindro pequeño de agua (*Water (SC)).* En la figura se muestran 2 situaciones: una fuente puntual (*PS*) y un cilindro pequeño de plomo (*Pb (SC)*). El primer ejemplo fue elegido para mostrar la magnitud del error cuando el tiempo muerto efectivo τ empleado para corregir las tasas sobreestima al valor real de la adquisición (lo que ocurre cuando se aplica el método uniparamentral usando el cilindro pequeño de agua (*Water (SC))* para la calibración). El segundo ejemplo, *Pb (SC)*, fue elegido porque es el punto que peor se ajusta a la interpolación del método propuesto (ver Figura R.2A, punto (37, 4.7)). Se observa que, para ambos ejemplos, el método 'SCR-based' proporciona mejores resultados que el uniparametral, con errores relativos inferiores al 7 % para el maniquí *Pb (SC)* e inferiores al 6% para la fuente puntual (*PS*), comparado con desviaciones hasta del 10% y mayores del 100% respectivamente para el método uniparamentral.

El ejemplo de la Figura R.2B muestra que el método uniparametral introduce un bias en las tasas corregidas, mayor cuanto más diferente es el SCR de la adquisición corregida comparado con la adquisición empleada en la calibración y mayor aún si el τ de la calibración sobreestima al de la adquisición corregida. Este bias será más importante cuanto mayor sean los bloques detectores del escáner (con mayor probabilidad de *pile-up*), por lo que el método propuesto ('SCR-based method') es altamente recomendable para escáneres clínicos PET empleados en mamografía (PEM), como por ejemplo los descritos en [Wang *et al.*, 2006a, Wu *et al.*, 2009], o para escáneres preclínicos de alta sensibilidad con detectores de grandes dimensiones colocados particularmente cerca, como por

ejemplo, [Seidel *et al.*, 2010, Zhang *et al.*, 2011].

Medida de desalineamientos en escáneres preclínicos basados en detectores plano-paralelos rotatorios

En esta sección mostramos que una caracterización geométrica es crítica en sistemas preclínicos, ya que un desalineamiento submilimétrico en un detector puede dar como resultado una notable degradación de la imagen y puede introducir importantes artefactos. Para demostrar este hecho, en este trabajo analizamos, utilizando simulaciones con PeneloPET, los efectos introducidos por los desalineamientos en los detectores de escáneres PET preclínicos basados en detectores rotatorios con geometría plano-paralela, definiendo un protocolo robusto y fácil de aplicar para la caracterización geométrica [Abella *et al.*, 2012]. El resultado de la etapa de calibración es utilizado para corregir los sinogramas a partir de los datos adquiridos en modo de lista.

Para cada tipo de desalineamiento (*offset*), estudiamos su efecto sobre la posición de las líneas de respuesta (*lines of response*, LORs) el sinograma 3D y la imagen reconstruida, calculando la tolerancia del sistema a cada tipo de desalineamiento. Estos efectos pueden ser clasificados de acuerdo con el esquema mostrado en la Figura R.3:

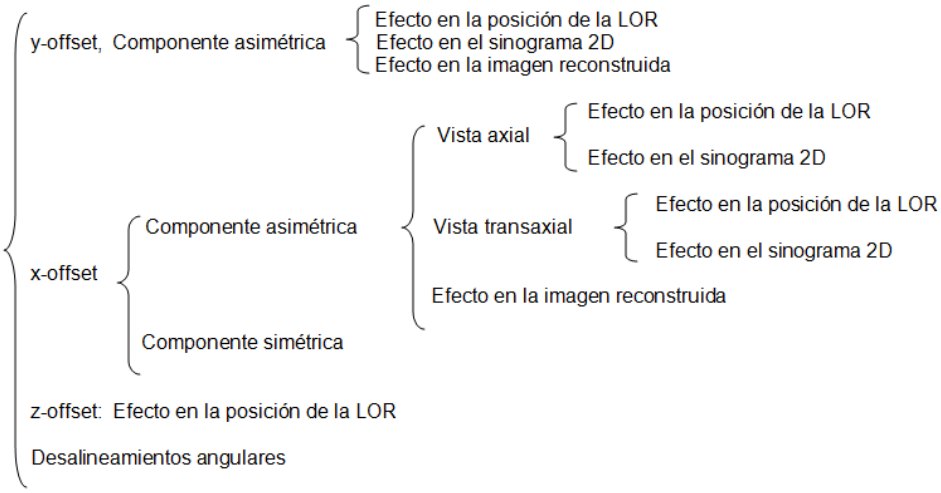

Figura R.3. *Clasificación de los desalineamientos considerados.*

La Table 25 resume los resultados obtenidos del análisis, indicando la expresión para calcular el mínimo valor del desalineamiento para producir un efecto apreciable (lo que llamamos 'tolerancia'), y el valor particular para el escáner rPET, sistema empleado en nuestro estudio.

Todos los desalineamientos listados en la Table 25 corresponden a un solo par de detectores. En un sistema con más de un par de detectores, tales como el estudiado aquí, hay dos parámetros de calibración adicionales para medir: z-offset entre pares de detectores y el ángulo entre pares de detectores. Estos *offsets* no se estudiaron mediante simulaciones, dada su sencilla corrección y por ellos no aparecen listados en la tabla.

Tabla R.1. *Resumen del estudio de los desalineamientos. Para cada tipo de offset la tabla indica la simulación (tipo de adquisición) empleada para evaluar su efecto en el sinograma y en la imagen, la expresión para calcular la tolerancia y su valor particular para el escáner rPET. (COR: centro de rotación)*

Desalineamiento	Adquisición	Efecto en el sinograma	Efecto en la imagen	Tolerancia	Valor para el escáner rPET
y-offset, afecta al COR (asimétrico)	Fuente puntual no centrada	*Gap* radial	Forma de media luna	Medio pitch	0.8 mm
y-offset, no afecta al COR (simétrico)	Fuente puntual no centrada	Mayor FWHM en la vista coronal	Pérdida de resolución transaxial	No considerado	No considerado
x-offset, afecta al COR (asimétrico)	Fuente puntual en el centro del FOV	Gap axial, centro de masas modificado y mayor FWHM en la vista coronal	Forma de media luna	$\Delta x = \left(R + l/2\right)\left[\frac{1}{\left(N/2 - 1.5\right)}\right]$	7 mm
x-offset, no afecta al COR (simétrico)	Fuente puntual no centrada	Mayor FWHM en la vista coronal	Pérdida de resolución axial y transaxial	No considerado	No considerado
z-offset	Cualquier fuente puntual	Mayor FWHM en la vista sagital	Pérdida de resolución axial	Pitch	1.6 mm
'Tilt' (eje *y*)	Fuente puntual no centrada	*Gap* radial	Pérdida de resolución axial	$\theta_{\min} = \arctan\frac{pitch}{(l/2)}$	14.9º
'*Slant*' (eje *z*)	Fuente puntual en cualquier posición conocida	Mayor FWHM en la vista sagital	Forma de media luna	$\theta_{\min} = \arctan\frac{pitch}{(l/2)}$	14.9º
'Skew'	Fuente puntual no centrada (x-y, z)	*Gap* radial y mayor FWHM en la vista axial	Pérdida de resolución transaxial y axial	$\xi_{\min} = \arcsin\left(\frac{pitch}{R - pitch/2}\right)$	4.2º

Los resultados de este estudio nos permitieron desarrollar un algoritmo de calibración para calcular los desalineamientos de los bloques detectores del escáner. Los datos de entrada para el algoritmo son dos adquisiciones en modo lista de una fuente puntual (en nuestro caso, fuente de ^{22}Na de 0.3 mm de diámetro, encapsulada en una caja de epoxi de 1 cm de lado). En la primera adquisición, la fuente se coloca en el centro del FOV ('*centered acquisition'*) y en la segunda la fuente se encuentra a 11 mm de distancia de ese centro en el plano transaxial ('*non-centered* acquisition'). Las reconstrucciones intermedias se genera por medio de SSRB (*span* = 1) seguido por una retroproyección filtrada 2D (2D-FBP) con un filtro rampa. El resultado del algoritmo de calibración es un fichero que contiene los valores de los desalineamientos. Este fichero es utilizado en reconstrucciones posteriores para generar un sinograma corregido en el que se traslada la posición de cada LOR de acuerdo con los desalineamientos estimados. La Figure 58 muestra un diagrama de flujo del proceso de calibración y la interfaz de la herramienta de calibración al final del proceso.

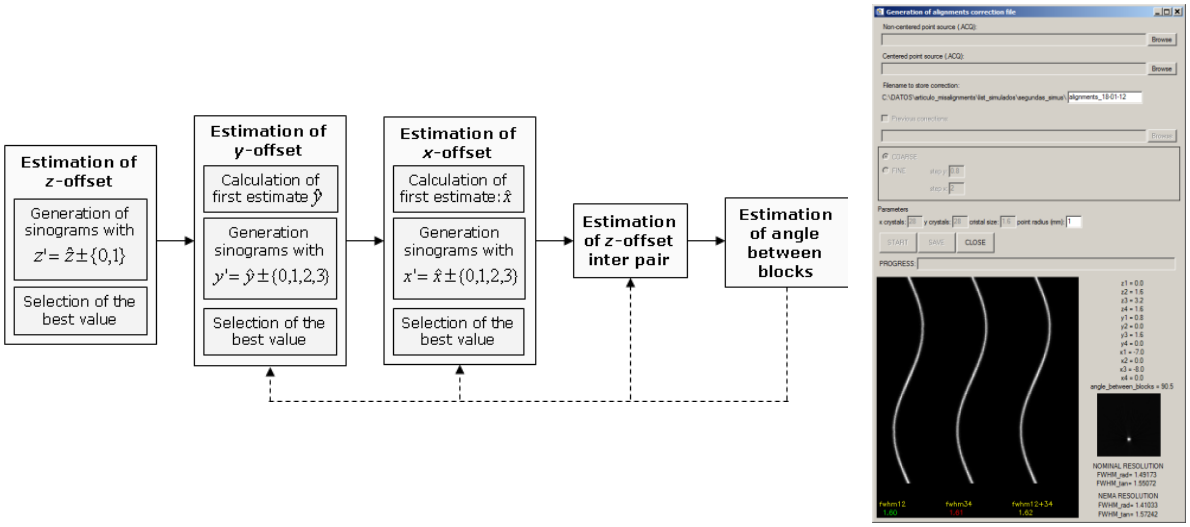

Figura R.4. *Diagrama de flujo del algoritmo de calibración. Las líneas discontinuas indican caminos iterativos para un ajuste fino de los valores de los offsets.* ***Derecha****: Interfaz de la herramienta de calibración al final del proceso que muestra un sinograma de cada par de detectores y el sinograma suma, los valores de desalineamientos encontrados y la resolución resultante.*

Para cada *offset*, el programa hace una primera estimación y guía al usuario a través de un procedimiento de ajuste interactivo. Después de una estimación inicial de todos los desalineamientos, en un proceso llamado ajuste grueso, el software ofrece al usuario la posibilidad de realizar más iteraciones del algoritmo de calibración con variaciones más pequeñas de los valores de los *offsets* (ajuste fino) hasta que el resultado sea satisfactorio. Cuando este proceso ha terminado para todos los posibles desalineamientos, los valores finales se guardan.

Este procedimiento se ha incorporado en el software del sistema comercial rPET [Vaquero *et al.*, 2004, Vaquero *et al.*, 2005a]. y puede ser fácilmente adaptado a geometrías similares, como los escáneres Yap-PET [Del Guerra *et al.*, 1998] y ClearPET [Khodaverdi *et al.*, 2005, Mosset *et al.*, 2004]. Su versatilidad ha sido ya demostrada en [Lage *et al.*, 2009].

Nuestros resultados destacan la importancia de una precisa caracterización de los desalineamientos de los detectores: un error de 0.8 mm en uno de detectores resulta en un aumento del 14% en la FWHM tangencial de una fuente puntual en el centro del FOV. Además de una pérdida de resolución, los errores de una mala alineación también producen artefactos que dan lugar a una grave degradación de la imagen reconstruida.

Corrección de atenuación en imágenes PET basada en imágenes CT en el escáner preclínico Argus PET/CT

La corrección de atenuación es una de las correcciones importantes que se requieren para el análisis cuantitativo de PET. Aunque la magnitud de esta corrección para animales pequeños es mucho menor que en humanos [Chow *et al.*, 2002], es importante corregir los datos para un análisis cuantitativo preciso de la distribución del trazador [Kinahan *et al.*, 2003]. Existen varios métodos de corrección de atenuación en PET [Kinahan *et al.*, 2003, Zaidi *et al.*, 2004]. Las propiedades del material dispersador pueden obtenerse utilizando imágenes de transmisión (lo que se llama mapa de atenuación), que pueden ser adquiridos ya sea con un PET o un escáner de rayos x (CT).

En este trabajo se describe un procedimiento para corregir la atenuación basado en una imagen de CT para el escáner Argus PET/CT. Las imágenes se reconstruyen con el código FIRST [Herraiz *et al.*, 2006], pero la corrección puede aplicarse con cualquier otro método de reconstrucción, ya que se aplica a los datos antes de la reconstrucción [Vicente *et al.*, 2010b].

La Figura R.5 muestra un diagrama de flujo con las pasos necesarios para corregir la atenuación en el escáner de Argus usando imágenes CT

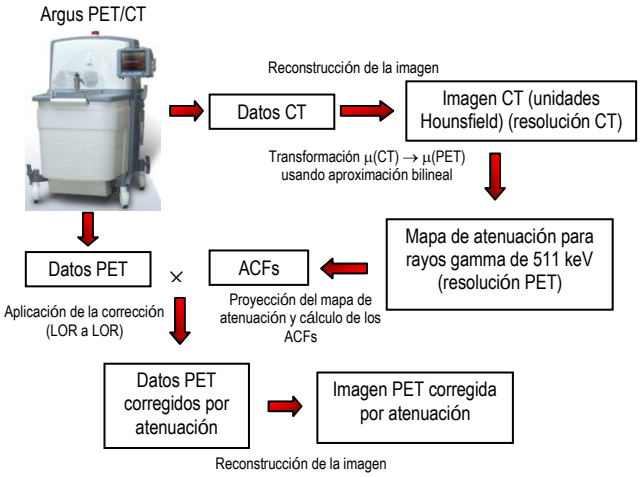

Figura R.5. *Diagrama de flujo para la corrección de atenuación usando imágenes CT en el escáner Argus PET/CT*

En este trabajo se compara un método de corrección de atenuación simple basado en un cilindro de agua del tamaño de campo de visión (corrección por defecto incluida en el código FIRST [Herraiz *et al.*, 2006], algoritmo de reconstrucción empleado para reconstruir las imágenes) con un método más preciso basado en imágenes CT (el implementado en este trabajo). Del análisis de los resultados concluimos que la corrección de atenuación basada en imágenes CT no sólo proporciona una mejor cuantificación, sino que también reduce la χ^2, lo que significa una mayor coherencia entre la imagen reconstruida y los datos adquiridos. El procedimiento ha sido incorporado en el software del escáner comercial Argus PET/CT.

Diseño de prototipos PET preclínicos

Desde el primer escáner PET preclínico [Watanabe *et al.*, 1992], los escáneres PET de pequeños animales están en continuo desarrollo. Los nuevos sistemas se producen con mayor sensibilidad, resolución espacial, y capacidad para adquirir tasas de conteo más altas [Wang *et al.*, 2006b, Bao *et al.*, 2009]. El diseño de un nuevo escáner PET preclínico es un proceso muy complejo que requiere tomar decisiones sobre un conjunto de aspectos de diferente naturaleza. Las simulaciones Monte Carlo se han convertido en una herramienta muy valiosa en las primeras etapas del proceso de diseño, lo que permite realizar estudios exhaustivos, teniendo en cuenta todos los componentes que forman el escáner [Heinrichs *et al.*, 2003].

Además de la simulación de los datos, es necesario desarrollar métodos de reconstrucción necesarios para procesar correctamente estos datos con el fin de obtener parámetros importantes del rendimiento del sistema, tales como la resolución espacial, y para evaluar la calidad de las imágenes finales. Para ello, los métodos de reconstrucción existentes tienen que ser modificados y ampliados para poder adaptarse a la geometría no convencional de algunos diseños.

Ejemplos de estas modificaciones en la simulación y en la reconstrucción se presentan en este capítulo. El propósito de este capítulo es el estudio, por medio de simulaciones Monte Carlo, de las principales características y las posibles modificaciones de dos nuevos prototipos preclínicos en fase de desarrollo en dos centros diferentes, donde el autor de esta tesis estuvo trabajando como parte del programa de estancias breves de la beca JAEPredoctoral (2008).

Escáner Zoom-in PET

En esta sección estudiamos el potencial de un nuevo prototipo, el 'Zoom-in PET' (o ZiPET), propuesto y diseñado por el *Department of Biomedical Engineering, University of California, (Davis, CA)* [Zhou and Qi, 2009, 2010, 2011, Qi *et al.*, 2011]. El sistema integra un detector de alta resolución en un escáner de microPET existente que actúa de forma análoga a una lupa para obtener datos de alta resolución de una pequeña parte del campo de visión definidos por una región de interés alrededor de la cara frontal del inserto (ver Figure 70). El diseño propuesto puede ofrecer una solución costo-efectiva para obtener imágenes de alta resolución para una región específica, sin la construcción de un sistema de anillo completo. Tal sistema puede ser útil para el estudio del cáncer usando modelos animales donde los tumores son a menudo cultivados cerca de la superficie de la piel y por lo tanto, permitir un cercano contacto con el detector de alta resolución. La Figure 70 muestra un esquema del prototipo simulado en este trabajo con el inserto de alta resolución situado en el centro de la dirección axial del escáner microPET II [Tai *et al.*, 2003].

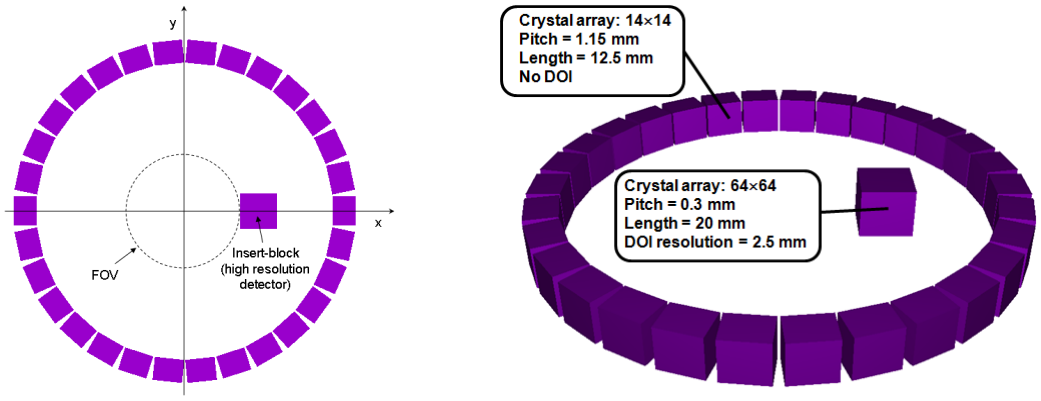

Figura R.6. *Vistas 2D (plano transaxial) [**izquierda**] y 3D [**derecha**] del escánere Zoom-in PET simulado en este trabajo.*

El escáner comercial microPET II (μPET en lo que sigue) consta de tres anillos axiales de detectores con un diámetro de 160 mm, cada uno formado por 30 módulos de detectores. Sin embargo, en este trabajo sólo se consideró uno de los tres anillos axiales para las simulaciones. Cada módulo detector de μPET consiste en una matriz de 14×14 de 1.0×1.0×12.5 mm^3 de cristales de LSO. La caracterización del escáner microPET II se ha publicado en [Tai *et al.*, 2003] y [Yang *et al.*, 2004].

El detector de alta resolución (inserto en lo que sigue) está compuesto por una matriz de 64×64 de dimensiones 0.3×0.3×20 mm^3 de cristales de LSO y puede proporcionar profundidad de interacción (DOI) para reducir los errores de paralaje. El DOI se obtiene utilizando una doble lectura, en las que los fotones ópticos generados por la matriz de cristales de centelleo son leídos por dos fotodiodos de avalancha sensibles a la posición (PSAPDs) uno en la parte delantera y la otra en el extremo posterior del detector [Yang *et al.*, 2006]. El valor del DOI se calcula tomando la relación de las señales de los dos PSAPDs proporcionar una medida continua de DOI para cada evento registrado.

En este trabajo utilizamos simulaciones Monte Carlo con el paquete de simulación PeneloPET [España *et al.*, 2009] para caracterizar el impacto de la introducción del detector de alta resolución (inserto) en el rendimiento del sistema, a excepción del aumento de la resolución espacial, que ya fue estudiado en trabajos anteriores con un análisis teórico y simulaciones básicas [Zhou and Qi, 2009], y mediciones experimentales [Qi *et al.*, 2011]. Para este fin, fue necesario introducir varias modificaciones en el código PeneloPET debido a la geometría no estándar del sistema con dos conjuntos diferentes de bloques detectores en diferentes posiciones radiales. En concreto las modificaciones incorporadas fueron:

1. En la definición de la geometría del escáner. Es necesario definir dos tipos de detectores: el anillo de detectores del escáner MicroPET II y el inserto de alta resolución.

2. Incluir la definición explícita de la matriz de coincidencias, que indica los bloques que se encuentran en coincidencia durante la adquisición, permitiendo coincidencias entre bloques del anillo de MicroPET II y entre el inserto y los detectores del anillo.

3. Acceso dinámico a la información de los parámetros de cada tipo de detector para cargar las propiedades adecuadas en cada interacción de un fotón en un bloque detector.

4. Modelado especial de la profundidad de interacción (DOI) para simular más precisamente el sistema de doble lectura del sistema real mediante PSAPDs.

5. Nuevos formatos para los archivos de salida para poder separar los datos de alta resolución (coincidencias entre el inserto y los detectores del anillo de MicroPET II) y los datos de baja resolución (coincidencias entre bloques del anillo)

La evaluación del rendimiento del sistema se centra en la sensibilidad, la capacidad de profundidad de interacción (DOI) del inserto y la curva NEC, ya que la resolución espacial se midió en trabajos anteriores [Zhou and Qi, 2009 2011] demostrando su mejora. De los resultados se puede afirmar que existe una evidente mejora en la sensibilidad cuando el inserto está incluido en el sistema. A pesar de esto, el diseño del sistema puede ser mejorado, dado que se ha demostrado, del análisis de las curvas NEC y de la sensibilidad, que el diseño actual con sólo un anillo axial en el sistema μPET y el tamaño propuesto para el inserto no proporcionan un rendimiento óptimo, ya que el número de coincidencias no deseadas como *pile-up*, *randoms*, auto-coincidencias y de *scatter*, aumenta drásticamente con la presencia del inserto. El análisis de la profundidad de interacción del inserto también sugiere la utilización de cristales más cortos, por ejemplo reduciendo su longitud 5 mm, lo que supone una menor degradación de la resolución a expensas de una pérdida pequeña de sensibilidad.

Estos resultados muestran un ejemplo de cómo los datos simulados pueden ayudar a guiar el diseño de nuevos prototipos, analizando todas las ventajas y desventajas antes de tomar una decisión final. En nuestro estudio, los resultados sugieren modificar la geometría del sistema incluyendo, por ejemplo, más anillos axiales en microPET II y tratar de blindar de alguna manera el inserto para evitar la detección de *singles* desde fuera del campo de visión axial.

Escáner NIH PPI

El escáner NIH PPI (‘*positron projection imager*’) fue diseñado como una opción de bajo coste para estudios con ratones [Seidel *et al.*, 2010]. El prototipo consta de dos detectores opuestos en coincidencia temporal compuestos de cristales pixelados de LYSO, montados en un dispositivo que permite tres separaciones entre los módulos: 39, 29 y 19 mm. El objeto/animal en estudio se coloca sobre una placa de plástico situado entre los detectores, los cuales se mantienen inmóviles durante la adquisición, haciendo al escáner PPI un sistema tomográfico de ángulo limitado. El campo de visión abarcado por los detectores es suficientemente grande para poder adquirir la imagen de todo el cuerpo de un ratón en una sola proyección.

Cada bloque detector está compuesto por una matriz de 26×59 cristales, cada uno con un tamaño de 1.5×1.5×12 mm^3 y un pitch de 1.6 mm. La matriz de cristales está ópticamente acoplada (mediante una grasa óptica) a un fotomultiplicador sensible a posición (modelo H8500C de Hamamatsu Corp., Bridgewater, NJ).

En este trabajo, se realiza un análisis cuantitativo del rendimiento del sistema en términos de sensibilidad, resolución y calidad de imagen mediante simulaciones Monte Carlo (utilizando PeneloPET). A pesar de que el escáner fue diseñado inicialmente para obtener imágenes en proyección

(2D), también exploramos la posibilidad de imágenes en 3D del sistema, evaluando la resolución espacial en diferentes posiciones del FOV y la calidad de las imágenes con adquisiciones reales. Con este fin, se implementaron distintas aproximaciones desarrollando diferentes métodos de reconstrucción, desde métodos que proporcionan imágenes planares, sin información en la dirección *Z*, hasta métodos más precisos en modo 3D basados en el código GFIRST [Herraiz *et al.*, 2011] con tres aproximaciones diferentes:

- En la primera, se utilizó una versión simplificada de la matriz de probabilidad, despreciando los efectos de resolución. Este método se empleó para medir la resolución espacial del sistema ya que la calidad de las imágenes resultantes es comparable, en términos de resolución espacial, a una reconstrucción FBP, el método de reconstrucción estándar para medir la resolución espacial en los escáneres PET.

- En el segundo método 3D, se incluyeron los efectos de resolución utilizando un kernel invariante de emborronamiento usando la PSF medida en fuentes puntuales reconstruidas con el método sin recuperación de resolución. Este kernel se usa con distinto ancho en la proyección y retroproyección para aumentar la velocidad de convergencia del algoritmo.

- Finalmente, se desarrolló un nuevo método 3D, mejorando el último método descrito con un componente de emborronado adicional para regularizar la convergencia en direcciones *X* e *Y [Vicente et al., 2012b]*.

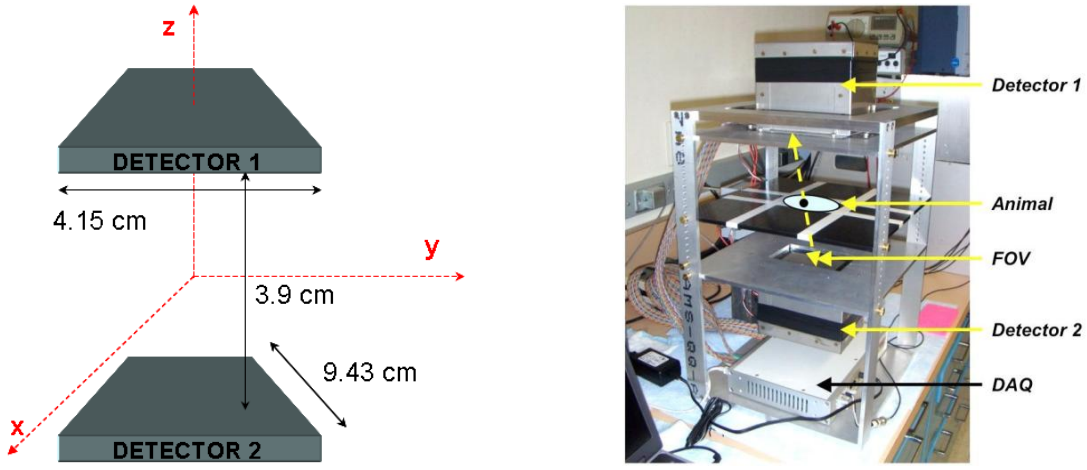

Figura R.7. ***Izquierda**: Esquema simplificado de la geometría del escáner NIH PPI. **Derecha**: Fotografía del prototipo.*

La caracterización realizada en este trabajo ha demostrado que el sistema PPI tiene valores de sensibilidades muy competitivos, siendo algunos valores experimentales de la sensibilidad en el centro del FOV por ejemplo: 10% a 100-650 keV, 7% a 250-650 keV y 5% a 400-650 keV. Estos resultados mejoran la sensibilidad del sistema PETbox [Zhang *et al.*, 2010, Zhang *et al.*, 2011], obteniendo un valor de sensibilidad para el PPI en 400-650 keV similar a la del PETbox en 100-650 keV. El sistema PPI también mejora la mayoría de los valores de sensibilidad de los escáneres de anillo completo. Con respecto a las medidas de resolución, el sistema tiene alta resolución en el plano XY con valores inferiores a 1.8 mm y prácticamente uniforme en todo el FOV. Sin embargo, la falta de datos en la dirección Z da como resultado una degradación de la resolución del sistema en dicha dirección, con valores en su mayoría por encima de 6 mm cuando no aplicamos recuperación de resolución en la reconstrucción. Estas diferencias se reducen utilizando la información de la PSF en la reconstrucción, obteniendo una resolución en Z todavía peor que en las otras direcciones, pero con valores menores de 1.8 mm en la dirección Z y por debajo de 1.4 mm en las otras dos direcciones.

Por último, las imágenes iniciales obtenidas, utilizando los métodos de reconstrucción antes mencionados, demuestran las capacidades de imagen del sistema PPI y el potencial del nuevo método

de reconstrucción con regularización, empleado para converger a imágenes con las propiedades deseadas.

Conclusiones

La investigación preclínica PET es una técnica compleja que ha ganado un creciente impacto en los últimos años, especialmente debido al desarrollo de sistemas PET específicos para pequeños animales. Quedan, sin embargo, retos importantes con respecto a la instrumentación, evaluación de datos y experimentación, que son necesarios superar con el fin de alcanzar datos preclínicos cuantitativos y fiables.

En esta tesis se han presentado aportaciones originales al estudio de las fuentes de error que limitan la calidad de las imágenes PET aportando nuevos métodos y algoritmos para compensar sus efectos y mejoras en las simulaciones Monte Carlo y en los métodos de reconstrucción para adaptar los códigos existentes a las geometrías no-convencionales de algunos diseños.

Las principales contribuciones de esta tesis son:

1. Una evaluación detallada del rendimiento de dos escáneres PET preclínicos con geometrías y características muy diferentes, el escáner SEDECAL rPET y el SEDECAL Argus, argumentando la importancia de tener protocolos estandarizados para garantizar una caracterización precisa. Se ha mostrado una comparación crítica de las características de los escáneres, comparándolas a su vez con otros escáneres PET preclínicos disponibles en el mercado, mostrando que ambos escáneres tienen prestaciones muy competitivas que mejoran en algunos parámetros las de otros sistemas comerciales.

2. Se ha demostrado que estos protocolos de caracterización no son perfectos, analizando en detalle algunos ejemplos y, con la ayuda de simulaciones muy detalladas y realistas, se han propuesto mejoras en los procedimientos. Un ejemplo es la propuesta de mejora del estándar NEMA para medir la fracción de dispersión, de manera que sea independiente del isótopo empleado en términos de rango de positrón. Esta extensión del protocolo NEMA incluye una desconvolución de los perfiles empleados en el método con una distribución unidimensional del rango del positrón con el fin de eliminar los efectos del rango. Este nuevo protocolo ha sido probado usando ^{68}Ga, un radionúclido con rango de positrón grande, obteniendo los mismos resultados que con ^{18}F, el isótopo propuesto por NEMA.

3. De las limitaciones observadas en los escáneres evaluados, se han desarrollado nuevos métodos y algoritmos relevantes no sólo para estos escáneres particulares, sino fácilmente adaptables a diferentes arquitecturas. En concreto:

   3.1. Un método para linealizar las tasas de coincidencias totales eliminando efectos no lineales debidos a las pérdidas por tiempo muerto y *pile-up* y a las ganancias debidas al *pile-up* dentro de la ventana de energía seleccionada. El método está basado en la relación lineal entre el tiempo muerto efectivo τ (que tiene en cuenta los efectos de tiempo muerto y *pile-up*), y la relación de *singles* con respecto a las coincidencias (*Singles-to-Coincidences ratio* SCR). Los resultados muestran que usando dicho método, la precisión en las tasas corregidas es inferior al 7%, incluso para actividades altas, evitando el sesgo introducido cuando se emplea un procedimiento uniparametral. El método ha sido validado usando datos reales y simulados de los escáneres rPET y Argus.

   3.2. Un protocolo de calibración, desarrollado e implementado en una herramienta de software, para compensar el efecto de los pequeños desalineamientos mecánicos en los sistemas PET preclínicos con detectores plano-paralelos rotatorios. Esta herramienta de calibración determina los desalineamientos dentro de una tolerancia aceptable en cada parámetro

geométrico. Los resultados han destacado la importancia de una precisa caracterización geométrica mostrando la aparición de artefactos y una importante pérdida de resolución en la imagen final si los desalineamientos en los detectores no son apropiadamente corregidos.

3.3. Una corrección de atenuación basada en imágenes de tomografía computarizada (CT). Los resultados han mostrando una mejora en las imágenes corregidas en términos de cuantificación y mayor consistencia entre los datos adquiridos y los estimados en la reconstrucción que cuando se emplean métodos más sencillos, como por ejemplo la corrección basada en un cilindro de agua del tamaño del campo de visión del escáner.

4. Haciendo uso de toda la experiencia adquirida en la caracterización de los escáneres y el estudio de las fuentes de error que limitan la calidad de las imágenes, se han utilizado simulaciones Monte Carlo para guiar el diseño de nuevos prototipos, realizando las modificaciones necesarias en los códigos Monte Carlo y en los métodos de reconstrucción empleados para adaptar los códigos existentes a la geometría no convencional de los nuevos diseños. En concreto, los escáneres estudiados son:

   4.1. *Zoom-in PET*: un detector de alta resolución introducido en el FOV del escáner microPET II (con sólo un anillo de detectores). Las simulaciones empleadas en este estudio se han realizado en una versión modificada de PeneloPET, que fue desarrollada para permitir la simulación de la geometría particular de este prototipo. Este estudio es un ejemplo de cómo las simulaciones Monte Carlo pueden ayudar al diseño de nuevos prototipos, analizando las ventajas y desventajas del sistema antes de tomar la decisión final. En concreto, los resultados de la caracterización de este prototipo sugieren una modificación de la geometría añadiendo, por ejemplo, más anillos de detectores al escáner MicroPET II y tratando de blindar el inserto para evitar la detección de *singles* provenientes de fuera del FOV.

   4.2. *NIH PPI*: escáner de bajo coste y alta sensibilidad consistente en dos detectores no rotatorios. Esta geometría hace que el prototipo tenga un muestreo pobre en la dirección de separación de los detectores, por lo que es necesario desarrollar nuevas aproximaciones y métodos de reconstrucción, como el presentado en esta tesis, que emplea una convolución regularizada para hacer la convergencia más isotrópica. La caracterización del prototipo ha demostrado que el sistema cumple con las especificaciones deseadas y las imágenes iniciales obtenidas, su capacidad de imagen 3D y el potencial del nuevo método de regularización desarrollado.

En resumen, esta tesis muestra la importancia de simulaciones Monte Carlo detalladas en la mejora del rendimiento de los escáneres existentes y de los protocolos de caracterización de los mismos, así como en el diseño de nuevos prototipos.

Los resultados descritos en las conclusiones 3.2 y 3.3 han sido transferidos a la industria y han sido integrados en los escáneres preclínicos de alta resolución fabricados por SEDECAL (Madrid, España) y distribuidos mundialmente.

Referencias

Abella, M., Vicente, E., Rodríguez-Ruano, A., España, S., Lage, E., Desco, M., Udias, J. M. & Vaquero, J. J. 2012. Misalignments calibration in small-animal PET scanners based on rotating planar detectors and parallel-beam geometry. *Phys Med Biol (Submitted)*.

Bao, Q., Newport, D., Chen, M., Stout, D. B. & Chatziioannou, A. F. 2009. Performance evaluation of the inveon dedicated PET preclinical tomograph based on the NEMA NU-4 standards. *J Nucl Med,* 50**,** 401-8.

Blanco, A. 2006. Positron Range Effects on the Spatial Resolution of RPC-PET. *In:* Nuclear Science Symposium Conference Record, 2006. IEEE, Oct. 29 2006-Nov. 1 2006 2006. 2570-2573.

Bloomfield, P. M., Rajeswaran, S., Spinks, T. J., Hume, S. P., Myers, R., Ashworth, S., Clifford, K. M., Jones, W. F., Byars, L. G., Young, J. & et al. 1995. The design and physical characteristics of a small animal positron emission tomograph. *Phys Med Biol,* 40**,** 1105-26.

Brownell, G. L., Burnham, C. A., Wilensky, S., Aronow, S., Kazemi, H. & Streider , D. 1969. New developments in positron scintigraphy and the application of cyclotron produced positron emitters. *In:* Medical Radioisotope Scintigraphy, 1969 Vienna, Austria. International Atomic Energy Agency, 163–176.

Burnham, C. A. & Brownell, G. L. 1972. A Multi-Crystal Positron Camera. *Nuclear Science, IEEE Transactions on,* 19**,** 201-205.

Cal-Gonzalez, J., Herraiz, J. L., Espana, S., Desco, M., Vaquero, J. J. & Udias, J. M. 2010. Validation of PeneloPET positron range estimations. *In:* Nuclear Science Symposium Conference Record (NSS/MIC), 2010 IEEE, Oct. 30 2010-Nov. 6 2010 2010. 2396-2399.

Chow, P. L., Rannou, R. & Chatziioannou, A. 2002. Attenuation correction for a 3D small animal PET tomograph, using x-ray microCT. *Mol. Imag. Biol.,* 4**,** S17–S18.

Del Guerra, A., Bartoli, A., Belcari, N., Herbert, D., Motta, A., Vaiano, A., Di Domenico, G., Sabba, N., Moretti, E., Zavattini, G., Lazzarotti, M., Sensi, L., Larobina, M. & Uccelli, L. 2006. Performance evaluation of the fully engineered YAP-(S)PET scanner for small animal imaging. *Nuclear Science, IEEE Transactions on,* 53**,** 1078-1083.

Del Guerra, A., Di Domenico, G., Scandola, M. & Zavattini, G. 1998. YAP-PET: first results of a small animal positron emission tomograph based on YAP:Ce finger crystals. *Nuclear Science, IEEE Transactions on,* 45**,** 3105-3108.

España, S., Herraiz, J. L., Vicente, E., Herranz, E., Vaquero, J. J., Desco, M. & Udias, J. M. 2007. Improved image reconstruction in small animal PET using a priori estimates of single-pixel events. *In:* Nuclear Science Symposium Conference Record, 2007. NSS '07. IEEE, Oct. 26 2007-Nov. 3 2007 2007. 3876-3880.

España, S., Herraiz, J. L., Vicente, E., Vaquero, J. J., Desco, M. & Udias, J. M. 2009. PeneloPET, a Monte Carlo PET simulation tool based on PENELOPE: features and validation. *Phys Med Biol,* 54**,** 1723-42.

Goertzen, A. L., Bao, Q., Bergeron, M., Blankemeyer, E., Blinder, S., Cañadas, M., Chatziioannou, A. F., Dinelle, K., Elhami, E., Jans, H.-S., Lage, E., Lecomte, R., Sossi, V., Surti, S., Tai, Y.-C., Vaquero, J. J., Vicente, E., Williams, D. A. & Laforest, R. 2012. NEMA NU 4-2008 Comparison of Preclinical PET Imaging Systems. *The Journal of Nuclear Medicine (Accepted)*.

Heinrichs, U., Pietrzyk, U. & Ziemons, K. 2003. Design optimization of the PMT-ClearPET prototypes based on simulation studies with GEANT3. *Nuclear Science, IEEE Transactions on,* 50**,** 1428-1432.

Herraiz, J. L., Espana, S., Vaquero, J. J., Desco, M. & Udias, J. M. 2006. FIRST: Fast Iterative Reconstruction Software for (PET) tomography. *Phys Med Biol,* 51**,** 4547-65.

Herraiz, J. L., España, S., Cabido, R., Montemayor, A. S., Desco, M., Vaquero, J. J. & Udias, J. M. 2011. GPU-Based Fast Iterative Reconstruction of Fully 3-D PET Sinograms. *Nuclear Science, IEEE Transactions on,* 58**,** 2257-2263.

Khodaverdi, M., Weber, S., Streun, M., Parl, C., Larue, H., Brandenburg, G., Bauer, A., Dehnhardt, M., Auffray, E., Boutemeur, M., Bruyndonckx, P., Choi, Y., D'Asseler, Y., Devroede, O., Dujardin, C., Fedorov, A., Heinrichs, U., Janier, M., Jung, J. H., Korjik, M., Krieguer, M., Largeron, G., Lartizien, C., Lecoq, P., Lemaitre, C., Leonard, S., Loude, J. F., Morel, C., Mosset, J. B., Pedrini, C., Petrosyan, A. G., Rey, M., Sappey-Marinier, D., Roldan, P. S., Simon, L., Song, T. Y., Staelens, S., Tavernier, S., Trummer, J., Van Holen, R., Vieira, J. M., Wieers, E., Wisniewska, M., Wisniewski, D., Wu, Y., Pietrzyk, U. & Ziemons, K. 2005. High resolution imaging with ClearPET™ Neuro - first animal images. *In:* Nuclear Science Symposium Conference Record, 2005 IEEE, 23-29 Oct. 2005 2005. 4 pp.

Kinahan, P. E., Hasegawa, B. H. & Beyer, T. 2003. X-ray-based attenuation correction for positron emission tomography/computed tomography scanners. *Semin Nucl Med,* 33**,** 166-79.

Knoll, G. F. 2000. *Radiation detection and measurement / Glenn F. Knoll,* New York :, Wiley.

Lage, E., Vaquero, J. J., Sisniega, A., Espana, S., Tapias, G., Abella, M., Rodriguez-Ruano, A., Ortuno, J. E., Udias, A. & Desco, M. 2009. Design and performance evaluation of a coplanar multimodality scanner for rodent imaging. *Phys Med Biol,* 54**,** 5427-41.

Mosset, J. B., Devroede, O., Krieguer, M., Rey, M., Vieira, J. M., Jung, J. H., Kuntner, C., Streun, M., Ziemons, K., Auffray, E., Sempere-Roldan, P., Lecoq, P., Bruyndonckx, P., Loude, J. F., Tavernier, S. & Morel, C. 2004. Development of an optimised LSO/LuYAP phoswich detector head for the ClearPET camera. *In:* Nuclear Science Symposium Conference Record, 2004 IEEE, 16-22 Oct. 2004 2004. 2439-2443 Vol. 4.

National Electrical Manufacturers Association (NEMA). 1994. Performance Measurements of Positron Emission Tomographs. NEMA Standards Publication NU2-1994. Rosslyn, VA. National Electrical Manufacturers Association

National Electrical Manufacturers Association (NEMA). 2001. Performance Measurements of Positron Emission Tomographs. NEMA Standards Publication NU2-2001. Rosslyn, VA. National Electrical Manufacturers

Association
National Electrical Manufacturers Association (NEMA). 2008. Performance Measurements of Small Animal Positron Emission Tomographs. NEMA Standards Publication NU4-2008. Rosslyn, VA. National Electrical Manufacturers Association
Pavlopoulos, S. & Tzanakos, G. 1993. Design and performance evaluation of a high resolution small animal positron tomograph. *In:* Nuclear Science Symposium and Medical Imaging Conference, 1993., 1993 IEEE Conference Record., 31 Oct-6 Nov 1993 1993. 1697-1701 vol.3.
Pavlopoulos, S. & Tzanakos, G. 1996. Design and performance evaluation of a high-resolution small animal positron tomograph. *Nuclear Science, IEEE Transactions on,* 43**,** 3249-3255.
Phelps, M. E., Hoffman, E. J., Mullani, N. A. & Ter-Pogossian, M. M. 1975. Application of annihilation coincidence detection to transaxial reconstruction tomography. *J Nucl Med,* 16**,** 210-24.
Qi, J., Yang, Y., Zhou, J., Wu, Y. & Cherry, S., R. 2011. Experimental assessment of resolution improvement of a zoom-in PET. *Physics in Medicine and Biology,* 56**,** N165.
Rogers, D. W. 2006. Fifty years of Monte Carlo simulations for medical physics. *Phys Med Biol,* 51**,** R287-301.
Seidel, J., Wenze, X., Kakareka, J. W., Pohida, T. J., Green, M. V. & Choyke, P. L. 2010. A positron projection imager for whole-body mouse imaging. *In:* Nuclear Science Symposium Conference Record (NSS/MIC), 2010 IEEE, Oct. 30 2010-Nov. 6 2010 2010. 2206-2209.
Sweet, W. H. 1951. The uses of nuclear disintegration in the diagnosis and treatment of brain tumor. *N Engl J Med,* 245**,** 875-8.
Tai, Y. C., Chatziioannou, A. F., Yang, Y., Silverman, R. W., Meadors, K., Siegel, S., Newport, D. F., Stickel, J. R. & Cherry, S. R. 2003. MicroPET II: design, development and initial performance of an improved microPET scanner for small-animal imaging. *Phys Med Biol,* 48**,** 1519-37.
Ter-Pogossian, M. M., Phelps, M. E., Hoffman, E. J. & Mullani, N. A. 1975. A positron-emission transaxial tomograph for nuclear imaging (PETT). *Radiology,* 114**,** 89-98.
Tzanakos, G. & Pavlopoulos, S. 1993. Design and performance evaluation of a new high resolution detector array module for PET. *In:* Nuclear Science Symposium and Medical Imaging Conference, 1993., 1993 IEEE Conference Record., 31 Oct-6 Nov 1993 1993. 1842-1846 vol.3.
Vaquero, J. J., Lage, E., Ricon, L., Abella, M., Vicente, E. & Desco, M. 2005a. rPET detectors design and data processing. *In:* Nuclear Science Symposium Conference Record, 2005 IEEE, 23-29 Oct. 2005 2005a. 2885-2889.
Vaquero, J. J., Lage, E., Ricón, L., Abella, M., Vicente, E. & Desco, M. 2005b. rPET Detectors Design and Data Processing. *IEEE Nuclear Science Symposium Conference Record*.
Vaquero, J. J., Molins, A., Ortuño, J., Pascau, J. & Desco, M. 2004. Preliminary results of the small animal rotational positron emission tomography scanner. *In:* Mol. Imag. Biol., 2004. 102.
Vicente, E., Herraiz, J. L., Canadas, M., Cal-Gonzalez, J., Espana, S., Desco, M., Vaquero, J. J. & Udias, J. M. 2010a. Validation of NEMA NU4-2008 Scatter Fraction estimation with 18F and 68Ga for the ARGUS small-animal PET scanner. *In:* Nuclear Science Symposium Conference Record (NSS/MIC), 2010 IEEE, Oct. 30 2010-Nov. 6 2010 2010a. 3553-3557.
Vicente, E., Herraiz, J. L., España, S., Herranz, E., Desco, M., Vaquero, J. J. & Udías, J. M. 2012a. Improved effective dead-time correction for PET scanners: Application to small-animal PET. *Phys Med Biol (Submitted)*.
Vicente, E., Herraiz, J. L., Seidel, J., Green, M. V., Desco, M., Vaquero, J. J. & Udias, J. M. 2012b. Regularization of 3D Iterative Reconstruction for a Limited-Angle PET Tomograph. *In:* Nuclear Science Symposium Conference Record (NSS/MIC), 2012 IEEE (*Accepted*), 2012b.
Vicente, E., Udías, A. L., Herraiz, J. L., Desco, M., Vaquero, J. J. & Udías, J. M. 2010b. Corrección de atenuación de imágenes PET usando datos de TAC en el escáner para animales pequeños Argus PET/CT. *Libro de Actas, CASEIB 2010*.
Vicente, E., Vaquero, J. J., Lage, E., Tapias, G., Abella, M., Herraiz, J. L., España, S., Udías, J. M. & Desco, M. 2006 Caracterización del Tomógrafo de Animales rPET. *Libro de Actas, CASEIB 2006*.
Wang, G. C., Huber, J. S., Moses, W. W., Qi, J. & Choong, W. S. 2006a. Characterization of the LBNL PEM camera. *Nuclear Science, IEEE Transactions on,* 53**,** 1129-1135.
Wang, Y., Seidel, J., Tsui, B. M., Vaquero, J. J. & Pomper, M. G. 2006b. Performance evaluation of the GE healthcare eXplore VISTA dual-ring small-animal PET scanner. *J Nucl Med,* 47**,** 1891-900.
Watanabe, M., Uchida, H., Okada, H., Shimizu, K., Satoh, N., Yoshikawa, E., Ohmura, T., Yamashita, T. & Tanaka, E. 1992. A high resolution PET for animal studies. *Medical Imaging, IEEE Transactions on,* 11**,** 577-580.
Wu, Y., Bowen, S. L., Yang, K., Packard, N., Fu, L., Burkett, G., Qi, J., Boone, J. M., Cherry, S. R. & Badawi, R. D. 2009. PET characteristics of a dedicated breast PET/CT scanner prototype. *Phys Med Biol,* 54**,** 4273-87.
Yamamoto, S., Amano, M., Miura, S., Iida, H. & Kanno, I. 1986. Deadtime correction method using random coincidence for PET. *J Nucl Med,* 27**,** 1925-8.
Yang, Y. & Cherry, S. R. 2006. Observations regarding scatter fraction and NEC measurements for small animal PET. *Nuclear Science, IEEE Transactions on,* 53**,** 127-132.
Yang, Y., Dokhale, P. A., Silverman, R. W., Shah, K. S., McClish, M. A., Farrell, R., Entine, G. & Cherry, S. R. 2006. Depth of interaction resolution measurements for a high resolution PET detector using position sensitive avalanche photodiodes. *Phys Med Biol,* 51**,** 2131-42.
Yang, Y., Tai, Y. C., Siegel, S., Newport, D. F., Bai, B., Li, Q., Leahy, R. M. & Cherry, S. R. 2004. Optimization and performance evaluation of the microPET II scanner for in vivo small-animal imaging. *Phys Med Biol,* 49**,** 2527-45.
Zaidi, H., Montandon, M. L. & Slosman, D. O. 2004. Attenuation compensation in cerebral 3D PET: effect of the attenuation map on absolute and relative quantitation. *Eur J Nucl Med Mol Imaging,* 31**,** 52-63.
Zhang, H., Bao, Q., Vu, N. T., Silverman, R. W., Taschereau, R., Berry-Pusey, B. N., Douraghy, A., Rannou, F. R., Stout, D.

B. & Chatziioannou, A. F. 2011. Performance evaluation of PETbox: a low cost bench top preclinical PET scanner. *Mol Imaging Biol,* 13**,** 949-61.

Zhang, H., Vu, N. T., Bao, Q., Silverman, R. W., Berry-Pusey, B. N., Douraghy, A., Williams, D. A., Rannou, F. R., Stout, D. B. & Chatziioannou, A. F. 2010. Performance Characteristics of BGO Detectors for a Low Cost Preclinical PET Scanner. *Nuclear Science, IEEE Transactions on,* 57**,** 1038-1044.

Zhou, J. & Qi, J. 2009. Theoretical analysis and simulation study of a high-resolution zoom-in PET system. *Physics in Medicine and Biology,* 54**,** 5193.

Zhou, J. & Qi, J. 2010. Efficient system modeling of a high-resolution zoom-in PET scanner. *In:* Nuclear Science Symposium Conference Record (NSS/MIC), 2010 IEEE, Oct. 30 2010-Nov. 6 2010 2010. 3501-3505.

Zhou, J. & Qi, J. 2011. Adaptive Imaging for Lesion Detection Using a Zoom-in PET System. *Medical Imaging, IEEE Transactions on,* 30**,** 119-130.